

MCGILL UNIVERSITY

DOCTORAL THESIS

**Observational probes of supermassive
black hole environments: from the event
horizon to the sphere of influence**

Author:

Hope BOYCE

Supervisor:

Prof. Daryl HAGGARD

*A thesis submitted in partial fulfillment of the requirements
for the degree of Doctor of Philosophy*

in the

McGill Space Institute & Department of Physics

McGill University

Tiohtià:ke/Montréal, Québec, Canada

©Hope Boyce, December 2022

Abstract

Observational probes of supermassive black hole environments: from the event horizon to the sphere of influence

by Hope BOYCE

There exists a two-way relationship between small-scale, short-timescale phenomena (e.g. transient accretion events) around supermassive black holes (SMBHs) and large-scale properties of their galaxies (e.g. size, mass, kinematics). This work focuses on characterizing SMBHs and their immediate environments. I present two investigations of Sagittarius A* (Sgr A*), the nearest SMBH to us, and a third investigation of the SMBH at the heart of NGC 1387. These three studies represent probes of SMBH environments at three differing spatial scales. In the first, coordinated multi-wavelength observations of Sgr A* are carefully analyzed, cross-correlated, and compared to spectral energy distributions modelling the matter accreting onto the black hole. The time scales of the variability suggest that the physical mechanisms may be operating on the scale of several Schwarzschild radii. The second investigation focuses on the multi-wavelength coordination during the 2017 Event Horizon Telescope Campaign to image Sgr A*. We characterize several X-ray flares and discuss the likely connection of this variability to the emission physics near the event horizon. The third investigation probes material out at the edge of the sphere of influence, where kinematic modelling of the molecular gas can accurately estimate the SMBH mass. With a central hole in the gas disk in NGC 1387, this exhibits the power of this method to estimate central BH mass even when emission is missing. I place these projects in the context of the literature and introduce ongoing projects that continue to probe SMBHs

and the environments at the centres of galaxies. Together these works span scales of 10s of parsecs down to a fraction of an AU. From the event horizon to the sphere of influence, this thesis demonstrates how gas dynamics in the centres of galaxies can be used to characterize the SMBHs that reside within.

Résumé

Observational probes of supermassive black hole environments: from the event horizon to the sphere of influence

par Hope BOYCE

Il existe une relation bidirectionnelle entre les phénomènes à petite échelle et à court terme autour des SMBH (e.g. les événements d'accrétion transitoires) et les propriétés à grande échelle de leurs galaxies (e.g. la taille, la masse, la cinématique). Ce travail se concentre sur la caractérisation des trous noirs supermassifs (SMBHs) et de leur environnement immédiat. Je présente deux études sur Sagittarius A* (Sgr A*), le SMBH le plus proche de nous, et une troisième étude sur le SMBH au cœur de NGC 1387. Ces trois études permettent de sonder l'environnement des SMBH à trois échelles spatiales différentes. Dans la première, des observations coordonnées de Sgr A* à plusieurs longueurs d'onde sont soigneusement analysées, mises en corrélation et comparées aux distributions spectrales d'énergie modélisant la matière qui s'accrète sur le trou noir. Les échelles de temps de la variabilité suggèrent que les mécanismes physiques peuvent fonctionner à l'échelle de plusieurs rayons de Schwarzschild. La deuxième enquête se concentre sur la coordination multi-longueurs d'onde pendant la campagne 2017 du télescope Event Horizon pour imager Sgr A*. Nous caractérisons plusieurs éruptions de X-rays et discutons la connexion probable de cette variabilité à la physique de l'émission près de l'horizon des événements. La troisième enquête sonde la matière au bord de la sphère d'influence, où la modélisation cinématique du gaz moléculaire peut estimer avec précision la masse du SMBH. Avec un trou central dans le disque de gaz de NGC 1387, cela démontre la puissance de cette

méthode pour estimer la masse centrale du SMBH même lorsque l'émission est absente. Je replace ces projets dans le contexte de la littérature et présente les projets en cours qui continuent à sonder les SMBH et les environnements au centre des galaxies. Ensemble, ces travaux couvrent des échelles allant de 10s de parsecs à une fraction d'UA. De l'horizon des événements à la sphère d'influence, cette thèse démontre comment la dynamique des gaz au centre des galaxies peut être utilisée pour caractériser les SMBHs qui y résident.

Acknowledgements

It has only been through the support of a large community of people that I have been able to produce this work and find myself at this point in my journey.

First of all I would like to thank my advisor, Daryl Haggard. Her genuine support and contagious enthusiasm were the most valuable encouragements for me each day. The commitment she has shown in fostering a supportive and friendly atmosphere for our group has been invaluable. Thank you for sharing your unending enthusiasm for black holes with me and for most of all your flawless success rate at making each time we meet end with an energizing and uplifting note. I cannot overstate how much your mentorship and kindness has meant to me.

I am grateful for Julie Hlavacek-Larrondo and Tracy Webb, my supervisory committee, for their interest in my research and career. I would also like to thank Martin Bureau and Tim Davis for their introduction to the wonderful world of molecular gas and for their support, patience, and enthusiasm throughout our shared projects. I am indebted to Gunther Witzel for his mentorship and wisdom on all topics Sgr A*, to Sebastiano von Fellenberg and Yigit Dallilar for their guidance when it came to SEDs, and to Joey Neilsen and Sera Markoff for their advice and expertise on the galactic center.

An enormous thank you to my first mentor in astronomy, Stan Shadick, who without which I would have never had the courage to apply to summer internships. Thank you especially to Nora Luetzgendorf who guided and encouraged me as a young scientist in leading my first manuscript. Thank you also to Shelley Wright who took me on as a summer undergraduate with no experience whatsoever, and to Tuan Do, for putting time into the summer program which helped inspire me to pursue graduate school.

To my fellow graduate students in Daryl's research group – thank you for your companionship during endless hack sessions and for the laughter over beers. To the wider

MSI and Rutherford student population – thank you for the solidarity we shared surviving aspects of studying in a global pandemic. A special thank you to all the treasured friends who I met throughout my time in graduate school.

Finally, thank you to the most important people in my life, who are my primary sources of light and joy. To my partner Shiny: you are brilliant, kind, and the person I most want to share my days with. Thank you for your fierce love and encouragement. I am eternally appreciative of both the bright energy and quiet care you always carry with you. To my sister Alison: it has been endlessly joyful to have you in my life. I am so proud of the person you are. Thank you for your clever jokes, your careful attention, and your wonderful friendship. To my sister Lorien: I learn more and more from you each day. Your wisdom and wit are unmatched. I feel tremendous pride and love to have you as a sibling and friend. To both of my sisters and my siblings in-law Arsh, Aman, Joyti, and Jasleen: thank you for all the heaps of laughter and love we've shared. I am so excited to continue our adventures. Finally, to my parents: Thank you for giving me the root of who I am. Thank you for always being there to talk with and lend a careful perspective. Thank you for growing with me and becoming my dear friends.

To all those named and everyone else who crossed my path and offered their kindness, inspiration, company and laughter, thank you.

Contributions

This research could not have been possible without the collaboration of many many people. Here I list the major contributions of myself and my collaborators. All other work presented in this thesis is my own unless indicated otherwise.

Introduction: Figure 1.1 is taken from [McConnell & Ma \(2013a\)](#). Figure 1.2 Is a combination of press images from NASA, ESA, STScI, Chandra, the UCLA Galactic Center Group, the GRAVITY Collaboration ([Gravity Collaboration et al., 2018a](#)), and the Event Horizon Telescope Collaboration ([Event Horizon Telescope Collaboration et al., 2022a](#)). The left panel of Figure 1.3 is a modified version of a Figure 6 in [Gillessen et al. \(2019\)](#) and the right panel is created by Martin Bureau. Text is my own. I annotated Figure 1.3 and produced Figure 1.4 and Figure 1.5.

Chapter 2: All co-authors of the resulting manuscript contributed in some way to the proposals, analysis, and interpretations in this work. They are all listed in Appendix D.1. Giovanni Fazio is the PI of the proposals for the *Sptizer* and *Chandra* data. Joe Hora reduced the *Sptizer* light curves. Giovanni Fazio reduced the *NuSTAR* light curves. Sebastiano von Fellenberg produced the VLT/GRAVITY light curve and integrated fluxes, which are published in [GRAVITY Collaboration et al. \(2021\)](#). Gunter Witzel produced the ALMA light curves. The Bayesian flare detection python routine `bblocks` is from [Williams et al. \(2017a\)](#). The z-transform discrete correlation function `ZDCF` is from [Alexander \(1997\)](#). Yigit Dallilar developed `flaremodel` ([Dallilar et al., 2022](#)).

I reduced the *Chandra* light curves and characterized the variability in all the data. I wrote the code to implement `zdcf` within the Monte-Carlo routine to assess correlated variability between light curves. I used `flaremodel` to fit the SEDs and explore difference scenarios for the radiative mechanisms. I produced all the tables and plots and wrote the vast majority of the text.

Chapter 3: Daryl Haggard, Michael Janssen, and Vincent Fish were the lead coordinators for the collaboration paper [Event Horizon Telescope Collaboration et al. \(2022b\)](#). The entire author list is listed in Appendix D.2. Shuo Zhang produced the *NuSTAR* light curves. Maciek Wielgus provided the ALMA and SMA light curves which are described in [Wielgus et al. \(2022\)](#). Data from the East Asian VLBI are from [Cho et al. \(2022\)](#). GMVA data are from [Issaoun et al. \(2019b\)](#). Joseph Neilsen jointly fit the *Chandra* and *NuSTAR* data to produce Figure 3.4 and Table 3.2. Gunther Witzel compiled the literature data points in Figure 3.5.

I reduced the *Chandra* light curves and characterized the flares with `bblocks`. I produced Figure 3.3, Figure 3.5, and Table 3.1. I prepared all the corresponding multiwavelength data products released with the paper. Text was collaboratively written by the paper coordinators along with myself and the small writing team. In particular I wrote significant portions of 3.4.2 and 3.5 and contributed to the Introduction (3.1) and Conclusions (3.6).

Chapter 4: Martin Bureau and Timothy Davis are the PIs for the ALMA data. Timothy Davis developed the `KinMS` and `gastimator` tools. Michele Cappellari developed `MgeFit`. Mark Smith developed `skysampler`.

I constructed and cleaned the ALMA datacubes. I produced the MGE and resulting mass model from the Hubble data with `MgeFit`. Utilizing `KinMS`, `gastimator`, and `skysampler` I fit the low resolution and high resolution data cubes to constrain the SMBH mass and produced all figures in the chapter.

Chapter 5: Gordon Garmire was the PI for *Chandra* data on August 13, 15, and 19 in 2019. Joseph Neilsen was the PI for *Chandra* data coordinated with the EHT in 2018 and 2022. Daryl Haggard was the PI for *Chandra* data coordinated with the EHT in 2021. Anan Lu analyzed the data for NGC 3169 and produced Figure 5.5. Figure 5.6 is courtesy of the WISDOM collaboration.

I reduced and analyzed all Chandra light curves presented and produced Figure 5.1, Figure 5.2, Figure 5.3, and Figure 5.4. Text is my own.

Appendices: I produced all text, figures and tables in the Appendices.

Contents

Abstract	i
Résumé	iii
Acknowledgements	v
Contributions	vii
1 Introduction	1
1.1 In the heart of every galaxy	1
1.1.1 Sphere of Influence	5
1.1.2 Approaching the Event Horizon	6
1.2 Techniques/Background	10
1.2.1 Spectral Energy Distribution	10
flaremodel	10
1.2.2 Cross-correlation	12
ZDCF	12
1.2.3 Kinematic Modelling	13
KinMS	13
1.3 This Dissertation	15
2 Multi-wavelength Variability of Sagittarius A*	16
2.1 Introduction	16

2.2	Observations and Data Reduction	22
2.2.1	Spitzer	22
2.2.2	Chandra	24
2.2.3	NuSTAR	25
2.2.4	GRAVITY	26
2.2.5	ALMA	26
2.3	Analysis	28
2.3.1	Flare Characterization	28
2.3.2	Multi-wavelength Timing	31
2.4	Discussion	35
2.4.1	(A) +SYNC+SYNC: An evolving synchrotron source	39
2.4.2	(B) SYNC+SYNC+SSC: An adiabatically cooling synchrotron source	40
2.4.3	(C) SYNC+SSC+SSC: An adiabatically cooling synchrotron source	43
2.5	Summary	49
3	Multi-wavelength Coordination with the Event Horizon Telescope	52
3.1	Introduction	53
3.2	Event Horizon Telescope Observing Campaign	57
3.3	EHT Data Calibration and Reduction	60
3.4	Multi-wavelength Observing Campaign	62
3.4.1	Supplementary Ground-based Observations	62
	East Asian VLBI Network	62
	Global 3 mm VLBI Array	63
	Very Large Telescope	63
3.4.2	Coordinated Space-based Observations	64
	Neil Gehrels Swift Observatory	64
	Chandra X-ray Observatory	65

	Nuclear Spectroscopic Telescope Array	66
	X-ray Flare Spectral Analysis	68
3.5	Final Data Products and Features	71
3.5.1	Event Horizon Telescope Data	71
3.5.2	Multi-wavelength Data	72
	mm, NIR, and X-ray data products	72
	Time-averaged spectral energy distribution	73
	Characteristic multi-wavelength variability	74
3.6	Summary and Conclusions	78
4	Measuring SMBH masses through molecular gas kinematics	81
4.1	Introduction	82
4.2	NGC 1387	85
4.3	ALMA Observations	86
4.3.1	Line Emission	87
4.4	Kinematic Modelling	87
4.4.1	Stellar Potential	89
4.4.2	Gas Distribution and Disk Properties	90
4.4.3	Best-fitting model	91
4.5	Discussion and Future Analysis	92
5	Discussion	97
5.1	Discussion of main projects	97
5.2	Current and Future Work	99
5.2.1	Sgr A* & M87*	99
	Multi-wavelength Variability of Sgr A*	100
	EHT 2018 2021 2022 data	101
	Double Peak	104

5.2.2	Extragalactic Studies	104
	Star Formation Characterization In Galactic Centers	104
5.3	Conclusion	108
A	Simultaneous NIR and X-ray Variability from Sgr A*	110
A.1	Time lags from the Spitzer–Chandra campaign	110
A.2	Summer 2019	112
A.3	Illustration of SED models (B) and (C)	112
B	Multiwavelength coordinaiton with EHT	115
C	Technical Justification of the SITELLE-WISDOM proposal	118
D	Full Author Lists and Acknowledgements	122
D.1	Chapter 2: Multi-wavelength Variability of Sagittarius A*	122
D.2	Chapter 3: Multi-wavelength Coordination with the Event Horizon Telescope	124

List of Figures

1.1	$M_{\text{BH}}-\sigma$ scaling relation	3
1.2	Multi-wavelength views of the Galactic Center	7
1.3	Measured density profile of Sgr A*'s accretion flow and the circular velocity – radius relation for SMBH mass measurements	8
1.4	Illustration of Sgr A*'s quiescent and variable SED	11
1.5	Density and circular velocity profiles of different galactic components	14
2.1	Simultaneous submm, IR, and X-ray light curves of Sgr A* from July 2019	23
2.2	Cross-correlating NuSTAR, Chandra, GRAVITY, and ALMA light curves against Spitzer on July 17/18, 2019	30
2.3	Cross-correlating ALMA light curves against Spitzer on July 21 and 26, 2019	32
2.4	Time lags between all multiwavelength observations and Spitzer 4.5 μm light curves for the Sgr A* July 2019 campaign	33
2.5	Illustration of the three example SED models at the time of the NIR/X-ray peak (t=0)	38
2.6	Snapshots of the time evolution of scenario (C) SYNC-SSC-SSC, fit under adiabatic expansion.	42
2.7	Light curves derived from equations 2.1, and 2.2 offset with the constant flux values originating from the putative constant synchrotron component	47
3.1	EHT 2017 observing schedules for Sgr A* and its calibrators, covering ob- servations on April 6–7 2017	57

3.2	Instrument coverage of Sgr A* during the 2017 April 3–15 multi-wavelength observing campaign	58
3.3	Light curves from ALMA and SMA along with (quasi-)simultaneous, coordinated Swift Chandra and NuSTAR observations on 2017 April 6, 7, and 11	67
3.4	Joint Chandra-NuSTAR spectra of flares from Sgr A*	68
3.5	The time-averaged SED for the compact Sgr A* source during the 2017 EHT run in the context of a historic quiescent + variable SED	75
4.1	Optical images of NGC 1387 from the ground and space	85
4.2	Moment maps and spectrum of the CO(2-1) emission in NGC 1387	88
4.3	MGE model of NGC 1387 overlaid on the HST image	90
4.4	The inner arcseconds of NGC 1387's central gas disk	92
4.5	Corner plot showing the covariances between all model parameters from our MCMC fit	93
4.6	Comparison between the PVD of the data and illustrative kinematic models	95
5.1	A comparison of Sgr A* and M87 Variability	100
5.2	Chandra 2–8 keV Sgr A* flare on August 20	101
5.3	Chandra 2–8 keV flare on April 24 of the 2018 EHT campaign	102
5.4	Both Chandra light curves of Sgr A* from the EHT 2022 campaign	103
5.5	H α and CO flux of NGC 3169, overlaid on a deep image taken with SITELLE along with the spatial distribution of molecular gas and HII regions	106
5.6	ALMA CO Integrated intensity maps of four 2022B SITELLE targets	107
A.1	Time lags between IR and X-ray flares as reported in this work in the context of the literature.	111
A.2	2-8 keV light curves of Sgr A* captured by Chandra in Summer 2019	113

A.3	Exaggerated illustration of SED models (B) and (C)	114
B.1	Chandra 2-8 keV light curves of Sgr A* during the 2018 EHT campaign . . .	116
B.2	Chandra 2-8 keV light curves of Sgr A* during the 2021 EHT campaign . . .	117
C.1	SITELLE SNR map of $H\beta$ for central region of NGC 3169 ($D\sim 23$ Mpc) . . .	120

List of Tables

2.1	Data sets analysed in this work.	21
2.2	Time delays with respect to 4.5 μm (Spitzer) for X-ray (NuSTAR, Chandra), $\sim 2 \mu\text{m}$ (GRAVITY), and 340 GHz (ALMA) variability.	34
2.3	Values for the Sgr A* SED observed by coordinated ground-based and space- based observatories on 2019 July 18.	43
2.4	Best fit parameters of scenario C: SYNC+SSC+SSC.	45
3.1	Values for the Sgr A* SED observed by coordinated ground-based and space- based observatories during the EHT 2017 run.	61
3.2	Chandra/NuSTAR Joint Spectral Parameters	70
4.1	MGE best-fitting Gaussians	91
4.2	Best-fitting model parameters with associated formal uncertainties	94
5.1	List of SITELLE Targets	108
A.1	Time Lags: Spitzer/Chandra Flares	112
C.1	Filter Configurations for SITELLE proposal	121

Chapter 1

Introduction

The study of supermassive black holes (SMBHs) is a humbling undertaking that touches on timescales of billions of years and on masses that are billions of times the mass of our own star. It may be impossible to intuit what these timescales and masses really mean, but it has been my privilege to glimpse some of that wonder that occurs deep in the centers of galaxies.

1.1 In the heart of every galaxy

The first observational evidence for the existence of SMBHs came from quasars, first described in [Schmidt \(1963\)](#) as “A Star-Like [quasi-stellar] Object with Large Red-Shift”. This object and many others like it were remarkable since absorption lines in their spectra indicated they were located extremely far away for something that shone so brightly, making them some of the most luminous objects in the universe. Along with being so bright, their rapid changes in flux implied that they would be tiny. The region in which the gravitational potential of the black hole dominates would become to be known as the sphere of influence (r_{sph}) and is typically 1 – 100 pc, corresponding to a size of 0.1'' – 1'' on the sky for nearby galaxies (distances of 1 – 20 Mpc). For accretion to be the explanation for quasars' luminosity, the central black hole was required to be $M_{\text{BH}} \sim 10^6 - 10^9 M_{\odot}$. Imagining material falling onto these massive objects and the potential energy that they would release,

the idea that quasars and active galactic nuclei (AGN) were powered through accretion onto SMBHs eventually became widely accepted (Hoyle & Fowler, 1963; Salpeter, 1964; Zel'dovich, 1964; Lynden-Bell & Rees, 1971).

It then took several decades for the direct dynamical influence of such a massive dark object to be observed in the centers of nearby galaxies. From the mid 80's to the mid 90's ground-based searches targeting the signature of increased velocity dispersion in nearby galactic centers yielded about seven detections (reviewed in Kormendy & Richstone, 1995). Then the launch of Hubble in the 1990's provided ~ 5 times better spatial resolution and enabled the first demographic studies of BHs and their host galaxies (Kormendy & Ho, 2013). Since then there have been an expanding suite of techniques and technological advances. For galaxies with AGN whose r_{sph} is unresolvable, the width of emission lines from the "broad-line region" can be used along with an approximation of the distance between the region and the black hole to estimate the central mass. Within r_{sph} , adaptive optics in the infrared increase the spatial resolution and minimize dust contamination for observations of stellar dynamics. Also probing the Keplerian rise in velocities, the dynamics of ionized or molecular gas disks can trace the signature of a SMBH's potential. Finally, megamaser disks in edge-on galaxies can trace these signatures at unprecedented distances away from the SMBH (e.g. Moran, 2008).

Figure 1.1 from McConnell & Ma (2013a) plots 72 SMBH mass measurements against their host galaxy's stellar velocity dispersion. This is an example of the now well known scaling relations between SMBHs and their host galaxy's properties (see also bulge luminosity and mass). Different types of galaxies follow M_{BH} -galaxy scaling relations distinctly (Figure 1.1). Crucially, the observational techniques used to measure SMBH masses also differ between galaxy types, with elliptical galaxies being easier to measure through stellar kinematics, spirals through ionized gas, and AGN hosts through maser kinematics. Though individual studies take great care to reduce bias, there remains a danger that observational biases muddy the waters in interpreting SMBH correlations among different

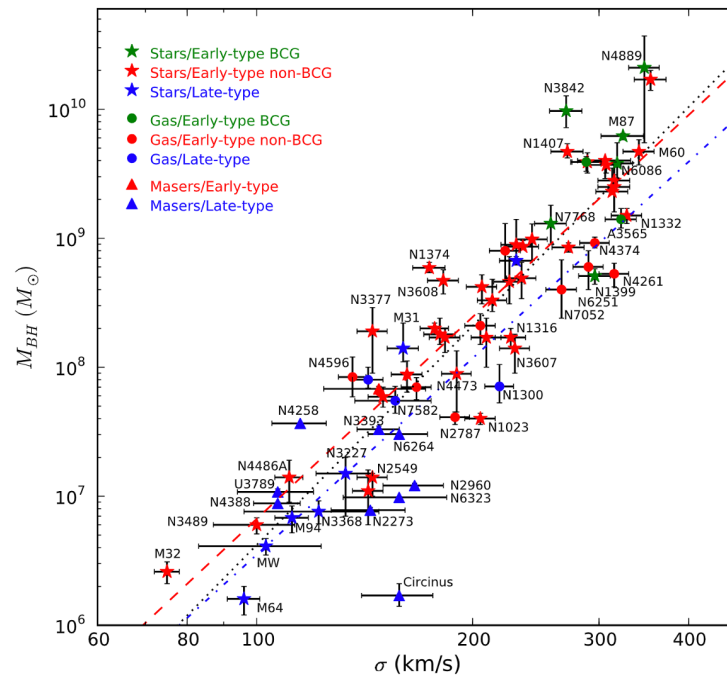


Figure 1.1 $M_{\text{BH}}-\sigma$ scaling relation of 72 galaxies from [McConnell & Ma \(2013a\)](#). Brightest cluster galaxies (BCGs) are indicated in green, elliptical galaxies are plotted in red, and late-type spiral galaxies are plotted in blue. Different symbols indicate the dynamic tracer used for the measurement from masers (triangles), stars (stars), to ionized gas (gas). The red line indicates a fit to the early-type galaxies only, while the blue line indicates a fit to the late-type galaxies and the black line is the fit to all galaxies.

galactic components and types. A method that could be widely applied to galaxy's of all types is required to disentangle true correlations from scatter (see Chapter 4).

Remarkably, though SMBHs environments are physically tiny on the scale of a galaxy (within the central few parsecs and orders of magnitude less massive), the correlation between them and characteristics of their host galaxies point to their influence on each other. This trend between the mass of the SMBH (M_{BH}) and velocity dispersion of the stars in the galactic bulge (σ) occurs across many orders of magnitude and indicates that the black hole and the host galaxy co-evolve — linked via physical mechanisms generically referred to as “feedback” (e.g., [McConnell & Ma, 2013b](#)). Many possible feedback mechanisms have been investigated, including (1) mechanical feedback whereby outflowing material from the accreting black hole sweeps up material and drives it across the galaxy,

changing the gas reservoir available for star formation (e.g., [McNamara & Nulsen, 2007](#); [Hlavacek-Larrondo et al., 2015](#)), (2) line driving and radiation pressure on dust whereby the hot photons from the SMBH's accretion disk heat and disperse gas and dust in the inner regions of the galaxy [Proga & Kallman](#) (e.g., 2004); [Ishibashi & Fabian](#) (e.g., 2015), and (3) columnated outflows or “jet-mode feedback”, which converts enormous quantities of gravitational energy to radiative energy but whose cross section of interaction with the host galaxy is small (e.g., [Best et al., 2005](#)). In the current favoured cosmological model of hierarchical structure formation, these inflows and outflows are likely triggered by galaxy collisions (and/or bar interactions), fuelling a peak in SMBH growth at redshift ~ 2 .

Sgr A*, the SMBH in the Milky Way, does not currently belong to the class of rapidly accreting black holes, a.k.a., active galactic nuclei (AGN). In fact, its present-day accretion rate is extremely small and would not be observable to an astronomer in a distant galaxy. There is evidence, however, that Sgr A* was much more active in the past. Studies of X-ray “light echoes” in the Galactic Centre point to outbursts from the SMBH as recent as 140 years and 240 years ago (e.g., [Clavel et al., 2013](#)), and outflows (“bubbles”) detected in the X-ray by XMM Newton ([Ponti et al., 2019](#)) and in γ -rays by the Fermi LAT ([Su et al., 2010](#)) point to even stronger outflows in the more distant past.

From both cosmological simulations and observations across galaxy types, there is strong evidence for both the host galaxy's influence on the SMBHs growth (e.g. merging galaxy's triggering massive accretion along with the central two SMBHs possibly merging) and the central SMBHs influence on the host (e.g. jets punching through to the edge of their galaxy, heating gas and quenching star formation). From the central stellar clusters to distant spiral arms and the most remote stars in the outskirts of elliptical galaxies, SMBHs seem to be connected at every scale of their galactic homes.

1.1.1 Sphere of Influence

To orient us with the range of spatial scales discussed in this thesis we introduce the Schwarzschild radius defined for for any black hole as

$$R_S = \frac{2GM_{\text{BH}}}{c^2} \quad (1.1)$$

where c is the speed of light.¹

The edge of the sphere of influence is typically $10^{5-7} R_S$, and is the region within which the gravitational potential of the SMBH dominates over that of the galaxy. It is not defined for isolated black holes but depends on both the mass of the BH and the galaxy (traced by σ , bulge luminosity):

$$r_{\text{sph}} = \frac{GM_{\text{BH}}}{\sigma^2} \quad (1.2)$$

where G is the gravitational constant, M_{BH} is the mass of the BH and σ is the velocity dispersion of the stars in the galactic bulge.

The Bondi radius is very similar in that it defines the radius within which surrounding gas and dust is likely to fall towards the BH and be accreted ($2GM/c_s^2$). Differentiating it from the sphere of influence is that it takes into account the sound speed of the medium (c_s) and the resulting accretion rate includes the medium's density as well as the relative speed of the BH through the material. Figure 1.3 marks the Bondi radius of Sgr A* at $\sim 10^5 R_S$.

There are several techniques to measure SMBH mass which trace the Keplerian velocities within the sphere of influence. These include modelling observed stellar dynamics with adaptive optics (typically $10^{3-5} R_S$), measuring maser emission in edge-on gas rich galaxies (e.g. Moran, 2008) that probe some of the smallest angular scales at a few milliarcseconds ($\sim 10^5 R_S$ for the observable galaxies that have molecular masing disks), mapping

¹299,000,000 m/s

ionized gas disks whose models (assuming the gas is in a dynamically cold disk) can be conceptually simpler than modelling the distribution and orbits of stars, and thanks to the exquisite resolving power of the Atacama Large Millimeter/submillimeter Array (ALMA), mapping molecular gas disks (e.g. [Davis et al., 2013a](#)). This method resolves molecular disks of nearby galaxies with typical beam sizes of ~ 0.1 arcseconds. Since the relatively rare maser targets are farther away probing molecular gas disks can reach scales of similar gravitational radii ($\sim 10^5 R_S$, see [Figure 1.3](#)).

The most convincing measurement of a SMBH is Sgr A* at the center of our galaxy. Sitting at the galactic center ~ 8 kiloparsecs (kpc) away, it is orders of magnitude closer than any other SMBH, which sit at distances of megaparsecs. Due to its proximity, ground-based observations have traced the orbits of individual stars over the last two decades to definitively infer that a dark mass of $\sim 4 \times 10^6 M_\odot$ ([Boehle et al., 2016a](#); [Gravity Collaboration et al., 2022](#)) must reside within the central few parsecs. The complete orbit of the closest observable star S2, has even validated relativistic predictions for redshift ([Do et al., 2019a](#); [Gravity Collaboration et al., 2018b](#)) and precession ([Gravity Collaboration et al., 2020a](#)) of the star's closest approach. [Figure 1.2](#) displays several of the varied multiwavelength views of our galactic center and Sgr A*'s position at the heart of it all.

1.1.2 Approaching the Event Horizon

Moving in much closer to the SMBH, we approach the event horizon. Technological advancements in optical interferometry have made it possible to precisely measure Sgr A*'s position on the sky and track its apparent motion during moments of increased infrared intensity ([Gravity Collaboration et al., 2018c](#)). During an infrared flare, Sgr A* appears to move in a circle on the sky – behaviour that is consistent with a hotspot in the accreting plasma orbiting the SMBH. Plasma at these distances from Sgr A* is likely hot, turbulent, and highly magnetized, though exactly how these temperatures, motions, and fields are

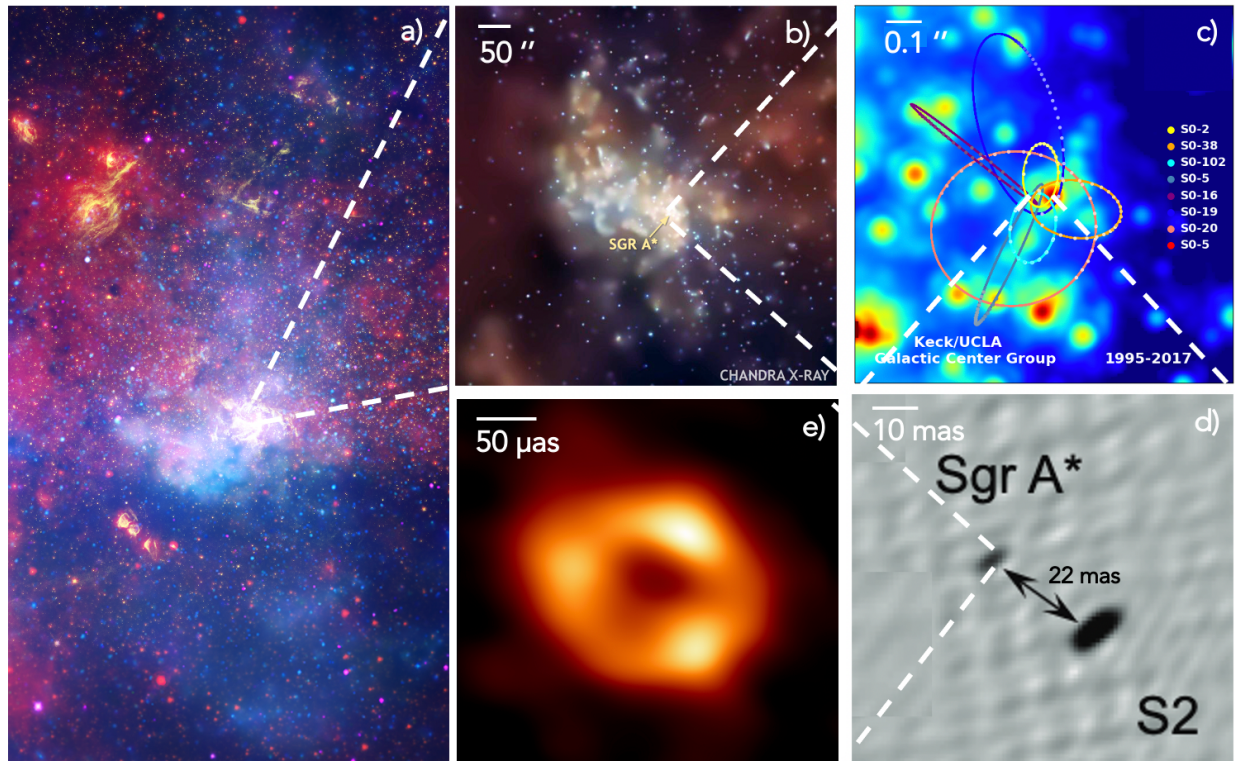


Figure 1.2 Multi-wavelength views of the Milky Way's galactic center and its supermassive black hole, Sgr A*. *a)* Large Scale view of the galactic center. Yellow emission is captured by Hubble and traces starlight and ionized gas in the near-infrared, red emission traces the glowing dust clouds in complex structures and is measured in the infrared with Spitzer, blue and violet traces heated gas at millions of degrees glowing in the X-ray and measured with Chandra. *b)* A zoomed in view of the inner X-ray structures from Chandra. *c)* From the Keck/UCLA Galactic Center Group, the near infrared view of the stars and their mapped orbits around Sgr A* within the innermost arcsecond (Ghez et al., 2008; Meyer et al., 2012). Orbits of these innermost stars are in the range $10^3\text{--}5 R_S$. *d)* Near simultaneous view of Sgr A* and the star S2 captured by the four-telescope optical interferometric instrument GRAVITY (Gravity Collaboration et al., 2018a). *e)* Interferometric submillimeter image of the Sgr A*, shown to be consistent with the expected appearance of a SMBH with mass $\sim 4 \times 10^6 M_\odot$ (Event Horizon Telescope Collaboration et al., 2022a). The radius of this ring is approximately $5 R_S$.

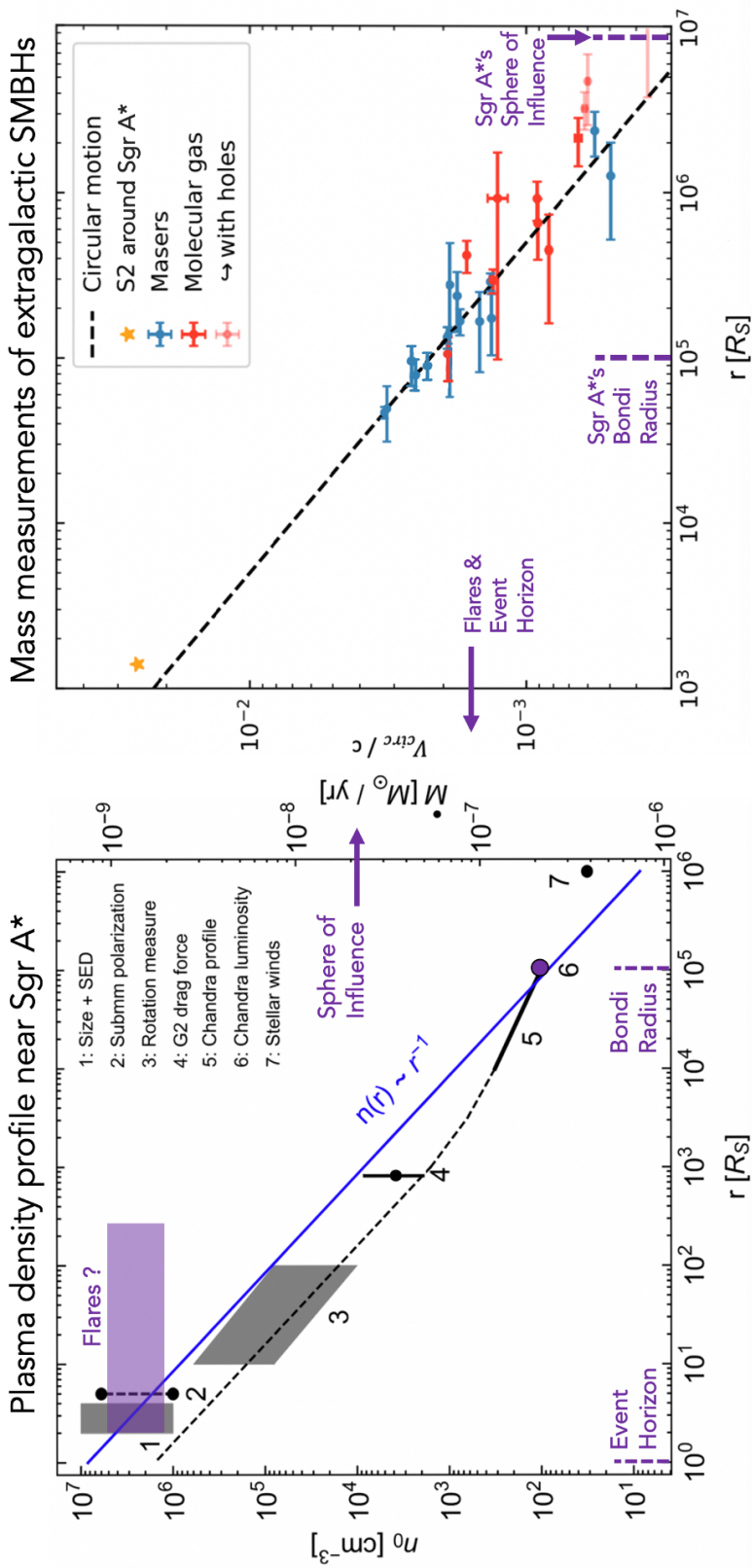


Figure 1.3 **Left:** Measured density profile of Sgr A*'s accretion flow. The sphere of influence, estimated from a measure of the Milky Way's bulge stellar velocity dispersion of $\sim 140\text{km/s}$ (Valenti et al., 2018), would be around $10^7 R_s$. Measurement 1 comes from one-zone models of the inner accretion zone using the resolved size (Doeleman et al., 2008a) and flux at the submillimeter peak of the SED (Bower et al., 2015a; von Fellenberg et al., 2018a). These are consistent with the results of detailed models using relativistic MHD simulations (e.g. Mościbrodzka et al., 2009a; Dexter et al., 2010; Shcherbakov et al., 2012a). Measurement 2 uses the submillimeter polarization and flux (Agoi, 2000; Quataert & Gruzinov, 2000). Measurement 3 is based on the rotation measure (Bower et al., 2003; Marrone et al., 2006a, 2007a). Measurement 4 is derived from detecting the drag force on G2 Gillessen et al. (2019). The X-ray profile as measured in Wang et al. (2013a) from Chandra data is shown as measurement 5, normalized to match the value in (Baganoff et al., 2003a, measurement 6). Measurement 7 is the value derived in Quataert (2004), who simulated the accretion onto Sgr A* from stellar winds. The blue line is the model from Xu et al. (2006a). The black, dashed line tries to reconcile the measurements at all radii, predicting a density of 10^6 cm^{-3} in the central region. The right ordinate axis shows the corresponding accretion rate for standard accretion theory assuming a scale height $H/R = 0.3$, viscosity parameter $\alpha = 0.1$ and a virial ion temperature. This is a modified version of Figure 6 in Gillessen et al. (2019). **Right:** Circular velocity – radius relation for molecular gas SMBH mass measurements (red points) megamaser (blue points) and Sgr A*'s mass measured through the orbit of the star S2 (yellow star).

characterized, where the plasma comes from, and what powers the variability at submillimeter, infrared, and X-ray wavelengths remains a mystery.

The light crossing time for Sgr A* is about 20s ($t_M = GM/c^3$) and the period for the innermost stable circular orbit (ISCO) is 4–30 minutes (Event Horizon Telescope Collaboration et al., 2022b). While the orbits of the S-stars that enabled the mass of Sgr A* to be measured are at about $10^4 - 10^5 R_S$, the timescales of the flickering that we see across the electromagnetic spectrum (minutes to hours), imply that the physics powering correspond to sizes that are only a few to 10s of R_S . Peering into this extreme environment, the global radio interferometer the Event Horizon Telescope (EHT) has managed to image the plasma immediately around Sgr A* at $\sim R_S$ (Event Horizon Telescope Collaboration et al., 2022a).

The theories and simulations of accretion around SMBHs are extremely rich and are starting to bridge the gap to match certain aspects of observations. For example, relativistic magneto-hydrodynamic (MHD) simulations of Sgr A* (e.g. Mościbrodzka et al., 2009a; Dexter et al., 2010; Shcherbakov et al., 2012a) are consistent with electron densities of 10^{6-7} cm^{-3} estimated from modelling the inner accretion flow with estimates of the submillimeter peak of the spectral energy distribution (SED; Bower et al., 2015a; von Fellenberg et al., 2018a). Observations are increasingly filling in the mysteries of the space between the Bondi radius and the Event Horizon, as illustrated in the left panel of Figure 1.3. This is an essential frontier in SMBH astrophysics since the cosmological simulations that inform much of our understanding of the universe are anchored by local measurements of BHs and their host galaxies. Currently, the Bondi radius is roughly the resolution limit of many simulations, and so accretion onto SMBHs from the edge of the Bondi radius down to the event horizon is a black box that only observations can begin to shed light on.

1.2 Techniques/Background

1.2.1 Spectral Energy Distribution

The spectral energy distribution of Sgr A* characterizes the brightness of our SMBH from radio to the submm, through the infrared, all the way up to X-rays. Sampling this broad spectrum at as many frequencies as possible builds up a picture of the radiative physics originating from the accreting plasma around the SMBH. The left side of Figure 1.4 sketches the typically observed SED of Sgr A* in black with some possible components identified in different colors. The red hump representing synchrotron emission originates from electrons accelerating in the magnetic field around the SMBH. This feature is thought to be relatively persistent as there likely exists a constant population of electrons whose energies are in a thermal distribution. Some of these electrons may get excited into a distribution with more electrons at higher energies, resulting in synchrotron emission represented by the orange curve. Where synchrotron processes occur, there will also likely be inverse-Compton processes (represented by the blue curve), during which some photons from the synchrotron emission interact with the same population of electrons undergoing acceleration and get up-scattered to higher frequencies. The exact shape of each component depends heavily on physical properties of the plasma like the distribution of electron energies, optical depth, the density of electrons, and the strength of the surrounding magnetic field. Finally, in the X-ray regime, persistent Bremsstrahlung emission is produced at distances far away from the SMBH.

flaremodel

To model SEDs in Chapter 2, we use `flaremodel`, an open-source Python code for numerically modeling one-zone synchrotron sources² developed by Dallilar et al. (2022). Parameters include n_e , electron density of the plasma, R_0 , radius of the homogeneous sphere,

²Available at <https://github.com/ydallilar/flaremodel>

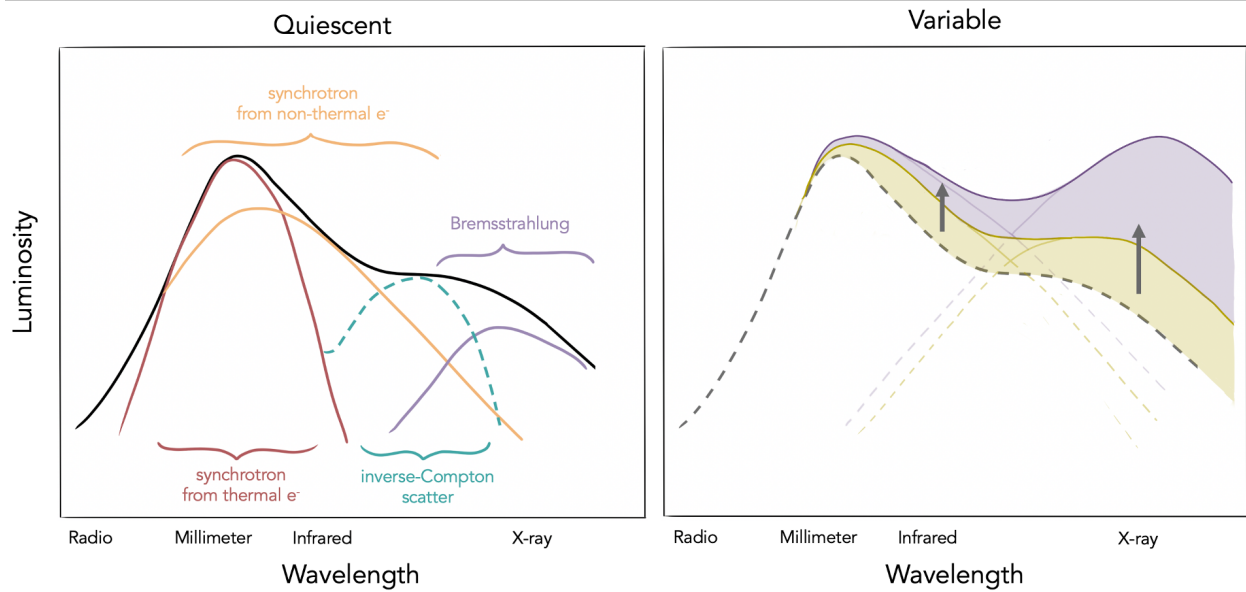


Figure 1.4 Illustration of Sgr A*'s quiescent and variable SED (luminosity vs. broadband wavelength). **Left:** The SED is composed of several co-added radiative processes, including synchrotron emission from thermal electrons (red solid line), synchrotron from non-thermal electrons (yellow solid line), inverse Compton scattering (teal dashed line), and thermal Bremsstrahlung radiation from the hot accretion flow at much larger radii (purple solid line). The synchrotron and inverse-Compton contributions vary during Sgr A*'s X-ray and NIR flaring events. The solid black line gives the full broadband SED for the components shown here. **Right:** Three examples of how the SED might change for flares of different luminosities (for the same SED contributions as are shown in the left-hand panel). The black dashed line corresponds to the total SED on the left, and the yellow and purple lines and shaded regions show possible SEDs for a moderate and bright flare, with energy injected primarily at X-ray and NIR wavelengths. For another illustration comparing two variable SED models, see Figure A.3 in Appendix A.

B , magnetic field strength, p , slope of electron distribution, γ_{max} , maximum Lorentz factor, and $\Delta\gamma$, the distance between the maximum and minimum γ in the electron distribution. The SED shapes and luminosities are sensitive to all parameters, but particularly distinguishing are the implied electron densities, magnetic field strength, and γ_{max} , which can be discussed within the context of observations of the galactic center that can probe these properties of the plasma at different distances from the SMBH (see Figure 1.3).

1.2.2 Cross-correlation

Variability is observed across all frequencies at which Sgr A* is detectable. Illustrated in the right panel of Figure 1.4, this is often most pronounced at submm, infrared, and X-ray wavelengths. Flares have often been observed to be correlated between frequencies, with the connection between infrared and X-ray being the strongest. Due to the serendipity required to catch flares at multiple wavelengths with multiple observatories, connecting individual events to definitive radiative processes remains a challenge. These simultaneous observations of multiwavelength variability will hold the key to understanding the physical phenomena of the plasma around Sgr A*. Chapters 2 and 3 both examine Sgr A*'s SED in two different observational contexts to constrain the radiative processes taking place.

ZDCF

To constrain correlations between flux increases at multiple wavelengths, we cross-correlate our observed light curves with the z-discrete correlation function $zdcf^3$, a tool capable of handling two unevenly sampled input light curves. In contrast to a classic cross-correlation function (ccf), the $zdcf$ does not interpolate the data or assume the light curves are smooth. Additionally, the $zdcf$ differs from other discrete correlation functions (dcf) by sorting all pairs of data points (a_i, b_j) by their time lags before binning them into chunks of equal population and calculating the correlation coefficients and errors on each bin. This ensures the resulting error bars are roughly equivalent to 1σ errors and that the correlation coefficients and their errors are always equal to or less than one.

³Available at <https://www.weizmann.ac.il/particle/tal/research-activities/software>

1.2.3 Kinematic Modelling

The circular velocity of a star (or parcel of gas) in orbit at a distance R around a mass M can be approximated by

$$v_{\text{circ}} \propto \sqrt{\frac{M}{R}} \quad (1.3)$$

The distribution of mass $M(r)$ inside R affects the shape of the resulting velocity curve. Figure 1.5 illustrates an example of a velocity curve for a galaxy containing a SMBH and typical distribution of stars sitting within a dark matter halo. The inset zooms into the center of the galaxy, where the influence of dark matter is minimal, and the signature of the central SMBH can be probed. Detecting elevated velocities of molecular gas at the centers of galaxies forms the basis of the work in Chapter 4.

KinMS

To model the gas disk at the center of NGC 1387 in Chapter 4, we utilize `KinMS`⁴, a flexible python package that can simulate gas distributions and create datacubes that can be compared to observations. Key inputs include properties of the gas disk (e.g. integrated flux, velocity dispersion, inclination, position angle, density profile, thickness), a model of the gravitational potential that the disk resides in (e.g. distribution of the stellar light of the galaxy and a prescription for converting this into mass M/L), and any central point mass large enough to affect the gas kinematics (e.g. a SMBH). For the purposes of detecting a central SMBH, the M/L assigned to the stellar light profile, the inclination of the disk, and any warps or irregularities to the gas distribution can significantly affect the measured velocities of the gas. If there is a Keplerian rise in the velocities near the center of the galaxy, a compact central mass is likely required to explain the data.

⁴Available at <https://github.com/TimothyADavis/KinMSpy>

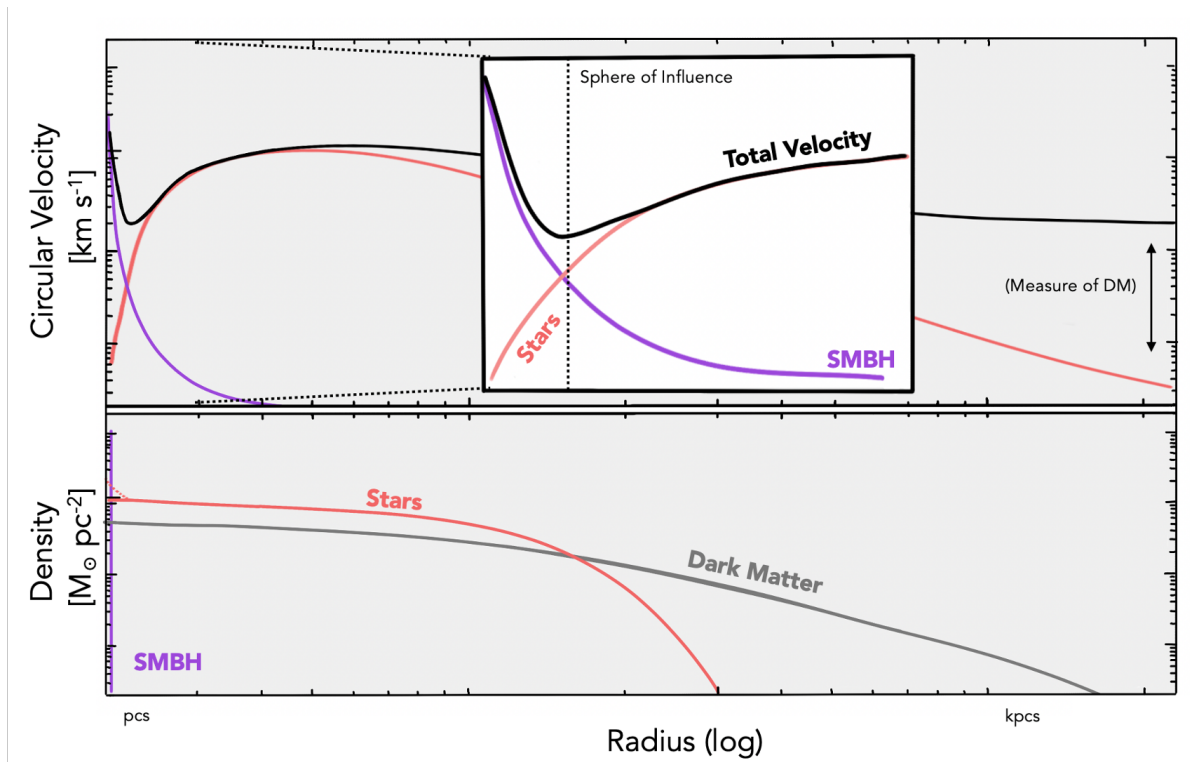


Figure 1.5 Illustration of the density and circular velocity profiles of different galactic components. **Top:** The purple line represents the rotation curve from a central point mass, the red line represents the rotation curve from a disk of stars, and the black line illustrates the total observed circular velocity of a material orbiting the center of a galaxy (including contribution from a dark matter halo). **Bottom:** Example density profiles that could qualitatively produce the rotation curves illustrated in the top panel. The purple, red and grey lines represent a central SMBH, a disk of stars, and a dark matter halo respectively. The stellar density profile may include a central peak if there is a nuclear star cluster (represented by the dashed red line).

1.3 This Dissertation

This work focuses on characterizing supermassive black holes (SMBHs) and their immediate environments. The three studies in this dissertation range from scales close to the black hole, where we image the event horizon and constrain models of accretion in strong gravitational and magnetic fields, and then move out to larger scales where we probe the kinematics of molecular gas orbiting out at the edge of the sphere of influence of an extragalactic SMBH. In the first investigation I focus on the multiwavelength flaring believed to originate close to Sgr A*, the central SMBH of the Milky Way ($\sim \text{few } R_S - 100 R_S$). Our second work probes even smaller scales around Sgr A*, where the Event Horizon Telescope (EHT) Collaboration has imaged the shadow of the supermassive black hole ($\sim R_S$). Though the spatial regions in these first two studies occupy a small physical portion of a galaxy's total extent, the third study of this thesis, moves out to $\sim 10^{5-7} R_S$ (10s of parsecs) where we present a measurement of the mass of the SMBH in the lenticular Fornax-cluster galaxy NGC 1387, obtained by modeling the kinematics of the molecular gas near the sphere of influence. From the event horizon to the sphere of influence, this thesis thus demonstrates how gas dynamics in the centres of galaxies can be used to characterize the SMBHs that reside within.

Text in this chapter is published in ApJ 931 7 (2022),
Multiwavelength Variability of Sagittarius A* in 2019 July
(Boyce et al.)

Chapter 2

Multi-wavelength Variability of Sagittarius A*

In our first investigation, we monitor the black hole at the centre of the Milky Way, Sagittarius A*, at multiple wavelengths over the course of three days in the summer of July 2019. At all monitored wavelengths, from X-rays to infrared to the submillimeter, the emission from Sgr A* is variable. We demonstrate that characterizing this emission and constraining the time lag(s) between variability at different wavelengths informs spectral energy distribution models of the accreting matter. These models in turn distinguish between the radiative mechanisms at play (e.g., synchrotron vs synchrotron self-Compton), which shed light on the physical mechanisms powering the observed flares originating from near the event horizon.

2.1 Introduction

Sagittarius A* (Sgr A*), the supermassive black hole (SMBH) sitting at the bottom of the central gravitational potential of the Milky Way, co-exists in a dynamic environment with

a dense stellar cluster, active star formation, and hot, inefficiently accreting gas. Over the past ~ 20 years, the mass ($\sim 4 \times 10^6 M_{\odot}$) and accretion rate ($\lesssim 10^{-7} M_{\odot} \text{yr}^{-1}$) of Sgr A* have been pinned down through careful analysis of stellar orbits (e.g., [Boehle et al., 2016a](#); [Gillessen et al., 2017](#)) and multi-wavelength flux measurements (e.g., [Baganoff et al., 2003b](#); [Marrone et al., 2006b, 2007b](#); [Shcherbakov et al., 2012b](#); [Yusef-Zadeh et al., 2015a](#); [Bower et al., 2018a](#)). These properties, along with its low bolometric-to-Eddington luminosity ratio ($L/L_{\text{Edd}} \sim 10^{-9}$; [Genzel et al., 2010a](#)) and characterizations of the quiescent spectral energy distribution (SED) have motivated models of advective and inefficient accretion flows (e.g., [Quataert, 2002a](#); [Baganoff et al., 2003b](#); [Yuan et al., 2003a](#); [Liu et al., 2004a](#); [Xu et al., 2006b](#); [Wang et al., 2013a](#)).

Though Sgr A* seems to be variable at every wavelength it has been observed, the physical mechanisms behind the changes in Sgr A*'s flux density remain uncertain. Physical models often invoke populations of accelerated electrons caused by magnetic reconnection events, jets, sudden disk instabilities, or other stochastic processes in the accretion flow (e.g., [Markoff et al., 2001](#); [Liu & Melia, 2002](#); [Yuan et al., 2003a](#); [Liu et al., 2004a](#); [Dexter et al., 2009](#); [Maitra et al., 2009](#); [Dodds-Eden et al., 2010](#); [Ball et al., 2016](#); [Li et al., 2017](#)). Additional models attempt to explain the variability in the context of tidal disruption of asteroids ([Čadež et al., 2008](#); [Kostić et al., 2009a](#); [Zubovas et al., 2012](#)) or expanding plasma blobs (e.g., [van der Laan, 1966](#); [Yusef-Zadeh et al., 2006a](#); [Marrone et al., 2008a](#); [Younsi & Wu, 2015](#); [Li et al., 2017](#)). Finally, emission may be amplified through strong gravitational lensing near the event horizon (e.g., [Chan et al., 2015](#)).

Variability in the NIR is expected to arise from a fluctuating non-thermal population of electrons. [Chen et al. \(2019\)](#) showed that Sgr A*'s IR variability was statistically consistent over two decades, never deviating from log-normal distribution of flux densities. This consistency was immediately challenged by the unprecedented IR brightness detected by [Do et al. \(2019b\)](#) in March 2019. Such a deviation from the usual statistical behaviour ([Do et al., 2009](#); [Meyer et al., 2009](#); [Dodds-Eden et al., 2011a](#); [Witzel et al., 2012a](#); [Hora et al.,](#)

2014; Witzel et al., 2018a) challenges the current model and could point to a dynamical interaction or a temporary change in Sgr A*'s accretion state.

The submm-THz bump in Sgr A*'s SED is often attributed to a steady synchrotron source originating from a thermal electron distribution (e.g., Bower et al., 2018a; von Fellenberg et al., 2018b). Submm flux from Sgr A* is variable down to timescales of seconds to hours (Murchikova & Witzel, 2021; Iwata et al., 2020a), suggesting source sizes on the same order as the BH's innermost stable orbit. Dexter et al. (2014) found an 8-hour characteristic timescale for the variability by analyzing light curves over a period of 10 years. Subroweit et al. (2017) presented a statistical analysis of submm variability at 345 GHz from 2008 to 2014, reporting a mean flux density measurement of ~ 3 Jy. In 190 hours of observations, the 345 GHz flux rose above 4.5 Jy only four times. Murchikova & Witzel (2021) reported observations of Sgr A* at 230 GHz in June 2019, finding that the mean flux level was 3.74 Jy: 20% higher than in 2015-2017 and 3% higher than levels in 2009-2012 and 2013-2014. Such variability (on the scale of ~ 10 years) is similar to the expected global mass accretion variability (Ressler et al., 2020).

Sgr A*'s faint, steady X-ray emission (Baganoff et al., 2001a, 2003b) is most likely thermal bremsstrahlung emission originating in the accretion flow near the Bondi radius (Quataert, 2002a; Baganoff et al., 2003b; Yuan et al., 2003a; Liu et al., 2004a; Xu et al., 2006b; Wang et al., 2013a). This quiescent state is interrupted about once per day by distinct X-ray flares of non-thermal emission presumed to be coming from very close to the black hole (Neilsen et al., 2013a, 2015a; Haggard et al., 2019a; Zhang et al., 2017a). The flux density distribution of the X-ray variability can be described by a power law (e.g., Neilsen et al., 2015a) or log-normal (Witzel et al., 2021a). Recent examination of long term X-ray variability suggests that Sgr A*'s flaring rate can change over the span of several years (Andrés et al., 2022).

There have been several studies reporting a correlation between submm and NIR/X-ray variability (e.g., Eckart et al., 2006b; Yusef-Zadeh et al., 2006b; Eckart et al., 2008a;

Yusef-Zadeh et al., 2009; Trap et al., 2011; Eckart et al., 2012; Mossoux et al., 2016; Fazio et al., 2018a). These provide increasing evidence that the submm and NIR/X-ray sources are physically or radiatively connected. Correlations between the radio and NIR remain less clear (Capellupo et al., 2017a).

To connect physical models with observables, studies have analyzed both the timing properties between wavelengths and SED characteristics of Sgr A* during quiescence and flares. They aim to put constraints on what radiative mechanisms must be at play. For example, there are models that predict simultaneity of NIR/X-ray flares through synchrotron self-Compton (SSC) processes (Markoff et al., 2001; Eckart et al., 2008b), those that cool the electrons of the synchrotron source to predict delayed low-frequency emission relative to the NIR/X-ray (e.g., Yusef-Zadeh et al., 2006b; Witzel et al., 2021a), and those that connect time lags to relativistic outflows (e.g., Brinkerink et al., 2021a). General-relativistic magneto-hydrodynamic (GRMHD) simulations also predict radiative models and observable SED characteristics scaled to Sgr A* (e.g., Mościbrodzka et al., 2009b, 2014), and even simulate light curves comparable to observations (Chatterjee et al., 2021).

There are several observational avenues that can be used to constrain properties of the plasma in the galactic centre. Observations of a magnetar at an angular distance of ~ 2.5 arcsec from Sgr A* (Mori et al., 2013; Rea et al., 2013) have been useful in constraining the interstellar scattering that affects observations in the vicinity of the SMBH (e.g. Bower et al., 2015b; Dexter et al., 2017). Such observations can constrain properties of the plasma and magnetic field (e.g. Eatough et al., 2013a). Even closer to the black hole, new observations by the Event Horizon Telescope (EHT) (Issaoun et al., 2021, e.g.,) and GRAVITY are beginning to probe the plasma and general relativistic effects near the event horizon. EHT observations of Sgr A* were collected in 2017, 2018, and are scheduled for 2022. Such high-resolution imaging will help untangle the dynamics of the plasma immediately around Sgr A* from the significant interstellar scattering between earth and the Galactic Center (e.g., Johnson et al., 2018; Issaoun et al., 2019a). Also probing near event-horizon scales,

the GRAVITY Collaboration has demonstrated that exceptionally precise near-infrared interferometry of Sgr A*'s position can probe the apparent motion of its centroid. This in turn can be successfully modelled as a hot-spot orbiting less than 10 gravitational radii away from the SMBH (Gravity Collaboration et al., 2018d).

Numerous joint X-ray and IR campaigns have observed Sgr A* over the last 16 years (Eckart et al., 2004, 2006b; Yusef-Zadeh et al., 2006b; Eckart et al., 2008b; Dodds-Eden et al., 2009a; Yusef-Zadeh et al., 2009, 2012a; Mossoux et al., 2016; Fazio et al., 2018a; Ponti et al., 2017a). Our joint Spitzer and Chandra study reported ~ 144 hours of coordinated observations collected between 2014 and 2017 (Boyce et al., 2019). These observations captured four modestly bright multi-wavelength flares from Sgr A*. Comparing the X-ray observations to simulations of the infrared statistical behaviour (Witzel et al., 2018a), the consistent observation of X-ray and IR events within 20 minutes of each-other point to a physical connection between the emission at these wavelengths, rather than chance association. In Boyce et al. (2019) we found the time lag between the peaks in the X-rays and the peaks in the IR was consistent with simultaneity and at most on order of 10~20 minutes.

Here we extend our original study by investigating the physical and temporal correlations between X-ray and IR variability with Spitzer and Chandra observations of Sgr A* in the summer of 2019, alongside simultaneous NuSTAR, GRAVITY, and ALMA monitoring. To constrain the particle acceleration responsible for flaring, Gravity Collaboration et al. (2021) analyze the Spitzer, GRAVITY, NuSTAR, and Chandra data of July 17–18 in the context of time-resolved SED modelling and found that the NIR and X-ray flare can be best modelled with a non-thermal synchrotron source. Michail et al. (2021a) combine the Spitzer NIR measurements with the 340 GHz ALMA measurements on July 18 to explore models that describe the NIR as SSC of a synchrotron source responsible for delayed submm emission adiabatically expanding. Bringing all available data together, this paper reports timing analysis between the five observatories on July 17–18, July 21, and July 26, and explores how SED models (see Section 2.4) can be constrained by the submm, NIR,

Table 2.1 Data sets analysed in this work.

Observatory	Date (UT)	OBSID	Start (UT)	End (UT)	Energy	Wavelength [frequency]	#Ant	Baselines (k λ)	calibrators
NuSTAR	2019-07-17	30502006002	21:51:09	08:34:21	3–70 keV	6.2–0.2 Å	-	-	-
	2019-07-26	30502006004	00:41:09	10:21:06	3–70 keV	6.2–0.2 Å	-	-	-
Chandra	2019-07-17	22230	22:51:26	14:51:26	2–8 keV	6.2–1.6 Å	-	-	-
	2019-07-21	20446	00:00:14	16:00:14	2–8 keV	6.2–1.6 Å	-	-	-
	2019-07-26	20447	01:32:40	17:32:40	2–8 keV	6.2–1.6 Å	-	-	-
GRAVITY	2019-07-17	0103.B-0032(D)	23:32:55	05:32:55	0.7–0.8 eV	2.2–1.65 μ m	-	-	-
Spitzer	2019-07-17	69965312	23:21:33	07:21:20	0.3 eV	4.5 μ m	-	-	-
	2019-07-18	69965568	07:25:02	15:24:49	0.3 eV	4.5 μ m	-	-	-
	2019-07-21	69965824	00:21:47	08:21:37	0.3 eV	4.5 μ m	-	-	-
	2019-07-21	69966080	08:24:49	16:25:05	0.3 eV	4.5 μ m	-	-	-
	2019-07-26	69966336	02:02:35	10:02:22	0.3 eV	4.5 μ m	-	-	-
2019-07-26	69966592	10:06:02	18:05:53	0.3 eV	4.5 μ m	-	-	-	
ALMA	2019-07-17	2018.A.00050.T	23:49:02	06:49:56	0.0014 eV	[340 GHz]	11	10.1–54.4	J1700-2610
	2019-07-20	2018.A.00050.T	03:55:59	06:47:57	0.0014 eV	[340 GHz]	11	10.1–54.4	J1733-3722
	2019-07-25	2018.A.00050.T	23:51:49	06:45:15	0.0014 eV	[340 GHz]	10	10.1–54.4	J1700-2610 J1717-3342

and X-ray timing data.

2.2 Observations and Data Reduction

The IRAC instrument (Fazio et al., 2004) on the Spitzer Space Telescope (Werner et al., 2004) observed Sgr A* at $4.5 \mu\text{m}$ for eight ~ 24 -hour-long stretches between 2013 and 2017. Six of these observations had simultaneous monitoring from the Chandra X-ray Observatory (Weisskopf et al., 2000) and are reported by Boyce et al. (2019). Since then, three additional epochs of simultaneous monitoring totalling ~ 48 -hours were observed. These additional epochs expand the total dataset to ~ 155 hours of simultaneous X-ray and IR data. Figure 2.1 displays these new 2019 epochs along with additional coordinated coverage from NuSTAR, GRAVITY, and ALMA. For an assumed distance of 8.2 kpc, $1'' = 0.040$ pc (Gravity Collaboration et al., 2019a)¹.

2.2.1 Spitzer

All Spitzer observations were collected in a similar manner as the previous epochs in the campaign. Hora et al. (2014) give a complete description of the Sgr A* Spitzer monitoring campaign. We offer a brief summary here. Three observing blocks were collected at $4.5 \mu\text{m}$ (filter width of $1 \mu\text{m}$) in each of the three 16 hour epochs: an initial mapping operation performed after the slew to the Sgr A* field followed by two successive 8 hour staring operations. Each staring operation began by using the “PCRS Pickup” mode to position Sgr A* on the center of pixel (16,16) in the IRAC subarray. The subarray mode for Spitzer/IRAC reads out 64 consecutive images (a “frame set”) of a 32×32 pixel region on the IRAC detector. This frame set is known as one Basic Calibrated Data product (BCD),

¹7.9 kpc would give $1'' = 0.038$ pc (Boehle et al., 2016b)

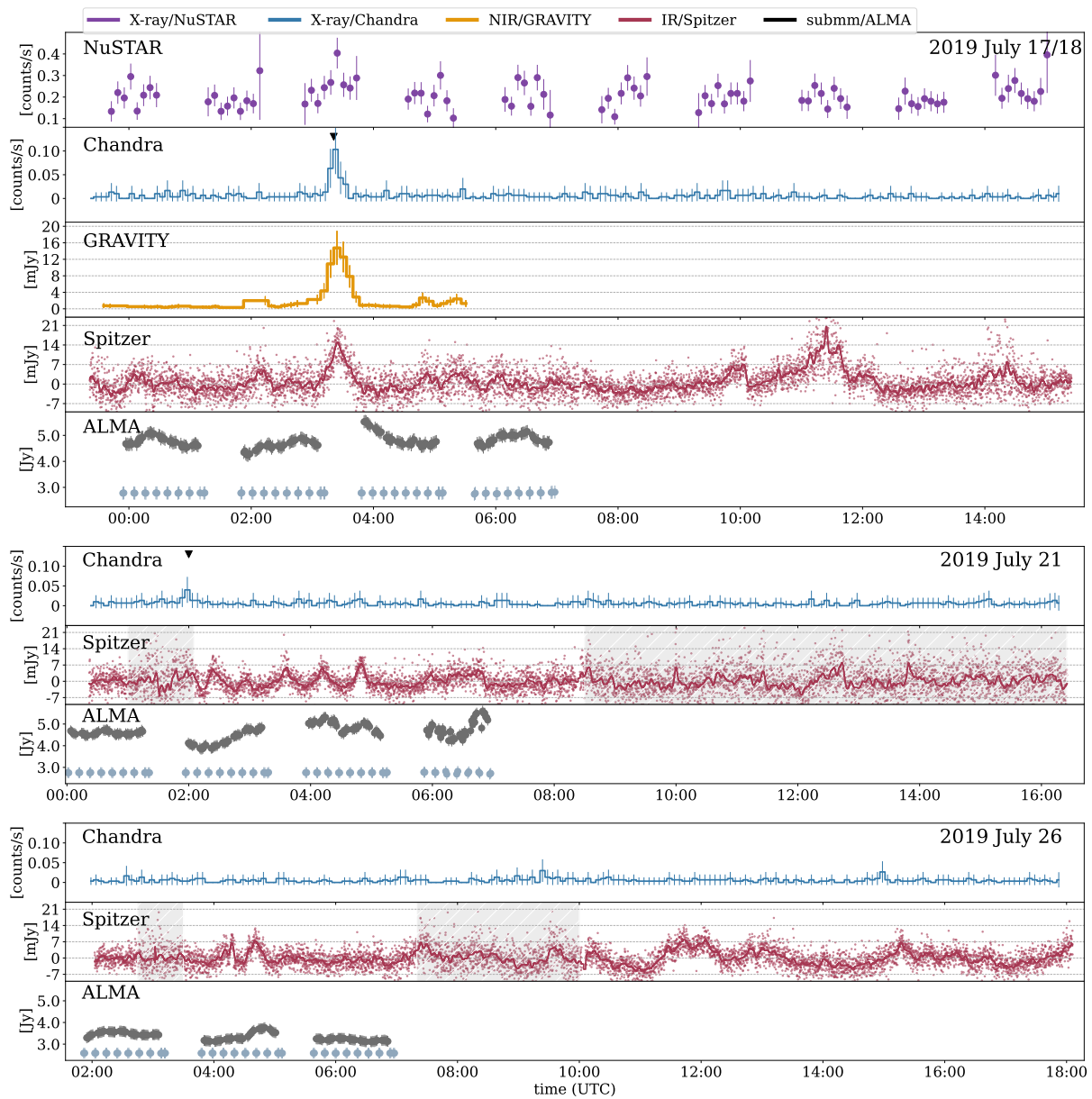


Figure 2.1 Simultaneous submm, IR, and X-ray light curves of Sgr A* from July 2019. The purple, blue, orange, red, and grey data show the NuSTAR 3–70 keV, Chandra 2–8 keV, GRAVITY 2.2 μm , Spitzer 4.5 μm , and ALMA 340 GHz data, respectively. The x-axis displays the barycentre-corrected UT on each date. Spitzer data at 4.5 μm is the excess flux density (mJy) of the pixel containing Sgr A* (see §2.1 of [Witzel et al., 2018a](#)) offset with a value of 1.9 mJy and de-reddened with the extinction $A_{K_s} = 2.42 \pm 0.002$ from [Fritz et al. \(2011\)](#). The red line shows the data binned over 3.5 minutes. Grey regions on July 21 and 26 indicate where the light curve is unreliable due to decreased signal-to-noise. The GRAVITY light curve was de-reddened assuming a K-band extinction of 2.42 ± 0.01 magnitudes. Significant X-ray flares in Chandra data are identified by the Bayesian Blocks routine ($p_0 = 0.05$) and indicated here with black arrows. ALMA calibrators are plotted in light grey for comparison.

which is the data format downloaded from the Spitzer Heritage Archive². Each component in the frame set is a 0.1 s 32×32 image, so one frame set takes 6.4 s to complete. After converting the pixel intensity into mJy, each frame set was combined into a single 32×32 image referred to as a “6.4 s BCD coadd”. Consecutive frame sets were typically separated by 2 s of telescope overheads, and this resulted in an observation cadence of approximately 8.4 s per frame.

To extract light curves of Sgr A* from the Spitzer/IRAC data, we used the same methodology as [Boyce et al. \(2019\)](#) and [Witzel et al. \(2018a\)](#), including an updated procedure based on the steps described in Appendix A1 of [Hora et al. \(2014\)](#). This procedure corrects for the varying intra-pixel sensitivity of the Spitzer/IRAC detector and the effect of nearby sources on the measured flux of Sgr A* as the telescope pointing jitters during the observations. The resulting light curves are the excess variable flux density in pixel (16,16) measured relative to the non-variable stellar background (~ 250 mJy). The baseline flux density of these IR light curves is unknown, though the value has been inferred to be 1.9 mJy from the cumulative distributions of flux densities of Sgr A* ([Witzel et al., 2018a](#)). As in [GRAVITY Collaboration et al. \(2021\)](#), we added an offset of 1.9 mJy and de-reddened the resulting values with the extinction $A_{K_s} = 2.42 \pm 0.002$ from [Fritz et al. \(2011\)](#) to produce the light curves plotted in [Figure 2.1](#).

2.2.2 Chandra

The simultaneous Chandra observations were acquired using the ACIS-S3 chip in the FAINT mode with a 1/8 subarray. The small subarray was chosen to avoid photon pileup during bright flares from Sgr A* and the nearby magnetar, SGR J1745–2900 ([Mori et al., 2013](#); [Rea et al., 2013](#); [Coti Zelati et al., 2015, 2017](#)).

²The Spitzer Heritage Archive (<http://irsa.ipac.caltech.edu>) is part of the NASA/ IPAC Infrared Science Archive, which is operated by the Jet Propulsion Laboratory, California Institute of Technology, under contract with the National Aeronautics and Space Administration.

We performed Chandra data reduction and analysis with CIAO v4.9 tools³ (Fruscione et al., 2006) and calibration database 4.7.3. The `chandra_repro` script was used to reprocess level 2 events files before the WCS coordinate system was updated (`wcs_update`). Barycentric corrections to the event times were performed with the CIAO tool `axbary`. We extracted a 2–8 keV light curve from a circular region of radius 1.25'' centered on Sgr A*. The small extraction region and energy range isolate Sgr A*'s emission from the nearby magnetar (e.g., Mori et al., 2013; Rea et al., 2013; Coti Zelati et al., 2017) and from the diffuse X-ray background (e.g., Baganoff et al., 2003b; Nowak et al., 2012a; Wang et al., 2013a). X-ray light curves are plotted in purple in Figure 2.1. Flux densities for SED modelling (Section 2.4) were corrected for dust scattering and absorption as described in GRAVITY Collaboration et al. (2021).

2.2.3 NuSTAR

The NuSTAR (Harrison et al., 2013a) data have been processed using the NuSTAR Data Analysis Software NUSTARDAS, HEASOFT v. 6.28, and CALDB v20200912. Data were filtered for periods of high instrumental background due to South Atlantic Anomaly passages and known bad detector pixels. We analysed the observations starting on July 17, 2019 21:51:09 and on July 26, 2019 00:41:09 (ObsID: 30502006002 and 30502006004, respectively). We applied the barycenter corrections. Light curves and spectra were extracted via the `nuproducts` tool from a region of radius 20'' centered on the position of Sgr A*. Because the focal plane modual B (FPMB) is contaminated by stray light from faraway bright X-ray sources outside of the field of view, we only present the analysis of the FPMA data (the results obtained with FPMB are consistent with the results). The light curves were accumulated in the 3–10 keV band and with 380 s time bins for comparison with the GRAVITY data. Bins with small fractional exposures were removed. Flux densities for SED

³Chandra Interactive Analysis of Observations (CIAO) software is available at <http://cxc.harvard.edu/ciao/>

modelling (Section 2.4) were corrected for dust scattering and absorption as described in [GRAVITY Collaboration et al. \(2021\)](#).

2.2.4 GRAVITY

The K-band (2.1–2.4 μm) GRAVITY light curve was derived from the coherent flux measurement of Sgr A* as described by [Gravity Collaboration et al. \(2020b\)](#) and [GRAVITY Collaboration et al. \(2021\)](#). We derived the flux ratios relative to S2 using separate observations. We de-reddened the flux assuming a K-band extinction of 2.42 ± 0.01 magnitudes. The light curve has been corrected for the contamination of S2 at the edge of the field of view and errors were scaled in the same way as described in [Gravity Collaboration et al. \(2020b\)](#). We ignored the contribution of the faint star S62 ([Gravity Collaboration et al., 2021](#)), which should amount to less than 0.1 mJy. The H-band light curve was also reduced but not used here as the lower signal-to-noise provided negligible improvement over the K-band data in constraining the timing. See [GRAVITY Collaboration et al. \(2021\)](#) for details.

2.2.5 ALMA

All three epochs of Spitzer data presented here were partly covered by ALMA observations⁴. Sgr A* was observed using the 7m ALMA compact array July 17/18 (see also [Michail et al., 2021a](#)), 21, and 26 in 2019. With eleven and ten (epoch of July 25/26) antennas, this compact configuration has fifty-five and forty-five unique projected baselines, respectively, from 8.904 m to 47.987 m (10.1 to 54.4 $k\lambda$). The corresponding maximal resolution is 4.6". The total continuum bandwidth was 2 GHz.

⁴project 2018.A.00050.T, PI: J.Carpenter

The quality assessment of the epochs by the ALMA pipeline was “semi-pass” for the first two epochs and “pass” for the last epoch⁵. Each epoch consisted of four observation blocks on Sgr A*, each ~ 76 min, with seven scans of ~ 7 min duration and an eighth scan that is shorter than 1min. Between each scan there is a gap of ~ 4 min, and between the observation blocks there are gaps of ~ 40 min. The data quality particularly suffered from the atmospheric conditions in the last observing block of each of the first two epochs, while all other blocks are of comparable quality.

Bandpass and gain were calibrated using calibrators J1337–1257 (block 1 of each epoch) and J1924–2914 (blocks 2–4 of each epoch). Gain and phase calibration were executed using the calibrators J1700–2610 (epoch 1, blocks 1–3; epoch 2), J1733–3722 (epoch 1, block 4), and J1717–3342 (epoch 3) in alternation with measurements of Sgr A*.

To derive light curves we first restored the gain-calibrated visibilities with the scripts `scriptForPi.py` which are part of the data archive. The resulting visibilities were then separated by source and spectral range. For each spectral window with science data (16, 18, 20, and 22), we chose the frequency range dominated by continuum emission as identified by the routine `hif_findcont` of the ALMA pipeline. We then applied three iterations of fitting a point source model to the visibilities (with the CASA routine `uvmodelfit`) and interleaved phase self-calibration (with the CASA routines `gaincal` and `applycal`). After a fourth fit with a point source model, we used the resulting flux density as our measurement. This algorithm was applied to visibilities of Sgr A* and the particular phase calibrator in time windows of 1 minute. The last 1-minute bin of each scan with just a few datapoints, as well as the last scans of observations blocks that are shorter than 1 minute, were discarded.

The resulting light curves have a regular cadence of 1 min and a total duration of 7 hours with 5 hours of data each. Heliocentric corrections of +7.366 min, +7.158 min, and

⁵Criteria described in the ALMA technical handbook <https://almascience.nrao.edu/documents-and-tools/cycle7/alma-technical-handbook/view>

+6.772 min were applied for the comparison with the Spitzer light curves. We estimate the absolute flux density calibration to be accurate within 10% uncertainty and the relative photometric precision to be $< 3\%$.

2.3 Analysis

2.3.1 Flare Characterization

To identify significant X-ray flares, we used the Bayesian Blocks algorithm as described by [Scargle \(1998\)](#) and [Scargle et al. \(2013a\)](#) and provided as a python routine by Peter K. G. Williams (`bblocks`; [Williams et al., 2017a](#)). We ran the algorithm using a 95% confidence interval (a false positive rate of $p_0 = 0.05$). This choice for p_0 implies that the probability that a change point is real is $1 - 0.05 = 95\%$, and the probability that a flare (at least two change points) is real is $1 - (p_0)^2 = 99.8\%$. Detected flares are indicated by triangles in [Figure 2.1](#).

We detected two Chandra X-ray flares during the total overlap-period of X-ray and IR, one on 2019 July 18 and one on 2019 July 21. The detection rate is consistent with past measurements of the average number of X-ray flares from Sgr A* ($\sim 1.1/\text{day}$; [Neilsen et al., 2015a](#); [Ponti et al., 2015](#)). The mean quiescent flux measured with Chandra during these epochs was 0.005 counts-per-second (cts/s), and while the flare detected on 2019 July 21 was similar to those reported by [Boyce et al. \(2019\)](#); (20 counts), the flare detected on July 18, 2019 had a total of 74 counts and was not bright enough for pile-up to significantly affect the measurement.

In contrast to the distinct peaks in the X-rays, the emission from Sgr A* at IR wavelengths is constantly varying. An apparent quasi-periodic feature appears in the Spitzer light curve on July 21. Such apparent periodicities can appear in processes described by correlated red-noise and the statistics of Sgr A*'s NIR variability is well described by a

red-noise process (e.g. [Do et al., 2009](#); [Witzel et al., 2012a](#)). There are also multiple IR peaks where we see no significant X-ray emission, even in cases when the IR emission is most elevated (e.g., ~ 6 mJy around 11:30 July 18), whereas the X-ray flare on July 18 was accompanied by a significant rise in the NIR flux density levels. This behaviour (NIR peaks accompanying X-ray flares but not the reverse) is consistent with all previous reported X-ray/IR observations of Sgr A* as well as recent simulations (e.g., [Witzel et al., 2021a](#)). We do not consider the X-ray flare with a lack of NIR rise around 02:00 July 21 as contradictory because the IRAC data exhibited higher-than-normal noise levels at this time due to poor stability in the telescope pointing. A rise in the submm flux at 06:30 on July 21 was not accompanied by corresponding variability X-ray, and has marginally significant higher-than average variability in the NIR. Additionally, on July 26 IR variability was observed along with a rise in the submm but with no corresponding flare in the X-ray.

With a K-band peak flux density of ~ 16 mJy, the NIR flare on July 18 can be classified as moderately bright in the context of previously observed variability ([GRAVITY Collaboration et al., 2021](#)) while the X-ray flare was fairly modest with a peak of 0.1 cts/s. This is a factor of ~ 2 brighter than the four faint flares with simultaneous Spitzer data reported by [Boyce et al. \(2019\)](#), but a factor of ~ 14 lower than the brightest X-ray flare observed ([Haggard et al., 2019a](#)). The brightest flare observed simultaneously in NIR and X-rays was reported by [Dodds-Eden et al. \(2009a\)](#), and had an L-band flux density of ~ 25 mJy and the 2-10 keV X-ray flare reaching ~ 1 cts/s. While the X-ray and NIR variability was moderate on July 18, this does not hold for 340 GHz, which at the highest point was 5.5 Jy, well above the typically measured quiescent levels of ~ 3 Jy ([Subroweit et al., 2017](#)). In fact, the mean flux density (~ 4.5 Jy) measured on July 18 and July 21, was also elevated with respect to historic levels.

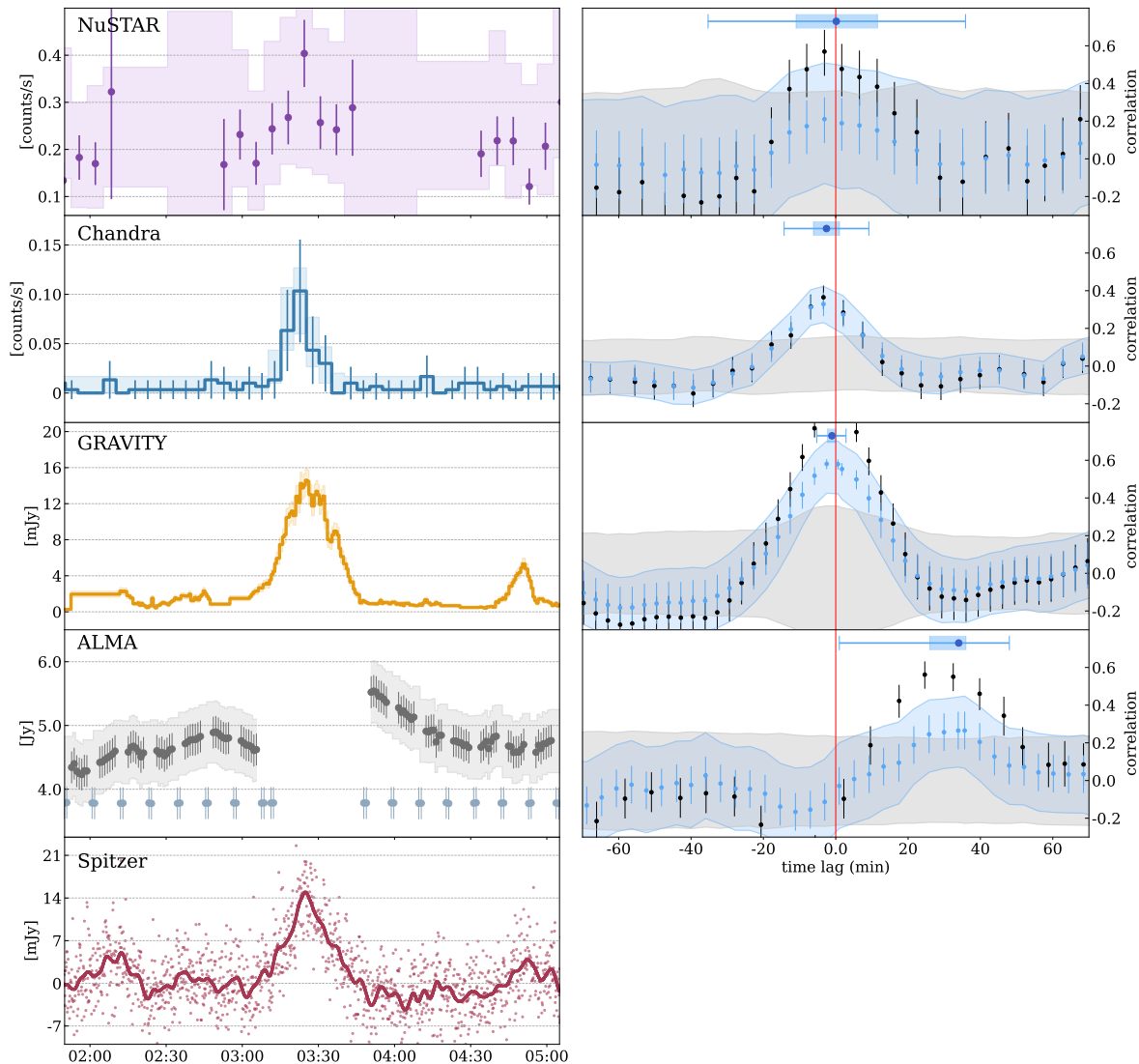


Figure 2.2 Results from running zDCF on the NuSTAR (purple), Chandra (blue), GRAVITY (orange), and ALMA (grey) light curves against the respective Spitzer (red) light curve on July 17/18, 2019. *Left panels:* Regions of the multiwavelength light curves during the X-ray/NIR flare. Their respective envelopes show the 95% range of the 10,000 Monte Carlo (MC) realizations. The x-axis displays the UTC time since the start of the Spitzer/IRAC observations. The bottom panels show the zDCF. *Right panels:* The blue points are the average cross correlation of all 10,000 MC realizations with the blue envelope capturing the 95% range. The grey envelope is the 95% range from the IR MC realizations with 10,000 realizations of simulated noise consistent with the characteristics of the second light curve’s emission (no flares). The significant time lags and confidence intervals are plotted as a single blue point in each panel, with the 68% interval represented by the blue shaded box, and the 99.7% interval represented with the thin error bar.

2.3.2 Multi-wavelength Timing

During the Chandra X-ray flare on July 18, the emission from Sgr A* at 4.5 μm and 2.2 μm rose within minutes of the X-ray peak. Nearly simultaneously, NuSTAR detected moderate X-ray variability through a measurement of increased count rate in a single 6 minute bin. At 340 GHz, ALMA observations also captured part of this flare, but missed the peak (Figure 2.2).

To quantify lags between the peaks of potentially associated activity in the these observations we followed [Boyce et al. \(2019\)](#). We utilized the FORTRAN 95 implementation⁶ of the z-transform discrete correlation function (ZDCF; [Alexander, 1997](#)). This tool estimates the cross-correlation function of two inputs without penalty for having a sparse or unevenly sampled light curve. We cross-correlated all observations relative to the simultaneous 4.5 μm Spitzer light curves binned at 3.5 min (red in Figures 2.1 and 2.2), which cover nearly all of the observing time of the other observatories.

To estimate the uncertainties in the measured time-lags, we cross-correlated each pair of data over 10,000 Monte-Carlo iterations. Bins of 3.5 min were chosen for the Spitzer data to increase efficiency of the cross-correlation Monte-Carlo analysis. Experiments with smaller bins yielded time-lags consistent with the results presented here. The uncertainty on the time lags was determined from the distribution of the 10,000 ZDCF peaks (see §3.2 of [Boyce et al., 2019](#)). The observed correlation function (black) displays a stronger signal of correlation than the spread of simulations (blue) because of the way the data points in the simulated light curves are chosen. Each data point in a simulated light curve is randomly selected from a Gaussian distribution centered on the observed flux value in that bin with a standard deviation equal to the 1-sigma errors on the measured data. Therefore, real correlations in the detailed shape of the light curve (e.g. a monotonic rise) may not be reproduced strongly in a given simulated instance. The height of the shaded blue

⁶Found at: www.weizmann.ac.il/weizsites/tal/research/software/

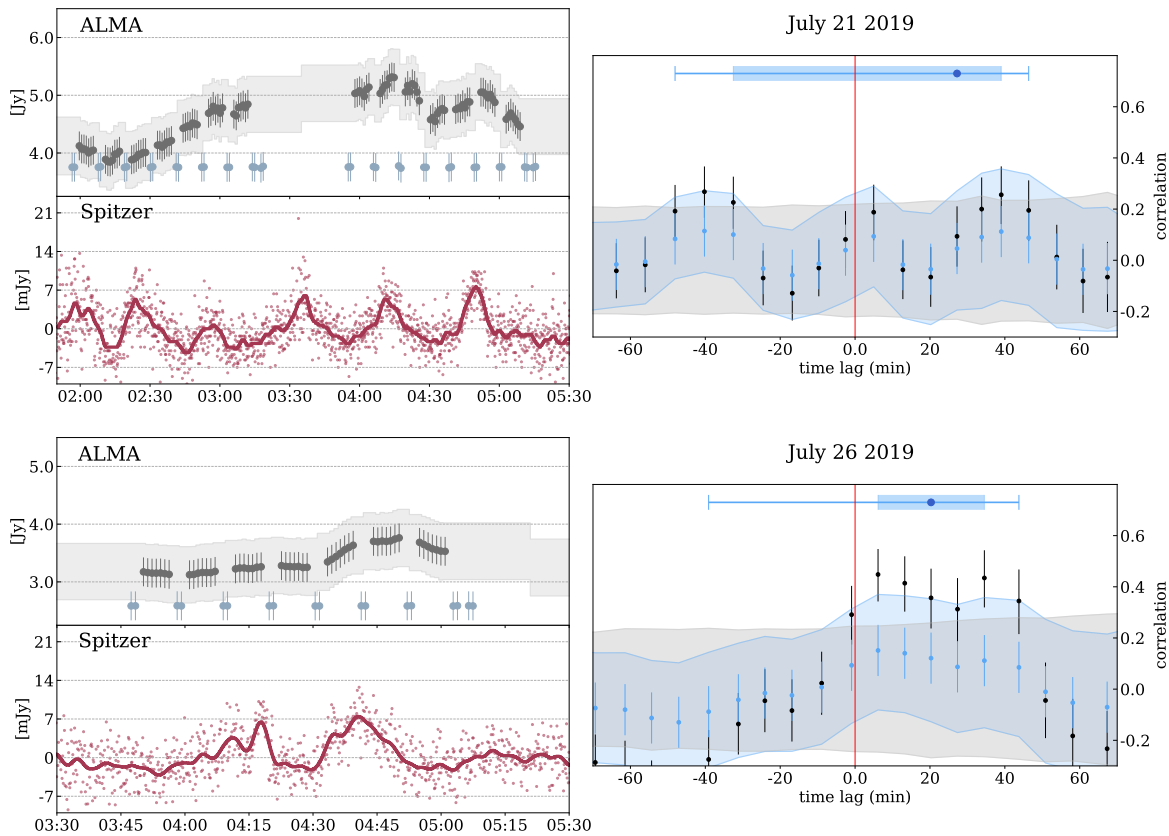


Figure 2.3 Results from running $ZDCF$ on the ALMA (grey) light curves against the respective Spitzer (red) light curve on July 21 and 26, 2019. *Left panels:* Regions of the light curves portions where we see significant IR activity in the overlapping data. The grey envelopes show the 95% range of the 10,000 Monte Carlo (MC) realizations. The x-axes display the UTC time since the start of the Spitzer/IRAC observations. *Right panels:* The blue points are the average cross correlation of all 10,000 MC realizations with the blue envelope capturing the 95% range. The grey envelope is the 95% range from the IR MC realizations with 10,000 realizations of simulated noise consistent with the RMS of the ALMA light curve's emission (no flares). The significant time lags and confidence intervals are plotted as a single blue point in each panel, with the 68% interval represented by the blue shaded box, and the 99.7% interval represented with the thin error bar.

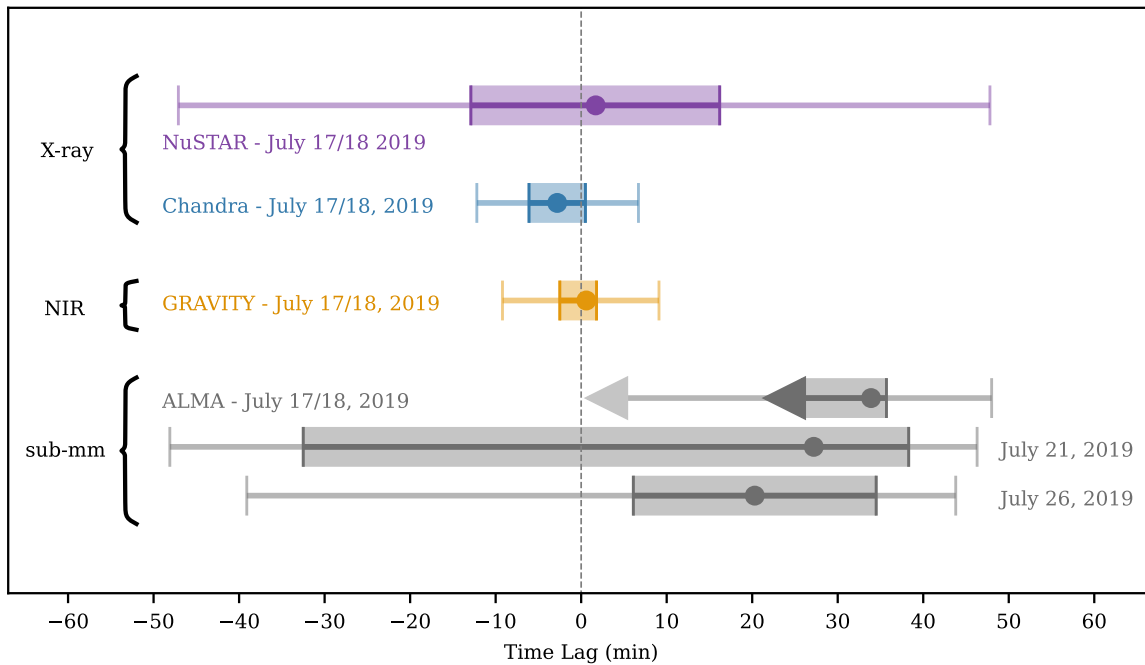


Figure 2.4 Time lags between all multiwavelength observations and Spitzer $4.5\mu\text{m}$ light curves for the Sgr A* July 2019 campaign. The purple, blue, orange and grey points show the NuSTAR 3–70 keV, Chandra 2–8 keV, GRAVITY K-band ($2.2\mu\text{m}$), and ALMA 340 GHz lags, respectively. The 68% confidence intervals are represented by the shaded boxes, and the 99.7% intervals are represented by the thin error bars. Because the measured submm lag on July 18 is an upper limit, the peak of the flare was not captured.

regions above the simulated noise can therefore be seen as a pessimistic indicator of how real the correlation is. Thus the width of the distribution of peak locations drawn from the simulations can conservatively estimate the uncertainty on the time lag. A positive time lag corresponds to variability in the the *NuSTAR*, *Chandra*, *GRAVITY*, or ALMA data lagging the $4.5\mu\text{m}$ Spitzer variability, while a negative time lag corresponds to variability leading $4.5\mu\text{m}$.

Spitzer–NuSTAR: Figure 2.2 shows the results of running the ZDCF on the 2019 July 18 epoch of the Spitzer data and the 6min binned NuSTAR light curve. The measured time lag for the flare plotted in Figure 2.4 and reported in Table 2.2 at $+2_{-15}^{+15}$ minutes, is consistent with simultaneity but less significant than the Chandra X-ray measurement due

to lower signal-to-noise and sensitivity in the data.

Spitzer–Chandra: The second row of Figure 2.2 shows the results of running the ZDCF on the 2019 July 17/18 epoch of the Spitzer data and 300s binned Chandra light curve. The measured time lag for the flare plotted in Figure 2.4 and reported in Table 2.2 at -3_{-3}^{+3} minutes is consistent with simultaneity.⁷

Table 2.2 Time delays with respect to $4.5 \mu\text{m}$ (Spitzer) for X-ray (NuSTAR, Chandra), $\sim 2 \mu\text{m}$ (GRAVITY), and 340 GHz (ALMA) variability.

Instrument	time lag (min)	68% interval	99.7% interval
July 18 2019:			
NuSTAR	$+2_{-15}^{+15}$	(-13,+16)	(-47, 48)
Chandra	-3_{-3}^{+3}	(-6,+0)	(-12, +7)
GRAVITY	$+0_{-3}^{+1}$	(-3,+1)	(-9, +9)
ALMA	$+34_{-8}^{+2}$	(+26,+36)	(+1, +48)
July 21 2019:			
ALMA	$+27_{-60}^{+12}$	(-33,+39)	(-48, +46)
July 26 2019:			
ALMA	$+20_{-14}^{+14}$	(+6,+35)	(-39, +44)

Note: Positive values mean peaks lag Spitzer peaks. Uncertainties on the time lag in the first column span the 68% confidence interval on the 10,000 MC runs. The second column displays the boundaries of this 68% confidence interval, while the third column contains the 99.7% confidence interval.

Spitzer–GRAVITY: The results of running the ZDCF on the 2019 July 17/18 epoch of the Spitzer data against the 40s binned K-band GRAVITY light curve are also shown in Figure 2.2. The measured time lag for the flare is plotted in yellow in Figure 2.4 and reported in Table 2.2 at $+0_{-3}^{+1}$ minutes, consistent with simultaneity.

Spitzer–ALMA: Figure 2.2 shows the results of running the ZDCF on the 2019 July 17/18 epoch of the Spitzer and 340 GHz ALMA light curves, while the cross correlation

⁷An updated barycenter correction was applied to all reductions of the current and previous the Chandra data. This slightly altered the original results from Boyce et al. (2019) but remained within the 1σ uncertainties. The time lags for those NIR/X-ray epochs were recalculated and reported in Boyce et al. (2021) as well as here in Table 2.2 and Figure A.1 in Appendix A.

of 2019 July 21st, and 26th data sets are plotted in Figure 2.3. The measured time lags for the variability on each date are plotted in grey in Figure 2.4 and reported in Table 2.2.

Only data from July 18 show a X-ray flare with significant simultaneous NIR activity. During this window of 02:30~05:00, ALMA measured significant variability but missed the crucial window of 03:00~03:50 in which the NIR and X-ray flares occurred. The observed peak submm flux occurred around 04:00 – right after the window of missing data but at a time when NIR and X-ray flux levels had returned to typical quiescent rates. The result from the ZDCF on the July 18 Spitzer-vs-ALMA data is a measured time lag of $+34_{-8}^{+2}$ minutes at 68% confidence and $+34_{-33}^{+14}$ at 99% confidence. It is therefore likely that the peak of the submm flux lagged the NIR and X-ray variability by 10s of minutes, though we must interpret ~ 35 min as an upper limit on the time-lag since the true peak was not observed.

Cross-correlating the Spitzer and ALMA light curves on July 21 and 26 followed the same method, and the results are displayed in Figure 2.3. Though there was not a significant X-ray flare, the NIR and submm show distinguishable variability. The cross-correlation of July 21 results in a lag of $+27_{-58}^{+12}$ minutes at 68% significance; a broad range that reaches over two marginally significant correlation peaks at around -40 and $+40$ minutes. The cross-correlation of July 26 results in a lag of $+20 \pm 14$ minutes at 68% significance; consistent with the lag detected on July 18, but is also consistent with simultaneity $\sim 20\%$ of the time. Figure 2.4 summarizes the results.

2.4 Discussion

Variability in the NIR has been successfully described by the intermittent acceleration of electrons in a turbulent accretion flow, most often modelled as non-thermal synchrotron emission with a varying cooling cutoff. This is supported by the observed linear polarization of the IR emission (Eckart et al., 2006a; Meyer et al., 2006, 2007; Trippe et al., 2007;

Yusef-Zadeh et al., 2007; Eckart et al., 2008b; Witzel et al., 2011; Shahzamanian et al., 2015), the spectral index at high flux densities ($\alpha \approx -0.6$; Hornstein et al., 2007; Bremer et al., 2011; Witzel et al., 2014), and the timescale of the variability, with factors of $\gtrsim 10$ changes within ~ 10 minutes (e.g., Genzel et al., 2003a; Ghez et al., 2004a; Witzel et al., 2018a).

The physical parameters of this turbulent acceleration of electrons (e.g., background magnetic field strength B , the Lorentz factor of the electrons γ , and the electron density n_e) and the details of the radiative processes linking the NIR variability to the X-ray flares are still uncertain. The processes often invoked to make this connection include (1) pure synchrotron from a sudden acceleration of electrons to a non-thermal distribution (e.g., Markoff et al., 2001; Dodds-Eden et al., 2009a; Barrière et al., 2014; Ponti et al., 2017a), (2) synchrotron self-Compton through the scattering of these non-thermal synchrotron photons up to X-ray energies (Markoff et al., 2001; Eckart et al., 2008b, 2012; Witzel et al., 2021a), and (3) inverse Compton scattering of radio and submm photons from the synchrotron source produced by the persistent large population of thermal electrons (Yusef-Zadeh et al., 2012a). All these scenarios can include changes in the source's magnetic field (B), electron density (n_e), and Lorentz factors (γ). The most likely scenario may be some combination of multiple processes, but the unpredictable nature of flares from around accreting BHs limits data collection, and often the best way forward is testing one scenario at a time.

More broadly, Sgr A*'s average SED is described by several varying components that could originate from different zones in the accretion flow. Though the connection between the NIR and X-ray is clear, it remains an open question whether submm variability could originate from the same source as the higher energy variability. Periods of increased submm variability can be described by separate, uncorrelated events that are occasionally coincident with NIR/X-ray flares. We ask whether the submm, NIR, and X-ray variability on July 18 could be explained through a single acceleration event, i.e. a single-zone modelled at the peak of the NIR/X-ray flare and tens of minutes later, when submm flux is

observed to be declining from an unknown peak value.

To tackle this question, we re-examine three different scenarios of (1) and (2), in light of the total dataset from the campaign presented here, wherein (A: 0-SYNC-SYNC) non-thermal emission originating from a single source of accelerated electrons is responsible for the NIR and X-ray while contribution to the submm is negligible, (B: SYNC-SYNC-SSC) non-thermal synchrotron emission is responsible for the submm and NIR while the X-rays are produced through SSC processes, and (C: SYNC-SSC-SSC) submm flux density is due to a non-thermal population of electrons emitting synchrotron radiation while both the NIR and X-ray are dominated by the SSC emission. IC scattering of external thermal submm photons (3) is not examined. All SEDs discussed in the following sections are produced with `flaremodel` (Dallilar et al., 2022), a code for numerically modelling one-zone synchrotron sources⁸.

Our multi-wavelength time-resolved data constrain the evolution of the source as these electrons cool and/or are continuously accelerated. We are motivated to test these single-zone descriptions because they do not over-fit our data by introducing complex geometries and because flaring in the NIR has been successfully described as originating from a compact, orbiting hot-spot on horizons scales (Gravity Collaboration et al., 2020c). Once electrons are accelerated, they may cool via several channels that would affect the accretion structure around a BH (e.g., synchrotron, bremsstrahlung, and inverse Compton processes, Yoon et al., 2020). Here we examine one possibility via cooling under adiabatic expansion, in which a uniform and spherical cloud of relativistic electrons is expanding and the cooling applies to electrons of all energies at the same rate set by the expansion speed. We refer to the time of the NIR/X-ray peak as $t=0$, and the time of the measured 340 GHz "peak" as $t=35$ min.

⁸Available at <https://github.com/ydallilar/flaremodel>

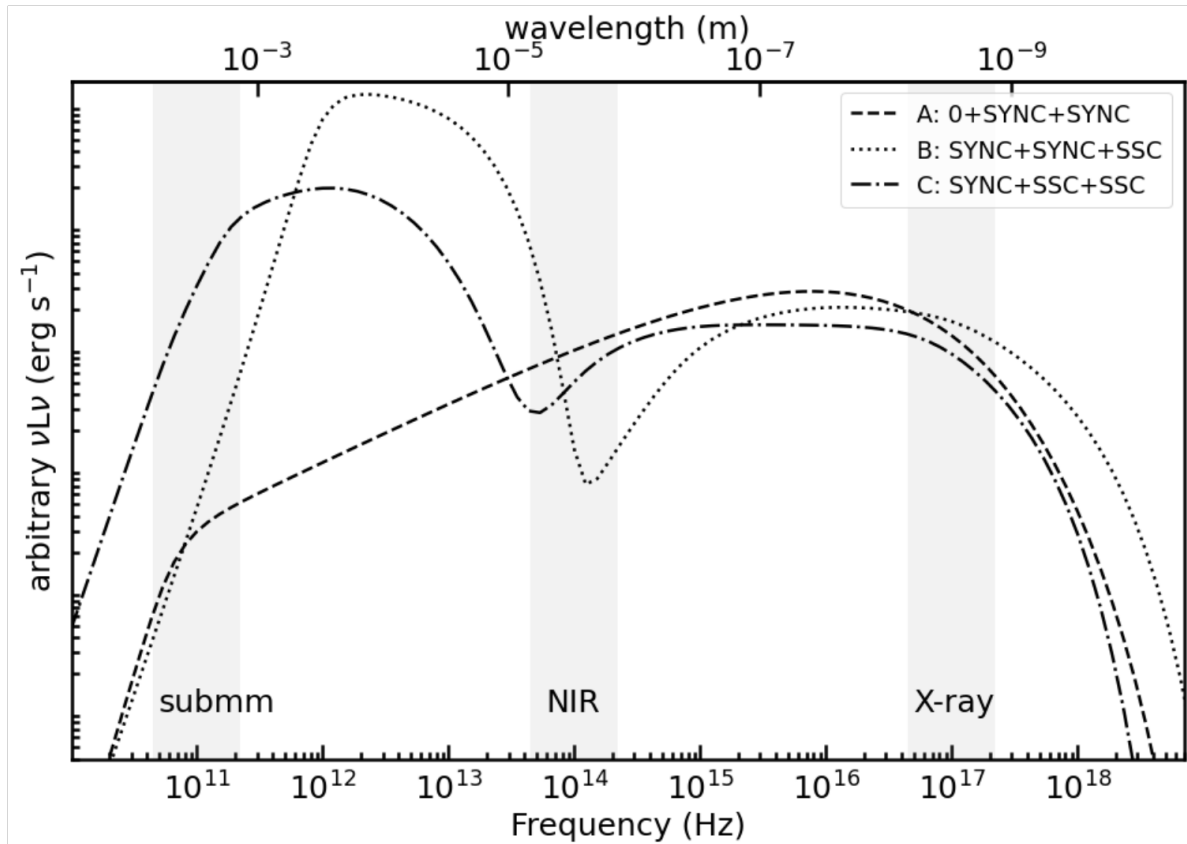


Figure 2.5 Illustration of the three example SED models at the time of the NIR/X-ray peak ($t=0$). (A): The dashed line represents model 0-SYNC-SYNC in which both the NIR and X-ray flux is described by a synchrotron source that contributes negligibly to the submm. (B): The dotted line represents model SYNC-SYNC-SSC in which the optically thick cut-off of the non-thermal SYNC component contributes to the submm, the varying optically thin cutoff of the same SYNC component contributes to the NIR, and the X-ray variability is produced through SSC. (C): The dash-dotted line represents model SYNC-SSC-SSC, in which submm flux can be explained through the optically thick SYNC, NIR flux is dominated by SSC, and the X-rays are also produced by SSC. The models illustrate the shape of the SEDs, but the relative vertical position (flux) of these example curves is arbitrary. Details described [Dallilar et al. \(2022\)](#). For an exaggerated illustration comparing models (B) and (C), see Figure A.3 in Appendix A.

2.4.1 (A) +SYNC+SYNC: An evolving synchrotron source

We consider the scenario where both the NIR and X-ray are produced by a single synchrotron spectrum originating from particle acceleration events involving magnetic reconnection and shocks in the accretion flow (e.g., [Markoff et al., 2001](#); [Dodds-Eden et al., 2009a](#); [Barrière et al., 2014](#); [Ponti et al., 2017a](#); [Rowan et al., 2017](#)). An example of this scenario is plotted as the dashed line in [Figure 2.5](#). With both bands being produced by a single non-thermal synchrotron source, the synchrotron cooling time in the NIR would far exceed the X-rays and the source would require sustained particle acceleration to produce observed X-ray flare durations of up to ~ 1 hour. In this scenario, rapid synchrotron cooling will cause fading in the higher energy X-rays sooner than in the NIR (e.g., see §4.1 of [Dodds-Eden et al., 2010](#)). This could manifest as a simultaneous rise with a time-delay between the X-ray and NIR flare “centres” of a few to 10s of minutes if the time resolution and signal-to-noise of our observed X-ray light curves were high enough ([Dodds-Eden et al., 2010](#)).

Cooling the best-fit synchrotron model of [GRAVITY Collaboration et al. \(2021\)](#) at time $t=0$ (via any cooling process) would result in a decrease in flux across the SED and would not produce appreciable flux in the submm. Therefore, if the NIR and X-ray variability is due to a purely SYNC component (see, e.g., [Ponti et al., 2017a](#)) then that same source could not explain the observed ~ 2 Jy increase in flux density at 340 GHz. The variability at these wavelength regimes must be physically uncorrelated or involve more complex models containing multiple zones of accelerated electrons in complex geometries. On the other hand, more complex models or geometries are difficult to include in the scenario wherein the submm flux correlates with NIR flares originating from a compact orbiting hot-spot on horizon scales ([Gravity Collaboration et al., 2020c](#)).

In summary, the best-fit cooled SYNC model described in [GRAVITY Collaboration et al. \(2021\)](#) accounts for the X-ray and NIR variability and does not require unusually

large electron densities. However, as this synchrotron source cools flux at all wavelengths decreases. A simultaneous or delayed $1 \sim 2$ Jy increase in the submm flux density requires invoking multiple non-thermal populations of accelerated electrons and would not be physically correlated through the evolution of the same SYNC source responsible for the NIR and X-rays.

2.4.2 (B) SYNC+SYNC+SSC: An adiabatically cooling synchrotron source

[Witzel et al. \(2021a\)](#) considers a simple physical model of a compact synchrotron component in Sgr A*'s accretion flow undergoing a sequence of:

1. injection of non-thermal electrons giving rise to detectable submm and NIR emission,
2. further injection, compression of the source, and increasing magnetic flux resulting in higher NIR levels and detectable X-ray emission, and
3. adiabatic expansion with little to no injection giving rise to maximum submm emission. (For a deeper description, see Section 4 of [Witzel et al., 2021a](#), along with their Figure 11.)

This sequence is based on the scenario that there exists a variable synchrotron spectrum arising from populations of non-thermal (accelerated) electrons in addition to the dominant thermal synchrotron radio component of Sgr A*'s SED. The NIR variability is then primarily due to the rapidly varying cooling cutoff of this spectrum. Correlated X-ray variability arises from the resulting SSC spectrum (with the high temporal frequency variability suppressed). This "slow" variability in the SSC X-rays is therefore related to physical changes in the synchrotron source itself (i.e., source size θ , magnetic flux B , and self-absorption properties which manifest in changes to the location of the peak flux and self-absorption frequency turnover of the synchrotron spectrum at submm wavelengths).

Delayed submm variability relative to NIR/X-ray is attributed to these physical changes in the source (e.g. cooling causes the SYNC component to shift to longer wavelengths).

This model predicts a delay in peak submm flux density on the order of 20 – 30 minutes, consistent with our upper limit of ~ 35 min. It also describes the correlation of the majority of NIR and X-ray flares in the literature. [Michail et al. \(2021a\)](#) consider an analogous description of the synchrotron source for the case that the 2018 July 18 NIR and submm emission were simultaneous and find that conditions with $p = 2.5$ describes the submm/IR flux increase well. In this case, simultaneity in submm and NIR could occur if conditions in the accretion flow produced a SYNC source with “optically thin” emission reaching from the submm regime to the NIR. This is incompatible with our observations in two ways: First, the SYNC spectrum whose peak is near 340 GHz and broadly reaches the NIR does not produce SSC in the correct regime to fit the NIR/X-ray data. Second, this SYNC spectrum rising in the submm and reaching the NIR would not have the spectral index observed in the IR.

For typical ranges of physical parameters most of the variable NIR flux is produced by the optically thin cutoff of the synchrotron component and is described by relatively steep flux spectral index ($F_\nu \propto \nu^\alpha$) in the range $-2.0 \lesssim \alpha \lesssim -0.8$, resulting in a negative or flat luminosity spectral index ($\beta = \alpha + 1$). An example of this model (with a steep negative spectral index) is plotted as the dotted line in [Figure 2.5](#).

[GRAVITY Collaboration et al. \(2021\)](#) measured the evolution of the NIR spectral index of the July 18 flare and found that the GRAVITY K–band to Spitzer M–band slope varied in the range $\alpha_{K-M} = [-0.8, 0.0]$, consistent with the canonical NIR spectral index for bright flares of $\alpha_{\text{NIR}} \sim -0.65$ ([Eisenhauer et al., 2005](#); [Ghez et al., 2005](#); [Gillessen et al., 2006](#); [Krabbe et al., 2006](#); [Hornstein et al., 2007](#); [Bremer et al., 2011](#); [Witzel et al., 2014](#), i.e., luminosity rising with shorter wavelengths). This is reflected in [Figure 2.6](#), where the orange points in the NIR band have positive β . Since this flare has a NIR spectral index $\alpha \sim -0.6$ at its peak ([Figure 2.6](#)), we favor descriptions with positive luminosity photon

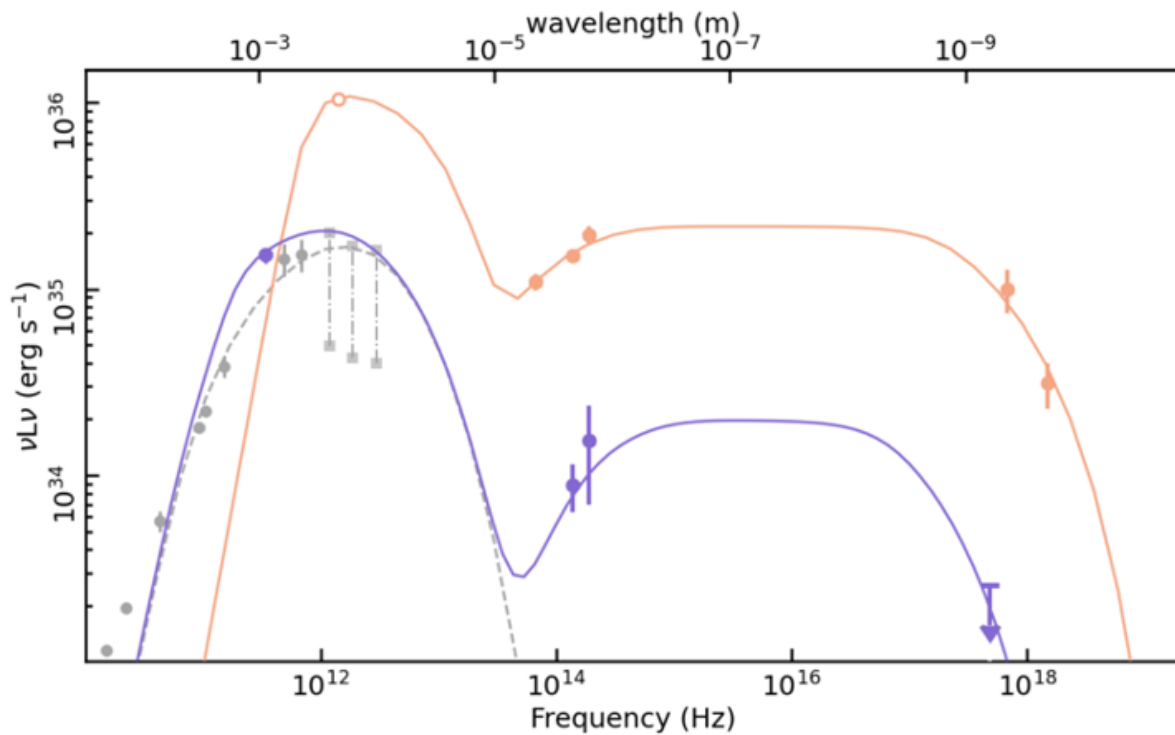


Figure 2.6 Snapshots of the time evolution of scenario (C) SYNC-SSC-SSC, fit under adiabatic expansion. Solid orange points are measured values at the peak of the NIR and X-ray flare, solid purple points are measured at the presumed “peak” of the 340 GHz flux ~ 35 min later. The open orange point at 1400 GHz is used as the starting point in the adiabatic expansion calculation described below. The historic quiescent SED in radio/submm is plotted in light grey with a thermal synchrotron component fit to these data as the grey dashed line. The solid lines are the best-fit models with the thermal component included. Observed values are tabulated in Table 2.3. Parameters for the fits are reported in Table 2.4.

Table 2.3 Values for the Sgr A* SED observed by coordinated ground-based and space-based observatories on 2019 July 18.

Observatory	Frequency [GHz]	$t = 0$ minutes		$t = 35$ minutes	
		Flux Density [Jy]	νL_ν [$\times 10^{34} \text{erg s}^{-1}$]	Flux Density [Jy]	νL_ν [$\times 10^{34} \text{erg s}^{-1}$]
ALMA ^a	340	–	–	2.6 ± 0.5	7.2 ± 1.4
Spitzer/M-band	6.7×10^4	$20.2 \pm 1.0 \times 10^{-3}$	10.9 ± 0.6	–	–
GRAVITY/K-band	1.4×10^5	$13.5 \pm 0.9 \times 10^{-3}$	15.0 ± 1.0	$0.8 \pm 0.2 \times 10^{-3}$	0.9 ± 0.3
GRAVITY/H-band	1.9×10^5	$12.7 \pm 1.4 \times 10^{-3}$	19.4 ± 2.2	$1.0 \pm 0.5 \times 10^{-3}$	1.5 ± 0.8
Chandra	6.8×10^8	$18.1 \pm 4.7 \times 10^{-7}$	10.0 ± 2.6	$< 7 \times 10^{-9}$	< 0.3
NuSTAR	1.5×10^9	$2.6 \pm 0.7 \times 10^{-7}$	3.1 ± 0.9	–	–

^aAfter subtracting the ~ 2 Jy contribution from the thermal component (grey line in Figure 2.6)

Note. — Note: Frequencies for X-ray observatories reflect the central frequency of the keV energy band within the observation bin.

indices ($\nu L_\nu \propto \nu^\beta$, $\beta = \alpha + 1$).

In summary, though this scenario could explain the temporal evolution of the correlated submm, NIR, and X-ray flux densities, the spectral index in the NIR disfavours a scenario in which the NIR is dominated by the optically thin component of the SYNC spectrum.

2.4.3 (C) SYNC+SSC+SSC: An adiabatically cooling synchrotron source

Another possibility is that both the X-ray and NIR flux may be dominated by SSC flux (i.e., photons being scattered to higher energies through interaction with the electrons producing the non-thermal synchrotron in the submm). In this scenario the NIR flux would derive from the rising side of the SSC component, rather than the optically-thin edge of the SYNC component (which is now shifted toward even longer wavelengths). An example of this SED is illustrated as the dashed-dotted line “C” in Figure 2.5.

Since the SYNC+SSC+SSC scenario predicts the correct range of NIR spectral indices, we fit this model with a synchrotron source that produces the 340 GHz flux increase that

can evolve under adiabatic expansion. If adiabatic cooling is dominant, the SYNC source expands and cools (without further electron injection), causing the turn-over of the SYNC component to march down to lower frequency as it fades. This results in a delay at longer wavelengths. If the true peak of the submm rise was simultaneous with the NIR/X-ray, the SYNC component of the SED must have peaked near 340 GHz. Such a SYNC spectrum could not then produce bright enough SSC emission to match the NIR/X-ray observations. We therefore consider the scenario in which the peak of the submm emission was delayed by 10s of minutes.

To test this scenario and leverage the submm flux measured with a delay, we use the methodology first described in [van der Laan \(1966\)](#) to parameterize the behaviour of the peak of the non-thermal SYNC component under adiabatic cooling. This method has been applied to interpret Sgr A* variability in the past (e.g. [Yusef-Zadeh et al., 2006a](#); [Eckart et al., 2008a](#))

The flux density as a function of frequency (ν) is parameterized as:

$$S(\nu, \rho) = (\nu/\nu_m)^{5/2} \rho^3 \frac{\left[1 - \exp \left\{ -\tau_m \left(\frac{\nu}{\nu_m} \right)^{-(p+4)/2} \rho^{-(2p+3)} \right\} \right]}{[1 - \exp(-\tau_m)]} \quad (2.1)$$

where ν_m is the frequency at which the flux density maximum of the spectrum occurs, p is the slope of the electron distribution, τ_m is the optical depth corresponding to the frequency at which the flux density is maximum and ρ is the relative radius of the source, which can be parameterized in terms of the expansion velocity v_{exp} , time (t), initial source size R_0 , and a deceleration parameter β (kept at standard value of 1.0 in our analyses):

$$\rho = \left(\frac{1 + v_{\text{exp}} c (t - t_0)}{R_0 \beta} \right)^\beta \quad (2.2)$$

To describe the broad-band SED, we numerically implement the SYNC-SSC model described in [Dallilar et al. \(2022\)](#), based on a non-thermal power-law-distributed electron

energy distribution. The physical parameters of this single-zone non-thermal synchrotron model are the electron density ($n_e \times 1\text{cm}^3$), the projected radius ($R, \mu\text{as}$), the magnetic field (B, G), the power law slope of the electron distribution (p), the maximum Lorentz factor (γ_{max}), and the minimum Lorentz factor (γ_{min}).

Plotted in orange points in Figure 2.6 are the observed X-ray and NIR data at the time of their peak ($t = 0$). Due to the gap in the observing window, we do not have a simultaneous measurement at 340 GHz. However, under the assumption that there is a significant time lag of ~ 35 min or less in the peak of the submm flux, the 340 GHz flux at $t = 0$ must be fainter than ~ 2 Jy (excess flux above historic quiescence; $5.5 \times 10^{34} \text{ erg s}^{-1}$ at 340 GHz). The orange line is the best-fit SSC-SSC SED that satisfies this constraint with χ_{red}^2 of 2.3. We find that the high H-band measurement is the data point most strongly preventing the fit from reaching $\chi_{\text{red}}^2 \sim 1$. Doubling the uncertainty on this point would result in $\chi_{\text{red}}^2 = 1.1$ with very similar values to those listed in Table 2.4.

In purple are the constraints in the NIR/X-ray once their flux has faded (at 35 min past peak) as well as the measured ‘‘peak’’ flux at 340 GHz. Fitting these data with the SYNC+SSC+SSC SED + SYNC thermal component (grey) yields χ_{red}^2 0.5, Physical parameters of these best-fits are tabulated in Table 2.4.

Table 2.4 Best fit parameters of scenario C: SYNC+SSC+SSC.

	$t = 0$	$t = 35 \text{ min}$
$\log(n_e \times 1\text{cm}^{-3})$	10.1 ± 0.8	9†
$R (\mu\text{as})^*$	11.2 ± 2.1	21 ± 2
$B (\text{G})$	25 ± 44	3.1 ± 0.8
p	3†	3†
γ_{max}	320 ± 110	410 ± 130
γ_{min}	3.8 ± 1.3	10.8 ± 3.4
χ_{red}^2	2.3	0.5

*: $1 \mu\text{as} = 0.0082 \text{ AU}$

†: value fixed

Taking the best-fit radius at $t = 0$ ($R_0 \sim 1.1 \times R_S$) and the peak flux at 1400 GHz

($10.8 - 1.5 = 9.3$ Jy after subtracting the thermal component from the peak in Figure 2.6) we apply Equations 2.1, and 2.2 (van der Laan, 1966) to match the peak flux in 340 GHz at $t = 35$ min. With the initial size of the region, R_0 , set at the best fit value, we can vary the expansion speed and find that a value of $v_{\text{exp}} \sim 0.014c$ reproduces the flux observed at the peak in 340 GHz (see Fig 2.7). This speed is consistent with other estimates of $v_{\text{exp}} \sim 0.003c - 0.02c$ found under the interpretation of an expanding plasmon (Yusef-Zadeh et al., 2006a, in the cm) and (Eckart et al., 2006b, 2008a; Marrone et al., 2008a; Eckart et al., 2012, NIR-submm). This calculation relies on the assumption that the peak in 340 GHz occurred at $t = 35$ min. If the peak happened earlier, we would require an even faster expansion speed to match the measured flux.

Scenario “C” (SYNC+SSC+SSC) can be interpreted as a particularly unusual version of scenario “B”, in which the same single zone model and radiation mechanisms could produce typical flux variations in the submm, NIR, and X-ray. In this picture the July 18 event’s unusually high submm flux is explained through uniquely high electron densities and a prediction of bright emission in the THz regime.

This interpretation relies on the validity of two unique characteristics: First, there must have been very high flux at \sim THz frequencies during the flare, something that has not been reported in campaigns aiming to characterize the quiescent THz spectrum (von Fellenberg et al., 2018b; Bower et al., 2019a), though at 850 GHz Serabyn et al. (1997a) report a measurement of ~ 3 Jy (2×10^{35} erg s $^{-1}$). An updated study on the flux density distribution at submm-THz is required to determine the likelihood of observing such a flare based on past observations at these frequencies. Second, electron densities in the SYNC source must have been several orders of magnitude higher than the implied densities of the average accretion flow from radio polarization studies ($\log n_e \sim 10$ compared to e.g. ~ 7 ; Bower et al., 2019a), which could be easier to achieve if Sgr A* were in an unusual state of increased accretion.

Average accretion rates for Sgr A* are estimated from the rotation measure in quiescent

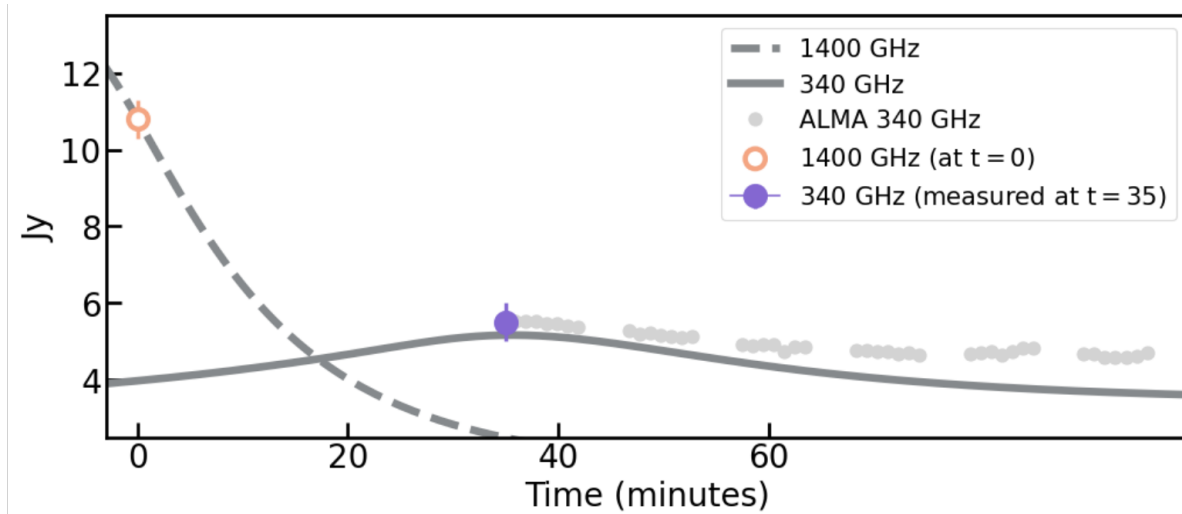


Figure 2.7 Light curves derived from equations 2.1, and 2.2 offset with the constant flux values originating from the putative constant synchrotron component that arises from a thermal distribution of electrons (dashed grey model in Figure 2.6; 1.5 Jy at 1400 GHz and 3.4 Jy at 340 GHz). A value of 9.3 Jy at 1.4 THz (10.8 Jy from Figure 2.6 – 1.5 Jy from the thermal component) is used in the calculation and evolved forward in time with expansion velocity $v_{\text{exp}} = 0.014c$. The purple data point (5.5 Jy) is the measured 340 GHz flux with the thermal synchrotron component (3.4 Jy) included.

submm observations, the last of which was [Bower et al. \(2018a\)](#), based on data obtained in 2016. The rotation measure has been observed to have short term variability and most estimates of Sgr A*'s accretion rate are cited from the value averaged over the long term (\sim years). Since then there have been hints that Sgr A*'s accretion state may not be so constant, particularly supported by the incredibly bright NIR flare observed in early 2019 ([Do et al., 2019b](#)), which fell outside of all previously-parameterized flux density distributions. If Sgr A* was indeed in a state of elevated accretion in 2019, then this could explain how this event is distinct from most previously observed flares. That is, a high sub-THz flux may be more easily achievable if electron densities as a whole were increased, allowing flaring conditions with $\log n_e \sim 10$.

Finally, the assumption that we have captured the peak of the 340 GHz flare is a large one. The start of the observing window around 03:45 catches the light curve in a descending state, with no indication of a turn-over (Figure 2.1). If we have not captured the peak

of the flare, that would allow the SYNC component in this SED to extend to lower energies at the time of the NIR/X-ray peak, though it would still remain significantly higher than the previously observed flux levels at these frequencies.

Fitting the temporally-resolved SED over six time-steps in the NIR and X-ray, [GRAVITY Collaboration et al. \(2021\)](#) conclude that the particle densities necessary for “C” SYNC+SSC+SSC ($\gg 10^9 \text{ cm}^{-3}$) would be extremely unlikely given the typical, average electron densities derived from modeling the radio to submm SED of Sgr A* with synchrotron emission from a thermal electron distribution (ambient $n_e < 10^7 \text{ cm}^{-3}$ [Bower et al., 2019a](#)). To fit an SED like “A” (0+SYNC+SYNC), a strong acceleration event is necessary ($\gamma_{\text{max}} \gg 10^4$), but the physical parameters of the source (including n_e) remain consistent with predictions from the literature.

Of course, adiabatic expansion is not the only scenario in which delayed and correlated emission between frequencies can arise. Interpreting 20–40 minute delays in the 20 to 40 GHz regime, [Falcke et al. \(2009\)](#) observed a frequency dependence of VLBI sizes and saw evidence for a relativistic outflow. Meanwhile [Brinkerink et al. \(2015a\)](#) derived relativistic outflow velocities of up to $\sim 0.77c$, through the progression of variability maxima from 100 to 19 GHz, and interpret this as a jet. Finally, it is always possible that the submm variability is not physically correlated with the NIR and arises from another component altogether. For example, single-zone modelling of M87’s jet and active galactic nucleus cannot fully describe the broadband SED, albeit the data most driving this conclusion are the high-energy γ -rays ([EHT MWL Science Working Group et al., 2021](#))

In summary, this single-zone adiabatic expansion model fits the data, with the caveat that the inferred submm-THz flux at $t = 0$ would have been much brighter than most observations at these frequencies. Accepting the plausibility of the scenario requires an electron density that would be extraordinarily high in comparison with estimated densities responsible for Sgr A*’s average accretion rate.

2.5 Summary

We report observations from a multi-wavelength campaign that simultaneously observed Sgr A* in July 2019 from the submm, to NIR, to X-ray. Cross correlating the light curves against the Spitzer NIR light curve on each date, we report the measured time lags between each wavelength.

- On July 17–18, a moderately bright NIR flare captured by Spitzer ($4.5\mu\text{m}$) and GRAVITY ($2.2\mu\text{m}$) occurred simultaneously with a faint X-ray flare captured by NuSTAR ($3 - 70\text{keV}$) and Chandra ($2 - 8\text{keV}$). Overlapping coverage at 340 GHz from ALMA missed the peak of the submm flare, but reveals very bright correlated flux ~ 35 min after the NIR/X-ray peak.
- On July 21, correlated submm/NIR flux variability remains consistent with simultaneity (no time lag).
- On July 26, we report a measured time lag of ~ 20 min between correlated submm and NIR variability with 68% confidence, though consistent with simultaneity at 98% confidence.

The flux and timing properties of the July 17–18 flare are considered in the context of three scenarios: “A” both NIR and X-ray due to emission from a synchrotron source, “B” submm and NIR due to a synchrotron source while X-ray arises as synchrotron self-Compton emission, and “C” submm due to a synchrotron source while both NIR/X-ray arise from synchrotron self-Compton. We are limited in what we constrain because we have not captured the peak of the 340 GHz flare, and can only measure an upper limit on the time-lag between it and the NIR. This event is particularly interesting because the submm flux is notably high (~ 5.5 Jy, very rarely observed at these frequencies), so if the peak is even higher, this could indicate that the radiative processes are non-typical when compared to conditions responsible for historic variability. In the scenario in which the

submm and NIR/X-ray variability are not physically correlated, a SYNC source fitted to the NIR/X-ray (scenario “A”) is allowed and does not require extraordinarily large electron densities ([GRAVITY Collaboration et al., 2021](#)).

To leverage the potentially delayed submm flux, we consider whether a synchrotron source cooled through adiabatic expansion can self-consistently describe the submm increase and the NIR/X-ray flux at peak and after. Consistent with our measurement, [Michail et al. \(2021a\)](#) report an upper limit on the time lag of less than 30 minutes. They also analyze the submm and mid-IR emission using adiabatically expanding synchrotron plasma models and find two cases that can describe the data. The first is a SYNC source with $p = 2.5$ responsible for simultaneous rise in the submm and NIR (analogous to scenario “B” SYNC+SYNC+SSC). We disfavour this scenario primarily since the predicted NIR spectral index is in tension with the observations, but also since a simultaneous rise in the submm and NIR would require a SYNC spectrum whose peak is near 340 GHz and broadly reaches the NIR, which does not produce SSC in the correct regime to fit the X-ray data. In their second case, a SYNC source with $p > 2.8$ has optically thick plasma conditions that evolve to optically thin in the submm on the time scale of 10s of minutes (analogous to scenario “C” SYNC+SSC+SSC). We find that this adiabatic expansion scenario producing SSC emission in the NIR and X-rays (scenario C) works only under the conditions that a very high submm/THz peak would occur at the time of the NIR/X-ray peak and that the electron density reaches $\log n_e \sim 10$.

Narrowing down the radiation mechanism powering and connecting variability across wavelength regimes brings the field closer to accurately describing the physical mechanisms that power the dramatic flux changes originating near the event horizon. Simultaneous, multi-wavelength observations of Sgr A* at all accessible frequencies remain essential to differentiate between various radiation mechanisms. Such observational campaigns are key to comparing to the state-of-the-art general-relativistic magneto-hydrodynamic

(GRMHD) simulations that can model details of accreting plasma in this extreme environment, where high resolution simulations have shown that sufficiently energetic plasma can be accelerated through magnetic reconnection (Ripperda et al., 2022). In particular, continued coordination between submm-radio observatories and the NIR/X-ray will strengthen or rule out the interpretation that these variable signals are physically connected. If simultaneous observations at THz frequencies are also captured during submm/NIR/X-ray variability, one could definitively constrain models in which the cooling SYNC component is responsible for the submm flux density increase and is correlated with NIR/X-ray SSC emission. Finally, coordinated multi-wavelength campaigns with the EHT and VLTI/GRAVITY will be key to interpreting the increasingly detailed view of this accreting SMBH on horizon scales.

Text in this chapter is published in ApJL 930 (2022),
L13 First Sagittarius A* Event Horizon Telescope Results. II.
EHT and Multiwavelength Observations, Data Processing, and
Calibration (The Event Horizon Telescope Collaboration et al.)

Chapter 3

Multi-wavelength Coordination with the Event Horizon Telescope

In our second study, we consider spatial scales even closer to the black hole and present the multiwavelength state that Sgr A* was in during the Event Horizon Telescope’s 2017 campaign to image the SMBH’s shadow. As the multi-wavelength working group, we coordinated simultaneous observing campaigns with telescopes across the globe and in space to capture the multi-wavelength behaviour of Sgr A* as it was being imaged by the EHT’s primary imaging arrays. We characterize several X-ray flares, the most significant of which does not have simultaneous EHT coverage but is followed by a significant increase in millimeter flux variability immediately after the X-ray outburst — this indicates a likely connection in the emission physics near the event horizon. The broadband flux densities measured during the campaign are found to be consistent with the historical quiescent and variable spectral energy distribution.

3.1 Introduction

The first legacy set of papers by the Event Horizon Telescope (EHT) focused on the supermassive black hole M87* ([Event Horizon Telescope Collaboration et al., 2019a,b,c,d,e,f](#), hereafter M87* Papers I, II, III, IV, V, and VI), but Sagittarius A* (Sgr A*) was the spark that motivated the formation of the EHT. This work presents novel EHT observations of Sgr A* at 1.3 mm, which serve as the foundation for the observational and theoretical papers presented in this second legacy series ([Event Horizon Telescope Collaboration et al., 2022a,b,c,d,e,f](#), hereafter Papers I, II, III, IV, V and VI).

Sgr A*, the $\sim 4 \times 10^6 M_{\odot}$ black hole at the center of our own Milky Way (at a distance of ~ 8 kpc), is the closest observable supermassive black hole (e.g., [Gravity Collaboration et al., 2019b](#); [Do et al., 2019a](#); [Reid & Brunthaler, 2020](#)). Among all known black holes, Sgr A* has the largest predicted angular diameter of the black hole shadow ($\sim 50 \mu\text{as}$, see [Paper III](#) and [Paper IV](#), and references therein). It is also a highly variable source, with flickering, flares, and other stochastic processes occurring across the electromagnetic spectrum on short and long timescales. These unique characteristics make Sgr A* an important laboratory for studying the fundamental physics and astrophysics of black holes at high angular resolution.

Sgr A* has been observed with millimeter very-long-baseline interferometry (VLBI) for over a quarter century. After initial successful 1 mm VLBI tests on quasars ([Padin et al., 1990](#); [Greve et al., 1995](#)), Sgr A* was first successfully detected on a VLBI baseline between the IRAM 30-m telescope on Pico Veleta (PV) in Spain and a single antenna of the Plateau de Bure Interferometer in France in 1995 ([Krichbaum et al., 1997](#)). This detection revealed a compact source, with a size of $(110 \pm 60) \mu\text{as}$ ([Krichbaum et al., 1998](#)). Early size measurements at 3 mm and 1 mm were larger than expected (cf. e.g., [Lo et al., 1998](#)), indicating that short-wavelength VLBI measures the intrinsic structure in Sgr A* rather than interstellar scattering along the line of sight. Subsequent VLBI experiments

using wider recorded bandwidth and three telescopes with longer baselines provided a tighter estimate of the source size, $43_{-8}^{+14} \mu\text{as}$, giving the first unambiguous detection of horizon-scale structure in Sgr A* (Doeleman et al., 2008b). Meanwhile, continued VLBI observations at $\lambda \gtrsim 3 \text{ mm}$ were better able to characterize the properties of the anisotropic interstellar scattering screen (e.g., Bower et al., 2004; Johnson et al., 2018).

Excitement from these VLBI measurements was further galvanized by crucial theoretical and technical advancements made in parallel. Simulations of Sgr A* by Falcke et al. (2000) demonstrated that a shadow of the sort originally predicted by Bardeen (1973) would be observable with millimeter-wavelength VLBI.¹ Technological advances greatly increased the capabilities of the growing EHT, as detailed in M87* Paper II. These advances led to a new era in which the detection of Sgr A* on long baselines at 1 mm became routine (Fish et al., 2011; Johnson et al., 2015; Fish et al., 2016; Lu et al., 2018). Most significantly, the phased Atacama Large Millimeter/submillimeter Array (ALMA) (Matthews et al., 2018) participated in its first EHT science observations in 2017, along with other antennas that added to the baseline coverage. Indeed, data from these observations produced the M87* total-intensity (M87* Paper I; M87* Paper II; M87* Paper III; M87* Paper IV; M87* Paper V; M87* Paper VI) and polarization results (Event Horizon Telescope Collaboration et al., 2021a,b, Papers VII and VIII hereafter), as well as high angular resolution images of extragalactic radio jets (Kim et al., 2020; Janssen et al., 2021). These data also motivate the Sgr A* results in this series.

As these VLBI discoveries were advancing, Sgr A* was also being studied intensively at other wavelengths. Radio, millimeter, infrared, and X-ray observations showed that Sgr A* has both a very low bolometric-to-Eddington luminosity ratio of $L/L_{\text{Edd}} \sim 10^{-9}$ (Genzel et al., 2010b), and a very low mass accretion rate of $\sim 10^{-9}$ to $10^{-7} M_{\odot} \text{ yr}^{-1}$ (Baganoff et al., 2003a; Marrone et al., 2006a, 2007a; Shcherbakov et al., 2012a; Yusef-Zadeh et al., 2015b). At most wavelengths, Sgr A*'s flux can be decomposed into a quiescent and

¹More details about the appearance of black holes are given in M87* Paper I.

variable component.

In the X-ray, Sgr A* is a persistent source, with a flux of about 3×10^{33} erg s⁻¹ (Baganoff et al., 2001b, 2003a) from thermal bremsstrahlung radiation originating from hot plasma near the Bondi radius (e.g., Quataert, 2002b; Baganoff et al., 2003a; Yuan et al., 2003b; Liu et al., 2004b; Wang et al., 2013b). Bright X-ray flares punctuate this emission about once per day and are characterized by non-thermal emission centered on the black hole (e.g., Neilsen et al., 2013b). Near infrared (NIR) detections of Sgr A* also reveal a highly variable source, with emission peaks observed more frequently than in the X-ray (Genzel et al., 2003b; Ghez et al., 2004b; Gravity Collaboration et al., 2020d). Both the X-ray and NIR variability occur on timescales of several hours, consistent with emission originating near the black hole's innermost stable circular orbit (ISCO), which depends on the black hole's mass and spin. Sgr A*'s mid-IR flux is only marginally detected (e.g., Iwata et al., 2020b) or it can be inferred indirectly from model fitting.

Millimeter polarimetry of Sgr A* reveals linearly polarized flux from an emitting region of ~ 10 Schwarzschild radii (R_S), which indicates a dense magnetized accretion flow again extending out to the Bondi radius. Bower et al. (2018b) find a mean rotation measure (RM) of $\sim -5 \times 10^5$ rad m⁻² that can be modeled as a radiatively inefficient accretion flow (RIAF) with an accretion rate of $\sim 10^{-8} M_\odot \text{yr}^{-1}$. Circular polarization is also detected at a mean value of $-1.1 \pm 0.2\%$. Both the RM and the circular polarization are variable on timescales of hours to months (Bower et al., 2018b).

Similarly, observations of Sgr A* between 15 and 43 GHz reveal variability at the 5–10% level on timescales shorter than four days (Macquart & Bower, 2006). Sgr A*'s flux density distribution at 217.5, 219.5, and 234.0 GHz was investigated recently by Iwata et al. (2020b); they find variability on timescales of \sim tens of minutes to hours, indicating that the emission at these wavelengths is also likely to arise near the ISCO.

Hence, in addition to the excitement around resolving Sgr A*'s intrinsic structure at 1.3 mm, it became clear that multi-wavelength observations during the EHT campaign

would offer the first opportunity to definitively connect the black hole’s variable flux components with changes observed at horizon scales.

In this work we present the first EHT 1.3 mm observations of Sgr A*, alongside multi-wavelength data collected contemporaneously in April 2017. Contemporaneous interferometric array data from ALMA and SMA have been analyzed and are described here (and presented in more detail in a companion paper, [Wielgus et al., 2022](#)). The campaign also includes observations from the East Asian VLBI Network (EAVN), the Global 3 mm VLBI Array (GMVA), the Very Large Telescope (VLT), the Neil Gehrels Swift Observatory, the Chandra X-ray Observatory, and the Nuclear Spectroscopic Telescope (NuSTAR). These coordinated observations provide (quasi-)simultaneous multi-wavelength coverage with exceptional spatial and spectral resolution. Since variability at timescales of minutes to hours can be probed on horizon scales by the EHT, and on a range of other spatial (and spectral) scales by these other observatories, combining them into a single “snapshot” spectral energy distribution (SED) maximizes the broadband constraints that the observations can place on theoretical models.

This manuscript ([Paper II](#)) is organized as follows. In [Section 3.2](#) we present an overview of the 2017 EHT observing campaign. [Section 3.3](#) delves more deeply into the EHT data calibration and reduction specific to these Sgr A* data. [Section 3.4](#) outlines the multi-wavelength (MWL) campaigns that accompanied the EHT observations. [Section 3.5](#) describes the resulting EHT and MWL data products, including those provided via a public data archive, and discusses these new observations in the context of longer-term monitoring campaigns that have characterized Sgr A*’s variability over more than 20 years. We offer a brief summary and conclusions in [Section 3.6](#).

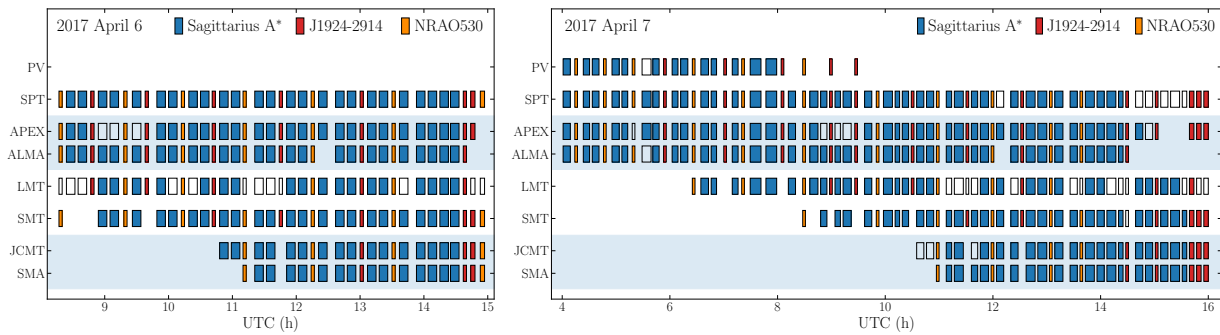


Figure 3.1 EHT 2017 observing schedules for Sgr A* and its calibrators (J1924–2914 and NRAO530), covering observations on April 6–7 2017. Empty rectangles represent scans that were scheduled but not observed successfully due to weather or technical issues. The filled rectangles represent scans corresponding to detections available in the final data set. Scan durations vary between 3 and 12 minutes, as reflected by the width of each rectangle. ALMA/APEX and JCMT/SMA are pairs of co-located stations (enclosed in light blue shaded regions), providing the same (u, v) -coverage.

3.2 Event Horizon Telescope Observing Campaign

The first EHT observations of Sgr A* were collected in April 2017, alongside contemporaneous broadband data — the coverage is shown in Figures 3.1 and 3.2. A detailed description of the EHT array and its instrumentation can be found in [M87* Paper II](#), with further details related to the 2017 observing campaign in [M87* Paper III](#). Here we provide a brief summary of this material, along with details pertinent to the observations of Sgr A* and associated calibration sources.

EHT observations were carried out with eight observatories at six locations: ALMA and the Atacama Pathfinder Experiment (APEX) on the Llano de Chajnantor in Chile, the Large Millimeter Telescope Alfonso Serrano (LMT) on Volcán Sierra Negra in Mexico, the James Clerk Maxwell Telescope (JCMT) and Submillimeter Array (SMA) on Maunakea in Hawai‘i, IRAM 30 m Telescope on Pico Veleta (PV) on Pico Veleta in Spain, the Submillimeter Telescope (SMT) on Mt. Graham in Arizona, and the South Pole Telescope (SPT) in Antarctica. The locations of these telescopes are plotted in Figure 1 of [Paper I](#).

Sgr A* was observed on five nights: 2017 April 5, 6, 7, 10, and 11. ALMA did not

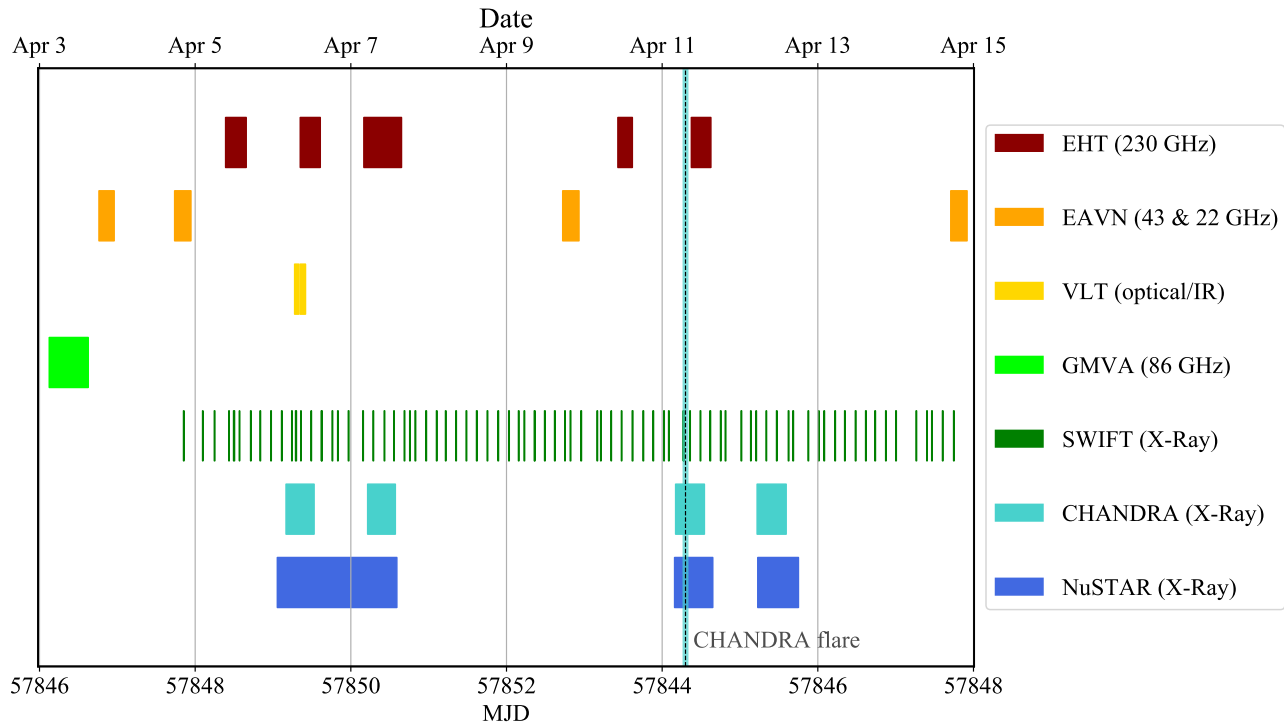


Figure 3.2 Instrument coverage of Sgr A* during the 2017 April 3–15 multi-wavelength observing campaign, which includes the East Asian VLBI Network (EAVN), the Global 3 mm VLBI Array (GMVA), the Very Large Telescope (VLT), the Neil Gehrels Swift Observatory (SWIFT), the Chandra X-ray Observatory (CHANDRA), and the Nuclear Spectroscopic Telescope (NuSTAR). For the EHT data described in this work we focus on April 6 and 7, which have the best (u, v) -coverage and for which detailed instrument and source coverage is shown in Figure 3.1. Details of the multi-wavelength campaign and spectral energy distribution are contained in Sections 3.4 and 3.5.2.

participate in the array for observations of Sgr A* on 2017 April 5 or 10. PV observed Sgr A* only on 2017 April 7. Weather conditions were good or excellent at all sites on all five observing nights. Median opacities on each night are provided in M87* Paper III. In this series of papers, we focus our analysis on April 6 and 7, which have the best (u, v) -coverage.

Two bands of approximately 2 GHz each were observed, centered at sky frequencies of 227.1 and 229.1 GHz (“low” and “high” bands, respectively). Single-dish stations recorded a 2-bit Nyquist-sampled bandwidth of 2048 MHz per polarization using Reconfigurable

Open Architecture Computing Hardware 2 (ROACH2) digital backends ([Vertatschitsch et al., 2015](#)). The SMA observed using six or seven telescopes (depending on the observing night) whose signals were summed using the SMA Wideband Astronomical ROACH2 Machine (SWARM; [Primiani et al., 2016](#); [Young et al., 2016](#)). Since SWARM produces data in the frequency domain at a different sampling rate than at other observatories, SMA data require a post-observation, pre-correlation pass through the Adaptive Phased-array and Heterogeneous Interpolating Downsampler for SWARM (APHIDS; see also the Appendix of [M87* Paper II](#)). ALMA observed as a phased array of 35–37 telescopes using the ALMA Phasing System ([Matthews et al., 2018](#)). Data were recorded onto Mark 6 VLBI Data Systems ([Whitney et al., 2013](#)).

All but two observatories recorded both left and right circular polarization (LCP and RCP respectively). The JCMT was equipped with a single-polarization receiver that observed RCP on 2017 April 5–7 and LCP on 2017 April 10–11. ALMA recorded both linear polarizations (X and Y).

The schedule consisted of scans of Sgr A* interleaved with scans of NRAO 530 (J1733–1304) and J1924–2914 as calibration sources. On 2017 April 6, observations commenced after the preceding target source, M87, set at ALMA. Generally, two eight-minute scans of Sgr A* were followed by a short (typically, three-minute) scan on a calibrator, with an eight-minute gap approximately every hour. The 2017 April 7 schedule, which did not include M87, started when Sgr A* rose above the 20 elevation limit at ALMA. Scan lengths on Sgr A* for this schedule were dithered between five and twelve minutes to reduce the effects of periodic sampling on detection of time variability associated with the ISCO period. On both nights, Sgr A* was observed until the source set below the local horizon at the SMT and LMT, which happens at approximately the same time. The scan coverage for these nights is shown in [Figure 3.1](#).

Data were correlated with the Distributed FX (DiFX) software correlation package

(Deller et al., 2011) at the two correlator centers at the Max-Planck-Institut für Radioastronomie in Bonn, Germany and MIT Haystack Observatory in Westford, Massachusetts; for details see [M87* Paper III](#). The CALC model was used for an a priori correction of rates and delays. Multiple correlation passes were required to diagnose and mitigate data issues, as discussed in the Appendix of [M87* Paper III](#); parameters hereafter refer to those for the final correlation (Rev7) used for science-release data. The final correlation produced 32 baseband channels, each 58 MHz wide with a spectral resolution of 0.5 MHz, and averaged to a 0.4 s accumulation period. The Sgr A* correlation center was set to $\alpha_{J2000} = 17^{\text{h}}45^{\text{m}}40.0356$, $\delta_{J2000} = -29^{\circ}00'28.240''$ ², based on the position of [Reid & Brunthaler \(2004\)](#) corrected to the epoch of observation for the apparent motion introduced by the orbit of the solar system around the Galaxy. The corrected position produced smaller residual delays and rates compared with the uncorrected position, resulting in a minor improvement in sensitivity. Subsequent to correlation, PolConvert ([Martí-Vidal et al., 2016](#)) was run to convert the mixed-polarization data products (XL, XR, YL, YR) to the circular basis on ALMA baselines, as described in [Goddi et al. \(2019\)](#).

3.3 EHT Data Calibration and Reduction

The EHT data calibration pathway is summarized in [Event Horizon Telescope Collaboration et al. \(Section 3 2022b\)](#) and aspects that are particular for the Sgr A* data are highlighted there. I don't include these descriptions here since it is not work that I directly contributed to. A comprehensive description of the EHT data reduction methods, combined with a recap of VLBI data calibration fundamentals, can also be found in [M87* Paper III](#).

²This position for Sgr A* is also adopted in the multi-wavelength analysis that follows.

Table 3.1 Values for the Sgr A* SED observed by coordinated ground-based and space-based observatories during the EHT 2017 run.

Observatory	Frequency [GHz]	νF_ν [$\times 10^{-12} \text{erg s}^{-1} \text{cm}^{-2}$]	Flux [Jy]	νL_ν [$\times 10^{34} \text{erg s}^{-1}$]
EAVN	22	0.24 ± 0.02	1.07 ± 0.11	0.19 ± 0.02
EAVN	43	0.58 ± 0.06	1.35 ± 0.14	0.48 ± 0.05
GMVA	86	1.63 ± 0.17	1.9 ± 0.2	1.3 ± 0.1
GMVA	88	1.67 ± 0.18	1.9 ± 0.2	1.4 ± 0.1
GMVA	98	1.96 ± 0.20	2.0 ± 0.2	1.6 ± 0.2
GMVA	100	2.10 ± 0.20	2.1 ± 0.2	1.67 ± 0.2
ALMA/SMA ^a	213-229	5.28 ± 0.44	2.4 ± 0.2	4.3 ± 0.4
VLT	1.38×10^5	< 4.12	< 0.003	< 3.4
Chandra/NuSTAR	5.68×10^8	$0.70^{+0.15}_{-0.20}$	$1.23^{+0.27}_{-0.35} \times 10^{-7}$	$0.57^{+0.13}_{-0.16}$
Chandra/NuSTAR	7.84×10^8	$0.49^{+0.06}_{-0.11}$	$6.27^{+0.74}_{-1.40} \times 10^{-8}$	$0.40^{+0.05}_{-0.09}$
Chandra/NuSTAR	1.08×10^9	$0.33^{+0.01}_{-0.05}$	$3.09^{+0.11}_{-0.46} \times 10^{-8}$	$0.27^{+0.01}_{-0.04}$
Chandra/NuSTAR	1.49×10^9	$0.25^{+0.25}_{-0.04}$	$1.71^{+1.71}_{-0.25} \times 10^{-8}$	$0.21^{+0.21}_{-0.03}$
Chandra/NuSTAR	2.06×10^9	$0.08^{+0.09}_{-0.02}$	$0.39^{+0.43}_{-0.11} \times 10^{-8}$	$0.06^{+0.07}_{-0.02}$
Chandra ^b	1.57×10^9	$5.63^{+5.06}_{-3.36}$	$3.6^{+3.2}_{-2.1} \times 10^{-7}$	$4.61^{+4.15}_{-2.76}$
NuSTAR ^b	9.55×10^9	$0.78^{+0.86}_{-0.73}$	$8.3^{+9.0}_{-7.6} \times 10^{-9}$	$0.64^{+0.70}_{-0.60}$

^aMean measurement across 213-229 GHz. The spectral index at these frequencies was observed to be close to zero ([Wielgus et al., 2022](#))

^b2017 April 11 X-ray flare.

Note. — Frequencies for X-ray observatories reflect the central frequency of the keV energy band within the observation bin.

3.4 Multi-wavelength Observing Campaign

In addition to the ALMA and SMA millimeter light curves collected as a part of the EHT observations (Figure 3.3, see also [Wielgus et al., 2022](#)), the 2017 Sgr A* EHT campaign includes observations from elite ground-based facilities (§3.4.1), including the East Asian VLBI Network, the Global 3 mm VLBI Array, the Very Large Telescope, as well as space-based telescopes (§3.4.2) including the Neil Gehrels Swift Observatory, the Chandra X-ray Observatory, and the Nuclear Spectroscopic Telescope. Figure 3.2 shows coverage of Sgr A* for each of these instruments during the campaign. These coordinated observations provide (quasi-)simultaneous wavelength coverage and enable detailed multi-wavelength variability studies that place broadband constraints on models (see [Paper V](#) and [Paper VI](#)). We describe these observations briefly here and place them in the broader EHT and Sgr A* historical context in Section 3.5.2.

3.4.1 Supplementary Ground-based Observations

East Asian VLBI Network

The East Asian VLBI Network (EAVN; e.g., [Wajima et al., 2016](#); [An et al., 2018](#); [Cui et al., 2021](#)) consists of the 7 telescopes of KaVA (KVN³ and VERA⁴ Array; e.g., [Lee et al. 2014](#); [Niinuma et al. 2015](#)), and additional telescopes of the Japanese VLBI Network (JVN; e.g., [Doi et al., 2006](#)) and the Chinese VLBI Network (CVN; e.g., [Zheng, 2015](#)). During the EHT 2017 window, four EAVN observations were carried out at 22 and 43 GHz ([Figure 3.2](#)). A single, symmetric Gaussian model was found to describe the intrinsic structure of Sgr A* at both wavelengths. The measured flux densities from Sgr A* at these frequencies are (1.07 ± 0.11) Jy and (1.35 ± 0.14) Jy, respectively ([Table 3.1](#)). Two of the on 2017 April 3 and 4 are (quasi-)simultaneous with the Global 3 mm VLBI Array observations ([Section 3.4.1](#))

³Korean VLBI Network: three 21 m telescopes in Korea (Yonsei, Ulsan, and Tamna)

⁴VLBI Exploration of Radio Astrometry: four 20 m telescopes in Japan (Mizusawa, Iriki, Ogasawara, and Ishigakijima)

as well as the EHT sessions (Cho et al., 2022). These measurements provide an estimated size and flux density of Sgr A* at 1.3 mm via extrapolation of power-law models (i.e., the intrinsic size scales with observing wavelength as a power-law with an index of $\sim 1.2 \pm 0.2$).

Global 3 mm VLBI Array

VLBI observations of Sgr A* at 86 GHz were conducted on 2017 April 3 with the Global Millimeter VLBI Array (GMVA)⁵. Eight Very Long Baseline Array antennas equipped with 86 GHz receivers, the Robert C. Byrd Green Bank Telescope (GBT), the Yebes 40 m telescope, the Effelsberg 100 m telescope, PV, and 37 phased ALMA antennas participated in the observation (project code MB007, published in Issaoun et al. 2019b).

The data were recorded with a bandwidth of 256 MHz for each polarization and fringes were detected out to $2.3 G\lambda$. The total on-source integration time on Sgr A* was 5.76 hr over a 12 hr track, with ALMA co-observing for 8 hr. The results of the experiment rule out jet-dominated radio emission models of Sgr A* with large viewing angles (> 20 deg) and provide stringent constraints on the amount of refractive noise added by the interstellar scattering screen towards the source (Issaoun et al., 2019b), discussed in more detail in Section 5.1.2 of Event Horizon Telescope Collaboration et al. (2022b). The total flux density measured at 86 GHz is (1.9 ± 0.2) Jy (Table 3.1).

Very Large Telescope

The Paranal Observatory's Nasmyth Adaptive Optics System (NAOS) and Near-Infrared Imager and Spectrograph (CONICA) instrument on the Very Large Telescope (VLT), also known as VLT/NACO, measured a K-band near infrared upper limit of 3 mJy during the 2017 April 7 EHT observing run (courtesy of the MPE Galactic Center Team). Ongoing observations with the new Very Large Telescope Interferometer GRAVITY instrument

⁵<https://www3.mpifr-bonn.mpg.de/div/vlbi/globalmm/>

(VLTI/GRAVITY, [Gravity Collaboration et al., 2017](#)) indicate that Sgr A*'s typical flux distribution in the NIR K-band changes slope at a median flux density of 1.1 ± 0.3 mJy, characteristic of Sgr A*'s quiescent NIR emission ([Gravity Collaboration et al., 2020d](#)).

3.4.2 Coordinated Space-based Observations

Neil Gehrels Swift Observatory

Observations from the Swift X-ray Telescope (XRT, [Gehrels et al., 2004](#); [Burrows et al., 2005](#)) were reprocessed with the latest calibration database files and the Swift tools contained in HEASOFT-v6.20⁶. Source flux in the 2–10 keV energy band is extracted from a 10 radius circular region centred on the position of Sgr A*. Count rates are reported as measured (e.g., [Degenaar et al., 2013a](#)), i.e., without any correction for the known significant absorption along the Sgr A* sightline ($N_{\text{H}} \sim 9 \times 10^{22} \text{ cm}^{-2}$).

There are 48 Swift observations of the Galactic center between 2017 April 5 and 2017 April 12, with a total exposure time of 26.3 ks ([Figure 3.2](#)). These observations include a dedicated dense sampling schedule to coincide with the EHT observing window and two observations from the regular Galactic center monitoring program ([Degenaar et al., 2013b, 2015](#); [van den Eijnden et al., 2021](#)). The average exposure time of the dense sampling was ~ 500 s, with an average interval between observations of ~ 3.5 hr.

In the 2017 April 7 Swift observation that overlaps the EHT window ([Figure 3.3](#)), a 2–10 keV flux is detected (0.023 ct s^{-1}) in excess of the 2017 2σ trend-line (0.018 ct s^{-1}), as measured from the cumulative flux distribution observed from Sgr A*. None of the Swift observations are simultaneous with the 2017 April 11 Chandra flare described in the following section.

⁶<https://heasarc.gsfc.nasa.gov/lheasoft/>

Chandra X-ray Observatory

A series of Chandra X-ray Observatory (Weisskopf et al., 2002) exposures of Sgr A* were acquired on 2017 April 6, 7, 11, and 12 using the ACIS-S3 chip in FAINT mode with a 1/8 subarray (observations IDs 19726, 19727, 20041, 20040; PI: Garmire), for a total of ~ 133 ks coordinated with the EHT campaign (Figure 3.2). The small subarray mitigates photon pileup during bright Sgr A* flares, as well as contamination from the magnetar SGR J1745–2900, which peaked at X-ray wavelengths in 2013 and has faded over the more than 6 years since (Mori et al., 2013; Rea et al., 2013, 2020; Coti Zelati et al., 2015, 2017). It also achieves a frame rate of 0.44 s vs. Chandra’s standard rate of 3.2 s.

Chandra data reduction and analysis are performed with the CIAO v4.13 package⁷ (Fruscione et al., 2006), CALDB v4.9.4. We use the `chandra_repro` script to reprocess the level 2 events files, update the WCS coordinate system (`wcs_update`), and apply barycentric corrections to the event times (`axbary`). The 2 – 8 keV light curves are then extracted from a circular region of radius 1.25 centered on the radio position of Sgr A*. Light curves for 2017 April 6, 7 and 11 are shown in Figure 3.3. Using the Bayesian Blocks algorithm (Scargle, 1998; Scargle et al., 2013b; Williams et al., 2017b), we search these light curves for flares and robustly detect one on 2017 April 11, with a second weaker detection on April 7 (orange histograms overplotted on the Chandra light curves in Fig. 3.3).

We use `specextract` to extract X-ray spectra and response files from a similar 1.25 region, centered on Sgr A*. Since our primary interest for this dataset is the flare emission, we do not extract background spectra from a separate spatial region. Instead, spectra of the quiescent off-flare intervals play the role of our background spectra.

The flare and off-flare intervals are identified by analyzing the X-ray light curves of each observation. For the easily detectable flare on 2017 April 11 (observation ID 20041), we use the direct Gaussian fitting method presented in Neilsen et al. (2013b). For 2017

⁷Chandra Interactive Analysis of Observations (CIAO) is available at <http://cxc.harvard.edu/ciao/>.

April 7 (observation ID 19727), we use the Bayesian Blocks decomposition (Scargle, 1998; Scargle et al., 2013b; Williams et al., 2017b); this method is better suited to detecting the sustained low-level activity apparent toward the end of the observation.

Nuclear Spectroscopic Telescope Array

X-ray observations from the Nuclear Spectroscopic Telescope Array (NuSTAR Harrison et al., 2013b) performed three Sgr A* observations from 2017 April 6 to 2017 April 11 (observation IDs: 30302006002, 30302006004, 30302006006). These provide a total exposure time of ~ 103.9 ks and were coordinated with the EHT campaign. We reduced the data using the NuSTAR Data Analysis Software NuSTARDAS-v.1.6.0⁸ and HEASOFT-v.6.19, filtered for periods of high instrumental background due to South Atlantic Anomaly (SAA) passages and known bad detector pixels. Photon arrival times were corrected for on-board clock drift and processed to the Solar System barycenter using the JPL-DE200 ephemeris. We used a source extraction region with 50 radius centered on the radio position of Sgr A* and extracted 3–79 keV light curves in 100 s bins with deadtime, PSF, and vignetting effects corrected (see Zhang et al., 2017b, for further details on NuSTAR Sgr A* data reduction). For all three observations we made use of the data obtained by both focal plane modules FPMA and FPMB.

For flare spectral analysis, we used `nuproducts` in HEASOFT-v.6.19 to create spectra and responses from 30 circular regions (as recommended for faint sources to minimize the background) centered on the coordinates of Sgr A*. As explained in 3.4.2, NuSTAR only partially detected a flare from Sgr A* on 2017 April 11 (observation ID 30302006004), hence we focus on this observation alone in the present work. The source spectrum was extracted from the NuSTAR Good Time Intervals (GTIS) that overlaps with the Chandra flare duration. The background spectrum was extracted from off-flare time intervals in the same observation.

⁸<https://heasarc.gsfc.nasa.gov/docs/nustar/analysis>.

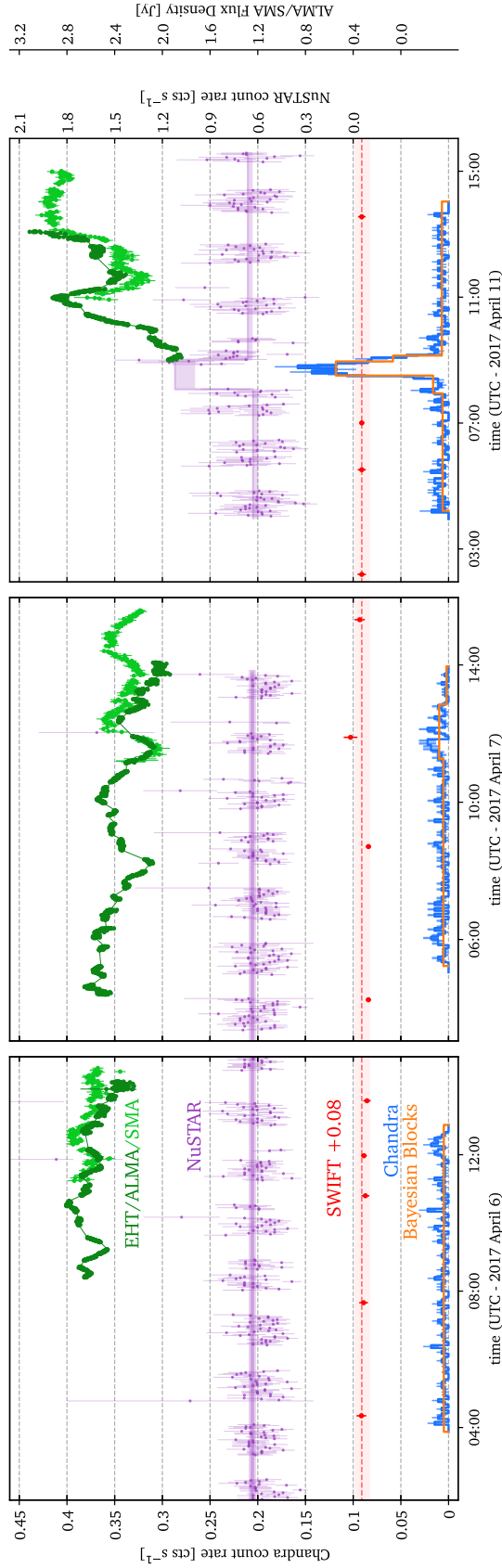


Figure 3.3 Light curves from ALMA at a 4 s cadence and SMA at a 62 s cadence at 229 GHz (dark and light green points, respectively; see [Wielgus et al., 2022](#), for details), along with (quasi-)simultaneous, coordinated Swift (red; 2–10 keV), Chandra (blue; 2–8 keV), and NuSTAR (purple; 3–79 keV) observations on 2017 April 6, 7, and 11. The long term average flux value of Sgr A* measured from Swift is plotted as a red dashed line with upper and lower 2σ percentiles for the 2017 cumulative flux distribution marked with a light red shaded region (e.g., [Degenaar et al., 2013b, 2015](#)). The Bayesian block flare detection algorithm ([Scargle, 1998](#); [Scargle et al., 2013b](#); [Williams et al., 2017b](#)) has been run on the Chandra and NuSTAR light curves and results, including flare detections on 7 and 11 April, are over-plotted as orange histograms on the Chandra data and purple histograms on the NuSTAR data.

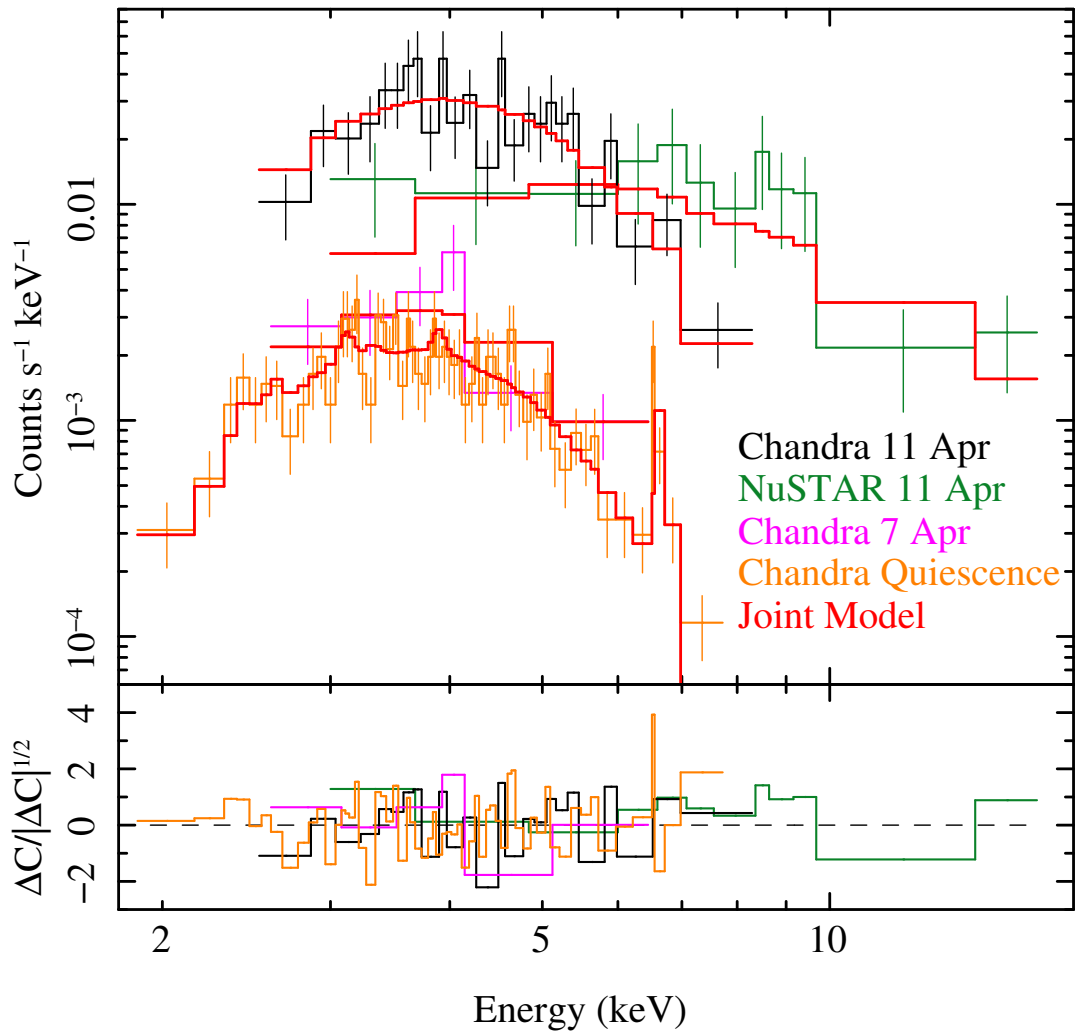


Figure 3.4 Joint Chandra-NuSTAR spectra of flares from Sgr A*. The magenta and black spectra are the Chandra flare spectra from 2017 April 7 and 2017 April 11, respectively; the 2017 April 11 NuSTAR FPMA and FPMB flare spectra are combined for plotting purposes and shown in green. The orange data are the combined spectrum from the off-flare quiescent intervals of all four Chandra observations. The model described in Section 3.4.2 is shown in red for each dataset.

X-ray Flare Spectral Analysis

To obtain the best constraint on the spectrum of Sgr A* during its faint and moderate X-ray flares, we performed joint Chandra/NuSTAR spectral analysis of the two flares described in Section 3.4.2. The following analysis was performed in ISIS v1.6.2-43 and

made use of Remeis `isiscripts`⁹. Chandra flare spectra were binned to a minimum of four channels and a signal-to-noise ratio (S/N) ratio of 3 above 0.5 keV while off-flare spectra were combined and binned to a minimum of two channels and S/N of 3; we fit bins contained within the interval 1–9 keV. The NuSTAR FPMA/FPMB spectra of the 2017 April 11 flare were binned to a combined minimum S/N of 2 and a minimum of three channels above 3 keV. We ignored all bins not fully contained within the interval 3–79 keV. The resulting spectra are shown in Figure 3.4.

Given the relatively small numbers of counts, we opted for simple absorbed power law models for the flare spectra and we compared our model to our data with Cash statistics (Cash, 1979). We used the `TBvarabs` model with Wilms abundances and Verner cross-sections (Verner et al., 1996; Wilms et al., 2000) and assumed a shared spectral index for both flares. (There is no conclusive evidence for a relationship between X-ray flare luminosity and X-ray spectral index; Neilsen et al. 2013b; Zhang et al. 2017c; Haggard et al. 2019b.) Because a portion of the 2017 April 11 flare fell within a gap in the NuSTAR light curve, we included a cross-normalization constant between our NuSTAR and Chandra spectra (as well as between the FPMA and FPMB spectra).

For NuSTAR, we simply defined the spectrum of the off-flare interval as the background file for the 2017 April 11 flare spectrum, but we had to treat the Chandra spectra differently because they are susceptible to pileup during flares (e.g., Nowak et al., 2012b), though fainter flares like those described here are not likely to be impacted. In particular, because pileup depends on the total count rate, not the background count rate, it is necessary to model the background spectrum and treat the flare emission as the sum of the background model and the absorbed power law. We fit the quiescent (off-flare) emission with a single `vapec` model; see Nowak et al. (2012b) for more details.

Once we had a satisfactory fit to the joint flare spectra, we used the `emcee` Markov

⁹This research has made use of a collection of ISIS functions (ISIScripts) provided by ECAP/Remeis observatory and MIT (<http://www.sternwarte.uni-erlangen.de/isis>)

Table 3.2. Chandra/NuSTAR Joint Spectral Parameters

Parameter	Value	Units
N_{H}	$17.8^{+3.5}_{-2.5}$	10^{22} cm^{-2}
Γ	$2.1^{+0.5}_{-0.4}$...
N_{FPMB}	$1.2^{+0.9}_{-0.4}$...
K_{vapec}	$0.0012^{+0.0009}_{-0.0005}$...
kT_{vapec}	$2^{+0.4}_{-0.5}$	keV
N_{ACIS}	$1^{+0.7}_{-0.3}$...
$F_{0704,2-10}$	$0.3^{+0.2}_{-0.2}$	$10^{-12} \text{ erg s}^{-1} \text{ cm}^{-2}$
$F_{0704,3-79}$	$0.5^{+0.8}_{-0.4}$	$10^{-12} \text{ erg s}^{-1} \text{ cm}^{-2}$
$F_{1104,2-10}$	$7.8^{+2.6}_{-3.9}$	$10^{-12} \text{ erg s}^{-1} \text{ cm}^{-2}$
$F_{1104,3-79}$	$15.4^{+8.9}_{-7.5}$	$10^{-12} \text{ erg s}^{-1} \text{ cm}^{-2}$
$F_{\text{Q},2-10}$	$0.5^{+0.2}_{-0.1}$	$10^{-12} \text{ erg s}^{-1} \text{ cm}^{-2}$
$F_{\text{Q},3-79}$	$0.31^{+0.05}_{-0.03}$	$10^{-12} \text{ erg s}^{-1} \text{ cm}^{-2}$

Note. — N_{H} is the X-ray absorbing column density. Γ is the flare photon index. N_{FPMB} is the cross-normalization of the NuSTAR FPMB relative to the FPMA. K_{vapec} and kT_{vapec} are the normalization and temperature of the quiescent vapec component. N_{ACIS} is the cross-normalization of the Chandra ACIS spectrum relative to NuSTAR. Flare (F_{0704} , F_{1104}) and quiescent fluxes (F_{Q}) are quoted for the intervals 2–10 keV and 3–79 keV — the X-ray quiescent and flare fluxes presented in Table 3.1 are νF_{ν} in units of $\text{erg s}^{-1} \text{ cm}^{-2}$, and so differ slightly from the integrated values quoted here. See §3.4.2 and §3.5.2 for further details.

Chain Monte Carlo (MCMC) routine to find credible intervals for our fit parameters. For our MCMC runs, we used 10 walkers (i.e., 10 members of the ensemble) for each of our 10 free parameters, and allowed them to evolve for 10,000 steps (a total of 1 million samples). These runs appear to converge within the first several tens of steps, so we discard the first 500 steps. We estimate an autocorrelation time for our parameter chains between ~ 200 and 400 steps, indicating that we have 2500–5000 independent samples of each parameter.

Finally, we calculate the minimum width 90% credible interval for each parameter. We compute the cumulative distribution function for the samples for each parameter and select the smallest interval that contains 90% of the samples. The results are given in Table

3.2. Sgr A* flares are highly absorbed, with a column density of $N_{\text{H}} = 17.8_{-2.5}^{+3.5} \text{ cm}^{-2}$; this is a bit higher than the values found by [Nowak et al. \(2012b\)](#) and [Wang et al. \(2013b\)](#), but the differences are within $1\text{-}\sigma$ in both cases. The photon index of the flare is $\Gamma = 2.1_{-0.4}^{+0.5}$, which is not well constrained but is consistent with other analyses of X-ray flares ([Porquet et al., 2008](#); [Nowak et al., 2012b](#); [Neilsen et al., 2013c](#); [Haggard et al., 2019b](#)). The 2017 April 7 flare is only detected at 99% confidence, but has an unabsorbed 2–10 keV flux of $F_{0704,2-10} = (0.3 \pm 0.2 \times 10^{-12}) \text{ erg s}^{-1} \text{ cm}^{-2}$ and a 3–79 keV flux $F_{0704,3-79} = (0.5_{-0.4}^{+0.8}) \times 10^{-12} \text{ erg s}^{-1} \text{ cm}^{-2}$. The 2017 April 11 flare has an unabsorbed 2–10 keV flux of $F_{1104,2-10} = (7.8_{-3.9}^{+2.6}) \times 10^{-12} \text{ erg s}^{-1} \text{ cm}^{-2}$, which rises to $F_{1104,3-79} = (15.4_{-7.5}^{+8.9}) \times 10^{-12} \text{ erg s}^{-1} \text{ cm}^{-2}$ over the interval 3–79 keV.

As reported in [Neilsen et al. \(2015b\)](#), the quiescent X-ray flux ($F_{\text{Q},2-10}$) results from an admixture of two components. At the faint end of Sgr A*'s flux distribution, there are both variable and steady components, with the variable component likely arising from unresolved faint flares which contribute $\sim 10\%$ of the apparent quiescent flux (see also [Neilsen et al., 2013d](#)). Adopting the 2 – 10 keV flux from this joint fit (Table 3.2) and allowing a generous $\sim 1/3$ contribution from unresolved X-ray flares, we estimate an upper limit on the median luminosity of $\sim 10^{33} \text{ erg s}^{-1}$. Larger flare contributions would be inconsistent with estimates that approximately 90% of the quiescent emission from Sgr A* is in fact associated with spatially resolved emission.

3.5 Final Data Products and Features

3.5.1 Event Horizon Telescope Data

The properties of the 2017 Sgr A* EHT VLBI data are described in [Event Horizon Telescope Collaboration et al. \(Section 5.1 2022b\)](#). Detailed in particular are the (u, v) -coverage, correlated flux densities, systematic error budgets, estimations for residual antenna-based

gain errors, the influence of interstellar scattering on the measured visibilities, conservative estimates for the size of Sgr A* at 1.3 mm, and an assessment of the source variability.

3.5.2 Multi-wavelength Data

mm, NIR, and X-ray data products

The supplementary ground- and space-based data products leveraged here are published in original works and/or are available in public archives.

EAVN observations of Sgr A* at 22 and 43 GHz are available in [Cho et al. \(2022\)](#), GMVA 86 GHz observations are published in [Issaoun et al. \(2019b\)](#), and a detailed discussion of the VLT/GRAVITY NIR flux distribution can be found in [Gravity Collaboration et al. \(2020d\)](#).

Chandra, Swift, and NuSTAR data products are available via NASA archives^{10,11,12} and are collected in the EHT data portal¹³ under the 2022-D01-02 code (DOI: <https://doi.org/10.25739/26fq-k306>). The repository contains the following data products:

1. Description of observations and data processing (format: text).
2. Fluxes from Swift-XRT observations (format: CSV).
3. Fluxes from Chandra observations (format: CSV).
4. Fluxes from NuSTAR observations (format: CSV).
5. Scripts, spectral, and response files for modeling Chandra and NuSTAR data (format: standard X-ray data formats).

¹⁰The Chandra Data Archive: <https://cxc.harvard.edu/cda/>.

¹¹The Swift Data Archive: <https://swift.gsfc.nasa.gov/archive/>.

¹²The NuSTAR Data Archive: https://heasarc.gsfc.nasa.gov/docs/nustar/nustar_archive.html.

¹³<https://eventhorizontelescope.org/for-astronomers/data>

6. Sampled posterior distributions of X-ray spectral model based on Chandra and NuSTAR data (format: FITS).

The EHT data portal also contains the broadband spectrum presented in Table 3.1 (see also §3.5.2 below) with frequency, flux density, its uncertainty, and instrument index (format: CSV).

Time-averaged spectral energy distribution

Figure 3.5 displays the SED for Sgr A* during the 2017 EHT campaign (open black circles) over-plotted on the historically observed broadband spectrum (colored points). The SED illustrates Sgr A*'s wide range of variable and non-variable states. Larger shaded swaths mark regions of the SED where the source is particularly variable; their bounds mark characteristic quiescent emission and high flux states, which can last for timescales of minutes to hours. (A time-binned historic SED representative of states without extreme variability is presented in Paper VI.) We do not plot a typical quiescent value for NuSTAR frequencies (3–79 keV) since upper-limits are complicated by contributions from non-Sgr A* sources in the galactic center. The flux and luminosity values from each observatory coordinating during the EHT campaign are listed in Table 3.1. The quiescent and flare X-ray luminosities in the SED are νL_ν in units of erg s^{-1} ; their equivalent νF_ν values in $\text{erg s}^{-1}\text{cm}^{-2}$ (Table 3.1) differ slightly from the integrated flux values in Table 3.2.

During the EHT run, Sgr A*'s SED is consistent with historical observations of the black hole in the radio, mm, NIR, and X-ray, as outlined in the Introduction and §3.5.2. For example, the moderately bright X-ray flare detected with Chandra and NuSTAR on 2017 April 11 falls within the range of previously observed X-ray flares (see §3.4.2 and Figure 3.5). Since Sgr A* is not in an exceptional state during the 2017 EHT campaign, these observational constraints on the broadband SED offer valuable priors on theoretical

models aiming to constraint GR, for example the Kerr metric investigation presented in [Paper VI](#).

[Paper V](#) in this series also uses these (quasi-)simultaneous EHT 1.3 mm and multi-wavelength constraints (on both luminosity and degree of variability) to aid in model selection and to provide a physical interpretation for these data, for example by testing aligned, tilted, and stellar wind-fed scenarios using time-dependent GRMHD models. They compare specifically to three MWL bands, 86 GHz, 2.2 μas , and X-ray, which are relatively independent and thus probe different physics, and find that no one existing model can meet all of the EHT and MWL constraints. These challenges motivate improvements to the GRMHD model suites, and encourage additional, joint EHT and MWL campaigns to fully characterize Sgr A*'s short and long term variability.

Characteristic multi-wavelength variability

Sgr A*'s multi-wavelength variability has been studied in detail for more than two decades. Substantial obscuration in the plane of the Galaxy blocks our view of its optical and UV emission, but observations at other wavelengths show flickering, flares, and other stochastic processes on long and short timescales (e.g., [Baganoff et al., 2001b](#); [Dodds-Eden et al., 2009c](#); [Nowak et al., 2012c](#); [Witzel et al., 2012b](#); [Neilsen et al., 2015b](#); [Bower et al., 2015c](#); [Haggard et al., 2019b](#); [Do et al., 2019c](#); [Gravity Collaboration et al., 2020d](#)). Theoretical models also anticipate that observations at different wavelengths will probe different size scales and resolutions (e.g., [Falcke & Markoff, 2013](#)). We briefly describe Sgr A*'s characteristic MWL variability, to put the X-ray flares ([§3.4.2](#)) and the broadband spectrum ([§3.5.2](#)) observed in 2017 into this broader context.

Sgr A*'s X-ray flux distribution can be decomposed into a steady quiescent component described by a Poisson process, and a variable power law component attributed to non-thermal flares that appear approximately once per day ([Neilsen et al., 2015b](#)). Sgr A*'s quiescent NIR light curves show a red noise process and a non-linear, non-Gaussian flux

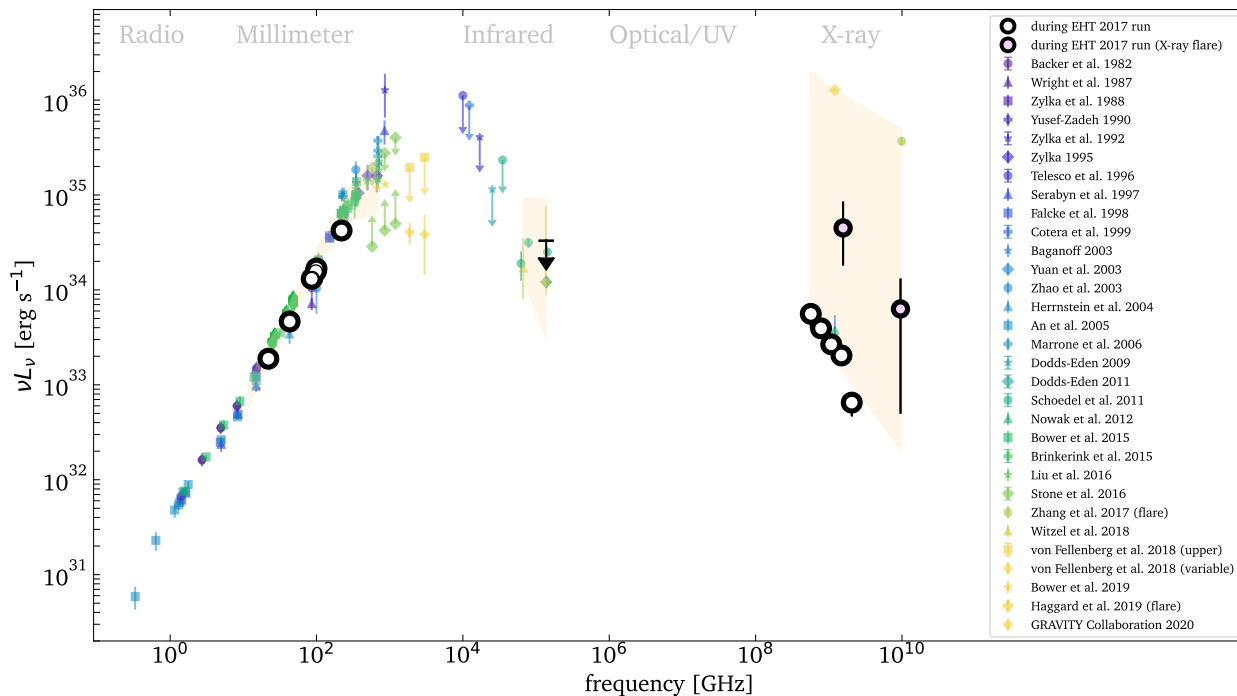


Figure 3.5 The time-averaged SED for the compact Sgr A* source during the 2017 EHT run is shown as black open circles and a NIR upper limit. Luminosities for the X-ray flare observed on 2017 April 11 are indicated as black circles filled with light purple. Table 3.1 lists the 2017 values in units of flux and luminosity. Colored background points display the historic SED of Sgr A* in flaring and quiescent states with the light yellow polygons indicating the range of previously observed variability (Backer, 1982; Zylka & Mezger, 1988; Wright et al., 1987; Yusef-Zadeh et al., 1990; Zylka et al., 1992, 1995; Telesco et al., 1996; Serabyn et al., 1997b; Falcke et al., 1998; Cotera et al., 1999; Baganoff et al., 2003c; Yuan et al., 2003b; Zhao et al., 2003; Herrnstein et al., 2004; An et al., 2005; Marrone et al., 2006c; Dodds-Eden et al., 2009b, 2011b; Schödel et al., 2011; Nowak et al., 2012c; Bower et al., 2015c; Brinkerink et al., 2015b; Liu et al., 2016; Stone et al., 2016; Zhang et al., 2017c; Witzel et al., 2018b; Haggard et al., 2019b; von Fellenberg et al., 2018a; Bower et al., 2019b; Gravity Collaboration et al., 2020d). A time-binned historic SED representative of states without extreme variability is presented in Paper VI.

density distribution, skewed to higher flux densities, which changes slope near a median flux density of 1.1 ± 0.3 mJy (flux densities below 0.1 mJy are rarely observed; e.g., [Witzel et al., 2012b](#); [Do et al., 2019c](#); [Gravity Collaboration et al., 2020d](#)). Thus the NIR flux can also be attributed to separate quiescent and variable components.

The X-ray and NIR variability timescales are both typically several hours, consistent with Sgr A*’s ISCO period of approximately 4–30 min for prograde orbits (vs. 5 days to 1 month for M87*; for further discussion of this comparison, see [Paper I](#)). Recently, the orbital motion of a compact polarized hot spot just outside of the ISCO has been offered as an explanation for high resolution, time resolved interferometric NIR observations ([Gravity Collaboration et al., 2018e](#)), reinforcing the notion that this may be a horizon-scale phenomena.

Correlations between the X-ray and NIR flux peaks (e.g., [Dodds-Eden et al., 2009c](#); [Ponti et al., 2017b](#); [Boyce et al., 2019](#); [GRAVITY Collaboration et al., 2021](#); [Michail et al., 2021b](#); [Boyce et al., 2022](#)) and similarities in their statistical properties and flux density distributions ([Witzel et al., 2012b, 2018c, 2021b](#); [Nielsen et al., 2015b](#)) point to a physical connection between the emission at these wavelengths, though the X-ray structure function seems to have less power at short timescales than the NIR structure function ([Witzel et al., 2012b, 2018b](#); [Nielsen et al., 2015b](#); [Witzel et al., 2021b](#)).

At submillimeter and radio wavelengths Sgr A* also shows a quiescent state superposed with almost continuous variability (e.g., [Miyazaki et al., 2004](#); [Macquart & Bower, 2006](#); [Yusef-Zadeh et al., 2011](#); [Brinkerink et al., 2015b](#)). These longer-duration flares may be delayed by a few hours relative to the X-ray/NIR flares, but simultaneous observations are sparse and the correlations remain tenuous ([Capellupo et al., 2017b](#)). Some submm flares have also been associated with NIR flares, while others show no correlation ([Marone et al., 2008b](#); [Morris et al., 2012](#); [Fazio et al., 2018b](#); [Michail et al., 2021b](#); [Boyce et al., 2022](#)). [Iwata et al. \(2020b\)](#) pursued a detailed study of Sgr A*’s flux density distribution at 217.5, 219.5, and 234.0 GHz, finding variability on timescales of ~ 10 ’s of minutes to hours

that is likely to arise near the ISCO. They find no lag between 217.5 and 234.0 GHz.

Analysis by [Wielgus et al. \(2022\)](#) based on the ALMA and SMA data associated with this 2017 EHT campaign show Sgr A* mostly in a quiescent state at 213, 220, and 229 GHz (Figs. 3.3 and 3.5), though the 2017 April 11 observations following the X-ray flare show enhanced millimeter wavelength variability. The mm light curves are consistent with a red noise process with the power spectral density slope between -2 and -3 on timescales between 1 minute and several hours. In an independent study, [Bower et al. \(2018b\)](#) detect both linear and circular polarization in Sgr A*'s millimeter emission. They find a mean rotation measure (RM) of $\sim -5 \times 10^5 \text{ rad m}^{-2}$ and variability on timescales of hours to months. Long-term variability in the RM (of order weeks to months) is likely due to turbulence in the accretion flow, while short-term variability seems to arise from complex emission and propagation effects near the black hole. They also detect circular polarization with a mean value of $-1.1 \pm 0.2\%$ that is variable on timescales of hours to months ([Bower et al., 2018b](#)). EHT polarimetric measurements of Sgr A* will be the subject of future works in this series.

These and other MWL observations have led to broad consensus that near Sgr A*'s event horizon there are two components: (1) a relatively stable quiescent accretion flow, and (2) flares or bright flux excursions that vary on shorter timescales. Accretion models for Sgr A* suggest that the system may drive a jet, and some data support this possibility. For example, an observed increase of variability amplitude with frequency and persistent time lags in the 18–43 GHz band may be indicative of a jet outflow ([Brinkerink et al., 2021b](#)). Yet despite this and other tentative claims at γ -ray, X-ray, and radio wavelengths (e.g., [Su & Finkbeiner, 2012](#); [Li et al., 2013](#); [Zhu et al., 2019](#); [Yusef-Zadeh et al., 2012b](#); [Rauch et al., 2016](#)), a jet has not yet been conclusively confirmed. The accretion flow and the jet base are both candidates to drive Sgr A*'s variability (e.g., the base of the jet very likely dominates the emission near M87*), yet while their timescales may be distinct, the base of a jet and a variable RIAF remain difficult to tell apart (see [Paper V](#)).

Interstellar scattering may induce additional variable signals over timescales similar to (or longer than) those from the quiescent accretion flow. For example, one explanation for the detectability of the GC magnetar was a variable scattering screen ([Eatough et al., 2013b](#); [Bower et al., 2014](#)). Meanwhile, interactions with orbiting objects may cause additional variability, e.g., disruptions of \sim km-sized rocky bodies, gaseous structures, or other interlopers ([Čadež et al., 2008](#); [Kostić et al., 2009b](#); [Zubovas et al., 2012](#); [Gillessen et al., 2012](#); [Ciurlo et al., 2020](#); [Peißker et al., 2021](#)). Contemporaneous observations with EHT and MWL facilities, particularly simultaneous capture of serendipitous events like flares, continue to offer the best opportunity for disentangling these contributions to Sgr A*'s variable emission.

3.6 Summary and Conclusions

Sgr A* and M87* are the primary targets of the EHT, for which the April 2017 observing campaign provided the required resolution and sensitivity to obtain horizon-scale images of these supermassive black holes. M87* total intensity and polarization results from the 2017 data have been published earlier ([M87* Paper I](#); [M87* Paper II](#); [M87* Paper III](#); [M87* Paper IV](#); [M87* Paper V](#); [M87* Paper VI](#); [M87* Paper VII](#); [M87* Paper VIII](#)). In this new series of papers ([Paper I](#); [Paper II](#); [Paper III](#); [Paper IV](#); [Paper V](#); [Paper VI](#)), we present the imaging, analysis, and interpretation of the 2017 Sgr A* EHT and accompanying data at X-ray, NIR, and millimeter wavelengths from EAVN, GMVA, VLT/NACO, Swift, Chandra, and NuSTAR. Sgr A* was observed by the EHT on 2017 April 5, 6, 7, 10, and 11. In this series of papers, we focus our analysis on the days with the best (u, v) -coverage, 2017 April 6 and 7; a detailed analysis of the full set of Sgr A* millimeter light curves can be found in the companion paper by [Wielgus et al. \(2022\)](#).

The calibrated visibility amplitudes can be described by a blurred ring with a diameter of $\sim 50 \mu\text{as}$ (a deeper discussion of the source size and morphology can be found in

[Paper II](#), [Paper III](#), and [Paper IV](#)). The majority of the total flux measured in our VLBI experiment arises from horizon scales in Sgr A*. Using multi-wavelength constraints on the interstellar scattering screen towards Sgr A*, we show that the scattering-induced angular broadening of the source is sub-dominant to the intrinsic source structure uncovered by the EHT. The refractive noise added by the scattering screen is only relevant for data at baseline lengths $\gtrsim 6 G\lambda$.

Without making strong assumptions about the source structure, we find a compact source size of 39–87 microarcseconds (μas) for Sgr A*, which is in agreement with earlier 1.3 mm VLBI observations of the source. A more precise modeling-based estimation of the source size is given in [Paper III](#). On 2017 April 6 and 7, the source was in a low luminosity state, where the total flux fluctuates around 2.4 Jy with a modulation index of less than 10%. The Sgr A* closure phases show clear intrinsic structural variability on timescales of a few minutes to a few hours that is further investigated in [Paper II](#); [Paper III](#); [Paper IV](#).

Multi-wavelength observations show that Sgr A* was in a mostly quiescent state, with broadband flux levels consistent with historical measures. We detect two X-ray flares: one very faint flare on 2017 April 7 and a brighter flare on 2017 April 11. The fainter 2017 April 7 flare is detected at low significance by Swift and Chandra, and the brighter 2017 April 11 flare is detected more confidently by Chandra and NuSTAR. ALMA and SMA 2017 April 11 observations begin immediately after the bright X-ray flare and show enhanced millimeter wavelength variability ([Wielgus et al., 2022](#)). These multi-wavelength data offer important constraints for theoretical models; indeed, no one of the GRMHD models presented in [Paper V](#) can match the full suite of multi-wavelength constraints. These unprecedented EHT and MWL data thus provide a rich opportunity to improve models of Sgr A* and to advance our understanding of the physics near the SMBH event horizon. The high quality, nearly simultaneous multi-wavelength SED is additionally valuable for understanding the priors for sophisticated tests of GR (see [Paper VI](#)). Looking ahead, future detailed analysis of the EHT and MWL observations on 2017 April 11

holds great promise for understanding the underlying mechanisms that drive Sgr A*'s flares and other variability.

Text in this chapter will be submitted to MNRAS,
as “WISDOM project λ . Constraining mass of the
central supermassive black hole in NGC 1387
with molecular gas” (Boyce et al.)

Chapter 4

Measuring SMBH masses through molecular gas kinematics

Though the spatial regions in Chapters 2 and 3 occupy a small physical portion of a galaxy’s total extent, the observed mass distributions of large samples of galaxies, which are built up over giga-years, correlate with the masses of their central black holes. In other words, there exists a two-way relationship between small-scale, short-timescale phenomena around SMBHs (AGN, transient accretion events, starbursts in a nuclear star cluster) and large-scale properties of their galaxies (size, mass, kinematics, stellar population). To accurately interpret these varied relationships, reliable measurements of the mass of the central SMBH across all types of galaxies is essential. Approaching the task systematically, the mm-Wave Interferometric Survey of Dark Object Masses (WISDOM) project targets a large sample of galaxies with signatures of central molecular gas. In the third study of this thesis, we present a measurement of the mass of the SMBH in the lenticular Fornax-cluster galaxy NGC 1387, obtained by modeling the kinematics of the molecular gas at the edge of the sphere of influence ($\sim 10^{5-7} R_S$, 10s of parsecs).

4.1 Introduction

At the heart of nearly every galaxy there exists an extremely large and concentrated amount of mass that is not detectable through any amount of intrinsic light. The common interpretation is that these are supermassive black holes (SMBHs), for which the most convincing evidence comes from (1) the orbits of stars around an extremely massive invisible point at the centre of our own galaxy and (2) the direct imaging of the shadow of M87's central black hole. Often surrounded by hot gas at 10^6 K (Quataert, 2002a) in the centres of nuclear star clusters reaching densities of 10^5 stars/pc³ (Pechetti et al., 2020), the environments immediately surrounding SMBHs are some of the most extreme in the universe. At these scales close to the black hole, studies can range from imaging the event horizon (Event Horizon Telescope Collaboration et al., 2019a, 2022a), to constraining models of accretion in strong gravitational and magnetic fields (Ripperda et al., 2022), to characterizing stellar populations in the nuclear star cluster (Kacharov et al., 2018). Out at larger scales, the potential jets and winds blown off of accretion disk can ionize gas, shock material (Moy & Rocca-Volmerange, 2002), and even trigger (Ishibashi & Fabian, 2012) or quench (Su et al., 2021) star formation. In turn, the large-scale distribution of stars and gas, the turbulence or regularity in their kinematics, and their quiescent or star-forming state affects the quantity and characteristics of the available material that could fall into the central potential and feed a growing SMBH (Gatti et al., 2015). Accurately interpreting these varied relationships requires determining the mass of central SMBHs across all types of galaxies.

The mass of a central black hole is typically inferred from the correlations with global galaxy properties (e.g. mass, velocity dispersion McConnell & Ma, 2013c) that are relatively easy to observe. Though useful as a coarse estimate, there is growing evidence that these correlations may not be reliable across different galaxy populations, contain sample biases, and are based on few datapoint with large uncertainties (Kormendy & Ho, 2013).

More directly, one can estimate a SMBH's mass through the observation of its gravitational influence. The region in which this influence is the dominant force (the sphere of influence) is the region in which the kinematics of orbiting material is driven primarily by the gravitational potential of the black hole. Therefore, directly observing the kinematics of gas and stars around a SMBH reliably estimates the BH mass. These methods include probing and modelling stellar kinematics (e.g. [Boehle et al., 2016a](#)), megamaser kinematics (e.g. [Greene et al., 2010](#)), ionized gas kinematics (e.g. [Barth et al., 2001](#)), and recently, molecular gas kinematics (e.g. [Davis et al., 2013a](#)).

Each method of estimating SMBH mass through gas or stellar kinematics comes with its own selection biases across galaxy types. For example, kinematic signatures from megamaser AGN, luminous stimulated emission from excited populations of atoms or molecules, are rare (e.g. in $\sim 5\%$ of objects searched in [Greene et al., 2010](#)), because they are only generated under special conditions and require the galaxy to be nearly edge on. They are typically found in the nuclei of Seyfert-2 type galaxies and in the nuclei of low mass, low-ionization nuclear emission region (LINER)-type galaxies ([Barth et al., 2001](#)). Though stellar kinematics have been key to measuring the mass of Sagittarius A* (the black hole at the centre of our Milky Way, [Boehle et al., 2016a](#)), and have successfully estimated SMBH masses in a range of galaxy types, the method can be easily hampered by dust contamination and requires either directly measuring individual stars or detecting strong absorption lines in stellar spectra. To minimize bias in the estimate of BH mass, it is essential to increase the sample of measured SMBHs over a diverse range of galaxy properties with a reliable method.

Fortunately, molecular gas disks can be found in a range of galaxies of all morphological types ([Davis et al., 2013a](#)) and in galaxies over a wide range of masses ([North et al., 2019](#)). These disks are relatively common ([Smith et al., 2021](#)), and well resolved with modern interferometers (e.g. the Atacama Large Millimeter/sub-millimeter Array (ALMA)). The observation of molecular gas probed through millimetre/sub-millimetre

transition lines is also free from dust attenuation. Therefore modelling the kinematics of these prevalent molecular gas disks can provide less biased estimates of SMBH masses over a range of galaxy types and sizes.

The mm-Wave Interferometric Survey of Dark Object Masses (WISDOM) aims to reliably estimate the masses of SMBHs across galaxy types with the same method: detecting the kinematics signature of SMBHs on central molecular gas disks. With many galaxies containing molecular gas at their center, this will enable the production of a catalogue of masses that minimizes measurement bias – allowing the true correlations between central SMBHs and the physical properties of their host galaxies to be revealed.

Since the original demonstration and characterization of this method with carbon monoxide (CO) by [Davis et al. \(2013a\)](#) and [Davis \(2014\)](#), there have been several mass measurements of SMBHs through the kinematics of molecular gas (see also [Yoon \(2017\)](#)). The method has applied to galaxies across the Hubble sequence from early type ([Onishi et al., 2017](#); [Barth et al., 2016b,a](#); [Davis et al., 2017, 2018](#); [Boizelle et al., 2019](#); [North et al., 2019](#)), to late type ([Onishi et al., 2015](#)). It has also been successful in galaxies with irregular gas distributions ([Smith et al., 2019](#)), with tori ([Combes et al., 2019](#)), and with radial filaments ([Nagai et al., 2019](#)).

In this work we present an estimate of the SMBH mass at the centre of the early-type galaxy NGC 1387. We start by describing the properties of NGC 1387 and summarize previous studies of it in section 2. In Section 3 we discuss our observations and their calibration, reduction, and imaging. We then describe the kinematic model and present the SMBH mass measurement in Section 4. Finally, in Section 5 we discuss the results and anticipate the next steps of analysis.

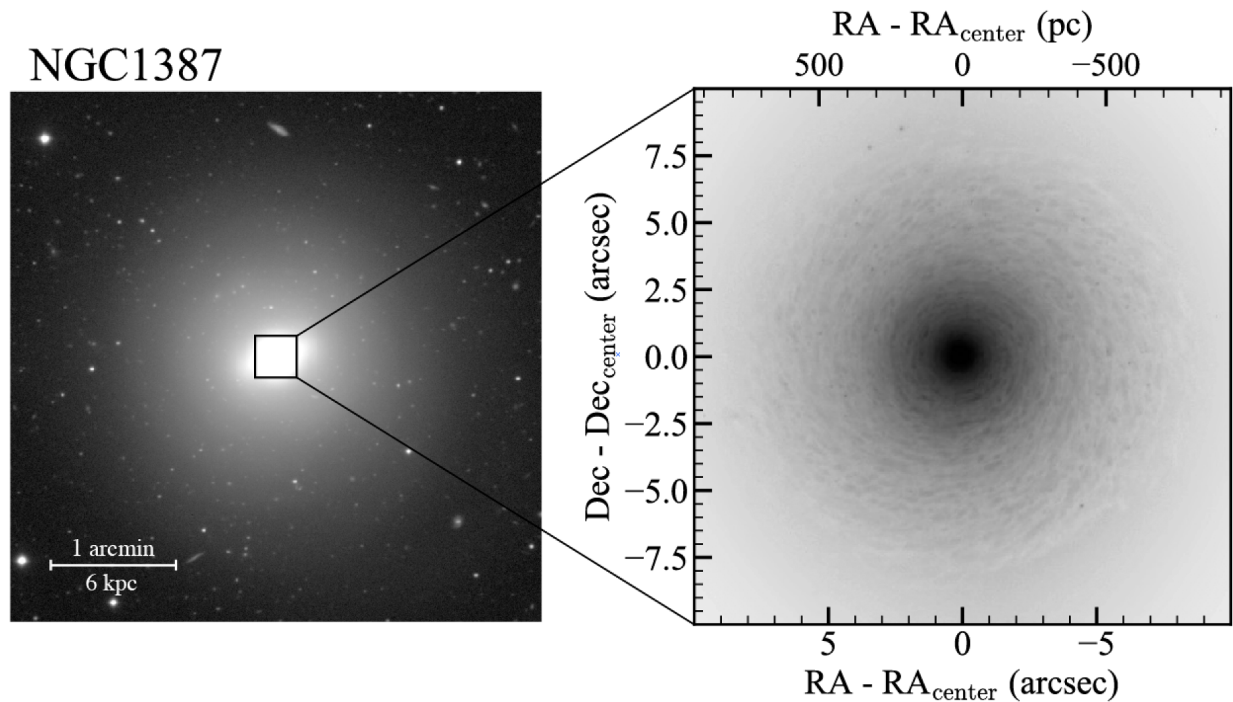


Figure 4.1 *Left*: Optical image of NGC 1387 from the Carnegie-Irvine Galaxy Survey (Ho et al., 2011). Imaged with the du Pont 2.5m telescope at Las Campanas Observatory. *Right*: HST/WFPC2 F606 image of the central 20''

4.2 NGC 1387

NGC 1387 is a nearly face-on lenticular galaxy with a bar structure embedded in an extensive stellar envelope. Deep within the stellar potential, Hubble images reveal a central disk of dust with a diameter of about 1.4 kpc (Figure 4.1). The galaxy sits near the centre of the Fornax cluster with an on-sky distance of about 12 arcminutes from NGC 1399. It is among the closest and brightest objects in the cluster at a distance of 16.2 ± 0.2 Mpc and with an apparent magnitude of $M_v = -20.95$. Adopting this distance throughout the paper, 1'' corresponds to 90 pc.

Liu et al. (2019) report the total stellar mass of the galaxy to be $M_{\text{stars}} = 6.55 \times 10^{10} M_{\odot}$ from the measurements cited in Turner et al. (2012). Using this measurement and assuming the bulge mass can approximate the majority of the stellar mass, the inferred SMBH mass would be $\log(7-7.5) M_{\odot}$ from the stellar mass scaling relation in McConnell

& Ma (2013c). For comparison, the inferred SMBH mass from the velocity dispersion scaling relation is $\log(7-7.4) M_{\odot}$ from the measured stellar velocity dispersion $\sigma \sim 140 \text{ km s}^{-1}$ (Liu et al., 2019). This measured dispersion can also estimate the radius of the sphere of influence of the SMBH, defined as $R_{\text{SoI}} = G \times M_{\text{BH}} / \sigma^2$. Therefore, the expected sphere of influence for NGC 1387 based on these measures is 2–25 pc (corresponding to 0.02–0.27 arcsec).

4.3 ALMA Observations

NGC 1387 was observed on three dates with the ALMA 12m array as part of the WISDOM programme 2016.1.00437.S. A window of 1.8 GHz centered on CO(2-1) line at 226.6 GHz captured a velocity coverage of 500 km s^{-1} with a raw channel width of 1.2 km s^{-1} . Three other windows targeted continuum emission, each with a width of 2 GHz. The raw data were calibrated using the standard ALMA pipeline.

To image the data, the COMMON ASTRONOMY SOFTWARE APPLICATIONS (CASA; McMullin et al., 2007) was used to combine all four measurement sets. The resulting data cube (RA, DEC, velocity) has a channel width of 10 km s^{-1} . Using a Briggs weighting with a robust parameter of 0.75 balanced requirements for sensitivity with resolving power to produce a synthesized beam with size $0.077'' \times 0.045''$. The corresponding spatial resolution is $6.9 \text{ pc} \times 4.1 \text{ pc}$, so that the predicted R_{SoI} could be resolved with about 4 synthesized beams if M_{SMBH} is $\sim 10^8 M_{\odot}$. If M_{SMBH} is $\sim 10^7 M_{\odot}$, then the sphere of influence will be smaller than the synthesised beam, but its kinematic signature could still be detectable if central gas velocities are higher than would be expected from the stellar potential alone. A pixel size of 0.015 was chosen so that approximately three would span the minor axis of the synthesized beam.

To isolate the line emission, continuum emission was detected, measured over the full line-free bandwidth, and then subtracted from the data in the uv-plane using the CASA

task `UVCONTSUB`. The continuum-subtracted cube was cleaned in interactively-identified regions¹ of source emission in each channel to a threshold equal to the rms noise of the dirty channels. The clean components were then added back and re-convolved using a Gaussian beam of FWHM equal to that of the dirty beam. This produced the final, reduced and fully calibrated CO(2–1) data cube of NGC 1387.

4.3.1 Line Emission

Figure 4.2 displays the CO(2-1) integrated spectrum, made by integrating over the central 20 arcseconds of the clean cube. Kinematic modelling was performed on the full three-dimensional data cube, but to visualize and help interpret the data, moment maps were created using a masked moment technique (e.g. Dame, 2011) and are also presented in Figure 4.2. The zeroth moment displays the integrated intensity of the CO(2-1) line, the first moment the mean velocity of the gas, and the second moment the velocity dispersion. The top panels of Figure 4.2 clearly display a regularly rotating and symmetrical gas disk. It extends $\sim 18 \times 18$ arcsec in projection (~ 800 pc \times 800 pc). The major-axis position–velocity diagram (PVD; Figure 4.2) was constructed by summing pixels within a 5-pixel wide pseudo-slit at a position angle of 244° . The lack of flux at the centre of the PVD arises from the hole we observe in the central arcsecond of the gas disk (see Figure 4.4).

4.4 Kinematic Modelling

The modelling of NGC 1387’s gas disk was carried out using the same methods as detailed in previous works of this series (e.g. Davis et al., 2017; Smith et al., 2019). Here we provide an outline of the method along with specific details that are unique to this target.

¹Using `tclean` with `interactive=True` still goes through many cycles of SNR cuts with an automatic procedure, such that the interactive steps involve manually selecting the very loose, broad regions where real emission is.

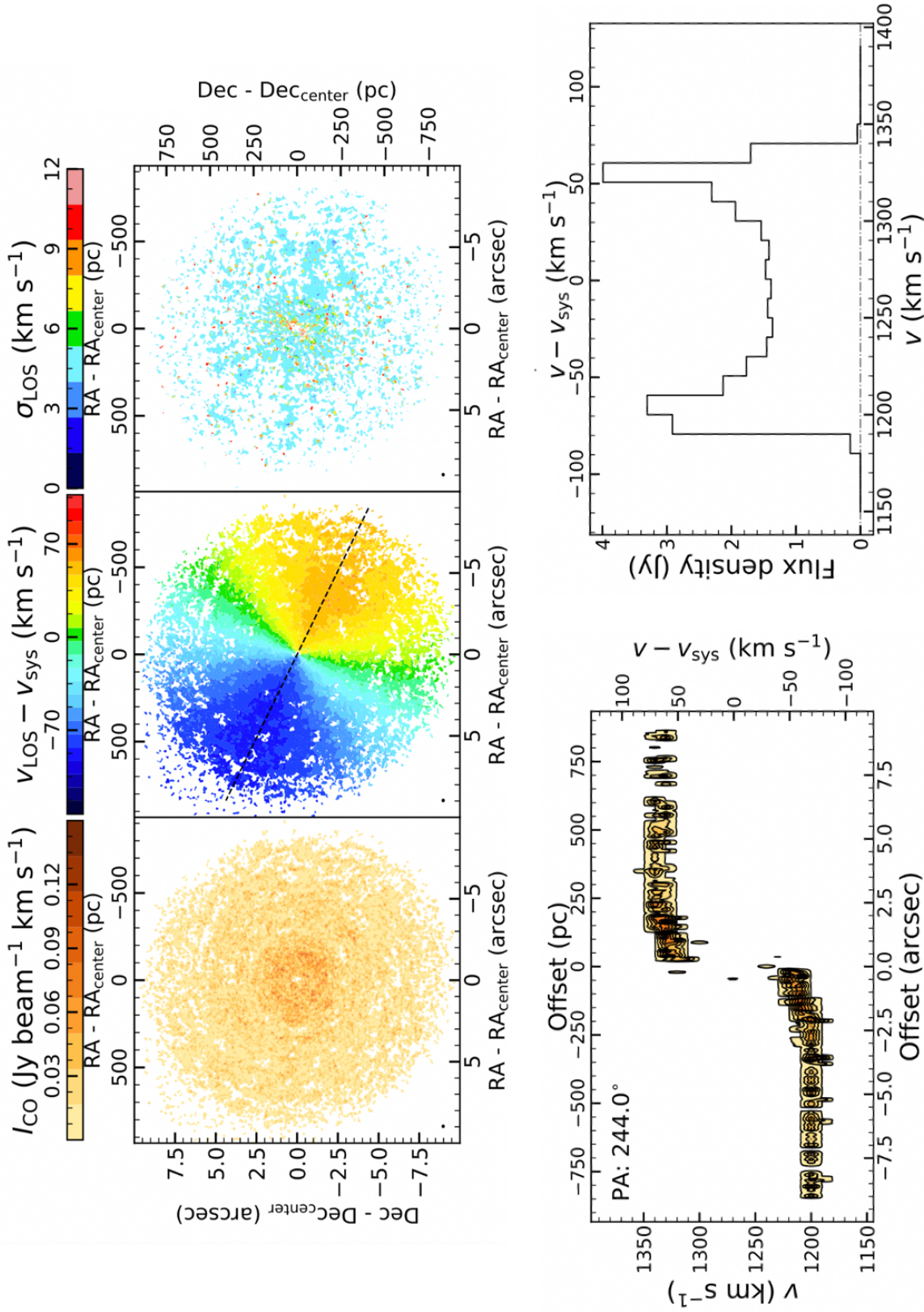


Figure 4.2 Moment maps and spectrum of the CO(2-1) emission in NGC 1387, from our ALMA data. *Top left*: zeroth moment displaying the integrated intensity of the CO(2-1) line; *Top middle*: first moment displaying the mean velocity of the gas; *Top right*: second moment displaying the velocity dispersion. *Bottom left*: major-axis position-velocity diagram (PVD); *Bottom right*: CO (2-1) integrated spectrum of the entire disk.

To create simulated data cubes we make use of the publicly available `KineMatic molecular Simulation (KinMS)`² mm-wave observation simulation tool first described in [Davis et al. \(2013b\)](#). As input, `KinMS` takes a gas disk’s physical parameters (e.g. the expected surface brightness distribution, inclination of the disk, and the position angle of the disk) as well as the galaxy’s circular velocity curve. This circular velocity curve is used to assign each simulated gas particle its expected velocity at its respective radius from the galaxy’s kinematic center (with the addition of a random velocity drawn from a distribution representing the velocity dispersion given by the user). `KinMS` then places each particle in the data cube by projecting their velocities along the line of sight according to the specified orientation of the disk on the sky. Applying observational effects such as velocity binning and simulating the properties of the true beam, `KinMS` generates a simulated interferometric data cube that we can directly compare to observations. By iteratively generating model data cubes, the model parameters are incrementally driven towards the best-fit values by a Markov chain Monte Carlo (MCMC) gibbs-sampler algorithm with adaptive stepping³.

4.4.1 Stellar Potential

We require an estimate of the galaxy’s stellar potential as a function of radius to estimate the circular velocity curve of the galaxy and model the kinematics of the molecular gas. Apart from any SMBH, we assume that the stellar mass dominates the potential in the central parts of the galaxy, and contributions from dark matter are negligible at small radii (e.g. [Cappellari et al., 2013](#)). To accomplish this we use a *Hubble Space Telescope (HST)* Near Infrared Camera and Multi-Object Spectrometer (NICMOS) F160W image of the galaxy centre in the near-infrared filter to minimize dust attenuation. This allows us to model the light as a sum of two dimensional (2D) gaussians via a Multi-Gaussian Expansion

²Python version: <https://github.com/TimothyADavis/KinMSpy>

³Found at: <https://github.com/TimothyADavis/GASimulator>

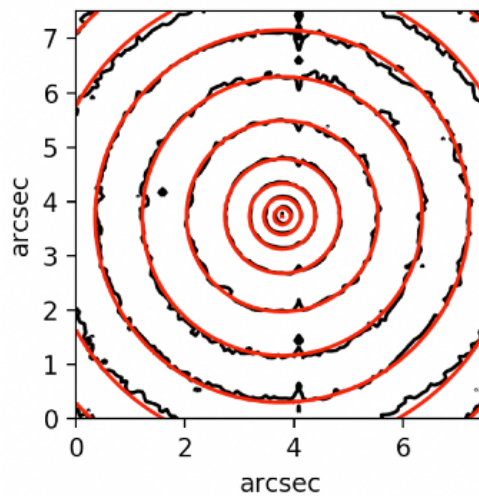


Figure 4.3 MGE model of NGC 1387 (red contours) overlaid on the HST NICMOS F160W image (black contours).

(MGE; [Emsellem et al., 1994](#)) using the python implementation `mgefit`⁴ by [Cappellari \(2002\)](#). Though the data may look smooth and gaussian by eye, the 2D profile requires multiple Gaussian components to approximate its' shape. The resulting MGE model is shown in Figure 4.3, with the values of each Gaussian listed in Table 4.1. The circular velocity curve is then calculated with `mge_vcirc` by de-projecting the 2D gaussians into 3D using the inclination of the gas disk and a transforming the distribution of stellar light into a mass distribution by adopting a mass-to-light ratio (M/L). This ratio is one of the key parameters included in the MCMC fit.

4.4.2 Gas Distribution and Disk Properties

Ultimately we must test whether a model with realistic mass-to-light (M/L) ratio assigned to the stellar light from our observed map requires the addition of a central SMBH to explain the observed kinematics of the CO disk. Such a model must also fit the geometry and distribution of the gas, and remain consistent with the inclination and position angle observed from the large scale gas disk.

⁴<https://www-astro.physics.ox.ac.uk/~cappellari/software/>

I ($L_{\odot, F160W} \text{ pc}^{-1}$)	σ_j (arcsec)	q_j
183,000	0.05	1.0
112,000	0.20	1.0
57,000	0.48	1.0
31,000	1.22	1.0
24,000	2.84	0.9

Table 4.1 MGE best-fitting Gaussians. Column 1 (I) lists the F160W central surface brightness, column 2 (σ_j) lists its standard deviation, and column 3 lists its axial ratio.

In principle, the gas distribution can be parameterized by an analytic model of an axisymmetric exponential disk, which has worked well in previous works (Onishi et al., 2017; Davis et al., 2017, 2018). However, the high spatial resolution provided by ALMA often reveals complexities in the gas distribution, and in our case, a non-symmetric central hole (Figure 4.4). In order to avoid adding complexity and higher dimensionality into an analytic model for the disk, we directly sample the observed gas distribution and use that as input particles into `KinMS`. The tool to achieve this (`skysampler`) is described in Smith et al. (2019).

4.4.3 Best-fitting model

We ran the MCMC chain for 100 000 steps. The best fitting model cube approximates the observed gas disk well. Figure 4.5 displays the covariances for each pair of input parameters and the 1D marginalization of each parameter. Preliminary tests suggest that the MCMC chain is well converged, but further work is underway to verify the robustness of these measurements (see Section 4.5). Table 4.2 lists the best-fitting and formal uncertainties of each model parameter. Figure 4.6 displays a slice of the best fit model as black contours on the orange data in the upper right panel. The best-fit inferred log of the SMBH mass is 7.7 ± 0.7 with a M/L of $0.39 \pm 0.20 M_{\odot}/L_{\odot, I}$, where both uncertainties are the 3σ

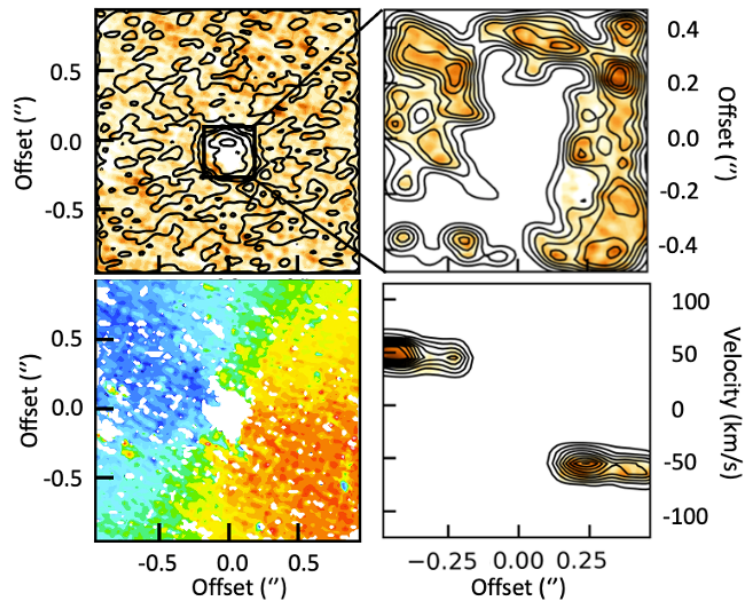


Figure 4.4 The inner arcseconds of NGC 1387's central gas disk. *Top left*: the integrated intensity of the CO(2-1) line; *Bottom left*: mean velocity; *Top Right*: a zoomed in view of the central hole in the CO(2-1) intensity; *Bottom Right*: the zoomed in PVD of the central arcsecond.

(99.7%) confidence level.

4.5 Discussion and Future Analysis

Since the molecular gas disc has a central hole, we do not capture the Keplerian increase of the rotation velocities where the SMBH dominates the mass distribution. We therefore rely on the accuracy of our stellar mass model to constrain the SMBH mass, observing an enhancement of the velocities in the inner arcsecond compared to those expected from the stellar mass alone. This is demonstrated in an examination of the major axis PVD in Figure 4.6, where increasing the M/L to fit the high velocities of the inner edge of the disk (bottom left panel) over predicts velocities at larger radii and fitting for the best M/L in the absence of a SMBH cannot fit the central components (upper right panel).

To address the impact that the uncertainty the inclination has on the SMBH mass, we

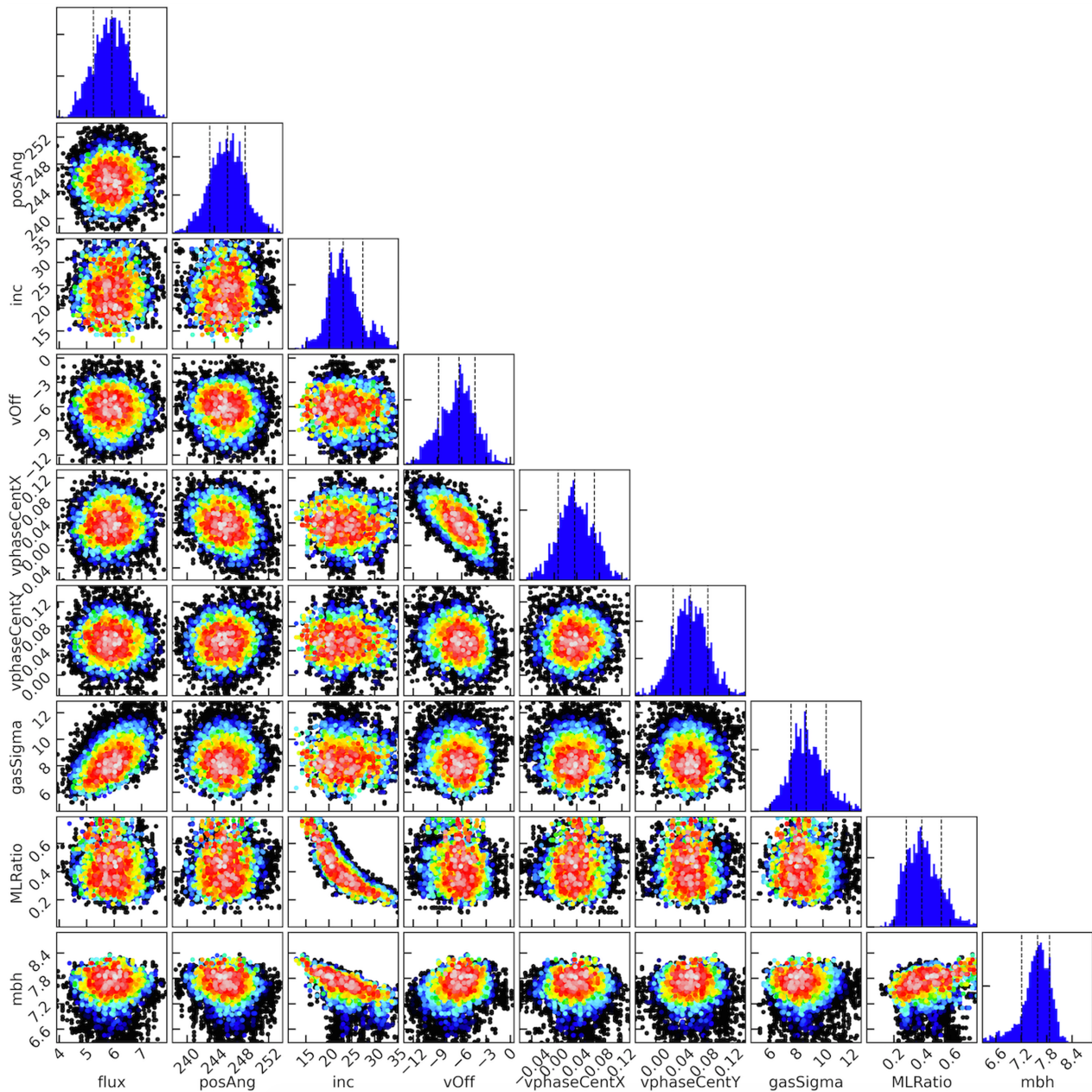


Figure 4.5 Corner plot showing the covariances between all model parameters from our MCMC fit. Each point is a realization of the model. Each histogram shows the 1D marginalisation of a model parameter, the central black lines denoting the median values. The other two dashed lines indicate the 68% confidence interval.

Parameter (1)	Priors (2)	Best-fit (3)	Median (4)	3σ error (5)
Mass Model				
log(SMBH mass) (M_{\odot})	$1 \rightarrow 10$	7.7	7.6	0.7
stellar M/L ($M_{\odot}/L_{\odot,I}$)	$0 \rightarrow 1$	0.39	0.39	0.20
Molecular Disc				
Integrated Intensity (flux; Jy km s^{-1})	$0 \rightarrow 10$	6.0	5.9	1.1
Gas velocity dispersion (km s^{-1})	$0 \rightarrow 15$	8.7	8.7	2.7
Viewing Geometry				
Inclination ($^{\circ}$)	$10 \rightarrow 60$	19.8	23.1	8.2
Position Angle ($^{\circ}$)	$150 \rightarrow 300$	246	247	7
Nuisance Parameters				
Centre RA Offset ($''$)	$-0.5 \rightarrow 0.5$	0.036	0.036	0.091
Centre Dec. Offset ($''$)	$-0.5 \rightarrow 0.5$	0.054	0.056	0.072
Centre Velocity Offset (km s^{-1})	$-20 \rightarrow 0$	-6.2	-6.3	4.9

Table 4.2 Best-fitting model parameters with associated formal uncertainties. Column 1 lists the input parameters for the dynamical model of NGC 1387's central gas disc and SMBH. Column 2 lists the range allowed for each parameter, between which we adopt a uniform prior, except for SMBH in which the prior is uniform in log-space. Column 3 lists the best-fitting parameter, while column 4 lists the median after marginalizing over all other parameters. Column 5 lists the 3σ (99.7%) confidence interval for each parameter.

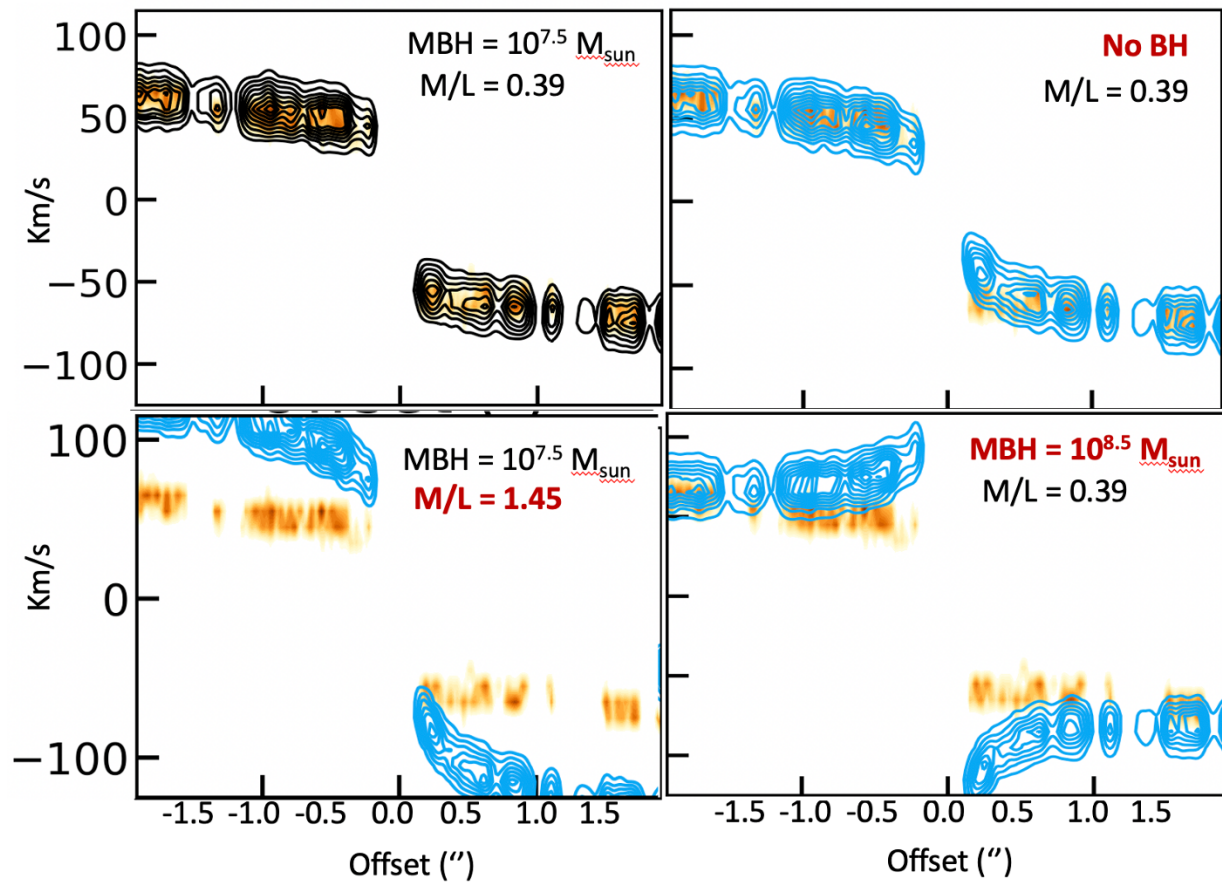


Figure 4.6 Comparison between the PVD of the data (orange), the best fitting model (black contours; upper right), and three kinematic models with the black hole mass or M/L altered (blue contours). These three models represent gas disks with no SMBH (upper right), a SMBH the same size as the best-fit model but an elevated M/L (bottom left), and a model with a SMBH that is too massive (bottom right).

will fit our kinematic model to the large scale (lower resolution) map of entire gas disk with an instance that does not include a BH. The presence or absence of a BH at this resolutions makes no impact on the gas kinematics and we can use the result to inform our prior on the inclination for the high-resolution zoomed-in fit. We will also explore whether a M/L ratio that changes with radius would easily explain the elevated velocities, though preliminary examination of the metallicity map from MUSE data does not suggest that a strong gradient in stellar population exists. Future analysis steps will also involve characterizing the continuum source to place it in the context of other AGN.

In summary, we have presented a mass measurement of the SMBH in NGC 1387 by modelling the kinematics of its central molecular gas disk. Our best fit model gives $M_{\text{BH}} = \log(7.7) \pm 0.7$, compared to $\log(7.2) M_{\odot}$ estimated from the measured stellar velocity dispersion $\sigma \sim 140 \text{ km s}^{-1}$ (Liu et al., 2019), showing good agreement with expectations. This marks the 8th SMBH mass measurement from the mm-Wave Interferometric Survey of Dark Object Masses (WISDOM). This work not only shows the power of ALMA to estimate SMBH masses, but also demonstrates that even in cases where a central hole in the gas prevents a complete sampling of the sphere of influence, a precise mass can still be obtained. Future analysis will validate whether the measurement remains robust when (1) fitting with a kinematic model with no SMBH, (2) using an informed prior on the inclination, and (3) examining scenarios in which the M/L ratio varies with radius.

Chapter 5

Discussion

5.1 Discussion of main projects

In this thesis we journey from the event horizon out to the edge of the sphere of influence, probing signatures of gas in the immediate environments of SMBH to both characterize their accretion and measure their mass.

In the first study, we report timing analysis of near-infrared (NIR), X-ray, and sub-millimeter (submm) data during a three-day coordinated campaign observing Sagittarius A*. Data were collected at $4.5\mu\text{m}$ with the Spitzer Space Telescope, $2 - 8$ keV with the Chandra X-ray Observatory, $3 - 70$ keV with NuSTAR, 340 GHz with ALMA, and at $2.2\mu\text{m}$ with the GRAVITY instrument on the Very Large Telescope Interferometer. Two dates show moderate variability with no significant lags between the submm and the infrared at 99% confidence. July 18 captured a moderately bright NIR flare ($F_K \sim 15$ mJy) simultaneous with an X-ray flare ($F_{2-10\text{keV}} \sim 0.1$ cts/s) that most likely preceded bright submm flux ($F_{340\text{GHz}} \sim 5.5$ Jy) by about $+34^{+14}_{-33}$ minutes at 99% confidence. The uncertainty in this lag is dominated by the fact that we did not observe the peak of the submm emission. A synchrotron source cooled through adiabatic expansion can describe a rise in the submm once the synchrotron-self-Compton NIR and X-ray peaks have faded. This model predicts high GHz and THz fluxes at the time of the NIR/X-ray peak and electron

densities well above those implied from average accretion rates for Sgr A*. However, the higher electron density postulated in this scenario would be in agreement with the idea that 2019 was an extraordinary epoch with a heightened accretion rate. Since the NIR and X-ray peaks can also be fit by a non-thermal synchrotron source with lower electron densities, we cannot rule out an unrelated chance coincidence of this bright submm flare with the NIR/X-ray emission.

In the second work, we present the multi-wavelength campaign coordinated with Event Horizon Telescope (EHT) 1.3 millimeter measurements of the radio source located at the position of Sgr A*, collected during the 2017 April 5–11 campaign. While the radio observations were carried out with eight facilities at six locations across the globe, contemporaneous multi-wavelength monitoring of Sgr A* was performed at 22, 43, and 86 GHz and at near infrared and X-ray wavelengths. Several X-ray flares from Sgr A* are detected by Chandra, one at low significance jointly with Swift on 2017 April 7 and the other at higher significance jointly with NuSTAR on 2017 April 11. The brighter April 11 flare is not observed simultaneously by the EHT but is followed by a significant increase in millimeter flux variability immediately after the X-ray outburst, indicating a likely connection in the emission physics near the event horizon. We compare Sgr A*'s broadband flux during the EHT campaign to its historical spectral energy distribution and find both the quiescent and flare emission are consistent with its long-term behaviour.

Finally, probing out past the sphere of influence, we present a measurement of the mass of the SMBH in the galaxy NGC 1387. A lenticular galaxy in the Fornax cluster, NGC 1387 contains a nearly face-on molecular gas disk at its centre. We map this disk through the detection of the CO(2– 1) emission line with data taken with the Atacama Large Millimeter/sub-millimeter Array (ALMA). Our data has a spatial resolution of 0.08 arcsec, and a spectral resolution of 10 km/s allowing us over beams within the central arcsecond. The molecular disk contains a central hole of about 0.25 arcsec, leaving us with a ring of gas in which we detect rotation velocities that require a Keplerian increase to

explain. We require a constant M/L ratio of 0.39 along with a SMBH mass of $\log(7.7) M_{\odot}$. This measurement marks the 8th SMBH mass measurement from the mm-Wave Interferometric Survey of Dark Object Masses (WISDOM), and demonstrates the power of this method to estimate central BH mass even when emission is missing from most of the central region containing the sphere of influence.

5.2 Current and Future Work

Building on these three studies, I am engaged in several ongoing and proposed projects that will continue to expand our understanding of SMBHs.

5.2.1 Sgr A* & M87*

The only two targets imaged at event horizon scales, Sgr A* ($\sim 4 \times 10^6 M_{\odot}$ [Event Horizon Telescope Collaboration et al., 2022a](#)) and M87* ($\sim 6 \times 10^9 M_{\odot}$ [Event Horizon Telescope Collaboration et al., 2019a](#)) have a wealth of multi-wavelength data to investigate. As can be seen in Figure 5.1, the characteristic timescales for these two SMBHs are significantly different. While Sgr A* varies on scales of minutes to hours, M87* varies on timescales of weeks to months. Their respective environments also differ greatly: while Sgr A* lives in our own (relatively quiet) spiral galaxy, M87* is over 1000 times more massive and sits at the center of the brightest galaxy in the Virgo cluster and is actively launching a radio jet. As the radio telescopes of the world turned to image the event horizons of these two SMBHs, a robust multi-wavelength campaign was coordinated to accompany them for every observing run. I am excited to begin to dig into these rich datasets and can't wait to see what information the light curves, MWL timing, and SED analyses hold.

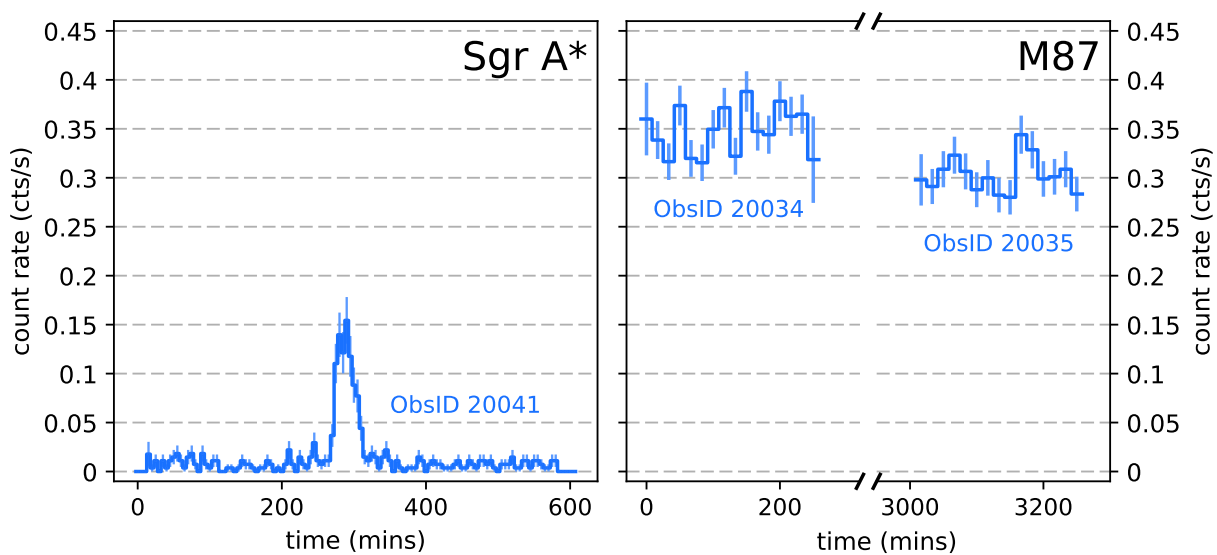


Figure 5.1 A Comparison of Sgr A* and M87*'s X-ray variability.

Multi-wavelength Variability of Sgr A*

In Appendix A Figure A.2 displays all the data from Chandra's observations of Sgr A* in the summer of 2019. July 17/18, 21, and 26 represent the last dates observed from the multi-year campaign between the Spitzer and Chandra. In total this campaign was ~ 150 hours of observations – this large allocation from two competitive space observatories is almost unprecedented. During this campaign, IR variability with correlated X-ray flares were observed several times. The results of cross correlating those flares that are statistically significant are presented in [Boyce et al. \(2019\)](#); [Boyce et al. \(2021\)](#) and [Boyce et al. \(2022\)](#) (Chapter 2). Appendix A reports the cross correlation between the IR and X-ray variability in the context of the literature.

In August 2019, coordinated observations of Sgr A* were also executed by GRAVITY, Chandra and ALMA. The 2-8 keV light curve on August 20th displays a double peaked flare brighter than all of the flares detected during the Spitzer-Chandra campaign. Though peaking at an impressive 0.6 counts/second and lasting almost 2 hours, it is not the brightest X-ray flare seen from Sgr A*. That record belongs to the flare discussed in [Haggard](#)

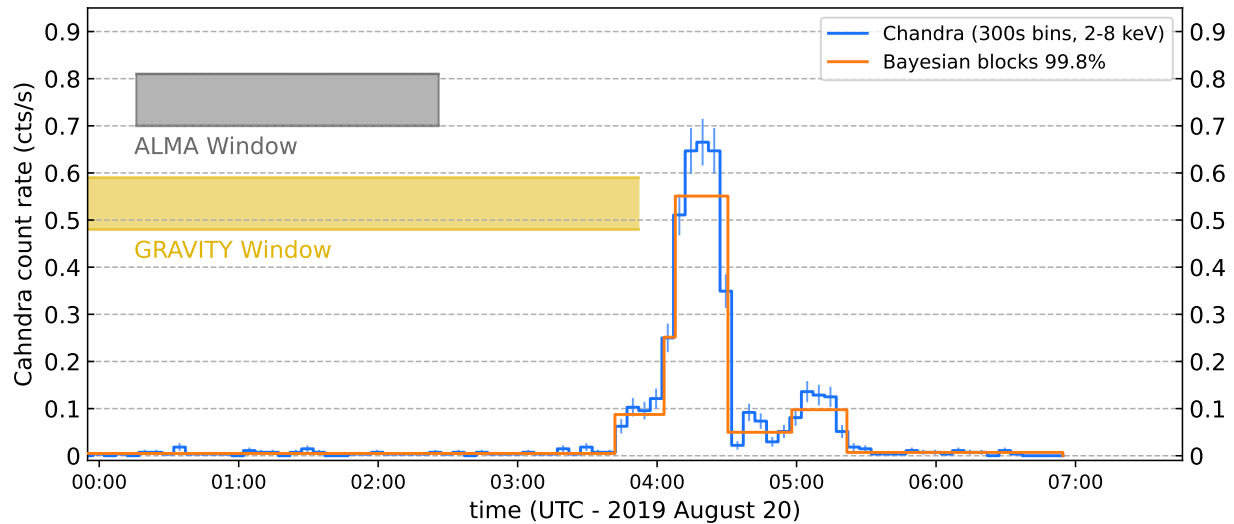


Figure 5.2 Chandra 2–8 keV Sgr A* flare on August 20, 2019. `bblocks` are indicated as orange histograms. The coordinated ALMA observing window is indicated in black. VLT/GRAVITY window is indicated in yellow.

[et al. \(2019b\)](#), peaking at over 1.0 count/s. The expected simultaneous IR flare would have been missed along with any delayed submm emission, but it is possible the ALMA and GRAVITY data contain correlated emission that does not show up in the X-ray, and all three windows can constrain the SED.

EHT 2018 2021 2022 data

The Multi-wavelength Working Group in the EHT has coordinated observations in all four years that the EHT has targeted Sgr A* and M87*. The 2017 data have been published ([Event Horizon Telescope Collaboration et al., 2019a, 2022a](#)), and the other three years all hold multiwavelength activity that hold promise in their potential to connect back to horizon scale physics if the EHT imaging can be robustly temporally compared. In all of the following analysis, I present a few glimpses at the coordinated Chandra X-ray data and unless otherwise specified, the Bayesian block flare detection algorithm (`bblocks` [Scargle, 1998](#); [Scargle et al., 2013b](#); [Williams et al., 2017b](#)) was used to identify significant

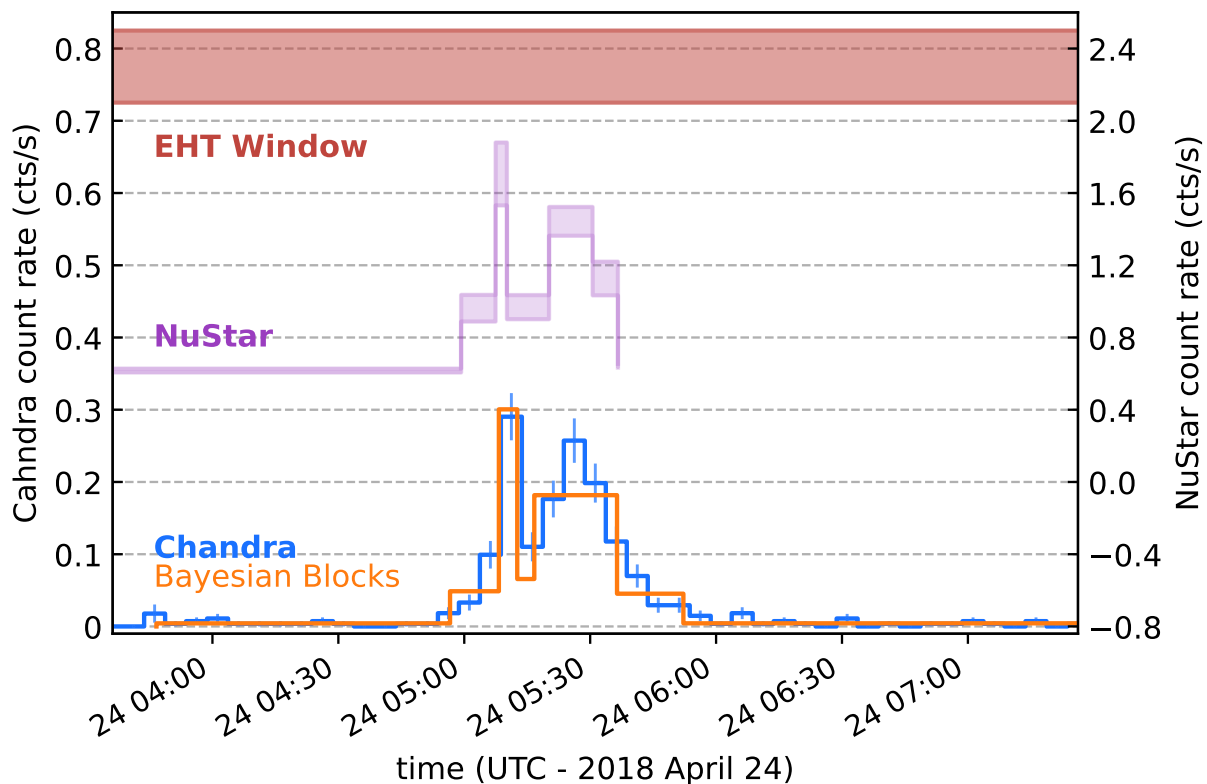


Figure 5.3 The significantly (99.8%) detected Chandra flare from Sgr A* on April 24, 2018. NuSTAR data is represented by the detected Bayesian blocks (Scargle, 1998; Scargle et al., 2013b; Williams et al., 2017b) and is plotted in purple. The detected blocks as identified with `bblocks` are over-plotted on the Chandra data as orange histograms. The red band across the top indicates the EHT observing window.

variability in the light curves¹.

During the 2018 campaign, Chandra observed Sgr A* for four 10h observations. A moderately bright flare was detected using `bblocks` on April 24. This flare along with the Bayesian block detections from NuSTAR and the EHT observing window is plotted in Figure 5.3. The red band across the top indicates that the EHT was actively observing Sgr A* at the same time that this flare was observed. The other three light curves (with no significant variability) are displayed in Figure B.1 of Appendix B.

¹We ran the algorithm using a 95% confidence interval (a false positive rate of $p_0 = 0.05$), implying that for p_0 the probability that a change point is real is $1 - 0.05 = 95\%$, and the probability that a flare (at least two change points) is real is $1 - (p_0)^2 = 99.8\%$.

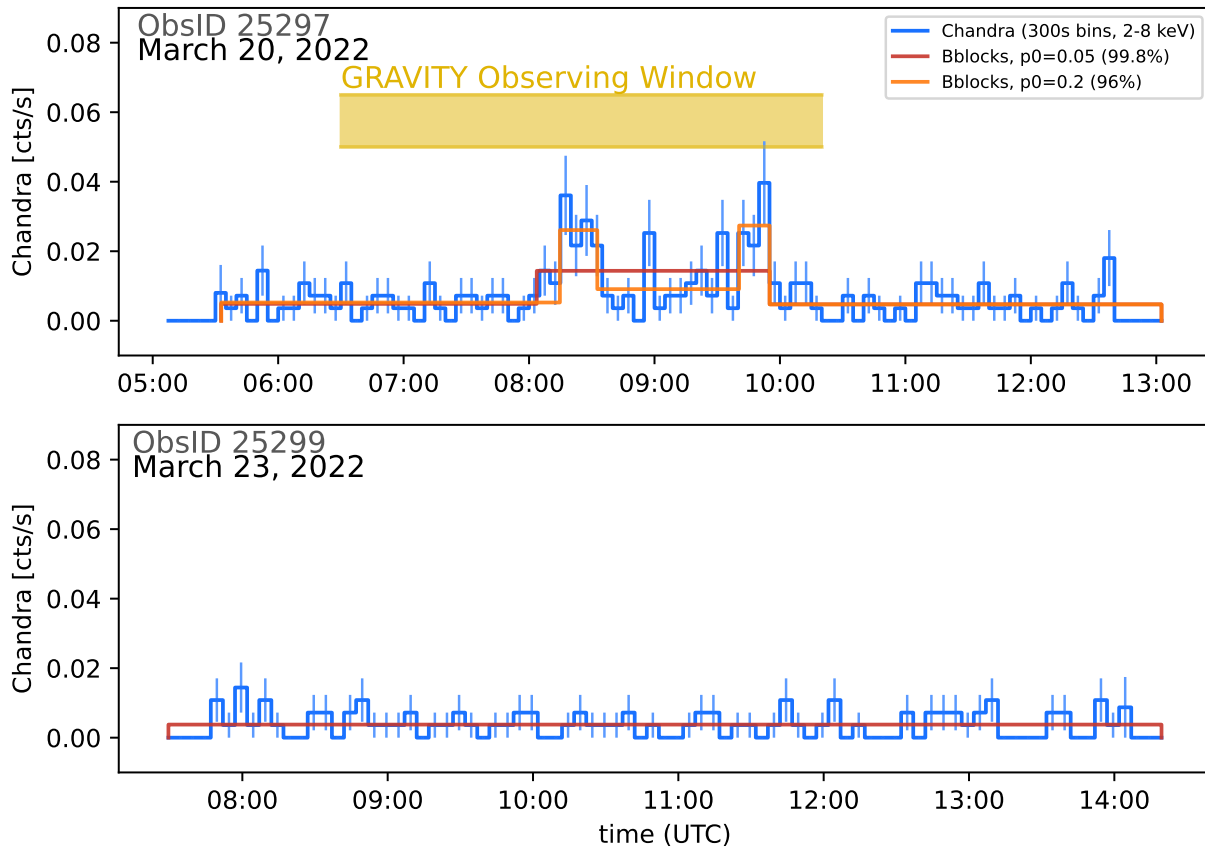


Figure 5.4 The two 2–8 keV Chandra light curves of Sgr A* from the 2022 EHT campaign. Significant variability is characterized by two different runs of `bblocks`, one that identifies ‘flares’ at 99.8% significance (red) and one at 96% significance (orange). The yellow band across the top indicates the GRAVITY (NIR) observing window.

During the 2021 campaign, Chandra observed Sgr A* for four 6.6h observations. Two flares were detected using the `bblocks` at 99.8% significance, though both were relatively faint, peaking around 0.04 counts per second. The four light curves are displayed in Figure B.2 of Appendix B.

During the 2022 campaign, Chandra observed Sgr A* twice, for 6–7h intervals. On March 20, a flare was detected at 99.8% significance with `bblocks`. Though relatively faint, peaking around 0.04 counts per second, the flare was captured simultaneous with the observing window of the NIR GRAVITY instrument on VLT. Since GRAVITY can detect the apparent motion of Sgr A*’s IR centroid due to potential orbiting hotspots in the

plasma ([Gravity Collaboration et al., 2018c](#)), the hint from Chandra that some event horizon activity may have occurred with simultaneous EHT coverage is extremely exciting. Now that Sgr A* has been imaged and characterized by the EHT in a state of relative quiescence (Chapter 3), it may be possible to interpret changes relative to the “baseline” static image and compare to GRAVITY and Chandra data.

Double Peak

It is notable that the three significant flares presented in the last section appear to have a double peaked structure. One possible explanation for a double peaked flare outside of chance coincidence invokes gravitational lensing of a hotspot in the plasma while it passes behind the SMBH. [Gravity Collaboration et al. \(2018d\)](#) observed a double peaked infrared flare in July 2018, and when comparing the duration of the total flux increase (~ 115 min) to the separation between the peaks (~ 40 min), the ratio is about 2.9. Without a physical interpretation, it is still interesting to compare to the analogous ratio of one of the brightest Chandra flares observed ([Haggard et al., 2019b](#)), which also has an apparent double peaked structure and a separation to total duration ratio of about 3.2. [Bouffard et al. \(2019\)](#) performed a statistical examination of all Chandra flares detected from up to 2018 and found that the frequency of apparent double peaked flares was consistent with the probability of a chance coincidence of two flares. Since then, the observation of these three flares may motivate another look at these statistics.

5.2.2 Extragalactic Studies

Star Formation Characterization In Galactic Centers

Though WISDOM’s primary goal is collecting high resolution molecular gas maps of the centers of galaxies to measure the mass of central SMBHs, such exquisite data can also be used to study the interstellar medium in these unique environments. In particular, if

a measure of star formation is in hand, then together with the cold gas measurements (a tracer of the fuel for star formation) one can calculate the *star formation efficiency* (SFE). Left undisturbed, cold gas should theoretically collapse to form stars on a free-fall time; instead the SFE is \sim two orders of magnitude lower than expected. Differing across starbursts, ellipticals, and deep in the bulges of galaxies, SFE is also clearly not universal (e.g. [Bigiel et al., 2008](#)).

During my degree I completed an internship at the Canada France Hawaii Telescope (CFHT) in which I worked closely with instrument scientists on a proposed project with the SITELLE instrument. As fourier-transform spectrograph, SITELLE produces a spectrum for each pixel in its impressive $11' \times 11'$ field of view [Drissen et al. \(2019\)](#). Since joining the WISDOM collaboration I have lead five proposals to observe WISDOM targets with SITELLE. Four of these have been successful (semesters 2020B, 2021A, 2021B, 2022B), with the first leading to a detailed study of NGC 3169 lead by my fellow PhD Candidate Anan Lu ([Lu et al., 2022](#)), and the most recent being awarded time with the highest ranking. Here I motivate the study of SFE in galactic centers using WISDOM and SITELLE.

A multitude of physical processes have been implicated to explain SF suppression, but the true cause remains unknown (e.g. [Kruijssen et al., 2014](#)). It is unclear how important this phenomenon is for the evolution of spiral bulges, with some objects showing enhanced SF, while others are suppressed (e.g. [Sandstrom et al., 2013](#)). SF in gas-rich early-type galaxies (ETGs) may also be suppressed, by a factor of ≈ 2.5 compared to normal spirals with the same gas surface density (e.g. [Saintonge et al., 2011, 2012](#); [Martig et al., 2013](#); [Davis et al., 2014](#)). SF suppression observed in ETGs may mimic that seen in the central regions of spirals, and in growing spheroids at higher z ([Lang et al., 2014](#); [Gobat et al., 2018](#)), or it may be a symptom of a more general process.

Many theories have been proposed to explain this phenomenon and describe the, as yet unknown, physics behind secular SF suppression. For instance, the low SFE of ETGs

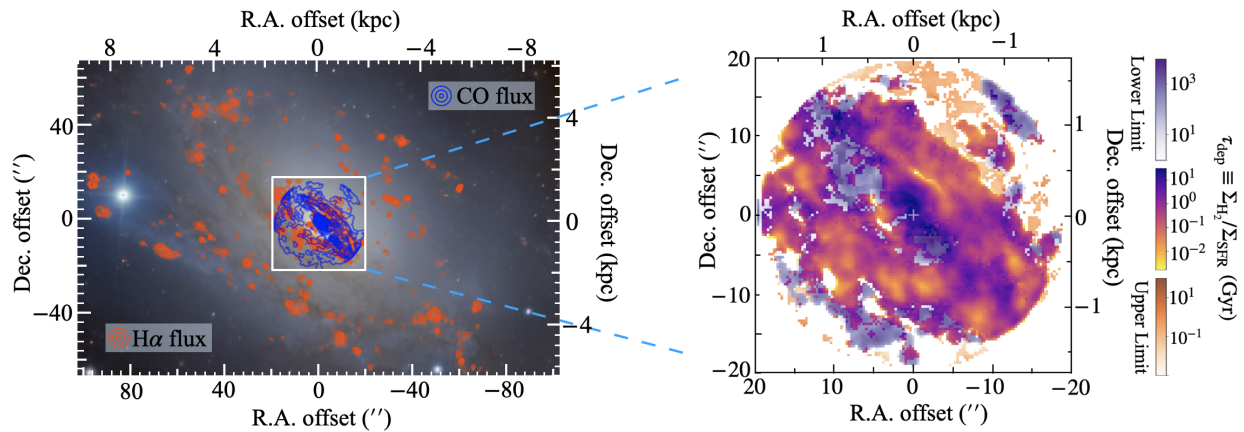


Figure 5.5 Left: H α and CO flux of NGC 3169, overlaid on a deep image taken with SITELLE. Right: Spatial distribution and overlap of molecular gas and HII regions. Orange-purple colors show the log of τ_{dep} (depletion time: the ratio of H $_2$ and SFR density). Blue color shows the lower limit of τ_{dep} from molecular gas surface density. Light orange color shows the upper limit of τ_{dep} from HII regions. For the full analysis see [Lu et al. \(2022\)](#).

may be caused by ‘morphological quenching’, where the nearly spherical potential holds gas stable against SF ([Martig et al., 2013, 2009](#)). Dynamical processes, such as shear, that pull clouds apart and stabilize them against gravitational collapse also cause of SF suppression in ETGs ([Davis et al., 2014](#)). It has also been suggested that, in spiral galaxies, gas streaming (non-circular inflow/outflow) motions may reduce SFEs in a similar way ([Meidt et al., 2013](#)). Meanwhile, others have argued that the surface density threshold for SF may be different in different environments ([Lada et al., 2010](#); [Heiderman et al., 2010](#)).

Spatial resolution is vital to disentangle these different mechanisms, which predict different radial dependencies. The bulge region of galaxies typically includes the inner kpc, and for ETGs, the inner-most 200 pc may be where SFE changes are most acute ([Davis et al., 2014](#)). Previous SFE studies use either global SFRs and gas surface densities to study objects in a statistical manner (e.g. [Li et al., 2018](#)) or measurements on kpc scales (e.g. [Lin et al., 2020](#)), both of which miss these nuanced changes in the bulge regions of galaxies. Recent surveys have successfully begun to combine high-resolution mm and optical data

to investigate the impact that morphology, environment and stellar feedback have on SF (e.g. PHANGS [Kruijssen et al., 2019](#)). Harnessing the power of SITELLE we can trace star-formation, metallicities, and gas kinematics in a set of galaxies for which there already exists high-resolution CO measurements, and determine the SFE on sub-kpc scales for a selection of targets complementary to those observed in previous surveys (greater variety of morphology and possible quenching factors, focusing on the bulge region).

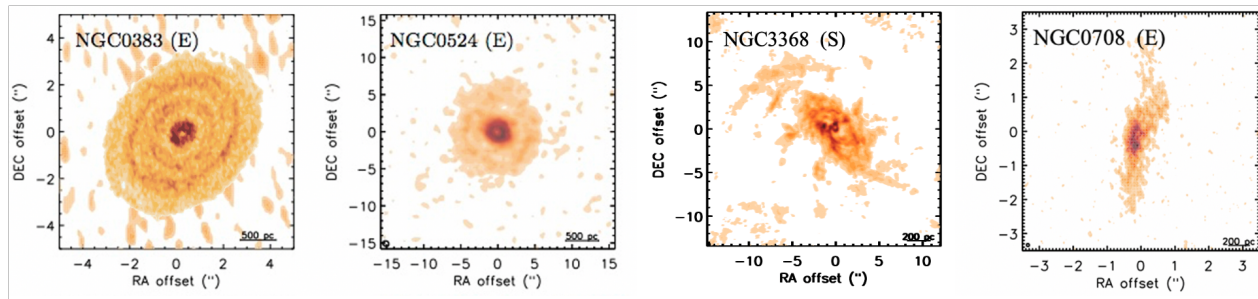


Figure 5.6 ALMA CO Integrated intensity maps of four 2022B targets, with name and morphological type (E/early, S/late) indicated for each. CO maps of the other six targets reach similar resolutions and depths.

SITELLE Observations and hypothesis testing: We have proposed to address these questions with SITELLE on CFHT, conducting a high-resolution investigation into SF suppression in 10 nearby galaxies (5 spiral galaxies and 5 ETGs) *for which there already exists ALMA observations (with <60 pc resolution; Figure 2)*. At the typical distance to these objects (30 Mpc) we can probe SF with $H\alpha$ and $H\beta$ using SITELLE with natural seeing observations of $\lesssim 1.0''$. Adaptively binning the higher-resolution CO data to the resolution of SITELLE will identify *in a spatially-resolved manner* which physical process(es) are suppressing SF in ETGs and if any of the same mechanisms are at play in the spiral galaxy bulges. Figure 1 presents the SITELLE/ALMA data for the test-galaxy NGC 3169 (*left*) and shows the SFE derived from the combined SITELLE/ $H\alpha$ and ALMA/CO data (*right*). Thanks to SITELLE's impressive field of view, we also measure SFR for many regions in the spiral arms and outer parts of the galaxy. These will form the basis of a complementary

Name	RA	DEC	Diam	Distance	1" scale	Type	M_K
0383	01:07:24.96	+32:24:45.2	0.5'	71 Mpc	345 pc	E	-25.8
0524 †	01:24:47.72	+09:32:19.8	1.5'	31 Mpc	150 pc	E	-24.7
0708	01:52:46.48	+36:09:06.6	0.8'	73 Mpc	350 pc	E	-25.7
3169 †	10:14:15.05	+03:27:57.9	1.4'	23 Mpc	110 pc	S	-24.1
3368	10:46:45.74	+11:49:11.8	2.1'	18 Mpc	85 pc	S	-23.7
3607	11:16:54.64	+18:03:06.3	1.3'	19 Mpc	90 pc	E	-24.7
4429	12:27:26.51	+11:06:27.8	1.4'	21 Mpc	100 pc	E	-24.3
4438	12:27:45.59	+13:00:31.8	1.9'	17 Mpc	80 pc	S	-23.8
4501	12:31:59.16	+14:25:13.4	2.3'	38 Mpc	180 pc	S	-24.7
3810	11:40:58.76	+11:28:16.1	1.3'	19 Mpc	90 pc	S	-23.2
5806	15:00:00.40	+01:53:28.7	3.2'	23 Mpc	110 pc	S	-23.2

Table 5.1 List of targets and their properties. The four bolded galaxies are our proposed targets for the 2022B semester. Names are NGC #'s. Diameters and M_K 's (tracing stellar mass) are from 2MASS.

† SN2 data has been collected for NGC 0524. SN2 and SN3 data has been collected for NGC 3169. Unbolded galaxies are only RA-compatible with CFHT semester A and have not yet been observed.

study of the rotation curve and ionizing environments at large radii.

We have been rewarded a total of **21.4 hours** with SITELLE in 2022B (9 hours at rank A) to map the SFR of four targets (Fig. 2) in this unique sample of nearby galaxies. We will join two sets of exquisite 3-D data to shed light on the *physical process(es)* which are suppressing star-formation in the centers of galaxies. Appendix C contains additional details of the technical justification for the project.

5.3 Conclusion

In this thesis, I have presented three projects probing the physics around SMBHs at different distances. From the event horizon to the edge of the sphere of influence energetic phenomena produce light across the electromagnetic spectrum. The investigation of simultaneous IR to submm to X-ray observations characterize radiative mechanisms producing

variability, while simultaneous multiwavelength observations along with interferometry can connect this variability to horizon-scale phenomena. Further out, the excitation of CO traces molecular gas disks at the centres of many galaxies across morphological types, allowing the mass of the central SMBH to be estimated.

In the near future we look forward to even more insights with three more years of EHT and MWL data in hand, rich simultaneous MWL data of Sgr A* from submm to X-ray, a growing sample of high resolution maps of galactic centers with molecular gas. Particularly exciting will be the next generation of GRMHD simulations. Developed by collaborators, this suite of general relativistic magnetohydrodynamic simulations of accretion and jets for supermassive black holes will be designed with tools that enable direct comparisons with our observational data (images and light curves). Upgrading and expanding EHT facilities will be able to fill in the gap between the large spatial scales on which extragalactic jets are observed and the detailed structure of the accretion flow we see around M87* and Sgr A*. Multiwavelength coordination will become increasingly important as advancing GRMHD models will be most stringently tested with the combination of horizon scale imaging with flux and variability measures across the electromagnetic spectrum. In the decades to come, the next generation gravitational wave observatory LISA (launch circa 2037), will open up frequencies that will allow for observations of binary SMBH systems. Next generation ground based facilities could probe the sphere of influence at angular resolutions comparable to ALMA, opening up a golden era of black hole demographic studies that can constrain the growth history of black holes, and their role in regulating galaxy formation. All together, observational probes of SMBHs continue to expand our understanding of what grows and glows at the centres of galaxies.

Appendix A

Simultaneous NIR and X-ray Variability from Sgr A*

A.1 Time lags from the Spitzer–Chandra campaign

Figure A.1 and Table A.1 present the timing analysis from the entire Spitzer–Chandra campaign. Several other works have reported simultaneous X-ray and IR observations of Sgr A*. Some report simultaneity between the X-ray and IR peaks, but do not report a time frame within which that claim can be considered valid (Yusef-Zadeh et al., 2006b, 2009; Trap et al., 2011). Those that constrain timing between X-ray and IR activity (Eckart et al., 2004, 2006b; Hornstein et al., 2007; Eckart et al., 2008b; Dodds-Eden et al., 2009a; Eckart et al., 2012; Ponti et al., 2017a; Hornstein et al., 2007; Yusef-Zadeh et al., 2012a) are plotted in the Appendix in Figure A.1 along with the *Spitzer*-Chandra results of this campaign.

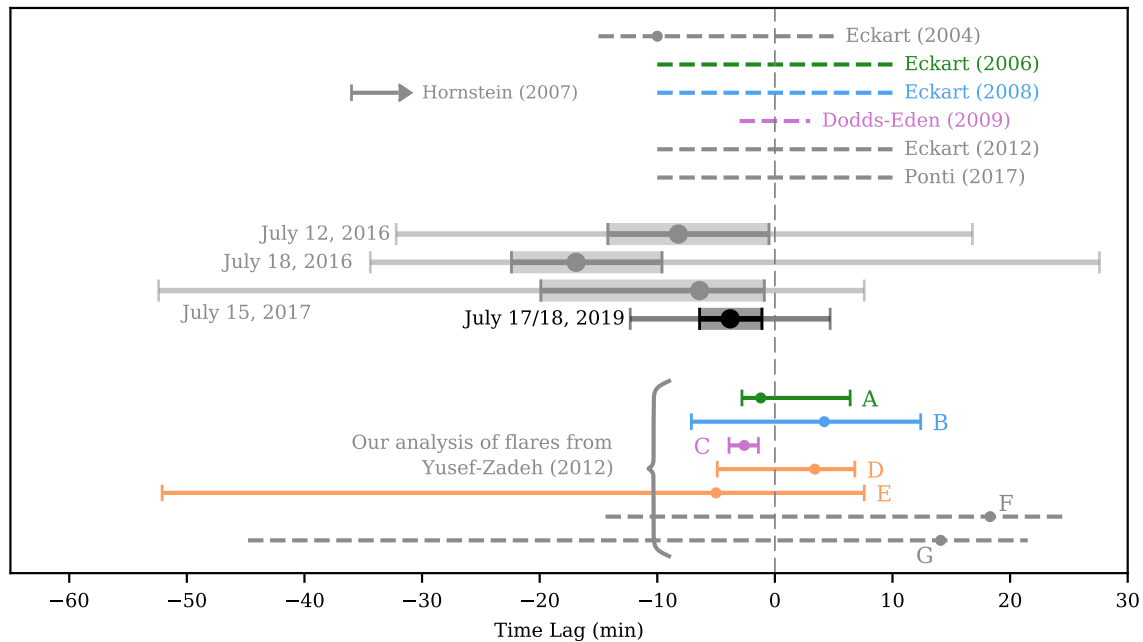


Figure A.1 Time lags between IR and X-ray flares as reported in this work and in the literature. Plotted with black circles are the time lags from the epochs in this Spitzer/Chandra campaign with significant X-ray and IR activity and their 68% confidence intervals. Plotted in solid-grey are the updated results from re-analyzing data in Boyce et al. (2019); Boyce et al. (2021). Regions marked with dashed lines come from works that describe the flares to be “simultaneous to within x minutes” but quote no uncertainties (Eckart et al., 2004, 2006b; Hornstein et al., 2007; Eckart et al., 2008b; Dodds-Eden et al., 2009a; Eckart et al., 2012; Ponti et al., 2017a). The upper limit from Hornstein et al. (2007) indicates an X-ray flare whose peak occurred 36 minutes before IR observations began. Yusef-Zadeh et al. (2012a) is the only work to report any correlation between the X-ray and IR with error bars. Boyce et al. (2019); Boyce et al. (2021) re-analyzed the seven flares presented in their work and we plot those results with 68% confidence intervals here. Five of these flares come from previously reported data sets (color coded as green, blue, magenta and orange for Eckart et al. (2006b), Eckart et al. (2008b), Dodds-Eden et al. (2009a), and Yusef-Zadeh et al. (2009) respectively) and two come from a previously un-reported data set (plotted in grey).

Table A.1 Time Lags: Spitzer/Chandra Flares

Date	time lag (min)	68% interval	99.7% interval
2016 July 12	$-13.5^{+5.2}_{-5.1}$	(-18.6, -8.3)	(-29.8, +2.8)
2016 July 18	$-14.4^{+20.4}_{-5.1}$	(-19.5, +6.0)	(-27.5, +18.6)
2017 July 15	$-10.9^{+3.7}_{-4.8}$	(-15.7, -7.2)	(-52.1, +0.4)
*2019 July 18	$-2.8^{+3.3}_{-3.3}$	(-6.1, +0.5)	(-12.2, +6.7)

***This work.**

Note: Negative values mean X-ray leads IR. Uncertainties on the time lag in the second column span the 68% confidence interval on the 10,000 MC runs. The second column displays the boundaries of this 68% confidence interval, while the third column displays the 99.7% confidence interval.

A.2 Summer 2019

Figure A.2 displays all the data from Chandra's observations of Sgr A* in the summer of 2019. July 17/18, 21, and 26 represent the last dates observed from the multi-year campaign between the Spitzer and Chandra. In August 2019, coordinated observations of Sgr A* were executed by GRAVITY, Chandra, and ALMA.

A.3 Illustration of SED models (B) and (C)

Figure A.3 illustrates two SED models discussed in Chapter 2, B: SYNC-SSC-SSC and C: SYNC-SYNC-SSC in purple and yellow respectively. Shapes are exaggerated to emphasize qualitative differences (NIR spectral index, increased THz flux, X-ray spectral index).

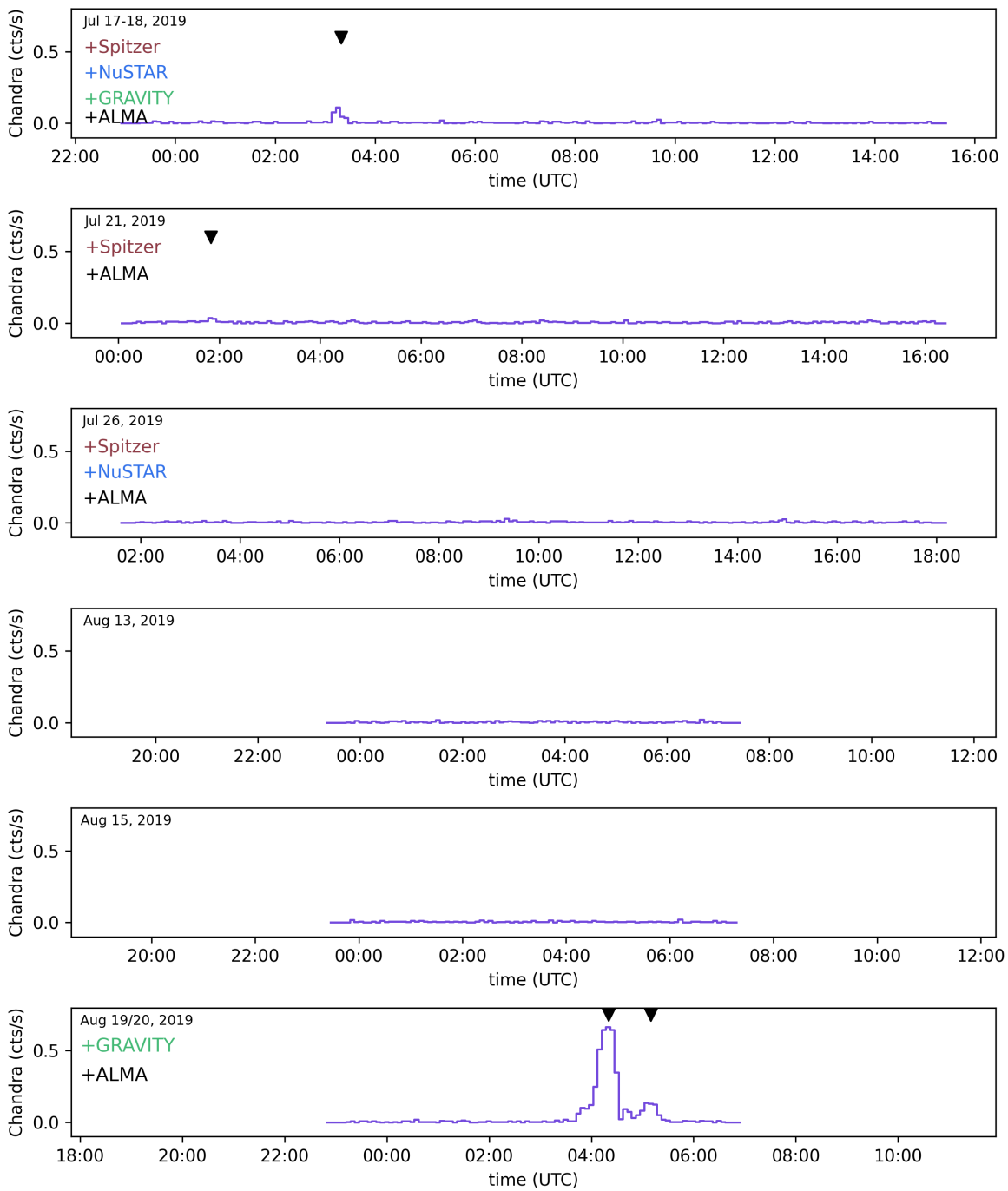


Figure A.2 2-8 keV light curves of Sgr A* captured by Chandra in Summer 2019. Flares detected with `bblocks` are indicated with black triangles. Coordinated observatories are labeled on each date.

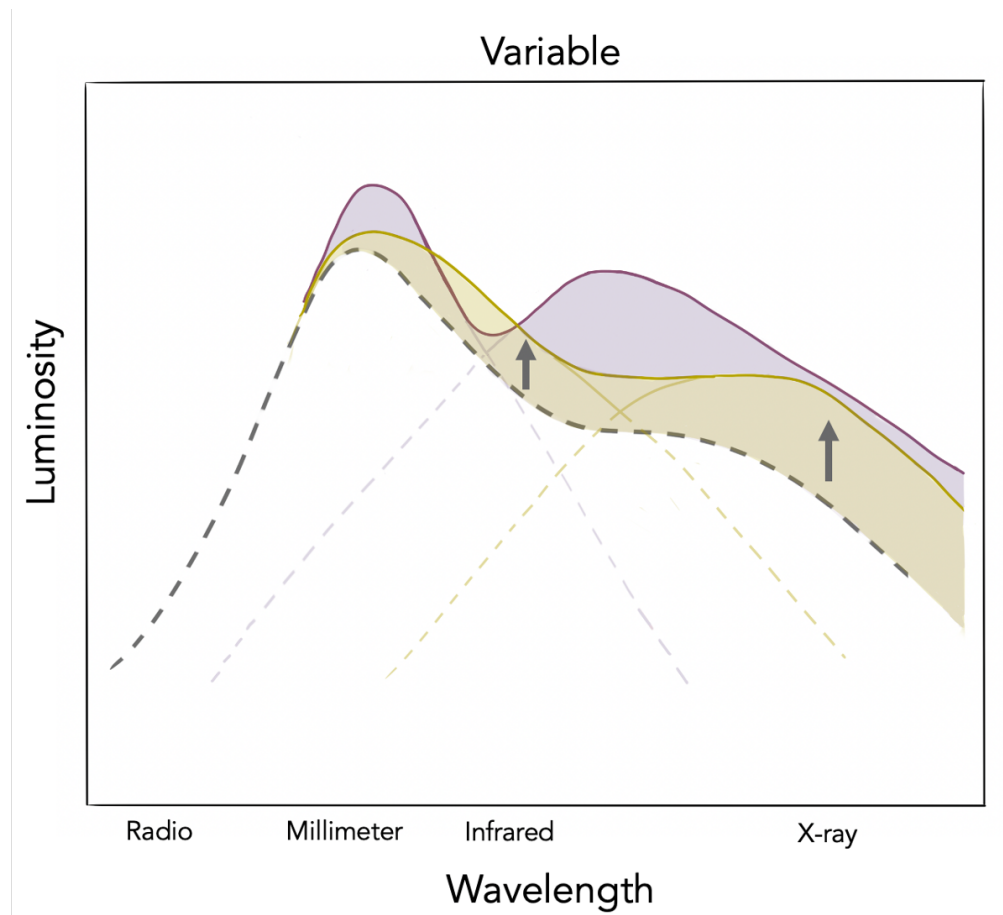


Figure A.3 Exaggerated illustration of SED models B: SYNC-SYNC-SSC and C: SYNC-SSC-SSC in yellow and purple respectively. A description of these models is found in Section 2.4.

Appendix B

Multiwavelength coordination with EHT

During the 2018 EHT campaign to image Sgr A*, Chandra observed X-ray light curves on April 20, 22, 24, and 25. All four light curves and the significantly detected flare on April 24 (98% confidence) are plotted in Figure [B.1](#).

During the 2021 EHT campaign to image Sgr A*, Chandra observed X-ray light curves on April 10, 11, 14, and 16. The light curves and significantly detected flares (98% confidence) are plotted in Figure [B.2](#).

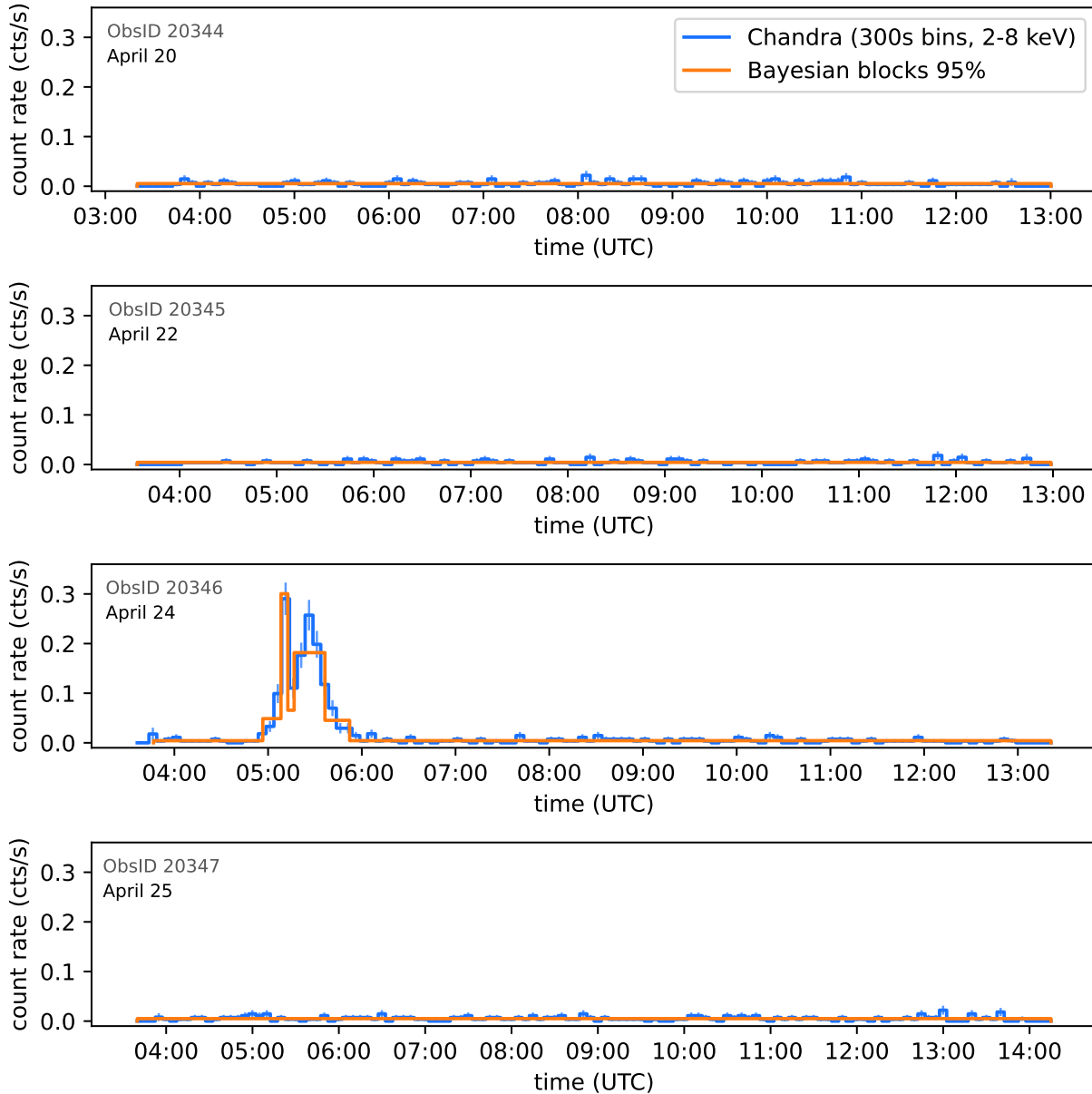


Figure B.1 Chandra 2-8 keV light curves of Sgr A* during the 2018 EHT campaign. The Bayesian block flare detection algorithm (Scargle, 1998; Scargle et al., 2013b; Williams et al., 2017b) has been run on the light curves and results, including the flare detection on 24 April, are over-plotted as orange histograms.

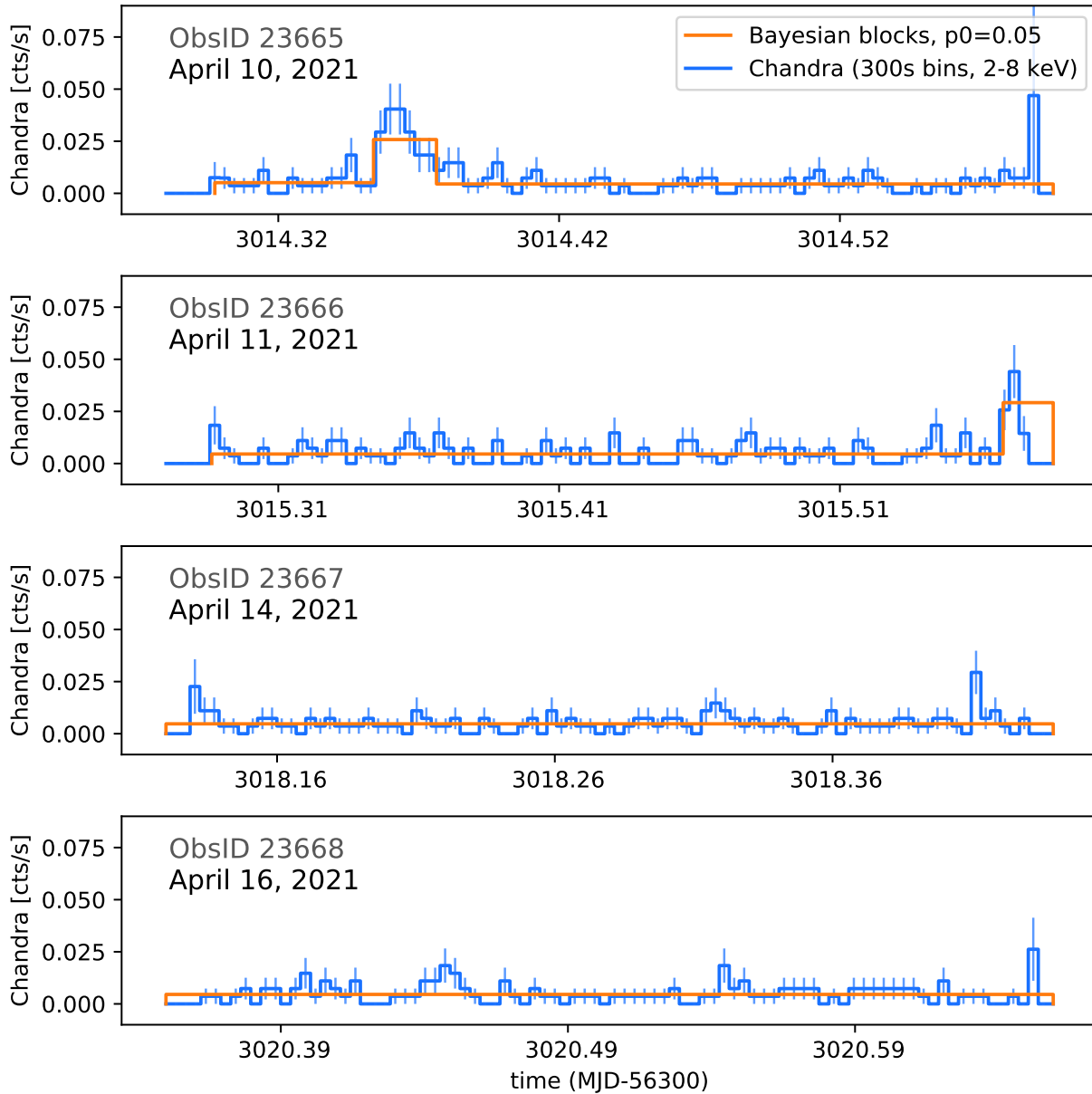


Figure B.2 Chandra 2-8 keV light curves of Sgr A* during the 2021 EHT campaign. The Bayesian block flare detection algorithm (Scargle, 1998; Scargle et al., 2013b; Williams et al., 2017b) has been run on the light curves and results, including flare detections on 10 and 11 April, are over-plotted as orange histograms.

Appendix C

Technical Justification of the SITELE-WISDOM proposal

Observations and Methods:

Since more than one process may be involved in the suppression of star formation, it is crucial that we observe both ETGs and spiral galaxies, sampling a range of stellar mass to capture the differences between bulge sizes, and a range of SF to probe suppressed and non-suppressed star-formation. Taking morphological type as an example, we run a null hypothesis test, asking with what confidence we could distinguish the degree of star-formation suppression in independent regions within two populations (e.g. early- and late-type galaxies). In the scenario that the two populations differ in their degree of SFR suppression by a factor of 2.5 and that the $1\text{-}\sigma$ scatter in SFR within each population is $\log \Sigma_{SFR} = 0.1$, we determined that 120 regions from each distribution is the minimum requirement to reject the null hypothesis (that the distributions are the same) 99.7% of the time. Estimating that we will get 24 regions of overlapping CO and H-alpha in each galaxy, we therefore require 5 targets in each morphological type (E/S) to ensure that the mass and SFE ranges are adequately covered while still detecting trends with morphologies. Since each galaxy provides 10s of regions, with the entire set we will test for correlations in hundreds of clouds across all aforementioned properties to distinguish

SFEs at high spatial resolution and pave the way for future comparative surveys.

Extinction-corrected $H\alpha$ remains the ‘gold standard’ for determining SFRs. We will use the kinematics of the CO-emitting gas and the SITELLE $H\alpha$ -emitting gas, with a model of the stellar potential from existing HST imaging to elucidate the causes of any SF suppression. We also have VLA 33 GHz measurements for some galaxies to help with extinction correction. Each suppression mechanism is identifiable by its radial and dynamical impacts. For instance shear-based quenching would only be visible in the central parts of the galaxy, where the shear lifetime becomes shorter than the cloud lifetime. Quenching from cloud stability (assessed through the virial parameter) would be fairly constant as a function of radius within the bulge, but decreasing in the disc. Environment-dependant thresholds for SF would display bimodal SFEs that correlate with the gas surface density. We can also estimate the magnitude of streaming motions, and use the line ratios of $[NII]/H\alpha$ and $[OIII]/H\beta$ to help constrain the scope of AGN’s impact.

Measured with SITELLE, $H\alpha$ (via SN3) and $H\beta$ (via SN2) will allow us to estimate the extinction (via the Balmer decrement) after modelling and subtracting the stellar continuum (e.g. [Drissen et al., 2019](#)) and obtain an accurate SFR. Its wide, fully-sampled FOV provides complete coverage of each target in one field.

The filter configurations summarized in Table 2 are driven by the need to detect the suppression of SF at surface densities of $\log \Sigma_{SFR} = -2.8 M_{\odot}/\text{yr}/\text{kpc}^2$, at least a factor of two below the value expected from the Kennicutt-Schmidt relation ($\log \Sigma_{SFR} \sim -2.5 M_{\odot}/\text{yr}/\text{kpc}^2$) at gas surface densities typically detected by ALMA ($\gtrsim 10 M_{\odot}/\text{pc}^2$). This corresponds to a limit on the surface brightness of $10^{-16} \text{ erg s}^{-1} \text{ cm}^{-2} \text{ arcsec}^{-2}$ at our typical target distance ($\sim 30 \text{ Mpc}$). The SNR calculations adopt a seeing of $1.0''$, an airmass of 1.2 and no extinction. To ensure that the $H\alpha$ line at 6563 \AA can be separated from $N[II]\lambda 6548,6583$ and to achieve a kinematic precision of $\sim 7 \text{ km/s}$ ($\lesssim 5\%$ systematic velocities) for $H\alpha$ gas detected at SNR 10, we request observations in SN3 at $R \sim 2000$ (337 steps). For the SN2 filter, a spectral resolution of 900 (197 steps) will be sufficient to separate $H\beta$

at 4861 Å from other significant lines (O[III] λ 4959, 5007). Figure 3 displays the H β SNR map for the central region of NGC 3169. Out of the 15774 H α pixels that passed a SNR >7 mask, 52% matching H β pixels contributed positively to the SNR of the final calibrated map, which is at the limit of satisfying extinction calibration purposes. This underscores the importance of observing H β /SN2 in ideal conditions.

For NGC 0524, and 3368 ($D\sim 25$ Mpc): To achieve SNR $\gtrsim 2$ on H β requires 40s per step (**2.4 hours**) on each target in SN2. Achieving SNR $\gtrsim 4$ on H α requires 20s per step (**2.2 hours**) on each target in SN3. For NGC 0383 and 0708 ($D\sim 70$ Mpc): To achieve SNR $\gtrsim 2$ on H β requires 70s per step (**4.0 hours**) on both targets in SN2. Achieving an SNR $\gtrsim 2$ on H α requires 30s per step (**3.2 hours**) on both targets in SN3. This results in a total of **21.4 hours** to cover these four targets.

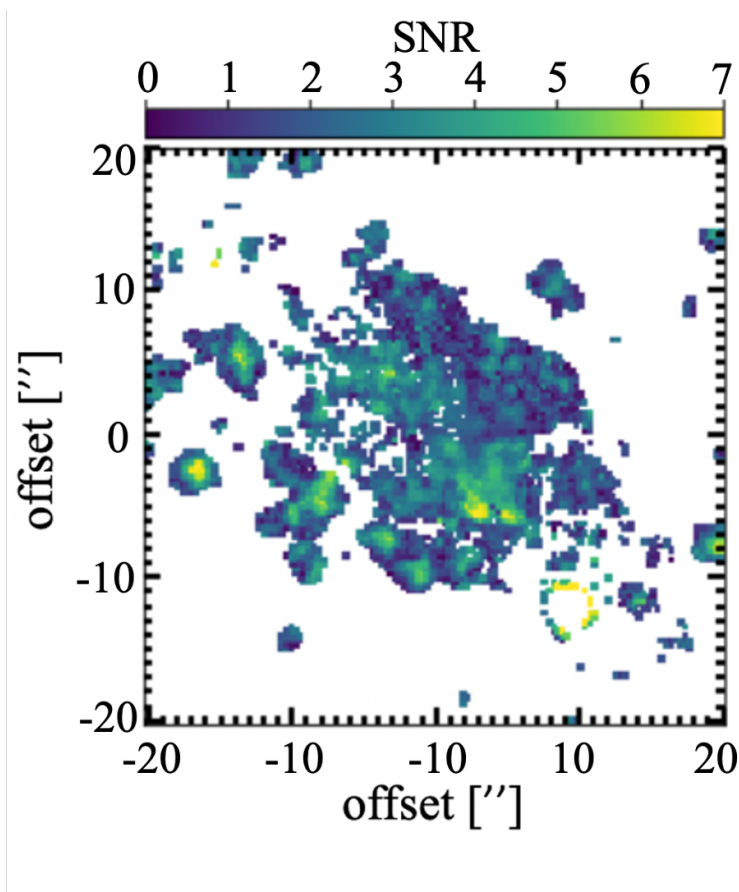


Figure C.1 SITELLE SNR map of H β for central region of NGC 3169 ($D\sim 23$ Mpc)

Table C.1 Filter Configurations. SNR is the value estimated by the SITELLE ETC for the relevant line in each filter ($H\beta$ and $H\alpha$) with 3x3 binning (since one resolution element will be $\lesssim 1.0''$ and SITELLE's pixels are $0.32''$). "low" assumes a $H\alpha$ surface brightness of 10^{-16} erg s^{-1} cm^{-2} arcsec $^{-2}$ for NGC 0524 and 3368 and 6×10^{-17} erg s^{-1} cm^{-2} arcsec $^{-2}$ for NGC 0383 and 0708 to reach the desired depth of Σ_{SFR} . "high" assumes a $H\alpha$ surface brightness of 5×10^{-15} erg s^{-1} cm^{-2} arcsec $^{-2}$ for all targets and is not at risk of saturation. Total times include the 3.25 seconds of overhead on each step. *NGC0524 only requires SN3.

Filter	Line	Moon	Spec. Res.	# of steps	NGC 0524*, 3368				NGC 0383, 0708			
					SNR low	SNR high	Exp time [s/step]	Tot. time [hr]	SNR low	SNR high	Exp time [s/step]	Tot. time [hr]
SN2	$H\beta$	new	900	197	2	80	40	2.4	1.7	105	70	4.0
SN3	$H\alpha$	quarter	2000	337	4	164	20	2.2	2	200	30	3.2

Appendix D

Full Author Lists and Acknowledgements

D.1 Chapter 2: Multi-wavelength Variability of Sagittarius

A*

The work presented in Chapter 2 can be found in the manuscript “Multiwavelength Variability of Sagittarius A* in 2019 July ” ([Boyce et al., 2022](#)). The full acknowledgements and author list are presented below, reflecting the collaborative effort that it took to conduct this study of Sgr A*.

We thank the GRAVITY collaboration for sharing the flux data for July 17/18 ([GRAVITY Collaboration et al., 2021](#)) and their valuable feedback on the analysis and text. We are grateful to Yigit Dallilar for help in the utilization of the `flaremodel` SED code ([Dallilar et al., 2022](#)), his expert guidance in the implementation of adiabatic expansion codes, and thank him for numerous fruitful scientific discussions. We are thankful for Gabriele Ponti’s helpful input and insightful discussions. We thank Eduardo Ros for his careful reading of the text and valuable clarifying comments. The authors are grateful for access to the privileged location of the high-altitude plateau Chajnantor in the land of the indigenous Likanantai people on which the ALMA telescope sits. HB and DH acknowledge and thank the diverse indigenous people on whose land

our home institutions reside in Tiohti:áke, including the Haudenosaunee and Anishinabeg peoples and the Kanien'kehá:ka Nation. The authors thank the anonymous referee for their constructive comments and insight. HB is grateful for support from the Natural Sciences and Engineering Research Council of Canada (NSERC) Alexander Graham Bell Canada Graduate Scholarship. HB and DH acknowledge funding from the NSERC Discovery Grant and the Canada Research Chairs (CRC) program. The scientific results reported in this article are based on observations made by the Chandra X-ray Observatory, the Spitzer Space Telescope, the Nuclear Spectroscopic Telescope Array (NuSTAR), the GRAVITY instrument on the Very Large Telescope, and the Atacama Large Millimeter/submillimeter Array (ALMA). We thank the Chandra, Spitzer, NuSTAR, ALMA, and GRAVITY scheduling, data processing, and archive teams for making these observations possible.

Software: CIAO [Fruscione et al. \(2006\)](#), NumPy [\(Jones et al., 2001\)](#), AstroPy [\(The Astropy Collaboration et al., 2018\)](#), matplotlib [\(Hunter, 2007\)](#), bayesian blocks [\(Williams et al., 2017a\)](#), zdcf [\(Alexander, 2013\)](#), flaremodel [\(Dallilar et al., 2022\)](#)

Facilities: Spitzer/IRAC, Chandra/ACIS, NuSTAR, VLTI/GRAVITY, ALMA

H. Boyce^{1,2}, D. Haggard^{1,2}, G. Witzel³, S. von Fellenberg³, S. P. Willner⁴, E. E. Becklin⁵, T. Do⁶, A. Eckart^{3,7}, G. G. Fazio⁴, M. A. Gurwell⁴, J. L. Hora⁴, S. Markoff^{8,9}, M. R. Morris⁵, J. Neilsen¹⁰, M. Nowak¹¹, H. A. Smith⁴, and S. Zhang¹²

¹ Department of Physics, McGill University, 3600 University Street, Montréal, QC H3A 2T8, Canada

² McGill Space Institute, McGill University, 3550 University Street, Montréal, QC H3A 2A7, Canada

³ Max-Planck-Institut für Radioastronomie, Auf dem Hügel 69, D-53121, Bonn, Germany

⁴ Center for Astrophysics | Harvard & Smithsonian, 60 Garden St., Cambridge, MA 02138-1516, USA

⁵ Department of Physics and Astronomy, University of California, Los Angeles, CA 90095-1547, USA

⁶ UCLA Galactic Center Group, Physics and Astronomy Department, University of California, Los Angeles, CA 90024, USA

⁷ Institute of Physics, University of Cologne, Zùlpicher Strae 77, 50937 Cologne, Germany

⁸ Anton Pannekoek Institute for Astronomy, University of Amsterdam, Science Park 904, 1098 XH Amsterdam, The Netherlands

⁹ Gravitation Astroparticle Physics Amsterdam (GRAPPA) Institute, University of Amsterdam, Science Park 904, 1098 XH Amsterdam, The Netherlands

¹⁰ Villanova University, Mendel Science Center Rm. 263B, 800 E Lancaster Ave, Villanova PA 19085, USA

¹¹ Physics Department, Washington University CB 1105, St Louis, MO 63130, USA

¹² Bard College, 30 Campus Road, Annandale-on-Hudson, New York, 12504, USA

D.2 Chapter 3: Multi-wavelength Coordination with the Event Horizon Telescope

The work presented in Chapter 3 can be found in the manuscript “First Sagittarius A* Event Horizon Telescope Results. II. EHT and Multi-wavelength Observations, Data Processing, and Calibration” ([Event Horizon Telescope Collaboration et al., 2022b](#)) for which I was a member of the core writing team. This paper is one of a suite of 10 papers detailing the first results from the Event Horizon Telescope’s observations of Sagittarius A*. The full acknowledgements and author list of Paper II are presented below, reflecting the enormous collaborative effort that it took to conduct this study of Sgr A*.

The Event Horizon Telescope Collaboration thanks the following organizations and programs: National Science Foundation (awards OISE-1743747, AST-1816420, AST-1716536, AST-1440254, AST-1935980); the Black Hole Initiative, which is funded by grants from the John Templeton Foundation and the Gordon and Betty Moore Foundation (although the opinions expressed in this work are those of the author(s) and do not necessarily reflect the views of these Foundations); NASA Hubble Fellowship grant HST-HF2-51431.001-A awarded by the Space Telescope Science Institute, which is operated by the Association of Universities for Research in Astronomy, Inc., for NASA, under contract NAS5-26555; the Academy of Finland (projects 274477, 284495, 312496, 315721); the Agencia Nacional de Investigación y Desarrollo (ANID),

Chile via NCN19_058 (TITANs) and Fondecyt 1221421, the Alexander von Humboldt Stiftung; an Alfred P. Sloan Research Fellowship; Allegro, the European ALMA Regional Centre node in the Netherlands, the NL astronomy research network NOVA and the astronomy institutes of the University of Amsterdam, Leiden University and Radboud University; the Institute for Advanced Study; the China Scholarship Council; Consejo Nacional de Ciencia y Tecnología (CONACYT, Mexico, projects U0004-246083, U0004-259839, F0003-272050, M0037-279006, F0003-281692, 104497, 275201, 263356); the Delaney Family via the Delaney Family John A. Wheeler Chair at Perimeter Institute; Dirección General de Asuntos del Personal Académico—Universidad Nacional Autónoma de México (DGAPA—UNAM, projects IN112417 and IN112820); the European Research Council Synergy Grant “BlackHoleCam: Imaging the Event Horizon of Black Holes” (grant 610058); the Generalitat Valenciana postdoctoral grant APOSTD/2018/177 and GenT Program (project CIDEAGENT/2018/021); MICINN Research Project PID2019-108995GB-C22; the European Research Council for advanced grant ‘JETSET: Launching, propagation and emission of relativistic jets from binary mergers and across mass scales’ (Grant No. 884631); the Istituto Nazionale di Fisica Nucleare (INFN) sezione di Napoli, iniziative specifiche TEONGRAV; the two Dutch National Supercomputers, Cartesius and Snellius (NWO Grant 2021.013); the International Max Planck Research School for Astronomy and Astrophysics at the Universities of Bonn and Cologne; DFG research grant “Jet physics on horizon scales and beyond” (Grant No. FR 4069/2- 1); Joint Princeton/Flatiron and Joint Columbia/Flatiron Postdoctoral Fellowships, research at the Flatiron Institute is supported by the Simons Foundation; the Japanese Government (Monbukagakusho: MEXT) Scholarship; the Japan Society for the Promotion of Science (JSPS) Grant-in-Aid for JSPS Research Fellowship (JP17J08829); the Key Research Program of Frontier Sciences, Chinese Academy of Sciences (CAS, grants QYZDJ-SSW-SLH057, QYZDJSSW-SYS008, ZDBS-LY-SLH011); the Leverhulme Trust Early Career Research Fellowship; the Max-Planck-Gesellschaft (MPG); the Max Planck Partner Group of the MPG and the CAS; the MEXT/JSPS KAKENHI (grants 18KK0090, JP21H01137, JP18H03721, JP18K13594, 18K03709, JP19K14761, 18H01245, 25120007); the Malaysian Fundamental Research Grant Scheme (FRGS) FRGS/1/2019/STG02/UM/02/6; the MIT International Science and Technology Initiatives (MISTI) Funds; the Ministry of Science and Technology (MOST) of Taiwan (103-2119-M-001-010-MY2, 105-2112-M-001-025-MY3, 105-2119-M-001-042, 106-2112-M-001-011, 106-2119-M-001-013, 106-2119-M-001-027, 106-2923-M-001-005, 107-2119-M-001-017, 107-2119-M-001-020, 107-2119-M-001-041, 107-2119-M-110-005, 107-2923-M-001-009, 108-2112-M-001-048, 108-2112-M-001-051, 108-2923-M-001-002, 109-2112-M-001-025, 109-2124-M-001-005, 109-2923-M-001-001, 110-2112-M-003-007-MY2, 110-2112-M-001-033, 110-2124-M-001-007, and 110-2923-M-001-001); the Ministry of Education (MoE) of Taiwan Yushan Young Scholar Program; the Physics Division, National Center for Theoretical Sciences of Taiwan;

the National Aeronautics and Space Administration (NASA, Fermi Guest Investigator grant 80NSSC20K1567, NASA Astrophysics Theory Program grant 80NSSC20K0527, NASA NuSTAR award 80NSSC20K0645); the National Institute of Natural Sciences (NINS) of Japan; the National Key Research and Development Program of China (grant 2016YFA0400704, 2017YFA0402703, 2016YFA0400702); the National Science Foundation (NSF, grants AST-0096454, AST-0352953, AST-0521233, AST-0705062, AST-0905844, AST-0922984, AST-1126433, AST-1140030, DGE-1144085, AST-1207704, AST-1207730, AST-1207752, MRI-1228509, OPP-1248097, AST-1310896, AST-1555365, AST-1614868, AST-1615796, AST-1715061, AST-1716327, AST-2034306); the Natural Science Foundation of China (grants 11650110427, 10625314, 11721303, 11725312, 11873028, 11933007, 11991052, 11991053, 12192220, 12192223); NWO grant number OCENW.KLEIN.113; a fellowship of China Postdoctoral Science Foundation (2020M671266); the Natural Sciences and Engineering Research Council of Canada (NSERC, including a Discovery Grant and the NSERC Alexander Graham Bell Canada Graduate Scholarships-Doctoral Program); the National Youth Thousand Talents Program of China; the National Research Foundation of Korea (the Global PhD Fellowship Grant: grants NRF-2015H1A2A1033752, the Korea Research Fellowship Program: NRF-2015H1D3A1066561, Basic Research Support Grant 2019R1F1A1059721, 2022R1C1C1005255); the Dutch Organization for Scientific Research (NWO) VICI award (grant 639.043.513) and Spinoza Prize SPI 78-409; the YCAA Prize Postdoctoral Fellowship. LM gratefully acknowledges support from an NSF Astronomy and Astrophysics Postdoctoral Fellowship under award no. AST-1903847. TK is supported by MEXT as "Program for Promoting Researches on the Supercomputer Fugaku" (Toward a unified view of the universe: from large scale structures to planets, JPMXP1020200109) and JICFuS. RPD and IN acknowledge funding by the South African Research Chairs Initiative, through the South African Radio Astronomy Observatory (SARAO, grant ID 77948), which is a facility of the National Research Foundation (NRF), an agency of the Department of Science and Innovation (DSI) of South Africa.

We thank the Onsala Space Observatory (OSO) national infrastructure, for the provisioning of its facilities/observational support (OSO receives funding through the Swedish Research Council under grant 2017-00648); the Perimeter Institute for Theoretical Physics (research at Perimeter Institute is supported by the Government of Canada through the Department of Innovation, Science and Economic Development and by the Province of Ontario through the Ministry of Research, Innovation and Science); the Spanish Ministerio de Ciencia e Innovación (grants PGC2018-098915-B-C21, AYA2016-80889-P, PID2019-108995GB-C21, PID2020-117404GB-C21); the University of Pretoria for financial aid in the provision of the new Cluster Server nodes and SuperMicro (USA) for a SEEDING GRANT approved towards these nodes in 2020; the State Agency for Research of the Spanish MCIU through the "Center of Excellence Severo Ochoa" award

for the Instituto de Astrofísica de Andalucía (SEV-2017- 0709); the Toray Science Foundation; the Consejería de Economía, Conocimiento, Empresas y Universidad of the Junta de Andalucía (grant P18-FR-1769), the Consejo Superior de Investigaciones Científicas (grant 2019AEP112); the M2FINDERS project which has received funding by the European Research Council (ERC) under the European Union’s Horizon 2020 Research and Innovation Programme (grant agreement No 101018682); the US Department of Energy (USDOE) through the Los Alamos National Laboratory (operated by Triad National Security, LLC, for the National Nuclear Security Administration of the USDOE (Contract 89233218CNA000001); the European Union’s Horizon 2020 research and innovation programme under grant agreement No 730562 RadioNet; Shanghai Pilot Program for Basic Research, Chinese Academy of Science, Shanghai Branch (JCYJ-SHFY-2021-013); ALMA North America Development Fund; the Academia Sinica; Chandra DD7-18089X and TM6- 17006X; the GenT Program (Generalitat Valenciana) Project CIDEAGENT/2018/021. This work used the Extreme Science and Engineering Discovery Environment (XSEDE), supported by NSF grant ACI-1548562, and CyVerse, supported by NSF grants DBI-0735191, DBI-1265383, and DBI-1743442. XSEDE Stampede2 resource at TACC was allocated through TG-AST170024 and TG-AST080026N. XSEDE JetStream resource at PTI and TACC was allocated through AST170028.

The simulations were performed in part on the SuperMUC cluster at the LRZ in Garching, on the LOEWE cluster in CSC in Frankfurt, and on the HazelHen cluster at the HLRS in Stuttgart. This research was enabled in part by support provided by Compute Ontario (<http://computeontario.ca>), Calcul Quebec (<http://www.calculquebec.ca>) and Compute Canada (<http://www.computecanada.ca>). CC acknowledges support from the Swedish Research Council (VR).

We thank the staff at the participating observatories, correlation centers, and institutions for their enthusiastic support. This paper makes use of the following ALMA data: ADS/JAO.ALMA#2016.1.01154.V. ALMA is a partnership of the European Southern Observatory (ESO; Europe, representing its member states), NSF, and National Institutes of Natural Sciences of Japan, together with National Research Council (Canada), Ministry of Science and Technology (MOST; Taiwan), Academia Sinica Institute of Astronomy and Astrophysics (ASIAA; Taiwan), and Korea Astronomy and Space Science Institute (KASI; Republic of Korea), in cooperation with the Republic of Chile. The Joint ALMA Observatory is operated by ESO, Associated Universities, Inc. (AUI)/NRAO, and the National Astronomical Observatory of Japan (NAOJ). The NRAO is a facility of the NSF operated under cooperative agreement by AUI. This research used resources of the Oak Ridge Leadership Computing Facility at the Oak Ridge National Laboratory, which is supported by the Office of Science of the U.S. Department of Energy under Contract No. DE-AC05-00OR22725. We also thank the Center for Computational Astrophysics, National Astronomical Observatory of Japan.

Support for this work was also provided by the NASA Hubble Fellowship grant HST-HF2-51431.001-A awarded by the Space Telescope Science Institute, which is operated by the Association of Universities for Research in Astronomy, Inc., for NASA, under contract NAS5-26555. HO and GM were supported by Virtual Institute of Accretion (VIA) postdoctoral fellowships from the Netherlands Research School for Astronomy (NOVA). APEX is a collaboration between the Max-Planck-Institut für Radioastronomie (Germany), ESO, and the Onsala Space Observatory (Sweden). The SMA is a joint project between the SAO and ASIAA and is funded by the Smithsonian Institution and the Academia Sinica. The JCMT is operated by the East Asian Observatory on behalf of the NAOJ, ASIAA, and KASI, as well as the Ministry of Finance of China, Chinese Academy of Sciences, and the National Key Research and Development Program (No. 2017YFA0402700) of China and Natural Science Foundation of China grant 11873028. Additional funding support for the JCMT is provided by the Science and Technologies Facility Council (UK) and participating universities in the UK and Canada. Simulations were performed in part on the SuperMUC cluster at the LRZ in Garching, on the LOEWE cluster in CSC in Frankfurt, on the HazelHen cluster at the HLRS in Stuttgart, and on the Pi2.0 and Siyuan Mark-I at Shanghai Jiao Tong University. The computer resources of the Finnish IT Center for Science (CSC) and the Finnish Computing Competence Infrastructure (FCCI) project are acknowledged. JO was supported by Basic Science Research Program through the National Research Foundation of Korea(NRF) funded by the Ministry of Education(NRF-2021R1A6A3A01086420; 2022R1C1C1005255). We thank Martin Shepherd for the addition of extra features in the Difmap software that were used for the CLEAN imaging results presented in this paper. The computing cluster of Shanghai VLBI correlator supported by the Special Fund for Astronomy from the Ministry of Finance in China is acknowledged. This work was supported by the Brain Pool Program through the National Research Foundation of Korea (NRF) funded by the Ministry of Science and ICT (019H1D3A1A01102564). This research is part of the Frontera computing project at the Texas Advanced Computing Center through the Frontera Large-Scale Community Partnerships allocation AST20023. Frontera is made possible by National Science Foundation award OAC-1818253. This research was carried out using resources provided by the Open Science Grid, which is supported by the National Science Foundation and the U.S. Department of Energy Office of Science.

The LMT is a project operated by the Instituto Nacional de Astrófica, Óptica, y Electrónica (Mexico) and the University of Massachusetts at Amherst (USA). The IRAM 30-m telescope on Pico Veleta, Spain is operated by IRAM and supported by CNRS (Centre National de la Recherche Scientifique, France), MPG (Max-Planck-Gesellschaft, Germany) and IGN (Instituto Geográfico Nacional, Spain). The SMT is operated by the Arizona Radio Observatory, a part of the Steward Observatory of the University of Arizona, with

financial support of operations from the State of Arizona and financial support for instrumentation development from the NSF. Support for SPT participation in the EHT is provided by the National Science Foundation through award OPP-1852617 to the University of Chicago. Partial support is also provided by the Kavli Institute of Cosmological Physics at the University of Chicago. The SPT hydrogen maser was provided on loan from the GLT, courtesy of ASIAA. Support for this work was provided by NASA through the NASA Hubble Fellowship grant #HST-HF2-51494.001 awarded by the Space Telescope Science Institute, which is operated by the Association of Universities for Research in Astronomy, Inc., for NASA, under contract NAS5-26555. Jongho Park acknowledges financial support through the EACOA Fellowship awarded by the East Asia Core Observatories Association, which consists of the Academia Sinica Institute of Astronomy and Astrophysics, the National Astronomical Observatory of Japan, Center for Astronomical Mega-Science, Chinese Academy of Sciences, and the Korea Astronomy and Space Science Institute.

The EHTC has received generous donations of FPGA chips from Xilinx Inc., under the Xilinx University Program. The EHTC has benefited from technology shared under open-source license by the Collaboration for Astronomy Signal Processing and Electronics Research (CASPER). The EHT project is grateful to T4Science and Microsemi for their assistance with Hydrogen Masers. This research has made use of NASA's Astrophysics Data System. We gratefully acknowledge the support provided by the extended staff of the ALMA, both from the inception of the ALMA Phasing Project through the observational campaigns of 2017 and 2018. We would like to thank A. Deller and W. Brisken for EHT-specific support with the use of DiFX. We acknowledge the significance that Maunakea, where the SMA and JCMT EHT stations are located, has for the indigenous Hawaiian people.

[Alphabetical author list begins on the next page]

- KAZUNORI AKIYAMA,^{1,2,3} ANTXON ALBERDI,⁴ WALTER ALEF,⁵ JUAN CARLOS ALGABA,⁶ RICHARD ANANTUA,^{3,7,8}
 KEIICHI ASADA,⁹ REBECCA AZULAY,^{10,11,5} UWE BACH,⁵ ANNE-KATHRIN BACZKO,⁵ DAVID BALL,¹² MISLAV BALOKOVIĆ,¹³
 JOHN BARRETT,¹ MICHl BAUBÖCK,¹⁴ BRADFORD A. BENSON,^{15,16} DAN BINTLEY,^{17,18} LINDY BLACKBURN,^{3,7}
 RAYMOND BLUNDELL,⁷ KATHERINE L. BOUMAN,¹⁹ GEOFFREY C. BOWER,^{20,21} HOPE BOYCE,^{22,23} MICHAEL BREMER,²⁴
 CHRISTIAAN D. BRINKERINK,²⁵ ROGER BRISSENEN,^{3,7} SILKE BRITZEN,⁵ AVERY E. BRODERICK,^{26,27,28}
 DOMINIQUE BROGUIERE,²⁴ THOMAS BRONZWAER,²⁵ SANDRA BUSTAMANTE,²⁹ DO-YOUNG BYUN,^{30,31}
 JOHN E. CARLSTROM,^{32,16,33,34} CHIARA CECCOBELLO,³⁵ ANDREW CHAEL,^{36,37} CHI-KWAN CHAN,^{12,38,39}
 KousHIK CHATTERJEE,^{3,7} SHAMI CHATTERJEE,⁴⁰ MING-TANG CHEN,²⁰ YONGJUN CHEN (陈永军),^{41,42} XIAOPENG CHENG,³⁰
 ILJE CHO,⁴ PIERRE CHRISTIAN,⁴³ NICHOLAS S. CONROY,^{44,7} JOHN E. CONWAY,³⁵ JAMES M. CORDES,⁴⁰
 THOMAS M. CRAWFORD,^{16,32} GEOFFREY B. CREW,¹ ALEJANDRO CRUZ-OSORIO,⁴⁵ YUZHU CUI (崔玉竹),^{46,47,48}
 JORDY DAVELAAR,^{49,50,25} MARIAFELICIA DE LAURENTIS,^{51,45,52} ROGER DEANE,^{53,54,55} JESSICA DEMPSEY,^{17,18,56}
 GREGORY DESVIGNES,^{5,57} JASON DEXTER,⁵⁸ VEDANT DHRUV,¹⁴ SHEPERD S. DOELEMEN,^{3,7} SEAN DOUGAL,¹²
 SERGIO A. DZIB,^{24,5} RALPH P. EATOUGH,^{59,5} RAZIEH EMAMI,⁷ HEINO FALCKE,²⁵ JOSEPH FARAH,^{60,61} VINCENT L. FISH,¹
 ED FOMALONT,⁶² H. ALYSON FORD,¹² RAQUEL FRAGA-ENCINAS,²⁵ WILLIAM T. FREEMAN,^{63,64} PER FRIBERG,^{17,18}
 CHRISTIAN M. FROMM,^{65,45,5} ANTONIO FUENTES,⁴ PETER GALISON,^{3,66,67} CHARLES F. GAMMIE,^{14,44,68} ROBERTO GARCÍA,²⁴
 OLIVIER GENTAZ,²⁴ BORIS GEORGIEV,^{27,28,26} CIRIACO GODDI,^{69,70} ROMAN GOLD,^{71,45} ARTURO I. GÓMEZ-RUIZ,^{72,73}
 JOSÉ L. GÓMEZ,⁴ MINFENG GU (顾敏峰),^{41,74} MARK GURWELL,⁷ KAZUHIRO HADA,^{47,48} DARYL HAGGARD,^{22,23}
 KARI HAWORTH,⁷ MICHAEL H. HECHT,¹ RONALD HESPER,⁷⁵ DIRK HEUMANN,¹² LUIS C. HO (何子山),^{76,77} PAUL HO,^{9,18}
 MAREKI HONMA,^{47,48,78} CHIH-WEI L. HUANG,⁹ LEI HUANG (黄磊),^{41,74} DAVID H. HUGHES,⁷² SHIRO IKEDA,^{2,79,80,81}
 C. M. VIOLETTE IMPELLIZZERI,^{82,62} MAKOTO INOUE,⁹ SARA ISSAOUN,^{7,37} DAVID J. JAMES,⁸³ BUELL T. JANNUZI,¹²
 MICHAEL JANSSEN,⁵ BRITTON JETER,⁹ WU JIANG (江悟),⁴¹ ALEJANDRA JIMÉNEZ-ROSALES,²⁵ MICHAEL D. JOHNSON,^{3,7}
 SVETLANA JORSTAD,⁸⁴ ABHISHEK V. JOSHI,¹⁴ TAEHYUN JUNG,^{30,31} MANSOUR KARAMI,^{26,27} RAMESH KARUPPUSAMY,⁵
 TOMOHISA KAWASHIMA,⁸⁵ GARRETT K. KEATING,⁷ MARK KETTENIS,⁸⁶ DONG-JIN KIM,⁵ JAE-YOUNG KIM,^{87,30,5}
 JONGSOO KIM,³⁰ JUNHAN KIM,^{12,19} MOTOKI KINO,^{2,88} JUN YI KOAY,⁹ PRASHANT KOCHERLAKOTA,⁴⁵ YUTARO KOFUJI,^{47,78}
 PATRICK M. KOCH,⁹ SHOKO KOYAMA,^{89,9} CARSTEN KRAMER,²⁴ MICHAEL KRAMER,⁵ THOMAS P. KRICHBAUM,⁵
 CHENG-YU KUO,^{90,9} NOEMI LA BELLA,²⁵ TOD R. LAUER,⁹¹ DAEYOUNG LEE,¹⁴ SANG-SUNG LEE,³⁰ PO KIN LEUNG,⁹²
 AVIAD LEVIS,¹⁹ ZHIYUAN LI (李志远),^{93,94} ROCCO LICO,^{4,95} GREG LINDAHL,⁷ MICHAEL LINDQVIST,³⁵ MIKHAIL LISAKOV,⁵
 JUN LIU (刘俊),⁵ KUO LIU,⁵ ELISABETTA LIUZZO,⁹⁶ WEN-PING LO,^{9,97} ANDREI P. LOBANOV,⁵ LAURENT LOINARD,^{98,99}
 COLIN J. LONSDALE,¹ RU-SEN LU (路如森),^{41,42,5} JIRONG MAO (毛基荣),^{100,101,102} NICOLA MARCHILI,^{96,5}
 SERA MARKOFF,^{103,104} DANIEL P. MARRONE,¹² ALAN P. MARSCHER,⁸⁴ IVÁN MARTÍ-VIDAL,^{10,11} SATOKI MATSUSHITA,⁹
 LYNN D. MATTHEWS,¹ LIA MEDEIROS,^{105,106,12} KARL M. MENTEN,⁵ DANIEL MICHALIK,^{107,16} IZUMI MIZUNO,^{17,18}
 YOSUKE MIZUNO,^{46,108,45} JAMES M. MORAN,^{3,7} KOTARO MORIYAMA,^{45,1,47} MONIKA MOSCIBRODZKA,²⁵
 CORNELIA MÜLLER,^{5,25} ALEJANDRO MUS,^{10,11} GIBWA MUSOKE,^{103,25} IOANNIS MYSERLIS,¹⁰⁹ ANDREW NADOLSKI,⁴⁴
 HIROSHI NAGAI,^{2,48} NEIL M. NAGAR,¹¹⁰ MASANORI NAKAMURA,^{111,9} RAMESH NARAYAN,^{3,7} GOPAL NARAYANAN,²⁹
 INIYAN NATARAJAN,^{53,112} ANTONIOS NATHANAIL,^{45,113} SANTIAGO NAVARRO FUENTES,¹⁰⁹ JOEY NEILSEN,¹¹⁴ ROBERTO NERI,²⁴
 CHUNGHONG NI,^{27,28,26} ARISTEIDIS NOUTSOS,⁵ MICHAEL A. NOWAK,¹¹⁵ JUNGHWAN OH,¹¹⁶ HIROKI OKINO,^{47,78}
 HÉCTOR OLIVARES,²⁵ GISELA N. ORTIZ-LEÓN,^{99,5} TOMOAKI OYAMA,⁴⁷ FERYAL ÖZEL,¹² DANIEL C. M. PALUMBO,^{3,7}
 GEORGIOS FILIPPOS PARASCHOS,⁵ JONGHO PARK,^{9,117} HARRIET PARSONS,^{17,18} NIMESH PATEL,⁷ UE-LI PEN,^{9,26,118,119,120}
 DOMINIC W. PESCE,^{7,3} VINCENT PIÉTU,²⁴ RICHARD PLAMBECK,¹²¹ ALEKSANDAR POPSTEFANIJA,²⁹ OLIVER PORTH,^{103,45}
 FELIX M. PÖTZL,^{122,5} BEN PRATHER,¹⁴ JORGE A. PRECIADO-LÓPEZ,²⁶ DIMITRIOS PSALTIS,¹² HUNG-YI PU,^{123,124,9}
 VENKATESH RAMAKRISHNAN,^{110,125,126} RAMPRASAD RAO,⁷ MARK G. RAWLINGS,^{127,17,18} ALEXANDER W. RAYMOND,^{3,7}
 LUCIANO REZZOLLA,^{45,128,129} ANGELO RICARTE,^{7,3} BART RIPPERDA,^{130,50} FREEK ROELOFS,^{7,3,25} ALAN ROGERS,¹
 EDUARDO ROS,⁵ CRISTINA ROMERO-CAÑAZALES,⁹ ARASH ROSHANINESHAT,¹² HELGE ROTTMANN,⁵ ALAN L. ROY,⁵
 IGNACIO RUIZ,¹⁰⁹ CHET RUSZCZYK,¹ KAZI L. J. RYGL,⁹⁶ SALVADOR SÁNCHEZ,¹⁰⁹ DAVID SÁNCHEZ-ARGÜELLES,^{72,73}
 MIGUEL SÁNCHEZ-PORTAL,¹⁰⁹ MAHITO SASADA,^{131,47,132} KAUSHIK SATAPATHY,¹² TUOMAS SAVOLAINEN,^{133,126,5}
 F. PETER SCHLOERB,²⁹ JONATHAN SCHONFELD,⁷ KARL-FRIEDRICH SCHUSTER,²⁴ LIJING SHAO,^{77,5}
 ZHIQIANG SHEN (沈志强),^{41,42} DES SMALL,⁸⁶ BONG WON SOHN,^{17,18,30,31,134} JASON SOOHOO,¹ KAMAL SOUCCAR,²⁹
 HE SUN (孙赫),¹⁹ FUMIE TAZAKI,⁴⁷ ALEXANDRA J. TETARENKO,^{135,37} PAUL TIEDE,^{7,3} REMO P. J. TILANUS,^{12,25,82,136}
 MICHAEL TITUS,¹ PABLO TORNE,^{109,5} EFTHALIA TRAIANOU,^{4,5} TYLER TRENT,¹² SASCHA TRIPPE,¹³⁷ MATTHEW TURK,⁴⁴
 ILSE VAN BEMMEL,⁸⁶ HUIB JAN VAN LANGEVELDE,^{86,82,138} DANIEL R. VAN ROSSUM,²⁵ JESSE VOS,²⁵ JAN WAGNER,⁵
 DEREK WARD-THOMPSON,¹³⁹ JOHN WARDLE,¹⁴⁰ JONATHAN WEINTROUB,^{3,7} NORBERT WEX,⁵ ROBERT WHARTON,⁵
 MACIEK WIELGUS,⁵ KAJ WIJK,¹⁴¹ GUNTHER WITZEL,⁵ MICHAEL F. WONDRAK,^{25,142} GEORGE N. WONG,^{106,143}
 QINGWEN WU (吴庆文),¹⁴⁴ PAUL YAMAGUCHI,⁷ DOOSOO YOON,¹⁰³ ANDRÉ YOUNG,²⁵ KEN YOUNG,⁷ ZIRI YOUNSI,^{145,45}
 FENG YUAN (袁峰),^{41,74,146} YE-FEI YUAN (袁业飞),^{17,18,147} J. ANTON ZENSUS,⁵ SHUO ZHANG,¹⁴⁸ GUANG-YAO ZHAO,⁴
 SHAN-SHAN ZHAO (赵彬彬),⁴¹ CLAUDIO AGURTO,¹⁴⁹ JUAN PABLO ARANEDA,¹⁴⁹ ORIEL ARRIAGADA,¹⁴⁹
 ALESSANDRA BERTARINI,^{5,150} RYAN BERTHOLD,¹⁷ JAY BLANCHARD,¹⁵¹ KEN BROWN,¹⁷ MAURICIO CÁRDENAS,¹⁴⁹
 MICHAEL CANTZLER,¹⁴⁹ PATRICIO CARO,¹⁴⁹ TIM C. CHUTER,¹⁷ MIROSLAW CIECHANOWICZ,^{5,149} IAIN M. COULSON,¹⁷
 JOSEPH CROWLEY,¹ NATHALIE DEGENAAR,¹⁰³ SVEN DORNBUSCH,⁵ CARLOS A. DURÁN,¹⁴⁹ KARL FORSTER,¹⁵²
 GERTIE GEERTSEMA,¹⁵³ EDOUARD GONZÁLEZ,¹⁴⁹ DAVE GRAHAM,⁵ FRÉDÉRIC GUETH,²⁴ CHIH-CHIANG HAN,⁹
 CRISTIAN HERRERA,¹⁴⁹ RUBEN HERRERO-ILLANA,¹⁵⁴ STEFAN HEYMINCK,⁵ JAMES HOGGE,¹⁷ YAU-DE HUANG,⁹ HOMIN JIANG,⁹
 DAVID JOHN,¹⁰⁹ THOMAS KLEIN,¹⁴⁹ DEREK KUBO,²⁰ JOHN KURODA,¹⁷ CALEB KWON,¹¹⁴ ROBERT LAING,^{155,156}
 CHING-TANG LIU,⁹ KUAN-YU LIU,^{9,17} FELIPE MAC-AULIFFE,¹⁴⁹ PIERRE MARTIN-COCHER,⁹ CALLIE MATULONIS,¹⁷

HUGO MESSIAS,^{154,149} ZHENG MEYER-ZHAO,⁵⁶ FRANCISCO MONTENEGRO-MONTES,¹⁴⁹ WILLIAM MONTGOMERIE,^{17,157}
 DIRK MUDERS,⁵ HIROAKI NISHIOKA,⁹ TIMOTHY J. NORTON,⁷ RODRIGO OLIVARES,¹⁴⁹
 JUAN PABLO PÉREZ-BEAUPUITS,^{149,5,158} RODRIGO PARRA,¹⁴⁹ MICHAEL POIRIER,¹ NICOLAS PRADEL,⁹
 PHILIPPE A. RAFFIN,²⁰ JORGE RAMÍREZ,¹⁴⁹ MARK REYNOLDS,¹⁵⁹ ALEJANDRO F. SAEZ-MADAIN,^{154,160} JORGE SANTANA,¹⁴⁹
 KEVIN M. SILVA,¹⁷ DON SOUSA,¹ WILLIAM STAHM,¹⁷ KARL TORSTENSSON,¹⁴⁹ PAULINA VENEGAS,¹⁴⁹ CRAIG WALTHER,¹⁷
 GUNDOLF WIECHING,⁵ RUDY WIJNANDS,¹⁰³ AND JAN G. A. WOUTERLOOT¹⁷

¹Massachusetts Institute of Technology Haystack Observatory, 99 Millstone Road, Westford, MA 01886, USA

²National Astronomical Observatory of Japan, 2-21-1 Osawa, Mitaka, Tokyo 181-8588, Japan

³Black Hole Initiative at Harvard University, 20 Garden Street, Cambridge, MA 02138, USA

⁴Instituto de Astrofísica de Andalucía-CSIC, Glorieta de la Astronomía s/n, E-18008 Granada, Spain

⁵Max-Planck-Institut für Radioastronomie, Auf dem Hügel 69, D-53121 Bonn, Germany

⁶Department of Physics, Faculty of Science, Universiti Malaya, 50603 Kuala Lumpur, Malaysia

⁷Center for Astrophysics | Harvard & Smithsonian, 60 Garden Street, Cambridge, MA 02138, USA

⁸Department of Physics & Astronomy, The University of Texas at San Antonio, One UTSA Circle, San Antonio, TX 78249, USA

⁹Institute of Astronomy and Astrophysics, Academia Sinica, 11F of Astronomy-Mathematics Building, AS/NTU No. 1, Sec. 4, Roosevelt Rd, Taipei 10617, Taiwan, R.O.C.

¹⁰Departament d'Astronomia i Astrofísica, Universitat de València, C. Dr. Moliner 50, E-46100 Burjassot, València, Spain

¹¹Observatori Astronòmic, Universitat de València, C. Catedrático José Beltrán 2, E-46980 Paterna, València, Spain

¹²Steward Observatory and Department of Astronomy, University of Arizona, 933 N. Cherry Ave., Tucson, AZ 85721, USA

¹³Yale Center for Astronomy & Astrophysics, Yale University, 52 Hillhouse Avenue, New Haven, CT 06511, USA

¹⁴Department of Physics, University of Illinois, 1110 West Green Street, Urbana, IL 61801, USA

¹⁵Fermi National Accelerator Laboratory, MS209, P.O. Box 500, Batavia, IL 60510, USA

¹⁶Department of Astronomy and Astrophysics, University of Chicago, 5640 South Ellis Avenue, Chicago, IL 60637, USA

¹⁷East Asian Observatory, 660 N. A'ohoku Place, Hilo, HI 96720, USA

¹⁸James Clerk Maxwell Telescope (JCMT), 660 N. A'ohoku Place, Hilo, HI 96720, USA

¹⁹California Institute of Technology, 1200 East California Boulevard, Pasadena, CA 91125, USA

²⁰Institute of Astronomy and Astrophysics, Academia Sinica, 645 N. A'ohoku Place, Hilo, HI 96720, USA

²¹Department of Physics and Astronomy, University of Hawaii at Manoa, 2505 Correa Road, Honolulu, HI 96822, USA

²²Department of Physics, McGill University, 3600 rue University, Montréal, QC H3A 2T8, Canada

²³McGill Space Institute, McGill University, 3550 rue University, Montréal, QC H3A 2A7, Canada

²⁴Institut de Radioastronomie Millimétrique (IRAM), 300 rue de la Piscine, F-38406 Saint Martin d'Hères, France

²⁵Department of Astrophysics, Institute for Mathematics, Astrophysics and Particle Physics (IMAPP), Radboud University, P.O. Box 9010, 6500 GL Nijmegen, The Netherlands

²⁶Perimeter Institute for Theoretical Physics, 31 Caroline Street North, Waterloo, ON, N2L 2Y5, Canada

²⁷Department of Physics and Astronomy, University of Waterloo, 200 University Avenue West, Waterloo, ON, N2L 3G1, Canada

²⁸Waterloo Centre for Astrophysics, University of Waterloo, Waterloo, ON, N2L 3G1, Canada

²⁹Department of Astronomy, University of Massachusetts, 01003, Amherst, MA, USA

³⁰Korea Astronomy and Space Science Institute, Daedeok-daero 776, Yuseong-gu, Daejeon 34055, Republic of Korea

³¹University of Science and Technology, Gajeong-ro 217, Yuseong-gu, Daejeon 34113, Republic of Korea

³²Kavli Institute for Cosmological Physics, University of Chicago, 5640 South Ellis Avenue, Chicago, IL 60637, USA

³³Department of Physics, University of Chicago, 5720 South Ellis Avenue, Chicago, IL 60637, USA

³⁴Enrico Fermi Institute, University of Chicago, 5640 South Ellis Avenue, Chicago, IL 60637, USA

³⁵Department of Space, Earth and Environment, Chalmers University of Technology, Onsala Space Observatory, SE-43992 Onsala, Sweden

³⁶Princeton Center for Theoretical Science, Jadwin Hall, Princeton University, Princeton, NJ 08544, USA

³⁷NASA Hubble Fellowship Program, Einstein Fellow

³⁸Data Science Institute, University of Arizona, 1230 N. Cherry Ave., Tucson, AZ 85721, USA

³⁹Program in Applied Mathematics, University of Arizona, 617 N. Santa Rita, Tucson, AZ 85721

⁴⁰Cornell Center for Astrophysics and Planetary Science, Cornell University, Ithaca, NY 14853, USA

⁴¹Shanghai Astronomical Observatory, Chinese Academy of Sciences, 80 Nandan Road, Shanghai 200030, People's Republic of China

⁴²Key Laboratory of Radio Astronomy, Chinese Academy of Sciences, Nanjing 210008, People's Republic of China

⁴³Physics Department, Fairfield University, 1073 North Benson Road, Fairfield, CT 06824, USA

⁴⁴Department of Astronomy, University of Illinois at Urbana-Champaign, 1002 West Green Street, Urbana, IL 61801, USA

⁴⁵Institut für Theoretische Physik, Goethe-Universität Frankfurt, Max-von-Laue-Straße 1, D-60438 Frankfurt am Main, Germany

⁴⁶Tsung-Dao Lee Institute, Shanghai Jiao Tong University, Shengrong Road 520, Shanghai, 201210, People's Republic of China

⁴⁷Mizusawa VLBI Observatory, National Astronomical Observatory of Japan, 2-12 Hoshigaoka, Mizusawa, Oshu, Iwate 023-0861, Japan

- ⁴⁸Department of Astronomical Science, The Graduate University for Advanced Studies (SOKENDAI), 2-21-1 Osawa, Mitaka, Tokyo 181-8588, Japan
- ⁴⁹Department of Astronomy and Columbia Astrophysics Laboratory, Columbia University, 550 W 120th Street, New York, NY 10027, USA
- ⁵⁰Center for Computational Astrophysics, Flatiron Institute, 162 Fifth Avenue, New York, NY 10010, USA
- ⁵¹Dipartimento di Fisica “E. Pancini”, Università di Napoli “Federico II”, Compl. Univ. di Monte S. Angelo, Edificio G, Via Cinthia, I-80126, Napoli, Italy
- ⁵²INFN Sez. di Napoli, Compl. Univ. di Monte S. Angelo, Edificio G, Via Cinthia, I-80126, Napoli, Italy
- ⁵³Wits Centre for Astrophysics, University of the Witwatersrand, 1 Jan Smuts Avenue, Braamfontein, Johannesburg 2050, South Africa
- ⁵⁴Department of Physics, University of Pretoria, Hatfield, Pretoria 0028, South Africa
- ⁵⁵Centre for Radio Astronomy Techniques and Technologies, Department of Physics and Electronics, Rhodes University, Makhanda 6140, South Africa
- ⁵⁶ASTRON, Oude Hoogeveensedijk 4, 7991 PD Dwingeloo, The Netherlands
- ⁵⁷LESIA, Observatoire de Paris, Université PSL, CNRS, Sorbonne Université, Université de Paris, 5 place Jules Janssen, 92195 Meudon, France
- ⁵⁸JILA and Department of Astrophysical and Planetary Sciences, University of Colorado, Boulder, CO 80309, USA
- ⁵⁹National Astronomical Observatories, Chinese Academy of Sciences, 20A Datun Road, Chaoyang District, Beijing 100101, PR China
- ⁶⁰Las Cumbres Observatory, 6740 Cortona Drive, Suite 102, Goleta, CA 93117-5575, USA
- ⁶¹Department of Physics, University of California, Santa Barbara, CA 93106-9530, USA
- ⁶²National Radio Astronomy Observatory, 520 Edgemont Road, Charlottesville, VA 22903, USA
- ⁶³Department of Electrical Engineering and Computer Science, Massachusetts Institute of Technology, 32-D476, 77 Massachusetts Ave., Cambridge, MA 02142, USA
- ⁶⁴Google Research, 355 Main St., Cambridge, MA 02142, USA
- ⁶⁵Institut für Theoretische Physik und Astrophysik, Universität Würzburg, Emil-Fischer-Str. 31, 97074 Würzburg, Germany
- ⁶⁶Department of History of Science, Harvard University, Cambridge, MA 02138, USA
- ⁶⁷Department of Physics, Harvard University, Cambridge, MA 02138, USA
- ⁶⁸NCSA, University of Illinois, 1205 W Clark St, Urbana, IL 61801, USA
- ⁶⁹Dipartimento di Fisica, Università degli Studi di Cagliari, SP Monserrato-Sestu km 0.7, I-09042 Monserrato, Italy
- ⁷⁰INAF - Osservatorio Astronomico di Cagliari, Via della Scienza 5, 09047, Selargius, CA, Italy
- ⁷¹CP3-Origins, University of Southern Denmark, Campusvej 55, DK-5230 Odense M, Denmark
- ⁷²Instituto Nacional de Astrofísica, Óptica y Electrónica. Apartado Postal 51 y 216, 72000. Puebla Pue., México
- ⁷³Consejo Nacional de Ciencia y Tecnología, Av. Insurgentes Sur 1582, 03940, Ciudad de México, México
- ⁷⁴Key Laboratory for Research in Galaxies and Cosmology, Chinese Academy of Sciences, Shanghai 200030, People’s Republic of China
- ⁷⁵NOVA Sub-mm Instrumentation Group, Kapteyn Astronomical Institute, University of Groningen, Landleven 12, 9747 AD Groningen, The Netherlands
- ⁷⁶Department of Astronomy, School of Physics, Peking University, Beijing 100871, People’s Republic of China
- ⁷⁷Kavli Institute for Astronomy and Astrophysics, Peking University, Beijing 100871, People’s Republic of China
- ⁷⁸Department of Astronomy, Graduate School of Science, The University of Tokyo, 7-3-1 Hongo, Bunkyo-ku, Tokyo 113-0033, Japan
- ⁷⁹The Institute of Statistical Mathematics, 10-3 Midori-cho, Tachikawa, Tokyo, 190-8562, Japan
- ⁸⁰Department of Statistical Science, The Graduate University for Advanced Studies (SOKENDAI), 10-3 Midori-cho, Tachikawa, Tokyo 190-8562, Japan
- ⁸¹Kavli Institute for the Physics and Mathematics of the Universe, The University of Tokyo, 5-1-5 Kashiwanoha, Kashiwa, 277-8583, Japan
- ⁸²Leiden Observatory, Leiden University, Postbus 2300, 9513 RA Leiden, The Netherlands
- ⁸³ASTRAVEO LLC, PO Box 1668, Gloucester, MA 01931
- ⁸⁴Institute for Astrophysical Research, Boston University, 725 Commonwealth Ave., Boston, MA 02215, USA
- ⁸⁵Institute for Cosmic Ray Research, The University of Tokyo, 5-1-5 Kashiwanoha, Kashiwa, Chiba 277-8582, Japan
- ⁸⁶Joint Institute for VLBI ERIC (JIVE), Oude Hoogeveensedijk 4, 7991 PD Dwingeloo, The Netherlands
- ⁸⁷Department of Astronomy and Atmospheric Sciences, Kyungpook National University, Daegu 702-701, Republic of Korea
- ⁸⁸Kogakuin University of Technology & Engineering, Academic Support Center, 2665-1 Nakano, Hachioji, Tokyo 192-0015, Japan
- ⁸⁹Niigata University, 8050 Ikarashi-nino-cho, Nishi-ku, Niigata 950-2181, Japan
- ⁹⁰Physics Department, National Sun Yat-Sen University, No. 70, Lien-Hai Road, Kaosiung City 80424, Taiwan, R.O.C.
- ⁹¹National Optical Astronomy Observatory, 950 N. Cherry Ave., Tucson, AZ 85719, USA
- ⁹²Department of Physics, The Chinese University of Hong Kong, Shatin, N. T., Hong Kong
- ⁹³School of Astronomy and Space Science, Nanjing University, Nanjing 210023, People’s Republic of China
- ⁹⁴Key Laboratory of Modern Astronomy and Astrophysics, Nanjing University, Nanjing 210023, People’s Republic of China
- ⁹⁵INAF-Istituto di Radioastronomia, Via P. Gobetti 101, I-40129 Bologna, Italy
- ⁹⁶INAF-Istituto di Radioastronomia & Italian ALMA Regional Centre, Via P. Gobetti 101, I-40129 Bologna, Italy

- ⁹⁷Department of Physics, National Taiwan University, No.1, Sect.4, Roosevelt Rd., Taipei 10617, Taiwan, R.O.C
- ⁹⁸Instituto de Radioastronomía y Astrofísica, Universidad Nacional Autónoma de México, Morelia 58089, México
- ⁹⁹Instituto de Astronomía, Universidad Nacional Autónoma de México (UNAM), Apdo Postal 70-264, Ciudad de México, México
- ¹⁰⁰Yunnan Observatories, Chinese Academy of Sciences, 650011 Kunming, Yunnan Province, People's Republic of China
- ¹⁰¹Center for Astronomical Mega-Science, Chinese Academy of Sciences, 20A Datun Road, Chaoyang District, Beijing, 100012, People's Republic of China
- ¹⁰²Key Laboratory for the Structure and Evolution of Celestial Objects, Chinese Academy of Sciences, 650011 Kunming, People's Republic of China
- ¹⁰³Anton Pannekoek Institute for Astronomy, University of Amsterdam, Science Park 904, 1098 XH, Amsterdam, The Netherlands
- ¹⁰⁴Gravitation and Astroparticle Physics Amsterdam (GRAPPA) Institute, University of Amsterdam, Science Park 904, 1098 XH Amsterdam, The Netherlands
- ¹⁰⁵NSF Astronomy and Astrophysics Postdoctoral Fellow
- ¹⁰⁶School of Natural Sciences, Institute for Advanced Study, 1 Einstein Drive, Princeton, NJ 08540, USA
- ¹⁰⁷Science Support Office, Directorate of Science, European Space Research and Technology Centre (ESA/ESTEC), Keplerlaan 1, 2201 AZ Noordwijk, The Netherlands
- ¹⁰⁸School of Physics and Astronomy, Shanghai Jiao Tong University, 800 Dongchuan Road, Shanghai, 200240, People's Republic of China
- ¹⁰⁹Institut de Radioastronomie Millimétrique (IRAM), Avenida Divina Pastora 7, Local 20, E-18012, Granada, Spain
- ¹¹⁰Astronomy Department, Universidad de Concepción, Casilla 160-C, Concepción, Chile
- ¹¹¹National Institute of Technology, Hachinohe College, 16-1 Uwanotai, Tamonoki, Hachinohe City, Aomori 039-1192, Japan
- ¹¹²South African Radio Astronomy Observatory, Observatory 7925, Cape Town, South Africa
- ¹¹³Department of Physics, National and Kapodistrian University of Athens, Panepistimiopolis, GR 15783 Zografos, Greece
- ¹¹⁴Department of Physics, Villanova University, 800 Lancaster Avenue, Villanova, PA 19085, USA
- ¹¹⁵Physics Department, Washington University CB 1105, St Louis, MO 63130, USA
- ¹¹⁶Sejong University, 209 Neungdong-ro, Gwangjin-gu, Seoul, Republic of Korea
- ¹¹⁷EACOA Fellow
- ¹¹⁸Canadian Institute for Theoretical Astrophysics, University of Toronto, 60 St. George Street, Toronto, ON, M5S 3H8, Canada
- ¹¹⁹Dunlap Institute for Astronomy and Astrophysics, University of Toronto, 50 St. George Street, Toronto, ON, M5S 3H4, Canada
- ¹²⁰Canadian Institute for Advanced Research, 180 Dundas St West, Toronto, ON, M5G 1Z8, Canada
- ¹²¹Radio Astronomy Laboratory, University of California, Berkeley, CA 94720, USA
- ¹²²Department of Physics, University College Cork, Kane Building, College Road, Cork T12 K8AF, Ireland
- ¹²³Department of Physics, National Taiwan Normal University, No. 88, Sec.4, Tingzhou Rd., Taipei 116, Taiwan, R.O.C.
- ¹²⁴Center of Astronomy and Gravitation, National Taiwan Normal University, No. 88, Sec. 4, Tingzhou Road, Taipei 116, Taiwan, R.O.C.
- ¹²⁵Finnish Centre for Astronomy with ESO, FI-20014 University of Turku, Finland
- ¹²⁶Aalto University Metsähovi Radio Observatory, Metsähovintie 114, FI-02540 Kylmälä, Finland
- ¹²⁷Gemini Observatory/NSF NOIRLab, 670 N. A'ohōkū Place, Hilo, HI 96720, USA
- ¹²⁸Frankfurt Institute for Advanced Studies, Ruth-Moufang-Strasse 1, 60438 Frankfurt, Germany
- ¹²⁹School of Mathematics, Trinity College, Dublin 2, Ireland
- ¹³⁰Department of Astrophysical Sciences, Peyton Hall, Princeton University, Princeton, NJ 08544, USA
- ¹³¹Department of Physics, Tokyo Institute of Technology, 2-12-1 Ookayama, Meguro-ku, Tokyo 152-8551, Japan
- ¹³²Hiroshima Astrophysical Science Center, Hiroshima University, 1-3-1 Kagamiyama, Higashi-Hiroshima, Hiroshima 739-8526, Japan
- ¹³³Aalto University Department of Electronics and Nanoengineering, PL 15500, FI-00076 Aalto, Finland
- ¹³⁴Department of Astronomy, Yonsei University, Yonsei-ro 50, Seodaemun-gu, 03722 Seoul, Republic of Korea
- ¹³⁵Department of Physics and Astronomy, Texas Tech University, Lubbock, Texas 79409-1051, USA
- ¹³⁶Netherlands Organisation for Scientific Research (NWO), Postbus 93138, 2509 AC Den Haag, The Netherlands
- ¹³⁷Department of Physics and Astronomy, Seoul National University, Gwanak-gu, Seoul 08826, Republic of Korea
- ¹³⁸University of New Mexico, Department of Physics and Astronomy, Albuquerque, NM 87131, USA
- ¹³⁹Jeremiah Horrocks Institute, University of Central Lancashire, Preston PR1 2HE, UK
- ¹⁴⁰Physics Department, Brandeis University, 415 South Street, Waltham, MA 02453, USA
- ¹⁴¹Tuorla Observatory, Department of Physics and Astronomy, University of Turku, Finland
- ¹⁴²Radboud Excellence Fellow of Radboud University, Nijmegen, The Netherlands
- ¹⁴³Princeton Gravity Initiative, Princeton University, Princeton, New Jersey 08544, USA
- ¹⁴⁴School of Physics, Huazhong University of Science and Technology, Wuhan, Hubei, 430074, People's Republic of China
- ¹⁴⁵Mullard Space Science Laboratory, University College London, Holmbury St. Mary, Dorking, Surrey, RH5 6NT, UK
- ¹⁴⁶School of Astronomy and Space Sciences, University of Chinese Academy of Sciences, No. 19A Yuquan Road, Beijing 100049, People's Republic of China
- ¹⁴⁷Astronomy Department, University of Science and Technology of China, Hefei 230026, People's Republic of China
- ¹⁴⁸Bard College, 30 Campus Road, Annandale-on-Hudson, NY, 12504

-
- ¹⁴⁹European Southern Observatory, Alonso de Córdova 3107, Vitacura, Casilla 19001, Santiago de Chile, Chile
- ¹⁵⁰Institute of Geodesy and Geoinformation, University of Bonn, D-53113 Bonn, Germany
- ¹⁵¹National Radio Astronomy Observatory, Socorro, NM 87801, USA
- ¹⁵²Space Radiation Laboratory, California Institute of Technology, 1200 East California Boulevard, Pasadena, CA 91125, USA
- ¹⁵³Research and Development Weather and Climate Models, Royal Netherlands Meteorological Institute, Utrechtseweg 297, 3731 GA, De Bilt, The Netherlands
- ¹⁵⁴Joint ALMA Observatory, Alonso de Córdova 3107, Vitacura 763-0355, Santiago de Chile, Chile
- ¹⁵⁵SKA Observatory, Jodrell Bank, Lower Withington, Macclesfield SK11 9FT
- ¹⁵⁶European Southern Observatory, Karl-Schwarzschild-Strasse 2, D-85478 Garching, Germany
- ¹⁵⁷SOFIA Science Center, Universities Space Research Association, NASA Ames Research Center, Moffett Field, CA 94035, USA
- ¹⁵⁸Centro de Astro-Ingeniería (AIUC), Pontificia Universidad Católica de Chile, Av. Vicuña Mackena 4860, Macul, Santiago, Chile
- ¹⁵⁹Department of Astronomy, University of Michigan, 1085 South University Avenue, Ann Arbor, MI 48109, USA
- ¹⁶⁰National Radio Astronomy Observatory, NRAO Technology Center, 1180 Boxwood Estate Road, Charlottesville, VA 22903, USA

References

- Agol, E. 2000, *ApJ*, 538, L121, doi: [10.1086/312818](https://doi.org/10.1086/312818)
- Alexander, T. 1997, in *Astrophysics and Space Science Library*, Vol. 218, *Astronomical Time Series*, ed. D. Maoz, A. Sternberg, & E. M. Leibowitz, 163, doi: [10.1007/978-94-015-8941-3_14](https://doi.org/10.1007/978-94-015-8941-3_14)
- Alexander, T. 2013, ArXiv e-prints. <https://arxiv.org/abs/1302.1508>
- An, T., Goss, W. M., Zhao, J.-H., et al. 2005, *ApJ*, 634, L49, doi: [10.1086/498687](https://doi.org/10.1086/498687)
- An, T., Sohn, B. W., & Imai, H. 2018, *Nature Astronomy*, 2, 118, doi: [10.1038/s41550-017-0277-z](https://doi.org/10.1038/s41550-017-0277-z)
- Andrés, A., van den Eijnden, J., Degenaar, N., et al. 2022, *MNRAS*, 510, 2851, doi: [10.1093/mnras/stab3407](https://doi.org/10.1093/mnras/stab3407)
- Backer, D. 1982, in *Extragalactic Radio Sources*, ed. D. S. Heeschen & C. M. Wade, Vol. 97, 389
- Baganoff, F. K., Bautz, M. W., Brandt, W. N., et al. 2001a, *Nature*, 413, 45, doi: [10.1038/35092510](https://doi.org/10.1038/35092510)
- . 2001b, *Nature*, 413, 45, doi: [10.1038/35092510](https://doi.org/10.1038/35092510)
- Baganoff, F. K., Maeda, Y., Morris, M., et al. 2003a, *ApJ*, 591, 891, doi: [10.1086/375145](https://doi.org/10.1086/375145)
- . 2003b, *ApJ*, 591, 891, doi: [10.1086/375145](https://doi.org/10.1086/375145)
- . 2003c, *ApJ*, 591, 891, doi: [10.1086/375145](https://doi.org/10.1086/375145)
- Ball, D., Özel, F., Psaltis, D., & Chan, C.-k. 2016, *ApJ*, 826, 77, doi: [10.3847/0004-637X/826/1/77](https://doi.org/10.3847/0004-637X/826/1/77)
- Bardeen, J. M. 1973, in *Black Holes (Les Astres Occlus)*, 215–239
- Barrière, N. M., Tomsick, J. A., Baganoff, F. K., et al. 2014, *ApJ*, 786, 46, doi: [10.1088/0004-637X/786/1/46](https://doi.org/10.1088/0004-637X/786/1/46)
- Barth, A. J., Boizelle, B. D., Darling, J., et al. 2016a, *ApJ*, 822, L28, doi: [10.3847/2041-8205/822/2/L28](https://doi.org/10.3847/2041-8205/822/2/L28)

- Barth, A. J., Darling, J., Baker, A. J., et al. 2016b, *ApJ*, 823, 51, doi: [10.3847/0004-637X/823/1/51](https://doi.org/10.3847/0004-637X/823/1/51)
- Barth, A. J., Sarzi, M., Ho, L. C., et al. 2001, in *Astronomical Society of the Pacific Conference Series*, Vol. 249, *The Central Kiloparsec of Starbursts and AGN: The La Palma Connection*, ed. J. H. Knapen, J. E. Beckman, I. Shlosman, & T. J. Mahoney, 370. <https://arxiv.org/abs/astro-ph/0110672>
- Best, P. N., Kauffmann, G., Heckman, T. M., et al. 2005, *MNRAS*, 362, 25, doi: [10.1111/j.1365-2966.2005.09192.x](https://doi.org/10.1111/j.1365-2966.2005.09192.x)
- Bigiel, F., Leroy, A., Walter, F., et al. 2008, *AJ*, 136, 2846, doi: [10.1088/0004-6256/136/6/2846](https://doi.org/10.1088/0004-6256/136/6/2846)
- Boehle, A., Ghez, A. M., Schödel, R., et al. 2016a, *ApJ*, 830, 17, doi: [10.3847/0004-637X/830/1/17](https://doi.org/10.3847/0004-637X/830/1/17)
- . 2016b, *ApJ*, 830, 17, doi: [10.3847/0004-637X/830/1/17](https://doi.org/10.3847/0004-637X/830/1/17)
- Boizelle, B. D., Barth, A. J., Walsh, J. L., et al. 2019, *ApJ*, 881, 10, doi: [10.3847/1538-4357/ab2a0a](https://doi.org/10.3847/1538-4357/ab2a0a)
- Bouffard, É., Haggard, D., Nowak, M. A., et al. 2019, *ApJ*, 884, 148, doi: [10.3847/1538-4357/ab4266](https://doi.org/10.3847/1538-4357/ab4266)
- Bower, G. C., Falcke, H., Herrnstein, R. M., et al. 2004, *Science*, 304, 704, doi: [10.1126/science.1094023](https://doi.org/10.1126/science.1094023)
- Bower, G. C., Wright, M. C. H., Falcke, H., & Backer, D. C. 2003, *ApJ*, 588, 331, doi: [10.1086/373989](https://doi.org/10.1086/373989)
- Bower, G. C., Deller, A., Demorest, P., et al. 2014, *ApJ*, 780, L2, doi: [10.1088/2041-8205/780/1/L2](https://doi.org/10.1088/2041-8205/780/1/L2)
- Bower, G. C., Markoff, S., Dexter, J., et al. 2015a, *ApJ*, 802, 69, doi: [10.1088/0004-637X/802/1/69](https://doi.org/10.1088/0004-637X/802/1/69)
- Bower, G. C., Deller, A., Demorest, P., et al. 2015b, *ApJ*, 798, 120, doi: [10.1088/0004-637X/798/2/120](https://doi.org/10.1088/0004-637X/798/2/120)
- Bower, G. C., Markoff, S., Dexter, J., et al. 2015c, *ApJ*, 802, 69, doi: [10.1088/0004-637X/802/1/69](https://doi.org/10.1088/0004-637X/802/1/69)
- Bower, G. C., Broderick, A., Dexter, J., et al. 2018a, *ApJ*, 868, 101, doi: [10.3847/1538-4357/aae983](https://doi.org/10.3847/1538-4357/aae983)
- . 2018b, *ApJ*, 868, 101, doi: [10.3847/1538-4357/aae983](https://doi.org/10.3847/1538-4357/aae983)
- Bower, G. C., Dexter, J., Asada, K., et al. 2019a, *ApJ*, 881, L2, doi: [10.3847/2041-8213/ab3397](https://doi.org/10.3847/2041-8213/ab3397)

- . 2019b, *ApJ*, 881, L2, doi: [10.3847/2041-8213/ab3397](https://doi.org/10.3847/2041-8213/ab3397)
- Boyce, H., Haggard, D., Witzel, G., et al. 2019, *ApJ*, 871, 161, doi: [10.3847/1538-4357/aaf71f](https://doi.org/10.3847/1538-4357/aaf71f)
- Boyce, H., Haggard, D., Witzel, G., et al. 2021, *The Astrophysical Journal*, 912, 168, doi: [10.3847/1538-4357/abefd2](https://doi.org/10.3847/1538-4357/abefd2)
- Boyce, H., Haggard, D., Witzel, G., et al. 2022, *ApJ*, 931, 7, doi: [10.3847/1538-4357/ac6104](https://doi.org/10.3847/1538-4357/ac6104)
- Bremer, M., Witzel, G., Eckart, A., et al. 2011, *AAP*, 532, A26, doi: [10.1051/0004-6361/201016134](https://doi.org/10.1051/0004-6361/201016134)
- Brinkerink, C., Falcke, H., Brunthaler, A., & Law, C. 2021a, arXiv e-prints, arXiv:2107.13402. <https://arxiv.org/abs/2107.13402>
- . 2021b, arXiv e-prints, arXiv:2107.13402. <https://arxiv.org/abs/2107.13402>
- Brinkerink, C. D., Falcke, H., Law, C. J., et al. 2015a, *A&A*, 576, A41, doi: [10.1051/0004-6361/201424783](https://doi.org/10.1051/0004-6361/201424783)
- . 2015b, *A&A*, 576, A41, doi: [10.1051/0004-6361/201424783](https://doi.org/10.1051/0004-6361/201424783)
- Burrows, D. N., Hill, J. E., Nousek, J. A., et al. 2005, *Space Sci. Rev.*, 120, 165, doi: [10.1007/s11214-005-5097-2](https://doi.org/10.1007/s11214-005-5097-2)
- Capellupo, D. M., Haggard, D., Choux, N., et al. 2017a, *ApJ*, 845, 35, doi: [10.3847/1538-4357/aa7da6](https://doi.org/10.3847/1538-4357/aa7da6)
- . 2017b, *ApJ*, 845, 35, doi: [10.3847/1538-4357/aa7da6](https://doi.org/10.3847/1538-4357/aa7da6)
- Cappellari, M. 2002, *MNRAS*, 333, 400, doi: [10.1046/j.1365-8711.2002.05412.x](https://doi.org/10.1046/j.1365-8711.2002.05412.x)
- Cappellari, M., Scott, N., Alatalo, K., et al. 2013, *MNRAS*, 432, 1709, doi: [10.1093/mnras/stt562](https://doi.org/10.1093/mnras/stt562)
- Cash, W. 1979, *ApJ*, 228, 939, doi: [10.1086/156922](https://doi.org/10.1086/156922)
- Chan, C.-k., Psaltis, D., Özel, F., et al. 2015, *ApJ*, 812, 103, doi: [10.1088/0004-637X/812/2/103](https://doi.org/10.1088/0004-637X/812/2/103)
- Chatterjee, K., Markoff, S., Neilsen, J., et al. 2021, *MNRAS*, 507, 5281, doi: [10.1093/mnras/stab2466](https://doi.org/10.1093/mnras/stab2466)
- Chen, Z., Gallego-Cano, E., Do, T., et al. 2019, *ApJL*, 882, L28, doi: [10.3847/2041-8213/ab3c68](https://doi.org/10.3847/2041-8213/ab3c68)
- Cho, I., Zhao, G.-Y., Kawashima, T., et al. 2022, *ApJ*, 926, 108, doi: [10.3847/1538-4357/ac4165](https://doi.org/10.3847/1538-4357/ac4165)

- Ciurlo, A., Campbell, R. D., Morris, M. R., et al. 2020, *Nature*, 577, 337, doi: [10.1038/s41586-019-1883-y](https://doi.org/10.1038/s41586-019-1883-y)
- Clavel, M., Terrier, R., Goldwurm, A., et al. 2013, *A&A*, 558, A32, doi: [10.1051/0004-6361/201321667](https://doi.org/10.1051/0004-6361/201321667)
- Combes, F., García-Burillo, S., Audibert, A., et al. 2019, *A&A*, 623, A79, doi: [10.1051/0004-6361/201834560](https://doi.org/10.1051/0004-6361/201834560)
- Cotera, A., Morris, M., Ghez, A. M., et al. 1999, in *Astronomical Society of the Pacific Conference Series*, Vol. 186, *The Central Parsecs of the Galaxy*, ed. H. Falcke, A. Cotera, W. J. Duschl, F. Melia, & M. J. Rieke, 240
- Coti Zelati, F., Rea, N., Papitto, A., et al. 2015, *MNRAS*, 449, 2685, doi: [10.1093/mnras/stv480](https://doi.org/10.1093/mnras/stv480)
- Coti Zelati, F., Rea, N., Turolla, R., et al. 2017, *MNRAS*, 471, 1819, doi: [10.1093/mnras/stx1700](https://doi.org/10.1093/mnras/stx1700)
- Cui, Y., Hada, K., Kino, M., et al. 2021, arXiv e-prints, arXiv:2104.05525. <https://arxiv.org/abs/2104.05525>
- Dallilar, Y., von Fellenberg, S., Bauboek, M., et al. 2022, *A&A*, 658, A111, doi: [10.1051/0004-6361/202142458](https://doi.org/10.1051/0004-6361/202142458)
- Dame, T. M. 2011, arXiv e-prints, arXiv:1101.1499. <https://arxiv.org/abs/1101.1499>
- Davis, T. A. 2014, *MNRAS*, 443, 911, doi: [10.1093/mnras/stu1163](https://doi.org/10.1093/mnras/stu1163)
- Davis, T. A., Bureau, M., Cappellari, M., Sarzi, M., & Blitz, L. 2013a, *Nature*, 494, 328, doi: [10.1038/nature11819](https://doi.org/10.1038/nature11819)
- Davis, T. A., Bureau, M., Onishi, K., et al. 2017, *MNRAS*, 468, 4675, doi: [10.1093/mnras/stw3217](https://doi.org/10.1093/mnras/stw3217)
- Davis, T. A., Alatalo, K., Bureau, M., et al. 2013b, *MNRAS*, 429, 534, doi: [10.1093/mnras/sts353](https://doi.org/10.1093/mnras/sts353)
- Davis, T. A., Young, L. M., Crocker, A. F., et al. 2014, *MNRAS*, 444, 3427, doi: [10.1093/mnras/stu570](https://doi.org/10.1093/mnras/stu570)
- Davis, T. A., Bureau, M., Onishi, K., et al. 2018, *MNRAS*, 473, 3818, doi: [10.1093/mnras/stx2600](https://doi.org/10.1093/mnras/stx2600)
- Degenaar, N., Miller, J. M., Kennea, J., et al. 2013a, *ApJ*, 769, 155, doi: [10.1088/0004-637X/769/2/155](https://doi.org/10.1088/0004-637X/769/2/155)
- . 2013b, *ApJ*, 769, 155, doi: [10.1088/0004-637X/769/2/155](https://doi.org/10.1088/0004-637X/769/2/155)

- Degenaar, N., Wijnands, R., Miller, J. M., et al. 2015, *Journal of High Energy Astrophysics*, 7, 137, doi: [10.1016/j.jheap.2015.03.005](https://doi.org/10.1016/j.jheap.2015.03.005)
- Deller, A. T., Brisken, W. F., Phillips, C. J., et al. 2011, *PASP*, 123, 275, doi: [10.1086/658907](https://doi.org/10.1086/658907)
- Dexter, J., Agol, E., & Fragile, P. C. 2009, *ApJL*, 703, L142, doi: [10.1088/0004-637X/703/2/L142](https://doi.org/10.1088/0004-637X/703/2/L142)
- Dexter, J., Agol, E., Fragile, P. C., & McKinney, J. C. 2010, *ApJ*, 717, 1092, doi: [10.1088/0004-637X/717/2/1092](https://doi.org/10.1088/0004-637X/717/2/1092)
- Dexter, J., Kelly, B., Bower, G. C., et al. 2014, *MNRAS*, 442, 2797, doi: [10.1093/mnras/stu1039](https://doi.org/10.1093/mnras/stu1039)
- Dexter, J., Deller, A., Bower, G. C., et al. 2017, *MNRAS*, 471, 3563, doi: [10.1093/mnras/stx1777](https://doi.org/10.1093/mnras/stx1777)
- Do, T., Ghez, A. M., Morris, M. R., et al. 2009, *ApJ*, 691, 1021, doi: [10.1088/0004-637X/691/2/1021](https://doi.org/10.1088/0004-637X/691/2/1021)
- Do, T., Hees, A., Ghez, A., et al. 2019a, *Science*, 365, 664, doi: [10.1126/science.aav8137](https://doi.org/10.1126/science.aav8137)
- Do, T., Witzel, G., Gautam, A. K., et al. 2019b, *ApJL*, 882, L27, doi: [10.3847/2041-8213/ab38c3](https://doi.org/10.3847/2041-8213/ab38c3)
- . 2019c, *ApJ*, 882, L27, doi: [10.3847/2041-8213/ab38c3](https://doi.org/10.3847/2041-8213/ab38c3)
- Dodds-Eden, K., Sharma, P., Quataert, E., et al. 2010, *ApJ*, 725, 450, doi: [10.1088/0004-637X/725/1/450](https://doi.org/10.1088/0004-637X/725/1/450)
- Dodds-Eden, K., Porquet, D., Trap, G., et al. 2009a, *ApJ*, 698, 676, doi: [10.1088/0004-637X/698/1/676](https://doi.org/10.1088/0004-637X/698/1/676)
- . 2009b, *ApJ*, 698, 676, doi: [10.1088/0004-637X/698/1/676](https://doi.org/10.1088/0004-637X/698/1/676)
- . 2009c, *ApJ*, 698, 676, doi: [10.1088/0004-637X/698/1/676](https://doi.org/10.1088/0004-637X/698/1/676)
- Dodds-Eden, K., Gillessen, S., Fritz, T. K., et al. 2011a, *ApJ*, 728, 37, doi: [10.1088/0004-637X/728/1/37](https://doi.org/10.1088/0004-637X/728/1/37)
- . 2011b, *ApJ*, 728, 37, doi: [10.1088/0004-637X/728/1/37](https://doi.org/10.1088/0004-637X/728/1/37)
- Doeleman, S. S., Weintroub, J., Rogers, A. E. E., et al. 2008a, *Nature*, 455, 78, doi: [10.1038/nature07245](https://doi.org/10.1038/nature07245)
- . 2008b, *Nature*, 455, 78, doi: [10.1038/nature07245](https://doi.org/10.1038/nature07245)

- Doi, A., Fujisawa, K., Harada, K., et al. 2006, in Proceedings of the 8th European VLBI Network Symposium, 71. <https://arxiv.org/abs/astro-ph/0612528>
- Drissen, L., Martin, T., Rousseau-Nepton, L., et al. 2019, MNRAS, 485, 3930, doi: [10.1093/mnras/stz627](https://doi.org/10.1093/mnras/stz627)
- Eatough, R. P., Falcke, H., Karuppusamy, R., et al. 2013a, Nature, 501, 391, doi: [10.1038/nature12499](https://doi.org/10.1038/nature12499)
- . 2013b, Nature, 501, 391, doi: [10.1038/nature12499](https://doi.org/10.1038/nature12499)
- Eckart, A., Schödel, R., Meyer, L., et al. 2006a, AAP, 455, 1, doi: [10.1051/0004-6361:20064948](https://doi.org/10.1051/0004-6361:20064948)
- Eckart, A., Baganoff, F. K., Morris, M., et al. 2004, AAP, 427, 1, doi: [10.1051/0004-6361:20040495](https://doi.org/10.1051/0004-6361:20040495)
- Eckart, A., Baganoff, F. K., Schödel, R., et al. 2006b, AAP, 450, 535, doi: [10.1051/0004-6361:20054418](https://doi.org/10.1051/0004-6361:20054418)
- Eckart, A., Schödel, R., García-Marín, M., et al. 2008a, AAP, 492, 337, doi: [10.1051/0004-6361:200810924](https://doi.org/10.1051/0004-6361:200810924)
- Eckart, A., Baganoff, F. K., Zamaninasab, M., et al. 2008b, AAP, 479, 625, doi: [10.1051/0004-6361:20078793](https://doi.org/10.1051/0004-6361:20078793)
- Eckart, A., García-Marín, M., Vogel, S. N., et al. 2012, AAP, 537, A52, doi: [10.1051/0004-6361/201117779](https://doi.org/10.1051/0004-6361/201117779)
- EHT MWL Science Working Group, Algaba, J. C., Anczarski, J., et al. 2021, ApJ, 911, L11, doi: [10.3847/2041-8213/abef71](https://doi.org/10.3847/2041-8213/abef71)
- Eisenhauer, F., Genzel, R., Alexander, T., et al. 2005, ApJ, 628, 246, doi: [10.1086/430667](https://doi.org/10.1086/430667)
- Emsellem, E., Monnet, G., Bacon, R., & Nieto, J. L. 1994, A&A, 285, 739
- Event Horizon Telescope Collaboration, Akiyama, K., Alberdi, A., et al. 2019a, ApJ, 875, L1, doi: [10.3847/2041-8213/ab0ec7](https://doi.org/10.3847/2041-8213/ab0ec7)
- . 2019b, ApJ, 875, L2, doi: [10.3847/2041-8213/ab0c96](https://doi.org/10.3847/2041-8213/ab0c96)
- . 2019c, ApJ, 875, L3, doi: [10.3847/2041-8213/ab0c57](https://doi.org/10.3847/2041-8213/ab0c57)
- . 2019d, ApJ, 875, L4, doi: [10.3847/2041-8213/ab0e85](https://doi.org/10.3847/2041-8213/ab0e85)
- . 2019e, ApJ, 875, L5, doi: [10.3847/2041-8213/ab0f43](https://doi.org/10.3847/2041-8213/ab0f43)
- . 2019f, ApJ, 875, L6, doi: [10.3847/2041-8213/ab1141](https://doi.org/10.3847/2041-8213/ab1141)
- Event Horizon Telescope Collaboration, Akiyama, K., Algaba, J. C., et al. 2021a, ApJ, 910, L12, doi: [10.3847/2041-8213/abe71d](https://doi.org/10.3847/2041-8213/abe71d)

- . 2021b, *ApJ*, 910, L13, doi: [10.3847/2041-8213/abe4de](https://doi.org/10.3847/2041-8213/abe4de)
- Event Horizon Telescope Collaboration, Akiyama, K., Alberdi, A., et al. 2022a, *ApJ*, 930, L12, doi: [10.3847/2041-8213/ac6674](https://doi.org/10.3847/2041-8213/ac6674)
- . 2022b, *ApJ*, 930, L13, doi: [10.3847/2041-8213/ac6675](https://doi.org/10.3847/2041-8213/ac6675)
- . 2022c, *ApJ*, 930, L14, doi: [10.3847/2041-8213/ac6429](https://doi.org/10.3847/2041-8213/ac6429)
- . 2022d, *ApJ*, 930, L15, doi: [10.3847/2041-8213/ac6736](https://doi.org/10.3847/2041-8213/ac6736)
- . 2022e, *ApJ*, 930, L16, doi: [10.3847/2041-8213/ac6672](https://doi.org/10.3847/2041-8213/ac6672)
- . 2022f, *ApJ*, 930, L17, doi: [10.3847/2041-8213/ac6756](https://doi.org/10.3847/2041-8213/ac6756)
- Falcke, H., Goss, W. M., Matsuo, H., et al. 1998, *ApJ*, 499, 731, doi: [10.1086/305687](https://doi.org/10.1086/305687)
- Falcke, H., Markoff, S., & Bower, G. C. 2009, *A&A*, 496, 77, doi: [10.1051/0004-6361/20078984](https://doi.org/10.1051/0004-6361/20078984)
- Falcke, H., & Markoff, S. B. 2013, *Classical and Quantum Gravity*, 30, 244003, doi: [10.1088/0264-9381/30/24/244003](https://doi.org/10.1088/0264-9381/30/24/244003)
- Falcke, H., Melia, F., & Agol, E. 2000, *ApJ*, 528, L13, doi: [10.1086/312423](https://doi.org/10.1086/312423)
- Fazio, G. G., Hora, J. L., Allen, L. E., et al. 2004, *ApJS*, 154, 10, doi: [10.1086/422843](https://doi.org/10.1086/422843)
- Fazio, G. G., Hora, J. L., Witzel, G., et al. 2018a, *ApJ*, 864, 58, doi: [10.3847/1538-4357/aad4a2](https://doi.org/10.3847/1538-4357/aad4a2)
- . 2018b, *ApJ*, 864, 58, doi: [10.3847/1538-4357/aad4a2](https://doi.org/10.3847/1538-4357/aad4a2)
- Fish, V. L., Doeleman, S. S., Beaudoin, C., et al. 2011, *ApJ*, 727, L36, doi: [10.1088/2041-8205/727/2/L36](https://doi.org/10.1088/2041-8205/727/2/L36)
- Fish, V. L., Johnson, M. D., Doeleman, S. S., et al. 2016, *ApJ*, 820, 90, doi: [10.3847/0004-637X/820/2/90](https://doi.org/10.3847/0004-637X/820/2/90)
- Fritz, T. K., Gillessen, S., Dodds-Eden, K., et al. 2011, *ApJ*, 737, 73, doi: [10.1088/0004-637X/737/2/73](https://doi.org/10.1088/0004-637X/737/2/73)
- Fruscione, A., McDowell, J. C., Allen, G. E., et al. 2006, in *SPIE, Vol. 6270, Society of Photo-Optical Instrumentation Engineers (SPIE) Conference Series*, 62701V, doi: [10.1117/12.671760](https://doi.org/10.1117/12.671760)
- Gatti, M., Lamastra, A., Menci, N., Bongiorno, A., & Fiore, F. 2015, *A&A*, 576, A32, doi: [10.1051/0004-6361/201425094](https://doi.org/10.1051/0004-6361/201425094)
- Gehrels, N., Chincarini, G., Giommi, P., et al. 2004, *ApJ*, 611, 1005, doi: [10.1086/422091](https://doi.org/10.1086/422091)

- Genzel, R., Eisenhauer, F., & Gillessen, S. 2010a, *Reviews of Modern Physics*, 82, 3121, doi: [10.1103/RevModPhys.82.3121](https://doi.org/10.1103/RevModPhys.82.3121)
- . 2010b, *Reviews of Modern Physics*, 82, 3121, doi: [10.1103/RevModPhys.82.3121](https://doi.org/10.1103/RevModPhys.82.3121)
- Genzel, R., Schödel, R., Ott, T., et al. 2003a, *Nature*, 425, 934, doi: [10.1038/nature02065](https://doi.org/10.1038/nature02065)
- . 2003b, *Nature*, 425, 934, doi: [10.1038/nature02065](https://doi.org/10.1038/nature02065)
- Ghez, A. M., Wright, S. A., Matthews, K., et al. 2004a, *ApJL*, 601, L159, doi: [10.1086/382024](https://doi.org/10.1086/382024)
- . 2004b, *ApJ*, 601, L159, doi: [10.1086/382024](https://doi.org/10.1086/382024)
- Ghez, A. M., Hornstein, S. D., Lu, J. R., et al. 2005, *ApJ*, 635, 1087, doi: [10.1086/497576](https://doi.org/10.1086/497576)
- Ghez, A. M., Salim, S., Weinberg, N. N., et al. 2008, *ApJ*, 689, 1044, doi: [10.1086/592738](https://doi.org/10.1086/592738)
- Gillessen, S., Eisenhauer, F., Quataert, E., et al. 2006, *The Astrophysical Journal*, 640, L163, doi: [10.1086/503557](https://doi.org/10.1086/503557)
- Gillessen, S., Genzel, R., Fritz, T. K., et al. 2012, *Nature*, 481, 51, doi: [10.1038/nature10652](https://doi.org/10.1038/nature10652)
- Gillessen, S., Plewa, P. M., Eisenhauer, F., et al. 2017, *ApJ*, 837, 30, doi: [10.3847/1538-4357/aa5c41](https://doi.org/10.3847/1538-4357/aa5c41)
- Gillessen, S., Plewa, P. M., Widmann, F., et al. 2019, *ApJ*, 871, 126, doi: [10.3847/1538-4357/aaf4f8](https://doi.org/10.3847/1538-4357/aaf4f8)
- Gobat, R., Daddi, E., Magdis, G., et al. 2018, *Nature Astronomy*, 2, 239, doi: [10.1038/s41550-017-0352-5](https://doi.org/10.1038/s41550-017-0352-5)
- Goddi, C., Martí-Vidal, I., Messias, H., et al. 2019, *PASP*, 131, 075003, doi: [10.1088/1538-3873/ab136a](https://doi.org/10.1088/1538-3873/ab136a)
- Gravity Collaboration, Abuter, R., Accardo, M., et al. 2017, *A&A*, 602, A94, doi: [10.1051/0004-6361/201730838](https://doi.org/10.1051/0004-6361/201730838)
- Gravity Collaboration, Abuter, R., Amorim, A., et al. 2018a, *A&A*, 615, L15, doi: [10.1051/0004-6361/201833718](https://doi.org/10.1051/0004-6361/201833718)
- . 2018b, *A&A*, 615, L15, doi: [10.1051/0004-6361/201833718](https://doi.org/10.1051/0004-6361/201833718)
- . 2018c, *A&A*, 618, L10, doi: [10.1051/0004-6361/201834294](https://doi.org/10.1051/0004-6361/201834294)
- . 2018d, *AAP*, 618, L10, doi: [10.1051/0004-6361/201834294](https://doi.org/10.1051/0004-6361/201834294)
- . 2018e, *A&A*, 618, L10, doi: [10.1051/0004-6361/201834294](https://doi.org/10.1051/0004-6361/201834294)
- . 2019a, *A&A*, 625, L10, doi: [10.1051/0004-6361/201935656](https://doi.org/10.1051/0004-6361/201935656)

- . 2019b, *A&A*, 625, L10, doi: [10.1051/0004-6361/201935656](https://doi.org/10.1051/0004-6361/201935656)
- . 2020a, *A&A*, 636, L5, doi: [10.1051/0004-6361/202037813](https://doi.org/10.1051/0004-6361/202037813)
- . 2020b, *A&A*, 638, A2, doi: [10.1051/0004-6361/202037717](https://doi.org/10.1051/0004-6361/202037717)
- Gravity Collaboration, Bauböck, M., Dexter, J., et al. 2020c, *A&A*, 635, A143, doi: [10.1051/0004-6361/201937233](https://doi.org/10.1051/0004-6361/201937233)
- Gravity Collaboration, Abuter, R., Amorim, A., et al. 2020d, *A&A*, 638, A2, doi: [10.1051/0004-6361/202037717](https://doi.org/10.1051/0004-6361/202037717)
- GRAVITY Collaboration, Abuter, R., Amorim, A., et al. 2021, *A&A*, 654, A22, doi: [10.1051/0004-6361/202140981](https://doi.org/10.1051/0004-6361/202140981)
- Gravity Collaboration, Abuter, R., Amorim, A., et al. 2021, *A&A*, 645, A127, doi: [10.1051/0004-6361/202039544](https://doi.org/10.1051/0004-6361/202039544)
- GRAVITY Collaboration, Abuter, R., Amorim, A., et al. 2021, *A&A*, 654, A22, doi: [10.1051/0004-6361/202140981](https://doi.org/10.1051/0004-6361/202140981)
- Gravity Collaboration, Abuter, R., Aymar, N., et al. 2022, *A&A*, 657, L12, doi: [10.1051/0004-6361/202142465](https://doi.org/10.1051/0004-6361/202142465)
- Greene, J. E., Peng, C. Y., Kim, M., et al. 2010, *ApJ*, 721, 26, doi: [10.1088/0004-637X/721/1/26](https://doi.org/10.1088/0004-637X/721/1/26)
- Greve, A., Torres, M., Wink, J. E., et al. 1995, *A&A*, 299, L33
- Haggard, D., Nynka, M., Mon, B., et al. 2019a, *ApJ*, 886, 96, doi: [10.3847/1538-4357/ab4a7f](https://doi.org/10.3847/1538-4357/ab4a7f)
- . 2019b, *ApJ*, 886, 96, doi: [10.3847/1538-4357/ab4a7f](https://doi.org/10.3847/1538-4357/ab4a7f)
- Harrison, F. A., Craig, W. W., Christensen, F. E., et al. 2013a, *ApJ*, 770, 103, doi: [10.1088/0004-637X/770/2/103](https://doi.org/10.1088/0004-637X/770/2/103)
- . 2013b, *ApJ*, 770, 103, doi: [10.1088/0004-637X/770/2/103](https://doi.org/10.1088/0004-637X/770/2/103)
- Heiderman, A., Evans, Neal J., I., Allen, L. E., Huard, T., & Heyer, M. 2010, *ApJ*, 723, 1019, doi: [10.1088/0004-637X/723/2/1019](https://doi.org/10.1088/0004-637X/723/2/1019)
- Herrnstein, R. M., Zhao, J.-H., Bower, G. C., & Goss, W. M. 2004, *AJ*, 127, 3399, doi: [10.1086/420711](https://doi.org/10.1086/420711)
- Hlavacek-Larrondo, J., McDonald, M., Benson, B. A., et al. 2015, *ApJ*, 805, 35, doi: [10.1088/0004-637X/805/1/35](https://doi.org/10.1088/0004-637X/805/1/35)
- Ho, L. C., Li, Z.-Y., Barth, A. J., Seigar, M. S., & Peng, C. Y. 2011, *ApJS*, 197, 21, doi: [10.1088/0067-0049/197/2/21](https://doi.org/10.1088/0067-0049/197/2/21)

- Hora, J. L., Witzel, G., Ashby, M. L. N., et al. 2014, *ApJ*, 793, 120, doi: [10.1088/0004-637X/793/2/120](https://doi.org/10.1088/0004-637X/793/2/120)
- Hornstein, S. D., Matthews, K., Ghez, A. M., et al. 2007, *ApJ*, 667, 900, doi: [10.1086/520762](https://doi.org/10.1086/520762)
- Hoyle, F., & Fowler, W. A. 1963, *Nature*, 197, 533, doi: [10.1038/197533a0](https://doi.org/10.1038/197533a0)
- Hunter, J. D. 2007, *Computing In Science & Engineering*, 9, 90, doi: [10.1109/MCSE.2007.55](https://doi.org/10.1109/MCSE.2007.55)
- Ishibashi, W., & Fabian, A. C. 2012, *MNRAS*, 427, 2998, doi: [10.1111/j.1365-2966.2012.22074.x](https://doi.org/10.1111/j.1365-2966.2012.22074.x)
- . 2015, *MNRAS*, 451, 93, doi: [10.1093/mnras/stv944](https://doi.org/10.1093/mnras/stv944)
- Issaoun, S., Johnson, M. D., Blackburn, L., et al. 2019a, *AAP*, 629, A32, doi: [10.1051/0004-6361/201936156](https://doi.org/10.1051/0004-6361/201936156)
- . 2019b, *ApJ*, 871, 30, doi: [10.3847/1538-4357/aaf732](https://doi.org/10.3847/1538-4357/aaf732)
- . 2021, *ApJ*, 915, 99, doi: [10.3847/1538-4357/ac00b0](https://doi.org/10.3847/1538-4357/ac00b0)
- Iwata, Y., Oka, T., Tsuboi, M., Miyoshi, M., & Takekawa, S. 2020a, *ApJ*, 892, L30, doi: [10.3847/2041-8213/ab800d](https://doi.org/10.3847/2041-8213/ab800d)
- . 2020b, *ApJ*, 892, L30, doi: [10.3847/2041-8213/ab800d](https://doi.org/10.3847/2041-8213/ab800d)
- Janssen, M., Falcke, H., Kadler, M., et al. 2021, *Nature Astronomy*, 5, 1017, doi: [10.1038/s41550-021-01417-w](https://doi.org/10.1038/s41550-021-01417-w)
- Johnson, M. D., Fish, V. L., Doeleman, S. S., et al. 2015, *Science*, 350, 1242, doi: [10.1126/science.aac7087](https://doi.org/10.1126/science.aac7087)
- Johnson, M. D., Narayan, R., Psaltis, D., et al. 2018, *ApJ*, 865, 104, doi: [10.3847/1538-4357/aadcff](https://doi.org/10.3847/1538-4357/aadcff)
- Jones, E., Oliphant, T., Peterson, P., et al. 2001, *SciPy: Open source scientific tools for Python*. <http://www.scipy.org/>
- Kacharov, N., Neumayer, N., Seth, A. C., et al. 2018, *MNRAS*, 480, 1973, doi: [10.1093/mnras/sty1985](https://doi.org/10.1093/mnras/sty1985)
- Kim, J.-Y., Krichbaum, T. P., Broderick, A. E., et al. 2020, *A&A*, 640, A69, doi: [10.1051/0004-6361/202037493](https://doi.org/10.1051/0004-6361/202037493)
- Kormendy, J., & Ho, L. C. 2013, *ARA&A*, 51, 511, doi: [10.1146/annurev-astro-082708-101811](https://doi.org/10.1146/annurev-astro-082708-101811)

- Kormendy, J., & Richstone, D. 1995, *ARA&A*, 33, 581, doi: [10.1146/annurev.aa.33.090195.003053](https://doi.org/10.1146/annurev.aa.33.090195.003053)
- Kostić, U., Čadež, A., Calvani, M., & Gomboc, A. 2009a, *AAP*, 496, 307, doi: [10.1051/0004-6361/200811059](https://doi.org/10.1051/0004-6361/200811059)
- Kostić, U., Čadež, A., Calvani, M., & Gomboc, A. 2009b, *A&A*, 496, 307, doi: [10.1051/0004-6361/200811059](https://doi.org/10.1051/0004-6361/200811059)
- Krabbe, A., Iserlohe, C., Larkin, J. E., et al. 2006, *ApJ*, 642, L145, doi: [10.1086/504587](https://doi.org/10.1086/504587)
- Krichbaum, T. P., Graham, D. A., Greve, A., et al. 1997, *A&A*, 323, L17
- Krichbaum, T. P., Graham, D. A., Witzel, A., et al. 1998, *A&A*, 335, L106
- Kruijssen, J. M. D., Longmore, S. N., Elmegreen, B. G., et al. 2014, *MNRAS*, 440, 3370, doi: [10.1093/mnras/stu494](https://doi.org/10.1093/mnras/stu494)
- Kruijssen, J. M. D., Schrubba, A., Chevance, M., et al. 2019, *Nature*, 569, 519, doi: [10.1038/s41586-019-1194-3](https://doi.org/10.1038/s41586-019-1194-3)
- Lada, C. J., Lombardi, M., & Alves, J. F. 2010, *ApJ*, 724, 687, doi: [10.1088/0004-637X/724/1/687](https://doi.org/10.1088/0004-637X/724/1/687)
- Lang, P., Wuyts, S., Somerville, R. S., et al. 2014, *ApJ*, 788, 11, doi: [10.1088/0004-637X/788/1/11](https://doi.org/10.1088/0004-637X/788/1/11)
- Lee, S.-S., Petrov, L., Byun, D.-Y., et al. 2014, *AJ*, 147, 77, doi: [10.1088/0004-6256/147/4/77](https://doi.org/10.1088/0004-6256/147/4/77)
- Li, H., Mao, S., Cappellari, M., et al. 2018, *MNRAS*, 476, 1765, doi: [10.1093/mnras/sty334](https://doi.org/10.1093/mnras/sty334)
- Li, Y.-P., Yuan, F., & Wang, Q. D. 2017, *MNRAS*, 468, 2552, doi: [10.1093/mnras/stx655](https://doi.org/10.1093/mnras/stx655)
- Li, Z., Morris, M. R., & Baganoff, F. K. 2013, *ApJ*, 779, 154, doi: [10.1088/0004-637X/779/2/154](https://doi.org/10.1088/0004-637X/779/2/154)
- Lin, L., Ellison, S. L., Pan, H.-A., et al. 2020, *ApJ*, 903, 145, doi: [10.3847/1538-4357/abba3a](https://doi.org/10.3847/1538-4357/abba3a)
- Liu, H. B., Wright, M. C. H., Zhao, J.-H., et al. 2016, *A&A*, 593, A107, doi: [10.1051/0004-6361/201628731](https://doi.org/10.1051/0004-6361/201628731)
- Liu, S., & Melia, F. 2002, *ApJL*, 566, L77, doi: [10.1086/339693](https://doi.org/10.1086/339693)
- Liu, S., Petrosian, V., & Melia, F. 2004a, *ApJL*, 611, L101, doi: [10.1086/423985](https://doi.org/10.1086/423985)
- . 2004b, *ApJ*, 611, L101, doi: [10.1086/423985](https://doi.org/10.1086/423985)

- Liu, Y., Peng, E. W., Jordán, A., et al. 2019, *ApJ*, 875, 156, doi: [10.3847/1538-4357/ab12d9](https://doi.org/10.3847/1538-4357/ab12d9)
- Lo, K. Y., Shen, Z.-Q., Zhao, J.-H., & Ho, P. T. P. 1998, *ApJ*, 508, L61, doi: [10.1086/311726](https://doi.org/10.1086/311726)
- Lu, A., Boyce, H., Haggard, D., et al. 2022, arXiv e-prints, arXiv:2206.03316. <https://arxiv.org/abs/2206.03316>
- Lu, R.-S., Krichbaum, T. P., Roy, A. L., et al. 2018, *ApJ*, 859, 60, doi: [10.3847/1538-4357/aabe2e](https://doi.org/10.3847/1538-4357/aabe2e)
- Lynden-Bell, D., & Rees, M. J. 1971, *MNRAS*, 152, 461, doi: [10.1093/mnras/152.4.461](https://doi.org/10.1093/mnras/152.4.461)
- Macquart, J.-P., & Bower, G. C. 2006, *ApJ*, 641, 302, doi: [10.1086/500317](https://doi.org/10.1086/500317)
- Maitra, D., Markoff, S., & Falcke, H. 2009, *AAP*, 508, L13, doi: [10.1051/0004-6361/200913163](https://doi.org/10.1051/0004-6361/200913163)
- Markoff, S., Falcke, H., Yuan, F., & Biermann, P. L. 2001, *AAP*, 379, L13, doi: [10.1051/0004-6361:20011346](https://doi.org/10.1051/0004-6361:20011346)
- Marrone, D. P., Moran, J. M., Zhao, J.-H., & Rao, R. 2006a, *ApJ*, 640, 308, doi: [10.1086/500106](https://doi.org/10.1086/500106)
- . 2006b, *ApJ*, 640, 308, doi: [10.1086/500106](https://doi.org/10.1086/500106)
- Marrone, D. P., Moran, J. M., Zhao, J.-H., & Rao, R. 2006c, in *Journal of Physics Conference Series*, Vol. 54, *Journal of Physics Conference Series*, 354–362, doi: [10.1088/1742-6596/54/1/056](https://doi.org/10.1088/1742-6596/54/1/056)
- . 2007a, *ApJ*, 654, L57, doi: [10.1086/510850](https://doi.org/10.1086/510850)
- . 2007b, *ApJL*, 654, L57, doi: [10.1086/510850](https://doi.org/10.1086/510850)
- Marrone, D. P., Baganoff, F. K., Morris, M. R., et al. 2008a, *ApJ*, 682, 373, doi: [10.1086/588806](https://doi.org/10.1086/588806)
- . 2008b, *ApJ*, 682, 373, doi: [10.1086/588806](https://doi.org/10.1086/588806)
- Martí-Vidal, I., Roy, A., Conway, J., & Zensus, A. J. 2016, *A&A*, 587, A143, doi: [10.1051/0004-6361/201526063](https://doi.org/10.1051/0004-6361/201526063)
- Martig, M., Bournaud, F., Teyssier, R., & Dekel, A. 2009, *ApJ*, 707, 250, doi: [10.1088/0004-637X/707/1/250](https://doi.org/10.1088/0004-637X/707/1/250)
- Martig, M., Crocker, A. F., Bournaud, F., et al. 2013, *MNRAS*, 432, 1914, doi: [10.1093/mnras/sts594](https://doi.org/10.1093/mnras/sts594)
- Matthews, L. D., Crew, G. B., Doeleman, S. S., et al. 2018, *PASP*, 130, 015002, doi: [10.1088/1538-3873/aa9c3d](https://doi.org/10.1088/1538-3873/aa9c3d)

- McConnell, N. J., & Ma, C.-P. 2013a, *ApJ*, 764, 184, doi: [10.1088/0004-637X/764/2/184](https://doi.org/10.1088/0004-637X/764/2/184)
- . 2013b, *ApJ*, 764, 184, doi: [10.1088/0004-637X/764/2/184](https://doi.org/10.1088/0004-637X/764/2/184)
- . 2013c, *ApJ*, 764, 184, doi: [10.1088/0004-637X/764/2/184](https://doi.org/10.1088/0004-637X/764/2/184)
- McMullin, J. P., Waters, B., Schiebel, D., Young, W., & Golap, K. 2007, in *Astronomical Society of the Pacific Conference Series*, Vol. 376, *Astronomical Data Analysis Software and Systems XVI*, ed. R. A. Shaw, F. Hill, & D. J. Bell, 127
- McNamara, B. R., & Nulsen, P. E. J. 2007, *ARA&A*, 45, 117, doi: [10.1146/annurev.astro.45.051806.110625](https://doi.org/10.1146/annurev.astro.45.051806.110625)
- Meidt, S. E., Schinnerer, E., García-Burillo, S., et al. 2013, *ApJ*, 779, 45, doi: [10.1088/0004-637X/779/1/45](https://doi.org/10.1088/0004-637X/779/1/45)
- Meyer, L., Do, T., Ghez, A., et al. 2009, *ApJL*, 694, L87, doi: [10.1088/0004-637X/694/1/L87](https://doi.org/10.1088/0004-637X/694/1/L87)
- Meyer, L., Eckart, A., Schödel, R., et al. 2006, *AAP*, 460, 15, doi: [10.1051/0004-6361:20065925](https://doi.org/10.1051/0004-6361:20065925)
- Meyer, L., Schödel, R., Eckart, A., et al. 2007, *AAP*, 473, 707, doi: [10.1051/0004-6361:20078009](https://doi.org/10.1051/0004-6361:20078009)
- Meyer, L., Ghez, A. M., Schödel, R., et al. 2012, *Science*, 338, 84, doi: [10.1126/science.1225506](https://doi.org/10.1126/science.1225506)
- Michail, J. M., Wardle, M., Yusef-Zadeh, F., & Kunneriath, D. 2021a, *ApJ*, 923, 54, doi: [10.3847/1538-4357/ac2d2c](https://doi.org/10.3847/1538-4357/ac2d2c)
- . 2021b, *ApJ*, 923, 54, doi: [10.3847/1538-4357/ac2d2c](https://doi.org/10.3847/1538-4357/ac2d2c)
- Miyazaki, A., Tsutsumi, T., & Tsuboi, M. 2004, *ApJ*, 611, L97, doi: [10.1086/424004](https://doi.org/10.1086/424004)
- Moran, J. M. 2008, in *Astronomical Society of the Pacific Conference Series*, Vol. 395, *Frontiers of Astrophysics: A Celebration of NRAO's 50th Anniversary*, ed. A. H. Bridle, J. J. Condon, & G. C. Hunt, 87. <https://arxiv.org/abs/0804.1063>
- Mori, K., Gotthelf, E. V., Zhang, S., et al. 2013, *ApJL*, 770, L23, doi: [10.1088/2041-8205/770/2/L23](https://doi.org/10.1088/2041-8205/770/2/L23)
- Morris, M. R., Meyer, L., & Ghez, A. M. 2012, *Research in Astronomy and Astrophysics*, 12, 995, doi: [10.1088/1674-4527/12/8/007](https://doi.org/10.1088/1674-4527/12/8/007)
- Mościbrodzka, M., Falcke, H., Shiokawa, H., & Gammie, C. F. 2014, *A&A*, 570, A7, doi: [10.1051/0004-6361/201424358](https://doi.org/10.1051/0004-6361/201424358)

- Mościbrodzka, M., Gammie, C. F., Dolence, J. C., Shiokawa, H., & Leung, P. K. 2009a, *ApJ*, 706, 497, doi: [10.1088/0004-637X/706/1/497](https://doi.org/10.1088/0004-637X/706/1/497)
- . 2009b, *ApJ*, 706, 497, doi: [10.1088/0004-637X/706/1/497](https://doi.org/10.1088/0004-637X/706/1/497)
- Mossoux, E., Grosso, N., Bushouse, H., et al. 2016, *AAP*, 589, A116, doi: [10.1051/0004-6361/201527554](https://doi.org/10.1051/0004-6361/201527554)
- Moy, E., & Rocca-Volmerange, B. 2002, *A&A*, 383, 46, doi: [10.1051/0004-6361:20011727](https://doi.org/10.1051/0004-6361:20011727)
- Murchikova, L., & Witzel, G. 2021, *ApJ*, 920, L7, doi: [10.3847/2041-8213/ac2308](https://doi.org/10.3847/2041-8213/ac2308)
- Nagai, H., Onishi, K., Kawakatu, N., et al. 2019, *ApJ*, 883, 193, doi: [10.3847/1538-4357/ab3e6e](https://doi.org/10.3847/1538-4357/ab3e6e)
- Neilsen, J., Nowak, M. A., Gammie, C., et al. 2013a, *ApJ*, 774, 42, doi: [10.1088/0004-637X/774/1/42](https://doi.org/10.1088/0004-637X/774/1/42)
- . 2013b, *ApJ*, 774, 42, doi: [10.1088/0004-637X/774/1/42](https://doi.org/10.1088/0004-637X/774/1/42)
- . 2013c, *ApJ*, 774, 42, doi: [10.1088/0004-637X/774/1/42](https://doi.org/10.1088/0004-637X/774/1/42)
- . 2013d, *ApJ*, 774, 42, doi: [10.1088/0004-637X/774/1/42](https://doi.org/10.1088/0004-637X/774/1/42)
- Neilsen, J., Markoff, S., Nowak, M. A., et al. 2015a, *ApJ*, 799, 199, doi: [10.1088/0004-637X/799/2/199](https://doi.org/10.1088/0004-637X/799/2/199)
- . 2015b, *ApJ*, 799, 199, doi: [10.1088/0004-637X/799/2/199](https://doi.org/10.1088/0004-637X/799/2/199)
- Niinuma, K., Lee, S.-S., Kino, M., & Sohn, B. W. 2015, *Publication of Korean Astronomical Society*, 30, 637, doi: [10.5303/PKAS.2015.30.2.637](https://doi.org/10.5303/PKAS.2015.30.2.637)
- North, E. V., Davis, T. A., Bureau, M., et al. 2019, *MNRAS*, 490, 319, doi: [10.1093/mnras/stz2598](https://doi.org/10.1093/mnras/stz2598)
- Nowak, M. A., Neilsen, J., Markoff, S. B., et al. 2012a, *ApJ*, 759, 95, doi: [10.1088/0004-637X/759/2/95](https://doi.org/10.1088/0004-637X/759/2/95)
- . 2012b, *ApJ*, 759, 95, doi: [10.1088/0004-637X/759/2/95](https://doi.org/10.1088/0004-637X/759/2/95)
- . 2012c, *ApJ*, 759, 95, doi: [10.1088/0004-637X/759/2/95](https://doi.org/10.1088/0004-637X/759/2/95)
- Onishi, K., Iguchi, S., Davis, T. A., et al. 2017, *MNRAS*, 468, 4663, doi: [10.1093/mnras/stx631](https://doi.org/10.1093/mnras/stx631)
- Onishi, K., Iguchi, S., Sheth, K., & Kohno, K. 2015, *ApJ*, 806, 39, doi: [10.1088/0004-637X/806/1/39](https://doi.org/10.1088/0004-637X/806/1/39)
- Padin, S., Woody, D. P., Hodges, M. W., et al. 1990, *ApJ*, 360, L11, doi: [10.1086/185800](https://doi.org/10.1086/185800)

- Pechetti, R., Seth, A., Neumayer, N., et al. 2020, *ApJ*, 900, 32, doi: [10.3847/1538-4357/abaaa7](https://doi.org/10.3847/1538-4357/abaaa7)
- Peißker, F., Zajaček, M., Eckart, A., et al. 2021, *ApJ*, 923, 69, doi: [10.3847/1538-4357/ac23df](https://doi.org/10.3847/1538-4357/ac23df)
- Ponti, G., De Marco, B., Morris, M. R., et al. 2015, *MNRAS*, 454, 1525, doi: [10.1093/mnras/stv1537](https://doi.org/10.1093/mnras/stv1537)
- Ponti, G., George, E., Scaringi, S., et al. 2017a, *MNRAS*, 468, 2447, doi: [10.1093/mnras/stx596](https://doi.org/10.1093/mnras/stx596)
- . 2017b, *MNRAS*, 468, 2447, doi: [10.1093/mnras/stx596](https://doi.org/10.1093/mnras/stx596)
- Ponti, G., Hofmann, F., Churazov, E., et al. 2019, *Nature*, 567, 347, doi: [10.1038/s41586-019-1009-6](https://doi.org/10.1038/s41586-019-1009-6)
- Porquet, D., Grosso, N., Predehl, P., et al. 2008, *A&A*, 488, 549, doi: [10.1051/0004-6361:200809986](https://doi.org/10.1051/0004-6361:200809986)
- Primiani, R. A., Young, K. H., Young, A., et al. 2016, *Journal of Astronomical Instrumentation*, 5, 1641006, doi: [10.1142/S2251171716410063](https://doi.org/10.1142/S2251171716410063)
- Proga, D., & Kallman, T. R. 2004, *ApJ*, 616, 688, doi: [10.1086/425117](https://doi.org/10.1086/425117)
- Quataert, E. 2002a, *ApJ*, 575, 855, doi: [10.1086/341425](https://doi.org/10.1086/341425)
- . 2002b, *ApJ*, 575, 855, doi: [10.1086/341425](https://doi.org/10.1086/341425)
- . 2004, *ApJ*, 613, 322, doi: [10.1086/422973](https://doi.org/10.1086/422973)
- Quataert, E., & Gruzinov, A. 2000, *ApJ*, 539, 809, doi: [10.1086/309267](https://doi.org/10.1086/309267)
- Rauch, C., Ros, E., Krichbaum, T. P., et al. 2016, *A&A*, 587, A37, doi: [10.1051/0004-6361/201527286](https://doi.org/10.1051/0004-6361/201527286)
- Rea, N., Esposito, P., Pons, J. A., et al. 2013, *ApJL*, 775, L34, doi: [10.1088/2041-8205/775/2/L34](https://doi.org/10.1088/2041-8205/775/2/L34)
- Rea, N., Coti Zelati, F., Viganò, D., et al. 2020, *ApJ*, 894, 159, doi: [10.3847/1538-4357/ab8387](https://doi.org/10.3847/1538-4357/ab8387)
- Reid, M. J., & Brunthaler, A. 2004, *ApJ*, 616, 872, doi: [10.1086/424960](https://doi.org/10.1086/424960)
- . 2020, *ApJ*, 892, 39, doi: [10.3847/1538-4357/ab76cd](https://doi.org/10.3847/1538-4357/ab76cd)
- Ressler, S. M., Quataert, E., & Stone, J. M. 2020, *MNRAS*, 492, 3272, doi: [10.1093/mnras/stz3605](https://doi.org/10.1093/mnras/stz3605)
- Ripperda, B., Liska, M., Chatterjee, K., et al. 2022, *ApJ*, 924, L32, doi: [10.3847/2041-8213/ac46a1](https://doi.org/10.3847/2041-8213/ac46a1)

- Rowan, M. E., Sironi, L., & Narayan, R. 2017, *ApJ*, 850, 29, doi: [10.3847/1538-4357/aa9380](https://doi.org/10.3847/1538-4357/aa9380)
- Saintonge, A., Kauffmann, G., Kramer, C., et al. 2011, *MNRAS*, 415, 32, doi: [10.1111/j.1365-2966.2011.18677.x](https://doi.org/10.1111/j.1365-2966.2011.18677.x)
- Saintonge, A., Tacconi, L. J., Fabello, S., et al. 2012, *ApJ*, 758, 73, doi: [10.1088/0004-637X/758/2/73](https://doi.org/10.1088/0004-637X/758/2/73)
- Salpeter, E. E. 1964, *ApJ*, 140, 796, doi: [10.1086/147973](https://doi.org/10.1086/147973)
- Sandstrom, K. M., Leroy, A. K., Walter, F., et al. 2013, *ApJ*, 777, 5, doi: [10.1088/0004-637X/777/1/5](https://doi.org/10.1088/0004-637X/777/1/5)
- Scargle, J. D. 1998, *ApJ*, 504, 405, doi: [10.1086/306064](https://doi.org/10.1086/306064)
- Scargle, J. D. 1998, *The Astrophysical Journal*, 504, 405, doi: [10.1086/306064](https://doi.org/10.1086/306064)
- Scargle, J. D., Norris, J. P., Jackson, B., & Chiang, J. 2013a, *ApJ*, 764, 167, doi: [10.1088/0004-637X/764/2/167](https://doi.org/10.1088/0004-637X/764/2/167)
- . 2013b, *ApJ*, 764, 167, doi: [10.1088/0004-637X/764/2/167](https://doi.org/10.1088/0004-637X/764/2/167)
- Schmidt, M. 1963, *Nature*, 197, 1040, doi: [10.1038/1971040a0](https://doi.org/10.1038/1971040a0)
- Schödel, R., Morris, M. R., Muzic, K., et al. 2011, *A&A*, 532, A83, doi: [10.1051/0004-6361/201116994](https://doi.org/10.1051/0004-6361/201116994)
- Serabyn, E., Carlstrom, J., Lay, O., et al. 1997a, *ApJL*, 490, L77, doi: [10.1086/311010](https://doi.org/10.1086/311010)
- . 1997b, *ApJ*, 490, L77, doi: [10.1086/311010](https://doi.org/10.1086/311010)
- Shahzamanian, B., Eckart, A., Valencia-S., M., et al. 2015, *AAP*, 576, A20, doi: [10.1051/0004-6361/201425239](https://doi.org/10.1051/0004-6361/201425239)
- Shcherbakov, R. V., Penna, R. F., & McKinney, J. C. 2012a, *ApJ*, 755, 133, doi: [10.1088/0004-637X/755/2/133](https://doi.org/10.1088/0004-637X/755/2/133)
- . 2012b, *ApJ*, 755, 133, doi: [10.1088/0004-637X/755/2/133](https://doi.org/10.1088/0004-637X/755/2/133)
- Smith, M. D., Bureau, M., Davis, T. A., et al. 2019, *MNRAS*, 485, 4359, doi: [10.1093/mnras/stz625](https://doi.org/10.1093/mnras/stz625)
- . 2021, *MNRAS*, 500, 1933, doi: [10.1093/mnras/staa3274](https://doi.org/10.1093/mnras/staa3274)
- Stone, J. M., Marrone, D. P., Dowell, C. D., et al. 2016, *ApJ*, 825, 32, doi: [10.3847/0004-637X/825/1/32](https://doi.org/10.3847/0004-637X/825/1/32)
- Su, K.-Y., Hopkins, P. F., Bryan, G. L., et al. 2021, *MNRAS*, 507, 175, doi: [10.1093/mnras/stab2021](https://doi.org/10.1093/mnras/stab2021)

- Su, M., & Finkbeiner, D. P. 2012, *ApJ*, 753, 61, doi: [10.1088/0004-637X/753/1/61](https://doi.org/10.1088/0004-637X/753/1/61)
- Su, M., Slatyer, T. R., & Finkbeiner, D. P. 2010, *ApJ*, 724, 1044, doi: [10.1088/0004-637X/724/2/1044](https://doi.org/10.1088/0004-637X/724/2/1044)
- Subroweit, M., García-Marín, M., Eckart, A., et al. 2017, *A&A*, 601, A80, doi: [10.1051/0004-6361/201628530](https://doi.org/10.1051/0004-6361/201628530)
- Telesco, C. M., Davidson, J. A., & Werner, M. W. 1996, *ApJ*, 456, 541, doi: [10.1086/176678](https://doi.org/10.1086/176678)
- The Astropy Collaboration, Price-Whelan, A. M., Sipőcz, B. M., et al. 2018, ArXiv e-prints. <https://arxiv.org/abs/1801.02634>
- Trap, G., Goldwurm, A., Dodds-Eden, K., et al. 2011, *AAP*, 528, A140, doi: [10.1051/0004-6361/201015157](https://doi.org/10.1051/0004-6361/201015157)
- Trippe, S., Paumard, T., Ott, T., et al. 2007, *MNRAS*, 375, 764, doi: [10.1111/j.1365-2966.2006.11338.x](https://doi.org/10.1111/j.1365-2966.2006.11338.x)
- Turner, M. L., Côté, P., Ferrarese, L., et al. 2012, *ApJS*, 203, 5, doi: [10.1088/0067-0049/203/1/5](https://doi.org/10.1088/0067-0049/203/1/5)
- Čadež, A., Calvani, M., & Kostić, U. 2008, *AAP*, 487, 527, doi: [10.1051/0004-6361:200809483](https://doi.org/10.1051/0004-6361:200809483)
- Valenti, E., Zoccali, M., Mucciarelli, A., et al. 2018, *A&A*, 616, A83, doi: [10.1051/0004-6361/201832905](https://doi.org/10.1051/0004-6361/201832905)
- van den Eijnden, J., A, A., B, B., & C, C. 2021, in prep., 00, 0, doi: TBD
- van der Laan, H. 1966, *Nature*, 211, 1131, doi: [10.1038/2111131a0](https://doi.org/10.1038/2111131a0)
- Čadež, A., Calvani, M., & Kostić, U. 2008, *A&A*, 487, 527, doi: [10.1051/0004-6361:200809483](https://doi.org/10.1051/0004-6361:200809483)
- Verner, D. A., Ferland, G. J., Korista, K. T., & Yakovlev, D. G. 1996, *ApJ*, 465, 487, doi: [10.1086/177435](https://doi.org/10.1086/177435)
- Vertatschitsch, L., Primiani, R., Young, A., et al. 2015, *PASP*, 127, 1226, doi: [10.1086/684513](https://doi.org/10.1086/684513)
- von Fellenberg, S. D., Gillessen, S., Graciá-Carpio, J., et al. 2018a, *ApJ*, 862, 129, doi: [10.3847/1538-4357/aacd4b](https://doi.org/10.3847/1538-4357/aacd4b)
- . 2018b, *ApJ*, 862, 129, doi: [10.3847/1538-4357/aacd4b](https://doi.org/10.3847/1538-4357/aacd4b)
- Wajima, K., Hagiwara, Y., An, T., et al. 2016, *The East-Asian VLBI Network*, ed. L. Qain & D. Li, Vol. 502 (Astronomical Society of the Pacific Conference Series), 81

- Wang, Q. D., Nowak, M. A., Markoff, S. B., et al. 2013a, *Science*, 341, 981, doi: [10.1126/science.1240755](https://doi.org/10.1126/science.1240755)
- . 2013b, *Science*, 341, 981, doi: [10.1126/science.1240755](https://doi.org/10.1126/science.1240755)
- Weisskopf, M. C., Brinkman, B., Canizares, C., et al. 2002, *PASP*, 114, 1, doi: [10.1086/338108](https://doi.org/10.1086/338108)
- Weisskopf, M. C., Tananbaum, H. D., Van Speybroeck, L. P., & O’Dell, S. L. 2000, in *SPIE*, Vol. 4012, *X-Ray Optics, Instruments, and Missions III*, ed. J. E. Truemper & B. Aschenbach, 2–16, doi: [10.1117/12.391545](https://doi.org/10.1117/12.391545)
- Werner, M. W., Roellig, T. L., Low, F. J., et al. 2004, *ApJS*, 154, 1, doi: [10.1086/422992](https://doi.org/10.1086/422992)
- Whitney, A. R., Beaudoin, C. J., Cappallo, R. J., et al. 2013, *PASP*, 125, 196, doi: [10.1086/669718](https://doi.org/10.1086/669718)
- Wielgus, M., Marchili, N., Martí-Vidal, I., et al. 2022, accepted by *ApJL*, 00, 0, doi: TBD
- Williams, P. K. G., Clavel, M., Newton, E., & Ryzhkov, D. 2017a, pwkit: Astronomical utilities in Python, *Astrophysics Source Code Library*. <http://ascl.net/1704.001>
- Williams, P. K. G., Clavel, M., Newton, E., & Ryzhkov, D. 2017b, pwkit: Astronomical utilities in Python. <http://ascl.net/1704.001>
- Wilms, J., Allen, A., & McCray, R. 2000, *ApJ*, 542, 914, doi: [10.1086/317016](https://doi.org/10.1086/317016)
- Witzel, G., Eckart, A., Buchholz, R. M., et al. 2011, *AAP*, 525, A130, doi: [10.1051/0004-6361/201015009](https://doi.org/10.1051/0004-6361/201015009)
- Witzel, G., Eckart, A., Bremer, M., et al. 2012a, *ApJS*, 203, 18, doi: [10.1088/0067-0049/203/2/18](https://doi.org/10.1088/0067-0049/203/2/18)
- . 2012b, *ApJS*, 203, 18, doi: [10.1088/0067-0049/203/2/18](https://doi.org/10.1088/0067-0049/203/2/18)
- Witzel, G., Morris, M., Ghez, A., et al. 2014, in *IAU Symposium*, Vol. 303, *The Galactic Center: Feeding and Feedback in a Normal Galactic Nucleus*, ed. L. O. Sjouwerman, C. C. Lang, & J. Ott, 274–282, doi: [10.1017/S1743921314000738](https://doi.org/10.1017/S1743921314000738)
- Witzel, G., Martinez, G., Hora, J., et al. 2018a, *ApJ*, 863, 15, doi: [10.3847/1538-4357/aace62](https://doi.org/10.3847/1538-4357/aace62)
- . 2018b, *ApJ*, 863, 15, doi: [10.3847/1538-4357/aace62](https://doi.org/10.3847/1538-4357/aace62)
- . 2018c, *ApJ*, 863, 15, doi: [10.3847/1538-4357/aace62](https://doi.org/10.3847/1538-4357/aace62)
- Witzel, G., Martinez, G., Willner, S. P., et al. 2021a, *ApJ*, 917, 73, doi: [10.3847/1538-4357/ac0891](https://doi.org/10.3847/1538-4357/ac0891)
- . 2021b, *ApJ*, 917, 73, doi: [10.3847/1538-4357/ac0891](https://doi.org/10.3847/1538-4357/ac0891)

- Wright, M. C. H., Genzel, R., Güsten, R., & Jaffe, D. T. 1987, in *American Institute of Physics Conference Series*, Vol. 155, *The Galactic Center*, ed. D. C. Backer, 133–137, doi: [10.1063/1.36411](https://doi.org/10.1063/1.36411)
- Xu, Y.-D., Narayan, R., Quataert, E., Yuan, F., & Baganoff, F. K. 2006a, *ApJ*, 640, 319, doi: [10.1086/499932](https://doi.org/10.1086/499932)
- . 2006b, *ApJ*, 640, 319, doi: [10.1086/499932](https://doi.org/10.1086/499932)
- Yoon, D., Chatterjee, K., Markoff, S. B., et al. 2020, *MNRAS*, 499, 3178, doi: [10.1093/mnras/staa3031](https://doi.org/10.1093/mnras/staa3031)
- Yoon, I. 2017, *MNRAS*, 466, 1987, doi: [10.1093/mnras/stw3171](https://doi.org/10.1093/mnras/stw3171)
- Young, A., Primiani, R., Weintroub, J., et al. 2016, in *Phased Array Systems and Technology (ARRAY, E1)*, doi: [10.1109/ARRAY.2016.7832576](https://doi.org/10.1109/ARRAY.2016.7832576)
- Younsi, Z., & Wu, K. 2015, *MNRAS*, 454, 3283, doi: [10.1093/mnras/stv2203](https://doi.org/10.1093/mnras/stv2203)
- Yuan, F., Quataert, E., & Narayan, R. 2003a, *ApJ*, 598, 301, doi: [10.1086/378716](https://doi.org/10.1086/378716)
- . 2003b, *ApJ*, 598, 301, doi: [10.1086/378716](https://doi.org/10.1086/378716)
- Yusef-Zadeh, F., Bushouse, H., Schödel, R., et al. 2015a, *ApJ*, 809, 10, doi: [10.1088/0004-637X/809/1/10](https://doi.org/10.1088/0004-637X/809/1/10)
- . 2015b, *ApJ*, 809, 10, doi: [10.1088/0004-637X/809/1/10](https://doi.org/10.1088/0004-637X/809/1/10)
- Yusef-Zadeh, F., Morris, M., & Ekers, R. D. 1990, *Nature*, 348, 45, doi: [10.1038/348045a0](https://doi.org/10.1038/348045a0)
- Yusef-Zadeh, F., Roberts, D., Wardle, M., Heinke, C. O., & Bower, G. C. 2006a, *ApJ*, 650, 189, doi: [10.1086/506375](https://doi.org/10.1086/506375)
- Yusef-Zadeh, F., Wardle, M., Cotton, W. D., Heinke, C. O., & Roberts, D. A. 2007, *ApJL*, 668, L47, doi: [10.1086/522622](https://doi.org/10.1086/522622)
- Yusef-Zadeh, F., Wardle, M., Miller-Jones, J. C. A., et al. 2011, *ApJ*, 729, 44, doi: [10.1088/0004-637X/729/1/44](https://doi.org/10.1088/0004-637X/729/1/44)
- Yusef-Zadeh, F., Bushouse, H., Dowell, C. D., et al. 2006b, *ApJ*, 644, 198, doi: [10.1086/503287](https://doi.org/10.1086/503287)
- Yusef-Zadeh, F., Bushouse, H., Wardle, M., et al. 2009, *ApJ*, 706, 348, doi: [10.1088/0004-637X/706/1/348](https://doi.org/10.1088/0004-637X/706/1/348)
- Yusef-Zadeh, F., Wardle, M., Dodds-Eden, K., et al. 2012a, *AJ*, 144, 1, doi: [10.1088/0004-6256/144/1/1](https://doi.org/10.1088/0004-6256/144/1/1)

- Yusef-Zadeh, F., Arendt, R., Bushouse, H., et al. 2012b, *ApJ*, 758, L11, doi: [10.1088/2041-8205/758/1/L11](https://doi.org/10.1088/2041-8205/758/1/L11)
- Zel'dovich, Y. B. 1964, *Soviet Physics Doklady*, 9, 195
- Zhang, S., Baganoff, F. K., Ponti, G., et al. 2017a, *ApJ*, 843, 96, doi: [10.3847/1538-4357/aa74e8](https://doi.org/10.3847/1538-4357/aa74e8)
- . 2017b, *ApJ*, 843, 96, doi: [10.3847/1538-4357/aa74e8](https://doi.org/10.3847/1538-4357/aa74e8)
- . 2017c, *ApJ*, 843, 96, doi: [10.3847/1538-4357/aa74e8](https://doi.org/10.3847/1538-4357/aa74e8)
- Zhao, J.-H., Young, K. H., Herrnstein, R. M., et al. 2003, *ApJ*, 586, L29, doi: [10.1086/374581](https://doi.org/10.1086/374581)
- Zheng, W. 2015, in *IAU General Assembly*, Vol. 29, 2255896
- Zhu, Z., Li, Z., Morris, M. R., Zhang, S., & Liu, S. 2019, *ApJ*, 875, 44, doi: [10.3847/1538-4357/ab0e05](https://doi.org/10.3847/1538-4357/ab0e05)
- Zubovas, K., Nayakshin, S., & Markoff, S. 2012, *MNRAS*, 421, 1315, doi: [10.1111/j.1365-2966.2011.20389.x](https://doi.org/10.1111/j.1365-2966.2011.20389.x)
- Zubovas, K., Nayakshin, S., & Markoff, S. 2012, *Monthly Notices of the Royal Astronomical Society*, 421, 1315, doi: [10.1111/j.1365-2966.2011.20389.x](https://doi.org/10.1111/j.1365-2966.2011.20389.x)
- Zylka, R., & Mezger, P. G. 1988, *A&A*, 190, L25
- Zylka, R., Mezger, P. G., & Lesch, H. 1992, *A&A*, 261, 119
- Zylka, R., Mezger, P. G., Ward-Thompson, D., Duschl, W. J., & Lesch, H. 1995, *A&A*, 297, 83. <https://arxiv.org/abs/astro-ph/9410086>